Molecular pathways of silica nanoparticle formation and biosilicification

Dominique Jeannette Tobler

Submitted in accordance with the requirements
for the degree of Doctor of Philosophy

The University of Leeds

School of Earth and Environment

May 2008

The candidate confirms that the work submitted is her own, except where work which has formed part of jointly-authored publications has been included. The contribution of the candidate and the other authors to this work has been explicitly indicated overleaf. The candidate confirms that appropriate credit has been given within the thesis where reference has been made to the work of others.

DECLARATION

Chapter 4 reproduces a manuscript in revision with *Geobiology:*

Tobler D. J., Stefánsson A. and Benning L. G. (2008, in revision) *In-situ* grown silica sinters in Icelandic geothermal areas.

Fieldwork was completed by DJT and LGB in various Icelandic geothermal areas. DJT was also assisted in the field by AS; AS collected slides at various time intervals and from various field sites which allowed long-term sinter growth experiments. The analyses of *in-situ* grown sinters and collected geothermal waters along with data interpretation, writing and production of figures were completed by DJT.

Chapter 5 reproduces a manuscript in preparation for submission to *Environmental Microbiology:*

Tobler D. J., Bailley X. and Benning L. G. (in prep) The effects of temperature, salinity, pH and sinter growth on microbial diversity in Icelandic geothermal waters.

Sample collection for 16S rDNA analyses was carried out in combination with the field experiments described in chapter 4 by DJT and LGB. The extraction of microbial DNA, PCR amplification and cloning was carried out by DJT and LGB in the Wairakei Analytical Laboratory at GNS Science, Taupo, NZ (under the supervision of Matthew Stott). For data analysis, DJT was assisted by XB; XB gave essential advice on how to analyse the sequence data (e.g., software packages, basic knowledge of phylogenetic trees). Data interpretation, writing and production of figures were completed by DJT, except where referenced in the text.

Chapter 6 reproduces a manuscript in the final stages of preparation for submission to *Geochimica et Cosmochimica Acta:*

Tobler D. J., Shaw S. and Benning L. G. (in prep) Quantification of initial steps of nucleation and growth of silica nanoparticles: an *in-situ* SAXS and DLS study.

In-situ SAXS experiments were completed by DJT, SS and LGB. SAXS data analysis was assisted by LGB and SS. All other laboratory work (e.g., DLS, SEM, (cryo-)TEM and solution analysis) and original interpretations were done by DJT. Discussion with co-authors helped to shape the ideas.

Chapter 7 reproduces a manuscript in preparation for submission to *Geochimica et Cosmochimica Acta:*

Tobler D. J. and Benning L. G. (in prep) The nucleation and growth of silica nanoparticles induced by cooling a supersaturated solution: an *in-situ* SAXS and DLS study.

In-situ SAXS experiments were completed by DJT and LGB. All other laboratory work (e.g., DLS, SEM, TEM and solution analysis), data analyses and original interpretations were done by DJT.

Chapter 8 in part reproduces an extended abstract accepted for publication as part of the 8th symposium on the Geochemistry of the Earth's Surface (August 2008)

Tobler D. J., Benning L. G. and Knapp J. (2008, accepted) The size and polydispersity of silica nanoparticles under simulated hot spring conditions.

The experiments were based on original ideas by LGB which were subsequently modified by DJT. The laboratory work and data analysis and interpretation were completed by DJT; discussions with co-authors helped to shape the ideas.

ACKNOWLEDGMENTS

Even though it is my name that figures on the front page of this thesis, completing it would not have been possible without invaluable help received from a number of people to whom I would like to express my gratitude.

Liane Benning for her enthusiastic and tireless guidance and support; for giving me endless opportunities to gain new experiences and to travel the world. Sincere thanks also to Jerry Knapp for supervision and for providing many helpful discussions.

Sam Shaw and Lois Davidson for helping with the analysis and the interpretation of SAXS data and for many valuable discussions.

Stefan Arnorsson, Andri Stefansson and Hanna Sisko Kaasalainen from the University of Iceland for arranging field logistics in Iceland and their assistance with sample collection. Thanks also to Vernon Phoenix for helpful advice and many "jolly" moments in Iceland.

Matthew Stott, Peter Dunfield and Michelle Crowe from GNS Science, Taupo for providing lab equipment and extensive help with the molecular biology work. Thanks also to Bruce Mountain for hosting me during my visit in Taupo and for field work assistance and ICP-OES analyses.

Peter Young and Xavier Bailley from the University of York for giving me essential advice and help on the analysis of bacterial DNA sequences.

John Harrington, Adrian Hick and David Parcej for their assistance with FEG-SEM, TEM and cryo-TEM work, respectively. Thanks also to Susanne Patel and Jennifer Green for help with DLS logistics, Stefan Hunger who carried out the IC analyses, and to Phil Fields and Anthony Windross from the workshop for their help with the set-up of my simulated hot spring.

I am sincerely grateful to EBI for sponsoring my PhD thesis and I would also like to thank The Geochemical Society, The Geochemistry Group, The Geological Society, The Society for General Microbiology, The Royal Society of Chemical Industry, and The Mineralogical Society for grants awarded during my PhD.

Many thanks to my uni friends Matt, Rachel, Rachael, Ian and James for sharing three years of tension and exasperation as well as many happy and invaluable memories.

And not least, I would like to thank my family; Mum, Dad, Nicole and Marco, and my close friends; Eleanor, Fiona, Vhairi and Helen for all your support and for keeping me smiling during this time.

ABSTRACT

Biosilicification and silica nanoparticle formation occur in many modern terrestrial environments and they also played an important role in ancient geological settings. This thesis presents results from (i) field studies in Icelandic geothermal waters that aimed at quantifying the parameters that control the growth rate and texture of sinters and the diversity and silicification of associated microbial communities and (ii) lab studies that focussed on the kinetics and mechanisms of silica nanoparticle formation under conditions mimicking natural geothermal environments.

The analysis of growth rates and textures of sinters from five geochemically very different Icelandic geothermal areas showed that the inorganic silica precipitation rate was strongly influenced by temperature, pH, ionic strength, and silica concentration. In addition, the presence of thick biofilms seemed to have aided the precipitation process by simply providing "sticky" surfaces. In turn, the structural and textural development of sinters was affected by the precipitation rate and mechanism (subaqueously and/or subaerially) as well as the presence and absence of microbial communities. As a result, porous, subaequeous sinters developed at sites with medium to high sinter growth rates and low microbial activity. Conversely, dense, heterogeneous sinters formed in geothermal waters characterized by low precipitation rates and extensive biofilms. With time these biofilms became fully silicified and well preserved within the sinter edifices. The diversity of microbial communities in hot spring environments appeared to be directly controlled by the physico-chemical conditions of the geothermal waters (i.e., T, pH, salinity and sinter growth rate) and the most dominant phylotypes were related to *Aquificae*, *Deinococci* and $\gamma-$*Proteobacteria*.

The rates and mechanisms of the initial steps of silica polymerisation and silica nanoparticle formation were quantified *in-situ* and time-resolved using synchrotron-based small angle x-ray scattering (SAXS). The experiments were carried out in near neutral pH solutions with initial SiO_2 between 640 – 1600 ppm, ionic strength of 0.02 – 0.22 M, and added organics (glucose, glutamic acid, xanthan gum). The polymerization reactions were induced either by neutralising a high pH solution or by rapid cooling of a supersaturated hot silica solution. From the analysis of the time-resolved SAXS data, a kinetic model for the nucleation and growth of silica nanoparticles was derived suggesting a 3 stage process: (1) homogeneous nucleation of critical nuclei (1 - 2 nm; depending on the concentration regimes), (2) 3-dimensional, surface-controlled particle growth following 1^{st} order reaction kinetics and (3) Ostwald ripening and particle aggregation. At the end of this 3-stage process, regardless of the tested silica concentration, ionic strength or added organics, the final particle diameter was about 8nm characterised by

open, polymeric (i.e., mass fractal) structures. The kinetics of particle growth were unaffected by the two different methods to induce silica polymerisation (pH-drop vs. T-drop) however, the growth processes proceeded substantially slower if silica polymerisation was induced by fast cooling as opposed to pH-drop. In contrast, the addition of organics did not affect the reaction rates.

The nucleation and growth of silica nanoparticles under constant re-supply of fresh silica solution (i.e., hot springs) was simulated using a flow-through geothermal simulator system. The effect of silica concentration ($[SiO_2]$), ionic strength (IS), temperature and organic additives on the size and polydispersity of silica nanoparticles was quantified. While the applied increase in IS did not affect the size (30 - 35 nm) and polydispersity (± 9 nm) observed at 58°C, an increase in $[SiO_2]$ notably enhanced silica polymerisation and also resulted in slightly smaller particle sizes. The biggest effect was observed with a decrease in temperature (58 to 33°C) or the addition of glucose: in both cases particle growth was restricted to sizes below 20 nm. Conversely, the addition of xanthan gum induced the development of a thin silica-rich film that enhanced silica aggregation.

LIST OF CONTENTS

LIST OF FIGURES

LIST OF TABLES

LIST OF EQUATIONS

No.	Equation	Term definition	Description
2.1	$H_4SiO_4 + H_4SiO_4 \rightarrow$ $(HO)_3Si–O-Si(OH)_3 + H_2O$	-	The initial steps of silica polymerisation occur via the coalescence of two monosilicic acid molecules (H_4SiO_4) and the expulsion of water.
2.2	$R_0 = 2V_m\sigma / R_cT\ln(S+1)$	R_0 is the critical nucleus radius, V_m is the molar volume, σ is the surface tension, R_c is the gas constant, and S is the supersaturation defined as $S = (C - C_s)/C_s$ with C being the actual concentration and C_s the solubility.	The Gibbs-Kelvin equation (Gibbs, 1961).
2.3	$-dC/dt = k(C - C_s)^{n_r}$	k is the rate constant, C is the concentration of monosilicic acid, C_s is the solubility of amorphous silica at a given temperature and n_r is the reaction order.	The rate equation mostly used to describe the time dependent depletion of monosilicic acid, i.e., the process of silica polymerisation.
3.1	$d(H) = KT/3\pi\eta D$	$d(H)$ is the hydrodynamic diameter, K is the Boltzmann constant, T is the absolute temperature (K), η is the viscosity of the fluid and D is the translational diffusion coefficient.	The Stokes-Einstein equation used in DLS to obtain particle size information.

3.2	$I(q) = \frac{N}{V} V_p^{\,2} (\Delta\rho)^2 P(q) S(q)$	$I(q)$ is the scattering intensity, N is the number of scattering particles, V is the irradiated volume, V_p is the volume of individual scattering entity, $\Delta\rho=\rho_p-\rho_s$ is the electron density contrast between solute and solvent, $P(q)$ is the form factor, and $S(q)$ is the structure factor.	Describes the behaviour of the scattered intensity as a function of the scattering vector q.
3.3	$I(q) = I_0 e^{\frac{-q^2 R_g^{\,2}}{3}}$	$I(q)$ is the scattering intensity, I_0 is the scattering intensity at q=0, Rg is the radius of gyration (Å).	The Guinier approximation used to determine Rg from the Guinier plot ln $I(q)$ *vs.* q^2.
3.4	$Rg^2 = \frac{3}{5} R^2$	R is the "true" particle radius of a sphere (Å).	The relationship between the radius of gyration and the "true" particle radius assuming a monodisperse system with spherical particles.
3.5	$Q = 2\pi^2 (\Delta\rho)^2 V$	Q is the invariant and $\Delta\rho$ is the electron density contrast.	The invariant is proportional to the total scattering volume and the mean-square electron density fluctuation.
3.6	$\alpha = 1 - e^{-(k(t-t_0))^n}$	a is the degree of the reaction, t_0 is the induction time (s), k is the rate constant (s^{-1}) and n is a constant related to the nucleation and reaction mechanisms and the growth dimensionality (Hulbert, 1969).	Johnson-Mehl-Avrami-Kolmogorov (JMAK) kinetic model (Johnson and Mehl, 1939; Avrami, 1939, 1940; Kolmogorov, 1937).
3.7	$\alpha = \frac{Rg^3{}_t}{Rg^3{}_{\max}}$	Rg_t is Rg at a given time, t(s), and Rg_{max} is Rg at the end of the reaction	Normalisation of the SAXS data according to the radius of gyration.

3.8	$k = \frac{G_0}{S_R - 1}$	S_R is the saturation ratio which is defined as $S_R = SI^{1/\nu}$. SI is the saturation index and ν is the stoichiometric coefficient (i.e., the sum of the stoichiometry of the products in the solubility expression).	The relationship between the rate constant, k and the initial growth rate, G_0 (s^{-1}).
3.9	$SI = IAP / K_{sp}$	IAP is the ionic activity product and K_{sp} is the solubility product.	The definition of the saturation index.

NOMENCLATURE

α	Progress of reaction (as a change in Rg^3 over time)
α_τ	Progress of reaction (as a change in I_0 over time)
η	Viscosity
λ	Wavelength
ν	Stoichiometric coefficient
θ	Scattering angle
$\Delta\rho$	Electron density contrast between solute and solvent, ρ_p-ρ_s
σ	Interfacial surface energy
C	Concentration
Cs	Solubility of amorphous silica
D	Translational diffusion coefficient
D_f	Fractal Dimension with D_m = mass fractals and D_s = surface fractals
d	Particle dimension
d(H)	Hydrodynamic particle diameter
G_0	Initial growth rate
$H_4SiO_{4(aq)}$	Monosilicic acid (i.e., monomeric / dissolved silica), also abbreviated as $SiO_2(aq)$
IAP	Ion Activity Product
IS	Ionic Strength
I(q)	Scattering Intensity
I_0	Extrapolated initial intensity of the scattering curve, I(q=0)
K	Boltzmann's constant
k	Rate constant
K_{sp}	Solubility product
m	Ostwald ripening exponent
n	JMAK exponent
n_r	Reaction order

N	Number of particles
P(q)	Form factor
p	Exponent related to the fractal dimension, D_f
T	Absolute temperature
t	Time
t_0	Induction time
Q	Invariant
q	Scattering vector
R	Particle radius
R_{max}	Maximum radius
Rg	Radius of gyration
R_0	Critical nucleus radii
R_f	Radius of the aggregate spatial dimension
R_c	Gas constant
s	Standard deviation
S	Supersaturation
SI	Saturation Index
S(q)	Structure factor
S_R	Saturation ratio
V	Scattering volume
V_p	Scattering volume of individual scattering entity (i.e., scattering particles)
V_m	Molar volume

LIST OF ACRONYMS AND ABBREVIATIONS

AWI	Air-water interface
BPR	Backpressure Regulator
BSL	A 2-D SAXS data manipulation package
CNT	Classical Nucleation Theory
CRYO-TEM	TEM-analysis in which samples are cryogenically quenched, stored and transferred
DIW	Deionised water (18 MΩ)
DLCA	Diffusion-limited Colloid Aggregation
DLS	Dynamic Light Scattering
DUBBLE	Dutch-Belgian beamline at ESRF
16S rDNA / rRNA	Small subunit (16S) ribosomal Deoxyribonucleic Acid (rDNA) / ribosomal Ribonucleic acid (rRNA); a section of prokaryotic DNA found in all bacteria and archaea
EDX	Energy Dispersive X-ray spectroscopy
EM	Electron Microscopy
EPS	Exopolysaccharide
ESRF	European Synchrotron Radiation Fascility
FEG	Field Emission Gun
GNOM	Program used for SAXS data processing (evaluates the *R*g and the PDF)
HR-TEM	High Resolution – Transmission Electron Microscopy
IC	Ion Chromatography
ICP-OES	Inductively Coupled Plasma Optical Emission Spectroscopy
JMAK	Johnson-Mehl-Avrami-Kolmogorov kinetic model
LSW	Mathematical model by Lifshitz and Slyozov (1961) and Wagner (1961) which describes Ostwald ripening
OA	Orientated Aggregation
OR	Ostwald ripening

PCR	Polymerase Chain Reaction
PDF	Pair Distribution Function
PHREEQC	Geochemical code (version 2.13.3; Parkhurst & Appelo, 1999)
RDP-II	Ribosomal Database Project II
RFLP	Restriction Fragment Length Polymorphism
RLCA	Reaction-limited Colloid Aggregation
SAXS	Small Angle X-ray Scattering
SEM	Scanning Electron Microscopy
SRS	Synchrotron Radiation Source (Daresbury Laboratories, UK)
TEM	Transmission Electron Microscopy
TEOS	Tetraalkoxysilane
WATEQ4	Database used for geochemical modelling using PHREEQC
XOTOKO	SAXS data reduction program (SRS software)
XRD	X-ray Diffraction

1 INTRODUCTION

This chapter summarizes the background and settings to the research and describes the motivation for this study. The importance of silica nanoparticle formation and biosilicification as it occurs in geothermal environments is outlined and the main aims along with the specific research objectives and a brief summary of the experimental approach are presented. The chapter ends with an outline of the thesis.

1.1 Background

The study of extreme environments and the organisms that inhabit them, i.e. extremophiles, has made the search for extinct and extant life on the ancient Earth as well as on other planets more plausible. Amongst terrestrial extreme environments, geothermal hot springs and vents and the associated silica sinters are well known analogues for early Earth conditions and several studies have characterised the structure and textures of silica sinters as well as the microbial communities thriving in these systems. These studies have shown that abundant and diverse microbial biofilms develop within and along silica-precipitating geothermal waters. With time these biofilms become completely silicified and ultimately end up being fully incorporated within the sinter rock record. The role microorganisms play in this silicification process seems minor and to date there are no signs that microorganisms influence the processes and kinetics of silica precipitation. However, microbial abundance and diversity as well as the process of microbial silicification are strongly influenced by the physico-chemical conditions of the waters in hot spring environments (e.g., temperature, pH, water chemistry) and they in turn affect sinter structure and texture as well as growth rates within individual geothermal systems. Therefore, in order to gain a more complete knowledge of the mechanisms leading to the microbial silicification and thus the preservation and fossilization of microorganisms in geothermal environments, the overall process of biosilicification has to be analysed step by step and the impact of individual parameters on each step has to be assessed. Furthermore, the rates and mechanisms of nucleation, growth and aggregation of silica nanoparticles in silica saturated geothermal waters and in the absence or presence of microbial surfaces have to be quantified.

Although silica precipitation aids microbial silicification and fossilization in geothermal environments, it is however of great disadvantage for geothermal power stations where heat extraction from fast cooling of high-temperature fluids supersaturated with silica can often lead to the formation of silica scales and thus blocking of the geothermal pipes. Therefore, a reduction or even a full inhibition of the silica scaling via appropriate handling procedures of

the geothermal waters might increase the efficiency of high-temperature geothermal resources. Again, for this a full understanding of the mechanisms and kinetics of silica polymerisation and silica nanoparticle formation as well as the parameters controlling these processes is needed.

Several experimental studies have focused on silica precipitation in inorganic natural solutions with the aim of understanding the natural formation of silica precipitates in geological settings. In most of these studies the main aim and approach was to quantify the changes in silica speciation in solution. So far, little effort has been made to quantify the formation of silica nanoparticles within the polymerising solution and to extract kinetic information on this process in the absence or presence of microorganisms and under conditions that mimic processes in geothermal settings.

Thus, there is still a need for (a) a more quantitative understanding of the formation of modern and ancient siliceous sinters (b) a more comprehensive quantification of the parameters that influence silica precipitation and microbial abundance and diversity in geothermal environments, and (c) a quantification of the mechanisms and kinetics of silica polymerisation and silica nanoparticle precipitation.

1.2 Research Objectives

The main aim of this research project was to quantify, via field and laboratory experimental studies, the molecular level mechanisms and processes leading to biosilicification in geothermal environments. The specific research objectives focused on two main elements:

(i) To quantify how geothermal solution chemistry, pH, and temperature, as well as the presence of microbial communities, affect the growth rates and structures of sinters forming in various active geothermal systems in Iceland and vice versa to link the geochemical / hydrodynamic regime with the community diversity found in these ecosystems.

(ii) To quantify the initial steps of silica polymerisation and silica nanoparticle formation in both inorganic and organic, low temperature solutions and to follow the same process under simulated hot spring conditions using microscopic, scattering and spectroscopic methods.

1.3 Experimental Approach

Details of all experimental approaches are fully described in chapter 3. Here, just a brief overview is given.

1.3.1 Field work

Field work concentrated on quantifying the sinter growth rates at several different Icelandic geothermal systems exhibiting very different physico-chemical conditions. At each location, *in-situ* sinter growth rates were quantified based on the amount of newly formed material that deposited on glass slides which acted as precipitation substrates. In addition, the morphology, textures and structures of the precipitates along with the associated microbial assemblages were characterised using electron microscopic techniques. The water chemistry at each location was analysed for cations and anions as well as total and monomeric silica contents, while powder X-ray diffraction was used to determine the mineralogy of the *in-situ* grown sinters. Finally, the diversity of the microbial assemblages was analysed and quantified using several molecular microbiology techniques.

1.3.2 Laboratory studies

For the laboratory studies, various flow-through systems, mimicking processes in active geothermal systems were developed. This permitted the quantification of the silica precipitation in both inorganic and biogenic systems. Several studies aimed at elucidating the initial steps of nucleation and growth of silica nanoparticles were carried out and the reactions were followed by a combination of solution and solid particle analyses. The nucleation and growth of the precipitating silica nanoparticles were monitored *in-situ* and in realtime using synchrotron-based Small Angle X-ray Scattering (SAXS) and conventional Dynamic Light Scattering (DLS). With both these methods, the changes in the size of growing silica nanoparticle could be followed from the very beginning of the reaction and at short time scales (seconds to minutes). These data were complemented by data from a suite of electron microscopic techniques. The microscopic data helped verify the results obtained by SAXS and DLS by providing snap-shots of the particle sizes and shapes at specific time steps during the reaction. Furthermore, the monomeric and total silica content as well as the concentration of added organics (in the biogenic systems) throughout the reactions were monitored using chemical analyses combined with spectrophotometric methods.

1.4 Thesis outline

This thesis consists of 9 chapters. Chapter 1 includes the introduction, background and the relevance of silica nanoparticle formation and biosilicification in geothermal environments whereas chapter 2 described the state of the art in our current knowledge. A detailed description of all methodologies and theoretical backgrounds used throughout the research are described in chapter 3. This is followed by four results chapters: Chapter 4 (Field Research - Part 1) describes the field study in Iceland and discusses the links between solution chemistry and sinter growth rates, sinter textures and structures as well the effects of microbial abundance on sinter growth. Chapter 5 (Field Research - Part 2) describes the molecular diversity of the mesophilic and thermophilic microbial communities associated with the various geothermal springs in Iceland. Chapters 6 to 8 describe the laboratory experiments designed to quantify the initial steps of the nucleation and growth of silica nanoparticles under various conditions using three different experimental set-ups. Finally, results from the entire thesis are discussed and summarised in chapter 9.

2 LITERATURE REVIEW

This chapter summarizes the literature related to biosilicification in hot spring environments and also provides an introduction into the literature on the mechanisms and kinetics of silica precipitation. The chapter is divided into two sections:

(i) The chemistry of silica; detailing the significance of silica in natural systems as well as the mechanisms and kinetics of silica polymerisation and silica nanoparticle formation in natural environments.

(ii) Silicification processes in geothermal areas; describing the process of sinter formation as well as the diversity of microbial communities in hot spring environments and detailing the interaction processes between microorganisms and silica during biosilicification.

2.1 The chemistry of silica

2.1.1 Silica in natural systems

Silicon (Si) is one of the most abundant elements in the Earth's crust, second only to oxygen. Due to its insoluble nature most of this silicon is found in rocks (as $SiO_{2(s)}$) and is thus not available to organisms. When silicon is in solution it is usually present in the form of monosilicic acid (dissolved silica, $H_4SiO_{4(aq)}$) comprising a silicon atom tetrahedrally coordinated to 4 hydroxyl groups. In aqueous solutions, as long as the silica concentration is below the equilibrium concentrations for amorphous hydrated silica (~110-120ppm at 25°C; Gunnarsson and Arnorsson, 2000) monosilicic acid remains stable in solution. The concentration of dissolved silica varies significantly between different natural environments (e.g., freshwater, seawater, hot springs) and is mostly determined by physico-chemical parameters including T, pH and salinity but also by processes such as water-rock interactions (mainly in geothermal areas) or the growth of diatoms and radiolarians (in marine settings). As a result, the concentration of dissolved silica in natural waters can be as low as 100ppb (seawater; Treguer et al., 1995) or as high as 1000ppm (geothermal deep waters at 300°C; Arnórsson et al., 1983b or surface effluents < 100°C, Mountain et al., 2003).

In geothermal environments when deep, hot and silica-rich fluids reach the surface, the immediate temperature and pressure drop will cause the solution to be highly supersaturated

with silica. At this point this will lead to the polymerisation of silica monomers due to a sudden surpassing of the equilibrium concentration, i.e., a drastic change in silica solubility. This in turn will result in the precipitation of silica nanoparticles that adhere/aggregate onto any substrate provided by the hot spring forming soft hydrated deposits which over time will transform into hard and compact sinters (a chemical, mainly siliceous sedimentary rock deposited by mineral springs, Fig. 2.1).

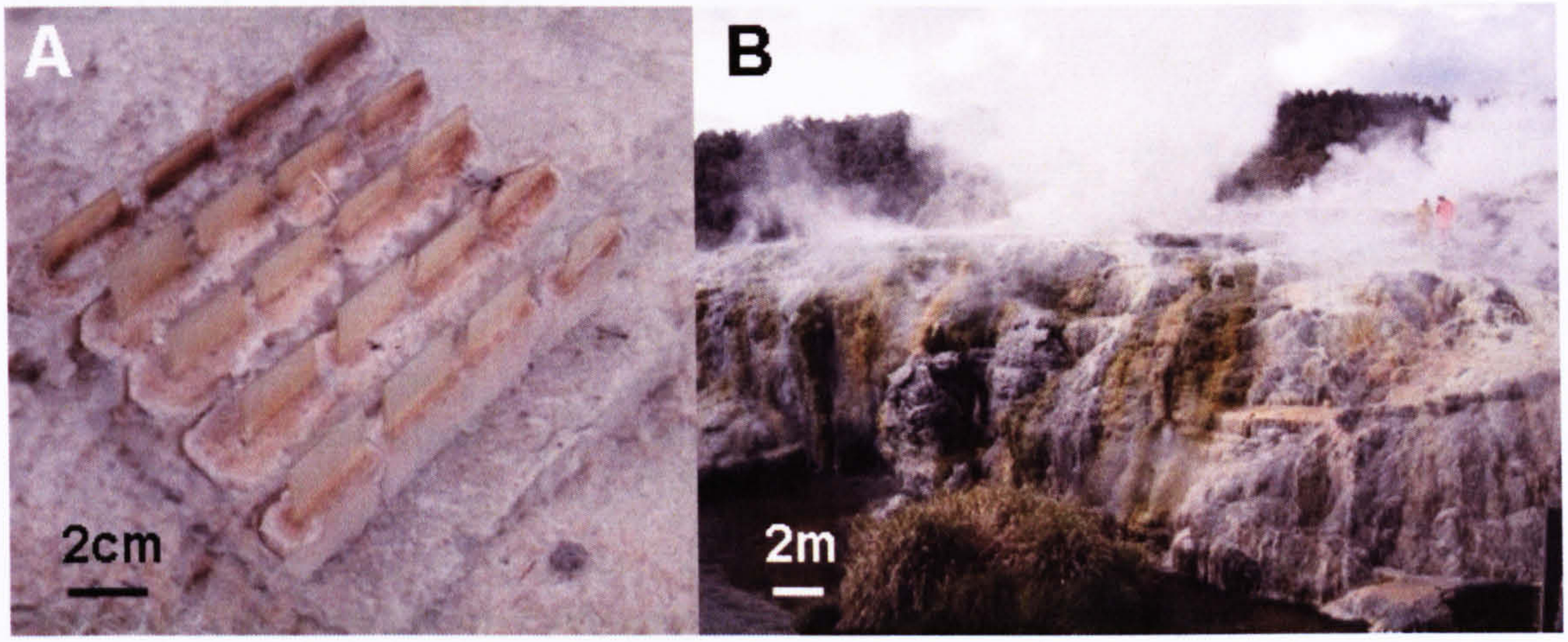

Figure 2.1: A) Teflon tray holding 20 glass slides covered in soft, white-orange precipitate (placed within the wastewater at Wairakei Terraces, Taupo, NZ, for 2 months) and B) dense compact sinter formed by the Pohutu Geyser, Whakarewarewa, Rotorua, NZ. In both pictures, the various colourations of the sinter deposits indicate the presence of diverse microbial biofilms.

2.1.2 Process of silica polymerisation and silica nanoparticle formation

Overview

Silica polymerisation and silica nanoparticle formation occur in diverse natural environments (e.g., brines, hot springs) and are crucial to the understanding of various geological and industrial processes (e.g., biosilicification, biomineralisation, silica diagenesis, silica sol formation). Several studies have focused on these processes with the aim to elucidate the exact mechanisms and kinetics behind silica polymerisation and the concomitant nucleation and growth of silica nanoparticle (e.g., Iler, 1979; Rothbaum and Rhode, 1979; Icopini et al., 2005). Overall, it is widely accepted that these processes are governed by three stages where the nucleation period of a silica nanosphere is followed by particle growth and particle

coarsening/aggregation. The initial step of silica polymerisation occurs via the coalescence of monosilicic acid molecules and the expulsion of water:

$$H_4SiO_4 + H_4SiO_4 \leftrightarrow (HO)_3Si\text{–}O\text{–}Si(OH)_3 + H_2O \quad \text{(Eq. 2.1)}$$

Further polymerisation leads to the formation of trimers, tetramers etc. to cyclic oligomers and eventually three-dimensional internally condensed nanospherical polymers (Fig. 2.2) which can also be described as $(SiO_2{*}xH_2O)_n$.

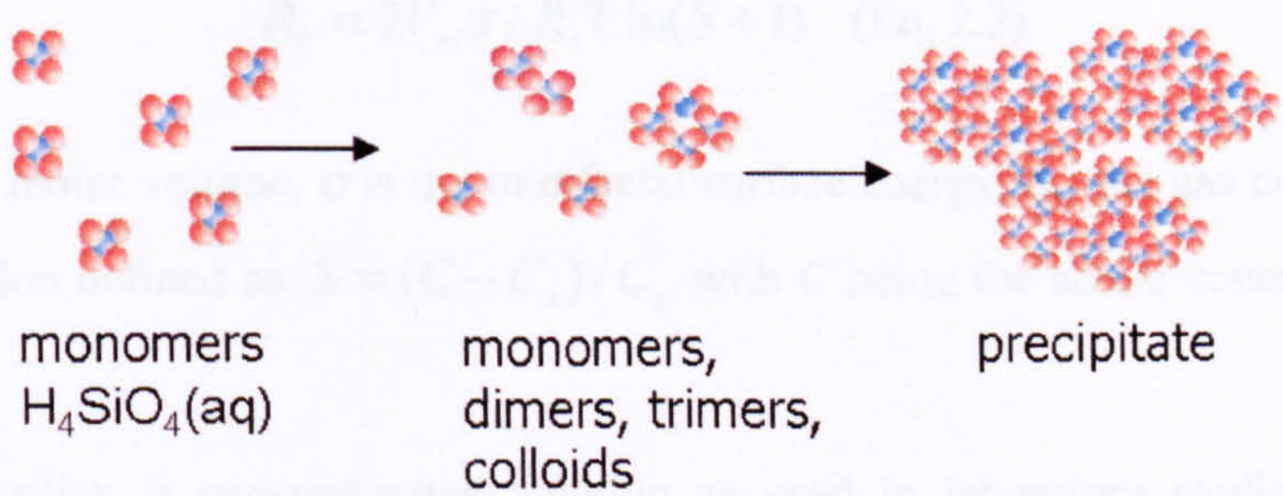

Figure 2.2: The process of silica polymerisation where silica monomers polymerise via dimers, trimers etc. to internally condensed silica nanoparticles that in turn further condense to large aggregates (blue spheres represent Si atoms and red spheres represent OH-groups).

During the second stage this nucleus (which is believed to be highly hydrated and to have a diameter of approximately 1-2nm; Iler, 1979) then grows by further accretion of monomers to trimers or larger oligomers (Perry and Keeling-Tucker, 2000). The last stage is known as coarsening or Ostwald ripening where larger particles grow at the expense of smaller ones which eventually dissolve. Particle coarsening will set in when the concentration of monosilicic acid approaches the solubility level and theoretically, the end of this three-stage process is reached when only clusters of particles remain in equilibrium with the monomeric solution (Madras and McCoy, 2002). However, in most natural cases the nanoparticles are not stable within the polymerising solution and they will start to aggregate before completion of the coarsening process (e.g., Iler, 1979; Perry, 2003; Benning et al., 2004 a, b and 2005; Icopini et al., 2005). Also, due to constant re-supply of silica within geothermal systems nucleation and growth will be a continuous process.

Nucleation mechanisms

Nucleation of a new phase (i.e., critical nucleus) can occur when the overall free energy of the system is at its lowest. If nucleation is initiated at nucleation sites (i.e., surfaces, suspended

particles, or bubbles) the process is called heterogeneous nucleation. During this process, some energy is released by the partial destruction of the previous surface allowing the new phase to form without the need of supersaturation. However, if nucleation occurs randomly and spontaneously without the use of surfaces, it is called homogeneous. For this, the solution needs to be supersaturated with respect to the new forming phase.

For homogeneous nucleation, the radius of the critical nucleus, R_0, in a supersaturated solution can be expressed using the Gibbs-Kelvin equation (Gibbs, 1961):

$$R_0 = 2V_m\sigma / R_cT\ln(S+1) \quad \text{(Eq. 2.2)}$$

where V_m is the molar volume, σ is the interfacial surface energy, R_c, the gas constant, and S is the supersaturation defined as $S = (C - C_s)/C_s$ with C being the actual concentration and C_s the solubility.

In the case of silica, a supersaturated solution as used in laboratory studies may undergo homogeneous nucleation from solution when care is taken to avoid impurities (e.g., colloids with large receptive surface areas). In most natural waters, however, where a variety of surfaces (e.g., colloids, rocks, microorganisms, plants) are present, nucleation will occur both in solution but also on any available surface (i.e., both homogeneous and heterogeneous processes). Therefore, depending on the natural system studied (e.g., brines, hot springs, seawater) the resulting silica phase will be highly variable from site to site. Microscopic observations of *in-situ* grown sinters (e.g., Mountain et al., 2003; Handley et al., 2005 and chapter 4 of this study) indicate that silica precipitates basically consist of nm sized silica nanoparticles and aggregates of up to 100 nm in size. From previous laboratory studies, the critical nucleus was estimated to be around 1 - 2 nm (e.g., Iler, 1979). This value is significantly smaller than the first nanoparticulate silica observed in field studies indicating that the bigger particles observed in natural samples will most probably represent either nanoparticles that have further grown (monomer/oligomer addition and/or Ostwald ripening) or larger aggregates of smaller nuclei.

Growth mechanisms

The classical growth theory assumes that the growth of the critical nucleus proceeds by atom-by-atom or molecule-by-molecule attachment. For this, the molecule diffuses to the particle surface where it will attach itself to a suitable growth site. This theory was originally developed for the growth on substrates but has also been shown to fit data obtained for the growth of nanoparticles (e.g., Matsoukas and Gulari, 1989; Andreassen, 2005; Zhai et al., 2006).

An alternative growth model is Ostwald ripening or coarsening (OR), which was first observed by Ostwald (1901). OR is essentially a mass transfer process where the larger particles grow at the expense of the smaller, less stable particles, which redissolve into the polymerising solution. The driving force for this coarsening process is the reduction of total surface free energy resulting in a decrease in number of particles per unit volume and an increase in mean particle size (Fig. 2.3). Furthermore, the shape of the size distribution is also affected and with increasing particle coarsening, the skewness of the particle size distribution will get more and more negative (Fig. 2.3; Nielsen, 1964 and references therein).

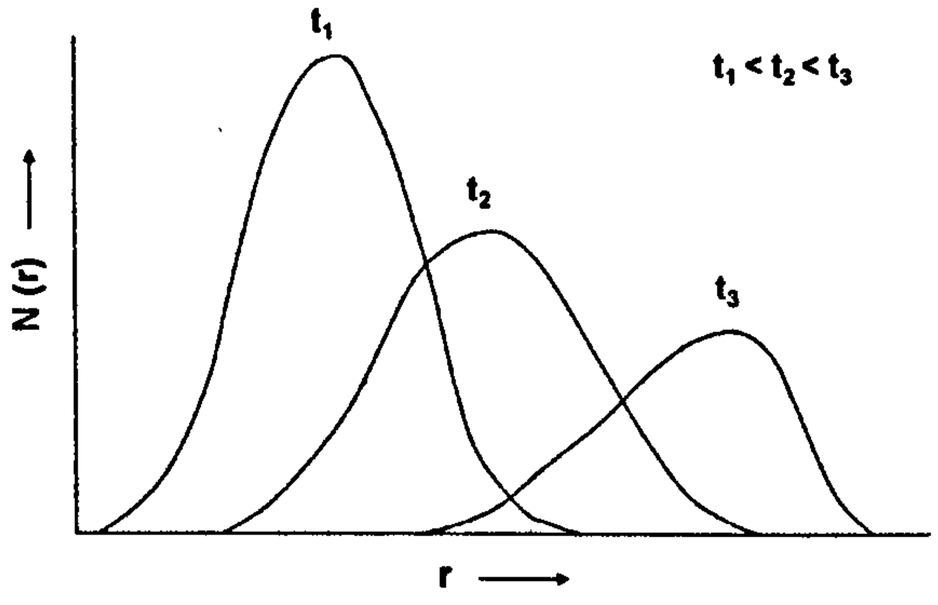

Figure 2.3: Time evolution of the particle size distribution during Ostwald ripening. Note that N(r) is the number of particles with mean radius, r. Besides the shift of the mean radius (r) to higher values, the distribution tends to broaden and also changes its skewness: its maximum moves to the right hand side of the mean radius, i.e., it has a negative skewness (adapted from Eberl, 1998).

Wagner (1961) and Lifshitz and Slyozov (1961) independently derived theoretical expressions for this process which are referred to as the LSW theory. Since then, several papers have analysed this process in more detail and have extended the LSW theory (e.g., Voorhees and Glicksman, 1984; Voorhees, 1985; Tokuyama et al., 1986; Yao et al., 1993; Madras and McCoy, 2001, 2002 and references therein). OR has been suggested as a suitable growth mechanisms for many systems, including crystallisation of metal alloys (e.g., Hardy and Voorhees, 1988; Lu, 1996), crystal growth in solution (e.g., Solomatov and Stevenson, 1993; Wong et al., 1998) or silica sols (e.g., Wijnen et al., 1991 and references therein). Despite this, it is quite difficult to fit the OR model to data from the growth of nanoparticles thus suggesting that Ostwald ripening may not occur in that many systems. This may be a consequence of the dependency of the process on the saturation state of the solution as this will determine the rate at which critical nuclei form and grow. If the solution is highly supersaturated, a lot of small nuclei will form instantaneously and before these nuclei can grow, the solution will have

reached the equilibrium concentration, i.e., the end of the reaction. However, if nucleation proceeds very slowly (e.g., due to less saturated conditions) fewer particles nucleate and these have time to coarsen as supersaturation slowly decreases.

Aggregation mechanisms

Concomitant with, and following particle growth and coarsening, particles tend to aggregate as a result of inter-particle forces. This process is essentially unavoidable and thus frequently encountered in natural environments. The formation of colloidal aggregates is random, resulting in different aggregate sizes. In general, aggregation depends on the repulsive forces between particles and thus the repulsive energy barrier between the two approaching particles. If this barrier is too high to be overcome, particles will not stick to each other and are thus stable within the solution. However, if this barrier is lowered particles will be able to aggregate. The two main models that are used to describe the aggregation of monodisperse colloids are diffusion-limited colloid aggregation (DLCA) and reaction-limited colloid aggregation (RLCA). If the aggregation process is only limited by the movement of two polymer units toward each other prior to encounter and formation of a cluster, aggregation is diffusion-limited. In such reactions, monomers or oligomers collide and combine instantaneously, producing a relatively porous aggregate. For the formation of critical nuclei of silica, the DLCA process has been confirmed experimentally (e.g., Beelen et al., 1989; Martin et al., 1990; Lin et al., 1990; Pontoni et al., 2002; Benning et al., 2005; Benning and Waychunas, 2008). However, if the aggregation rate is limited by the probability of these collisions to overcome the repulsive barrier (termed sticking probability; Everett, 1988; Gedde, 1995) the process is reaction-limited. Therefore, usually RLCA is much slower than DLCA as in RLCA only a small fraction of all collisions are successful whereas in DLCA every collision will lead to the formation of a new aggregate. For silica, the RLCA process occurs in reactions with organics (i.e., alkoxide-driven Stöber process) and results in a more compact aggregate structure during slow condensation (Martin, 1987; Lin et al., 1990). It needs to be noted that for silica nanoparticles, aggregation is an irreversible process and the formed clusters/aggregates will continue to diffuse, collide and aggregate to form even larger and more complex structures (Lin et al., 1990).

To describe the structure and complexity of the formed aggregates, a fractal geometry concept has been introduced (Pfeifer and Obert, 1989; Lin et al., 1990). In this concept, the various phases that form during the process of nucleation, growth and aggregation are described by fractal objects with a fractal dimension D_f. The fractal dimension, D_f, usually lies between 1.4 and 3 and is related to the number of primary particles (N) by a power law $N \sim R_f^{Df}$, where R_f is the radius of the aggregate spatial dimension.

For silica, the relationship between aggregation mechanisms and fractal dimension has been investigated by only a few organically controlled silica nanoparticle formation studies (e.g., Martin et al., 1990; Lin et al., 1990). It has been shown that for DLCA, D_f = 1.7 - 1.8 (determined experimentally by light and X-ray scattering methods) whereas for RLCA, D_f was found to vary between 2.1 and 2.2 (Martin, 1990; Lin et al., 1990). This indicates that these fractal dimensions can be associated with a kinetic process: objects that form during fast aggregation (DLCA) have low fractal dimensions whereas slow aggregation (RLCA) produces objects with high fractal dimensions thus exhibiting a more compact aggregate structure.

These results were supported by Benning et al. (2004b) who derived aggregation rates and mechanisms from silicification experiments in the presence of cyanobacterial cells. They did not determine the fractal dimensions directly from their experiments but based on theoretical calculations (after Hulbert, 1969 and Gedde, 1995), Benning et al. (2004b) were able to show that the nucleation, growth and aggregation of silica nanoparticles on cynanobacterial surfaces is governed by a 2 stage process. The initial phase where the formation of new hydrated polysaccharides polymers leads to the increase in thickness of the exopolymeric polysaccharide sheath and where silica nanoparticles nucleate and grow was dominated by a fast, diffusion-limited process ($n \sim D_f$, n of 1.8 and 2.2). This was then followed by a slower, reaction-limited process (n of 3.4 and 3.8) where silica nanoparticles accumulate on cyanobacterial sheaths (Benning and Waychunas, 2008).

2.1.3 Factors governing silica polymerisation and silica nanoparticle formation

To induce extensive silica polymerisation a pH around 6 to 9 is needed (Fig. 2.4). Minimum polymerisation rates are found at pH below 3, while above pH 9, the solubility of amorphous silica increases rapidly, thus also reducing the extent to which polymerisation takes place (Fig. 2.4, e.g., Alexander et al., 1954; Iler, 1979; Chan et al., 1989; Gunnarsson and Arnórsson, 2003).

Figure 2.4: Silica solubility as a function of pH (Alexander et al., 1954).

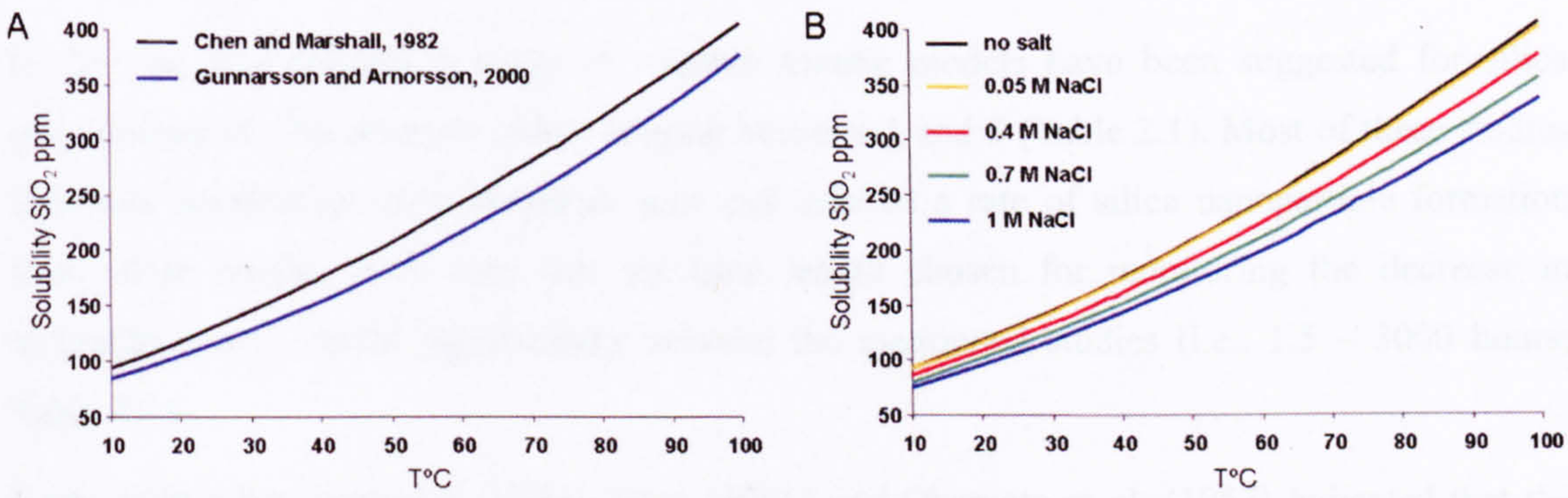

Figure 2.5: Solubility of amorphous silica as a function of temperature (A) in pure solutions and (B) in solutions with added NaCl (data from Chen and Marshall, 1982).

Next to solution pH, other factors like temperature, ionic strength, and silica concentration influence the degree of silica saturation and thus the kinetics of silica polymerisation (e.g., Moulik and Mullick, 1966; Iler, 1979; Crerar et al., 1981; Rothbaum and Wilson, 1977; Rothbaum and Rhode, 1979; Makrides et al., 1980; Weres et al., 1981; Icopini et al., 2005, Conrad et al., 2007). Despite some discrepancy between reported solubility data, the solubility of amorphous silica is enhanced with increasing temperature (Fig. 2.5A) which in turn reduces the rates of silica polymerisation and precipitation (Gunnarsson and Arnórsson, 2003). In Figure 2.5B the effects of moderate to high salt concentrations (i.e., ionic strength) on amorphous silica solubility are shown ("salt-effect"). With increasing salt concentration, the silica solubility decreases and the polymerisation rate is thus enhanced (Fig. 2.5B; Marshall and Warakomski, 1980; Marshall and Chen, 1982). In addition, the "salt effect" is more pronounced at higher temperatures. However, the degree of silica saturation (i.e., silica polymerisation) mainly

depends on the concentration of dissolved silica within the studied water. In the case of geothermal systems, the dissolved silica concentration within the ascending geothermal fluid (Fig. 2.4 and 2.5) is controlled by chalcedony and quartz equilibrium in deep aquifer geothermal waters below and above 180°C (Arnórsson, 1975).

Overall, an induction period can precede the polymerisation reaction during which little or no silica polymerisation takes place. The length of this induction period is controlled by the same factors that determine silica polymerisation (i.e., T, pH, IS and silica concentration) and it is lowered by an increasing degree of supersaturation (e.g., White et al., 1956; Iler, 1979; Rothbaum and Rhode, 1979; Gunnarsson and Arnórsson, 2003; Icopini et al., 2005, Conrad et al., 2007).

2.1.4 Kinetic models proposed for silica polymerisation / silica nanoparticle formation.

In the last few decades a range of reaction kinetic models have been suggested for silica polymerisation with reaction orders ranging between 1 and 5 (Table 2.1). Most of these studies followed the changes in monosilicic acid and inferred a rate of silica nanoparticle formation from these results. Also note that the time length chosen for monitoring the decrease in monosilicic acid varied significantly between the mentioned studies (i.e., 1.5 – 3000 hours; Table 2.1).

Early studies by Alexander (1954), Goto (1956) and Okamoto et al. (1957) indicated that the reaction order was dependent on the solution pH, with a 2nd order rate dependence for silica condensation between pH 3 – 7 and a third order rate dependence for pH > 7 and pH < 3 (Table 2.1). These results agreed with observations made by Kitahara (1960). In contrast, Baumann (1959) proposed that during silica polymerisation the reaction order varied between 1 and 5 as a function of both silica concentration and pH.

Most of these reaction orders were determined by fitting the time-dependent depletion of monosilicic acid (in the reacting solution) to the rate equation first used by Goto (1956):

$$-dC/dt = k(C - C_s)^{n_r} \quad \text{(Eq. 2.3)}$$

where k is the rate constant, C the concentration of monosilicic acid, Cs the solubility of amorphous silica at a given temperature and n_r the reaction order.

Table 2.1: Summary of reported experimentally derived kinetic models for the decrease in monosilicic acid during the process of silica polymerisation.

Study	pH	T (°C)	SiO_2 (ppm)	max. reaction time (h)	[1]Reaction order, n
Alexander (1954)	1 - 6	1.9	6000	170	3 for pH<3.2 2 for pH>3.2
Goto (1956), Okamoto et al. (1957)	7-10	22.3	200 - 900	144	3
Baumann (1959)	0.5 - 9	30	400 - 4000	7	1 to 5
Kitahara (1960)	3 - 10	0 - 100	500 - 800	5	2 for pH<7.5 3 for pH>7.5
Bishop and Bear (1972)	8.5	25 - 45	300	200	2
Rothbaum and Wilson (1977)	7.8 - 8.7	50 - 120	500 - 1000	1000	5 to 8
Rothbaum and Rhode (1979)	7-8	5 - 180	300 - 1300	1200	4
Markrides et al. (1977, 1980)	4.5 - 6.5	75 - 105	700 - 1200	22	[3]0
[2]Peck and Axtmann (1979)	4.5 - 8.5	25 - 95	400 - 1000	-	1
[4,5]Weres et al. (1981)	2.5 - 8	50 - 100	500 - 1200	1.5	1 for $S>S_t$ 5 for $S<S_t$
Crerar et al. (1981)	7	25	1000	22	1
Icopini et al. (2005), Conrad et al. (2007)	3 - 11	25	250 - 1250	3000	4

[1]Reported rate laws were derived via the equation $-dC / dt \sim k(C-C_s)^n$ following the method described by Goto (1956).
[2]Peck and Axtmann (1979) analysed experiments reported by Makrides et al. (1980) and Rothbaum and Wilson (1977).
[3]Makrides (1977, 1980) postulated that particle growth preceeding the induction and nucleation phase was linear with time.
[4]Weres et al. (1981) used the same model as proposed by Makrides et al. (1977, 1980) and Peck and Axtmann (1979).
[5]Weres et al. (1981) proposed a 5th order rate law up to a certain silica concentration, S_t (unknown), and a 1st order rate > S_t.

More recent studies (Peck and Axtmann, 1979; Crerar et al., 1981; Rothbaum and Rhode, 1979; Weres et al., 1981; Icopini et al., 2005, Conrad et al., 2007) have successfully described the complete polymerisation process with a single kinetic model (i.e., with no variation in reaction order with pH), yet the results of these studies disagree on the order of the reaction (Table 2.1). Peck and Axtmann (1979) proposed a first order reaction with respect to monosilicic acid concentration and a dependency on the total surface area of the growing particles. Furthermore, they postulated that towards the later stages of silica polymerisation, the reaction may be limited

by monomer diffusion to the particle surface. Crerar et al. (1981) supported these findings but indicated that the end of the reaction was not diffusion-limited as proposed by Peck and Axtmann (1979) and instead was characterised by ripening. Interestingly, Rimstidt and Barnes (1980) have successfully employed a first order reaction model to both silica precipitation as well as silica dissolution.

Other studies postulated reaction orders higher than 1 (Table 2.1). Rothbaum and Rhode (1979) investigated the effect of temperatures (between 5 and 180°C) and pH (7 to 8) on the kinetics of silica polymerisation and showed that, after an initial induction time, the maximum reaction rate had a fourth order dependence relative to the normalised monosilicic acid concentration. More recently, Icopini et al. (2005) and Conrad et al. (2007) reported a fourth order decrease of monosilicic acid over time (Table 2.1) and showed that the rate constant was linearly dependent on solution pH.

The plethora of reported reaction models for the kinetics and mechanisms of silica polymerisation demonstrates that the polymerisation reaction maybe too complex to be described by a single equation. It is also possible that different mechanisms of polymerisation / silica nanoparticle growth operate under different physico-chemical conditions and time scales which can be further complicated by the occurrence of an induction period. Therefore, in order to obtain a full understanding of this process, a molecular approach that follows the changes in monosilicic acid concentration combined with the quantification of the forming silica nanoparticles is needed.

2.1.5 Organic-templated silica polymerisation and nanoparticle formation for industrial applications

The formation of silica nanoparticles is also important in industrial processes. For example, applications where the specific structural properties of silica nanoparticles (e.g., swelling capacity, strength, durability, thermal stability) make them highly desirable nanomaterials such as computer, biotechnology, catalysis and chromatography. As a result, the synthesis of highly monodisperse, spherical and compact silica particles (Fig. 2.6) through techniques such as the Stöber method (Stöber et al., 1968) is well established. The Stöber method is based on the hydrolysis and condensation of tetraalkoxysilane (TEOS) in alcoholic solutions (e.g., ethanol, methanol) and under basic conditions (ammonia).

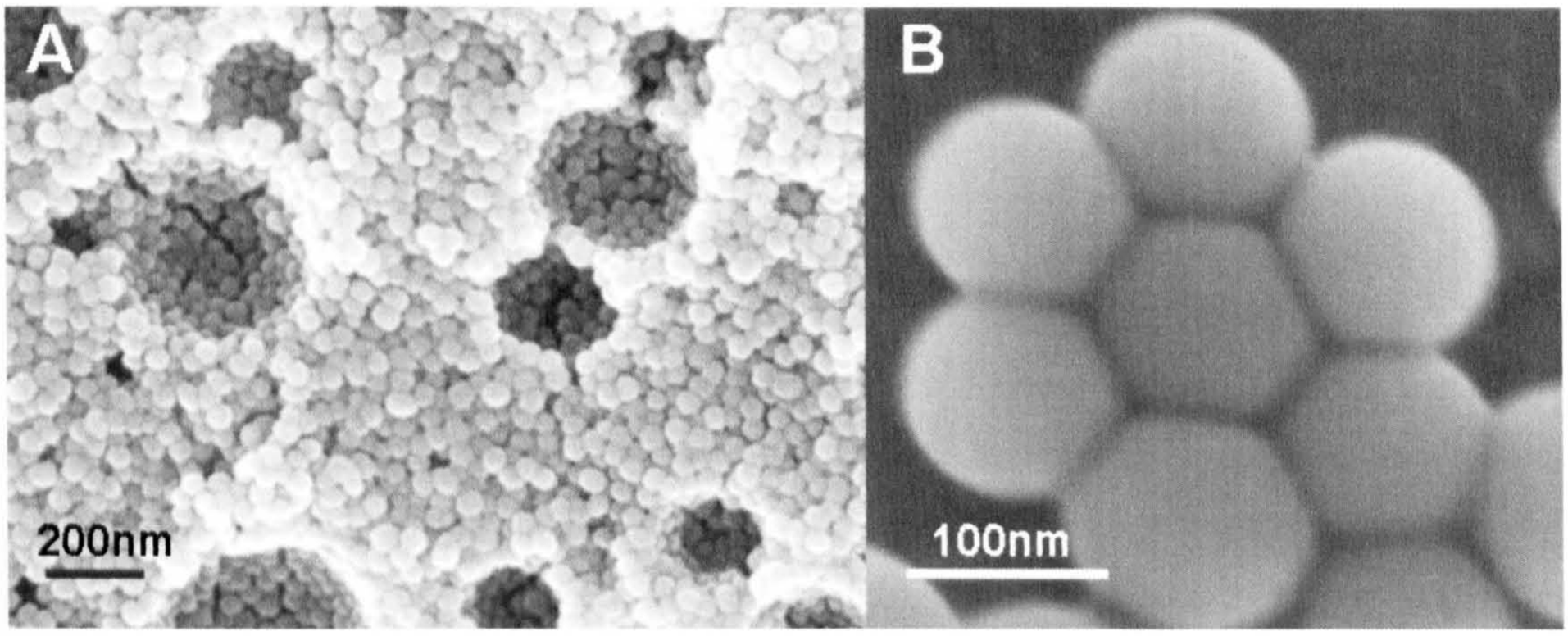

Figure 2.6: Highly monodisperse and spherical silica nanoparticles synthesised during the current study using the Stöber method. TEOS:H_2O:NH_3 ratio for A) 0.1 : 3 : 0.5 M and for B) 0.1 : 20 : 0.5 M.

The mechanisms and kinetics underlying these processes have been the subject of extensive laboratory investigations. Multiple techniques such as Small Angle X-Ray Scattering (SAXS), Dynamic and Static Light Scattering (DLS, SLS), ^{29}Si NMR, Raman spectroscopy and Transmission Electron Microscopy (e.g., Bogush et al., 1988; Matsoukas and Gulari, 1988; Moreira et al., 1991; van Blaaderen et al., 1992; Bailey and Mecartney, 1992; Boukari et al., 1997, 2000; Pontoni et al., 2002; Green et al., 2003a,b) have been applied to derive models that describe the formation of alkoxide based silica particles and their growth under a variety of reactants (e.g., silicon alkoxides and water) and catalysts (e.g., ammonia) concentrations.

Despite the plethora of research for industrial applications, the Stoeber method is not representative of silica nanoparticle formation in natural environments and the derived models are not transferable. Nevertheless, it is worth noting that the formation of silica sols via the alkoxide route and the changes in properties of the silica nanoparticles themselves have been studied using *in-situ* and time-resolved methods similar to those that were applied in the present study. Therefore, these alkoxide studies are very useful in terms of data processing and interpretation (specifically for SAXS data) and will thus be important for data analysis in chapter 6 and 7. In contrast, most studies of inorganic silica polymerisation and nanoparticle formation (see previous section 2.1.4) followed the polymerisation processes via the changes in solution chemistry and did not quantify the nucleation and growth of the silica nanoparticles.

2.2 Silicification processes in geothermal areas

2.2.1 Chemical composition of hot spring waters

Most geothermal systems are the result of infiltration of meteoric fluids into the Earth's crust, heating of those fluids up to T > 300°C, and consequent buoyant upflow. The heat engines for these systems in most areas of the world are considered to be igneous intrusions associated with active or very recent volcanic activity. The geothermal fluids discharged at the surface therefore may contain components of surface water (including rainwater, lake and river water, and shallow groundwater), deeply penetrating groundwaters and seawater (in the vicinity of the coast), metamorphic and also magmatic waters. Due to the interactions processes between the circulating fluids and the enclosing wall rocks (in the subsurface), the chemistry of the effluent waters can differ enormously between hot springs and are generally characterised by high amounts of SiO_2 and variable concentrations of Na^+, K^+, Li^+, Ca^{2+}, Al^{3+}, $Fe^{2+/3+}$, Mg^{2+}, As^{3-}, Cl^-, HCO_3^- and H_2S. Similarly, the wide varieties in circulating fluids and wall rock composition also lead to large differences in the effluent fluid pH, which can displays highly acidic to alkaline values (with extremes of pH 2 - 3 and > 11 having been measured at e.g., Rotokawa, New Zealand and The Cedars, N-California, respectively). Overall, acidic spring waters are predominantly the result of abiotic oxidation of H_2S and / or SO_2 that move upward with the geothermal steam and by mixing with the shallow groundwater. In contrast, alkaline waters mainly result from quickly ascending deep fluids which exhibit H_2S separation and loss of CO_2 during boiling / evaporation.

2.2.2 Silica precipitation in geothermal waters

In the case of silica the first phase which precipitates from a supersaturated silica solution is opal-A (SiO_2*nH_2O), a non-stoichiometric inorganic polymer made up of a mixture of SiO_2 and H_2O units in various ratios. The water content of opal-A can be between 1-15% (e.g., Krauskopf, 1956; Segnit et al., 1965; Huang and Vogler, 1972; Jones and Renault, 2004) and this water is either bound as network water or as liquid water in interstices (e.g., Langer and Florke, 1974; Knauth and Epstein, 1982). The majority of siliceous sinter forming within geothermal hot springs in New Zealand, Iceland or Yellowstone (USA) are composed of opal-A. However, opal-A is an unstable, hydrous mineral that will transform to moganite, christobalite or opal-CT and eventually to chalcedony and quartz. These transformations are favoured by the passage of time, high-temperature and high-pressure conditions and/or alkaline pH-conditions (e.g., Williams et al., 1985; Fournier, 1985; Herdianita et al., 2000; Lynne et al.

2006). They involve loss of water, repeated dissolution-precipitation, replacement and recrystallisation reactions which generally lead to an increase in particle density and an overall reduction in porosity (e.g., Iler, 1979; Fournier, 1985, Herdianita et al., 2000).

The precipitation of opal-A and the formation of silica sinters requires that the rising fluids are supersaturated with respect to amorphous silica, a steady supply of solute that carries dissolved silica and the presence of suitable nucleation sites. In hot spring pools where high silica supersaturation prevails, the precipitation of amorphous silica (opal-A) will occur via silica polymerisation, which will lead to the precipitation of nanoparticulate amorphous silica in the aqueous phase (homogeneous nucleation) as well as on any substrate present in the pool basins (heterogeneous nucleation on microbial mats, plants, trees, etc.). The rate of amorphous silica deposition is invariably linked to the rate of silica polymerisation, and thus an increased rate of silica polymerisation will lead to an increased silica precipitation. Mechanisms triggering silica polymerisation and precipitation are either rapid cooling of geothermal fluids at ambient air temperatures, pressure drop, evaporative concentrations, rapid acidification of alkaline silica-supersaturated waters at fluid interfaces (change in pH), steam loss of a rising fluid or cation effect (Al in solution). From all these parameters influencing silica precipitation and polymerisation, cooling is believed to be the predominant abiotic process controlling the precipitation of sub-aqueous amorphous silica (Guidry and Chafetz, 2002). It has to be noted that many silica sinters encountered in thermal hot spring areas are often formed sub-aerially (above the air-water interface, AWI) and therefore other hydrodynamic processes including wave action, capillary action, diffusion and splash must also be invoked to fully explain their formation (e.g., Mountain et al., 2003; Handley et al., 2005).

2.2.3 Microbial communities within silica depositing hot springs

In the past, the microbial diversity of natural environments has mainly depended on the ability to isolate into pure culture sample from the field. However, most organisms can not be "captured" in this way and it has been estimated that more than 99% of organisms seen microscopically can not be isolated by cultivable techniques (e.g., Amann et al. 1995, Pace, 1997). Therefore, the diversity of many microbial ecosystems is now usually studied with molecular methods (e.g., analysis of small-subunit rRNA / rDNA by sequencing, denaturing gradient gel electrophoresis, restriction fragment polymorphism analysis, i.e., RFLP) for which only a gene sequence, not a functioning cell, is required to identify the organism in terms of its phylogenetic type. Several studies indicated that using molecular techniques the detected microbial diversity is 100 to 1000 times greater than that by cultivation alone (e.g., Hugenholtz et al., 1998; Pace, 1997; Skirnisdottir et al., 2000 and references therein). Furthermore,

sequencing of rRNA genes from the environment is a very powerful tool as it provides information on both the phylogenetic relationship and the population structure of the microbial community.

Phylogenetic studies using 16S rRNA analysis combined with cultivation studies have shown that an abundant diversity of thermophilic microorganisms are inhabiting neutral to alkaline (pH 7 - 9), silica precipitating hot springs around the world (e.g., Japan, New Zealand, Iceland, Yellowstone National Park). The bacterial communities in these springs are dominated by organisms belonging to the order *Aquificales* (e.g., Reysenbach et al., 1994; Huber et al., 1998; Hugenholtz et al., 1998; Skirnisdottir et al., 2000; Hjorleifsdottir et al., 2001; Takacs et al., 2001; Blank et al., 2002; Eder and Huber, 2002; Nakagawa and Fukui, 2002). *Aquificales* species are mainly obligatory chemolithotropic, aerobic organisms that belong to one of the earliest branching orders of the domain *Bacteria*. Recent cultivation of Aquificales species, i.e., *Thermocrinis ruber*, (a pink filament isolated from Octopus Sping in Yellowstone National Park; Huber et al., 1998) and *Sulfurihydrogenibium kristjanssoni* (isolated from a terrestrial Icelandic hot spring; Flores et al., 2008) suggested that primary production in these ecosystems is by chemoautrotrophic hydrogen and sulfur oxidation. Other abundant organisms in these ecosystems include members of the genus *Thermus* (e.g., Brock and Freeze, 1969; Kristjansson and Alfredsson, 1983; Hudson et al., 1987; Kristjansson et al., 1994; Williams et al. 1995; Skirnisdottir et al., 2000; Reysenbach et al., 2000; Chung et al., 2000; Hjorleifsdottir et al., 2001; Blank et al., 2002). *Thermus* species are chemoorganotrophic, aerobic bacteria using organic substrates for their growth and are ubiquitous to most hot springs with neutral to alkaline pH (max. pH ~ 9.5) and temperatures up to 85°C (Alfredsson and Kristjansson, 1995). The most abundant *Thermus* species isolated from these environments include *Thermus aquaticus* (so far only isolated in hot springs in Yellowstone National Park, Brock and Freeze, 1969), *Thermus filiformis* (so far only found in New Zealand, Hudson et al., 1987), *Thermus scotoductus* (Iceland, Kristjansson et al. 1994), *Thermus brockianus* (Yellowstone National Park, Williams et al. 1995), *Thermus igniterra* and *Thermus antranikianii* (Iceland, Chung et al. 2000). Other organisms in these ecosystems include members of the *Bacilli*, the *Nitrospira*, the fermentative *Thermotogales*, and the sulphate-reducing *Thermodesulfobacterium* group. Similar to *Thermus*, *Bacilli* and *Nitrospira* species are chemoorganothrophic, aerobic bacteria while representatives of the *Thermotogales* and *Thermodesulfobacterium* are mostly anaerobic bacteria but can also use organic substrates for their growth (i.e., chemoorganotrophic). However, the phylogenetic analysis via sequencing also reveals many new and unknown species (e.g., new candidate division from Obsidian Pool, YNP; Blank et al., 2002 and reference therein) and unless new cultured representatives from these divisions can be found, a definitive placement of their root is not possible.

Compared to bacterial community studies, the diversity of archaeal species in high temperature hot springs has so far not been analysed as frequently. A reason for this may be that PCR amplification using archaeal-specific primers was not always successful (e.g., Graber et al., 2001; Blank et al., 2002). Nevertheless, a few studies (e.g., Barns et al., 1994; Reysenbach et al., 2000; Skirnisdottir et al., 2000) were successful in detecting archaeal communities in geothermal ecosystems and they revealed the existence of a plethora of novel *Archaea*. Representatives of *Korarchaeota*, *Thermofilum* and uncultured *Crenarchaeota* are the most abundant archaeal species in these systems and these have been detected in several hot springs in Yellowstone National Park (e.g., Obsidian Pool, Sylvan Spring, Calcite Spring; Barns et al. 1994; Reysenbach et al., 2000; Meyer-Dombard et al., 2005) as well as in Iceland (e.g., Hengill area, Skirnisdottir et al., 2000; Kvist et al., 2006).

A few studies (e.g., Skirnisdottir et al., 2000; Fouke et al., 2003; Meyer-Dombard et al., 2005; Purcell et al., 2006) have tried to link the diversity of microbial communities with the physico-chemical conditions of the studied hot spring. They showed that the complexity of the metabolic framework and the microbial community structure correlate well with temperature and sulphide concentration but they also noted that other parameters including pH, availability of other energy sources and organic substrates have to be considered. These studies further demonstrated the high variations in physico-chemical conditions between hot springs and thus the need for more analogues studies to obtain a more in depth understanding of the parameters that control the biodiversity pattern in these ecosystems.

2.2.4 Textures and structures of silica sinters

Several studies have reported on the close association of microorganisms with the formation of silica sinters from a variety of hot springs, including Yellowstone National Park, USA (e.g., Walter et al., 1972, 1976; Ferris et al., 1986; Hinman and Lindstrom, 1996; Cady and Farmer, 1996; Guidry and Chafetz, 2003; Lowe et al., 2001), Geysir and Krisuvik, Iceland (e.g., Schultze-Lam et al., 1995; Konhauser and Ferris, 1996), Kenya (e.g., Jones and Renaut, 1996), Otake geothermal power plant, Japan (e.g., Inagaki et al., 1997; Inagaki et al., 2003) and several sites in the Taupo Volcanic Zone, New Zealand (e.g., Renault et al., 1996; Jones et al., 1997, 1998, 2000; Mountain et al., 2001, 2003; Handley et al., 2005). These studies also showed that the development of sinter textures is dependent on the relative rates of silica precipitation and biofilm growth, the mechanisms triggering precipitation as well as the type of microorganisms thriving within these systems. Therefore, depending on the hot spring's hydrodynamic and geochemical regime a series of different biofacies can be identified (e.g., spicules, columnar and

stratiform microstromatolites, oncoids and coccoid microbial mats; Jones et al., 1997, 1998, 2000, 2003, 2004).

To date, only few studies (e.g., Mountain et al., 2003; Handley et al., 2005) have quantified the rate of sinter formation and linked the observations to the formed textures and structures as well as the geochemical / hydrodynamic regime of the studied waters. For example, during high silica growth rates (≥2mg/slide/day; Handley et al., 2005) sinter formation can exceed biofilm growth and the fabric of sinters formed will be governed only by physico-chemical parameters (e.g., Mountain et al., 2003; Handley et al., 2005). The sinter textures that develop in the vicinity of the AWI, where evaporation and cooling processes dominate, are dense and mostly dominated by fine granular silica layers. In contrast, in the submerged parts of the slides, porous-granular sinter deposits form due to the prolonged period of polymerisation. Conversely, at moderate to low deposition rates, extensive biofilms can develop and sinter fabrics will be influenced by these microbial mats, as they provide the architectural framework upon and around which sinters will grow (e.g., Cady and Farmer, 1996; Mountain et al., 2003; Handley et al., 2005). Close to the AWI, spicular sinters and silica terraces (subaerially) form whereas porous-filamentous or flat, laminated silica crusts dominate the subaqueous parts of the slides. This has been observed previously by Mountain et al. (2003) and Handley et al. (2005) who characterized *in-situ* grown sinters from Champagne Pool, in the Waiotapu geothermal area, NZ. In the case where silica precipitation rates are lower than biofilm growth, extensive microbial mats will form along and within hot springs and continuous deposition of silica nanospheres onto their surfaces will eventually lead to complete microbial silicification and preservation within the sinter edifice (e.g., Walter et al., 1972; Ferris et al., 1986; Schultze-Lam et al., 1995; Cady and Farmer, 1996; Konhauser and Ferris, 1996; Jones et al.,1998; Konhauser et al., 2001; Mountain et al., 2003).

2.2.5 Process of biosilicification

Most studies related to biogenic silicification processes focus on the role of amorphous silica in the build-up of diatoms, radiolarians and sponges in the modern oceans (which are undersaturated with respect to silica). It is well-known that the amorphous silica in these organisms (particularly in size, shape and orientation) is controlled primarily by the templating functions of glycoproteins and polypeptides (e.g. silaffin and silicatein; Benning et al., 2005 and references therein). Furthermore, amorphous silica is also known to cycle through higher plants in which silica appears to protect the plants against pathogens and insects (Benning et al., 2005 and references therein). However, this thesis focus solely on the silicification of microorganisms

in geothermal environments and the following literature review will thus only discuss laboratory and field studies that analysed microbial silicification processes in such environments.

Microbial cell wall properties and silicification process

Most microorganisms have no known metabolic requirement for silica, and thus the silicification of microorganisms is mostly controlled by the physical nature of their surfaces. Several studies (e.g., Schultze-Lam et al., 1996; Fein et al., 1997; Cox et al., 1999, Yee et al., 2004) have shown that the microbial surface exhibits a wide variety of different functional groups (i.e., carboxyl, hydroxyl, phosphate and amine) and that at neutral pH microbial surfaces are usually neutrally or negatively charged. Similarly, dissolved silica (H_4SiO_4) is neutrally charged at ~ pH 7, while silica nanoparticles are negatively charged (Iler, 1979 and references therein). As a result silica has a very low affinity for the microbial surface.

Phoenix et al. (2002) and Yee et al. (2004) showed that the sheath of *Calothrix* (cyanobacteria common in hot springs) is electrically neutral at pH 7, and that its surface consists predominantly of neutral sugars, along with smaller amounts of negatively-charged carboxyl groups and positively-charged amino groups, in approximately equal proportions. They suggested that the low reactivity of the exopolymeric sheath of *Calothrix* gives its surface hydrophobic characteristics facilitating their attachment to solid submerged substrates (i.e., siliceous sinters). In addition, the sheath's electroneutrality makes it less repulsive towards the polymeric silica fraction and colloidal silica in solution and these properties may actually aid in the silicification process.

In an early attempt to describe the mechanism of silicification Leo and Barghoorn (1976) suggested that monomeric or low molecular weight polymeric silica was bound to the microbial surface through hydrogen bonding. Heaney and Yates (1998) supported this idea, although their study indicated that it was not the monomeric silica that bound to the surface but that the polymeric/colloidal fractions (where hydroxyl groups are still exposed on the surface) were responsible for the immobilization of the silica from solution. These results were recently confirmed by Lalonde et al. (2005) who studied the silicification of thermophilic bacteria (*Sulfurihydrogenibium azorense)*. They showed that silica adsorption is limited to silica nanoparticles, but also that the magnitude of silica adsorption, i.e., the degree of silicification, was dependent on its chemolithoautotrophic pathway; H_2-oxidizing cultures removed small quantities of nanoparticulate silica, whereas S°-oxidizing cultures did not.

Adhesion of silica nanoparticles onto the microbial cell wall may also occur via cation bridging. This process mainly applies for negative charged microbial surfaces (e.g., *Bacillus subtilis*)

which exhibit a much larger electrostatic repulsion towards polymeric silica than cyanobacteria like *Calothrix* (e.g., Yee et al., 2003). For such anionically-charged cell wall surfaces, silicification requires a cation bridge (e.g., Fe^{3+}, Al^{3+}) in order to overcome the electrostatic charge repulsion between the organic ligands and silica species. Several studies (e.g., Fein et al., 2002, Urrutia and Beveridge, 1994; Yokoyama et al., 2004; Yee et al., 2003; Phoenix et al., 2003) have demonstrated that dissolved cations like Fe^{3+} and Al^{3+} readily bind to the organic ligands that occur on the cell surface. Furthermore, Fein et al. (1997) showed that in undersaturated systems, bacteria pre-coated with Fe^{3+} and Al^{3+} hydroxides could act as templates for silica deposition and that virtually all of the monomeric silica was removed from solution.

Phoenix et al. (2003) and Yee et al. (2003) did similar studies to Fein et al. (1997) but they used supersaturated solutions exhibiting a higher Si/Fe-ratio, which was more representative to those found in modern hot springs. In their experiments they measured the effects of iron bridging in mixed Fe-Si solutions but the *Bacillus subtilis* cells they used were not pre-coated with iron. Their results suggested that in natural hot spring systems, where the concentration of soluble silica far exceeds that of iron, the amount of iron immobilized onto the microbial mats is insignificant compared to the abiotic reactions of silica with $Fe(OH)_3$ and thus, the vast majority of silica precipitated will occur without the aid of a cation bridge.

Yokoyama et al. (2004) presented a method to distinguish between siliceous sinter formed purely inorganically or by cation-bridging on microbial surfaces. They showed that if aluminium ions embedded in siliceous sinter deposits are present as 4-coordinated Al, then the deposit was formed by inorganic reactions between monosilicic acid and Al ions. Al ions bound to the surface of microbes, however seem to be present as 6-coordinated Al and can thus be distinguished from pure inorganic precipitation. They also showed that the effect of cation-bridging was more pronounced further downstream the studied hot spring at lower temperature and where biofilms were more abundant.

Yee et al. (2000) studied adsorption behaviour of *Bacillus subtilis* cells onto either corundum or quartz as a function of time, pH, ionic strength and biomass to mineral ratio. Their results indicated that bacterial-mineral adsorption is mainly driven by hydrophobicity, but that electrostatic interactions also play an important role. Furthermore, they showed that increasing ionic strength limited interaction between the bacterial and mineral surface and despite being oppositely charged, adsorption was reduced.

Microbial response to silica biomineralisation

Batch silicification experiments with undersaturated silica solutions equilibrated with microbial cells (e.g., Fein et al., 2002, Yee et al., 2003) showed that monomeric silica immobilization by microbes is minimal and that the role microorganisms play in the silicification process may have been overestimated. However, these studies are not representative of a true silicification process taking place in natural hot spring systems, where a constant re-supply of aqueous silica guarantees supersaturated conditions and a continual polymerisation reaction controlled by various physico-chemical parameters. Recent studies (Phoenix et al., 2000, Benning et al., 2004a, b) have demonstrated that cyanobacteria (*Calothrix*) repeatedly exposed to regularly refreshed, supersaturated polymerising silica solution can lead to extensive biomineralisation and that similar textures and structures to natural sinter deposits are formed.

Benning et al. (2004a, b) used high resolution synchrotron radiation Fourier-transform infrared micro-spectroscopy (SR-FTIR) to study *in-situ* and in vivo, the effect of increasing silica load on cyanobacterial filaments. Their results suggested a three-step reaction, where in the first stage the sheath (exopolysaccharides, EPS) of the cyanobacteria thickens in response to incubation in a silica-supersaturated medium. This occurs in parallel with the thermodynamically driven polymerisation of the monosilicic acid and the formation of silica nanoparticles. In a second stage, the thick EPS acts as a template for the accumulation of amorphous silica nanoparticles on the cell surface (Benning et al., 2004a, b). During the last step, silica particles grow progressively by the continuous formation of inorganic silane bonds, and by the aggregation of the existing particles leading ultimately to the development of thick aggregates, and eventually full cyanobacterial encasing / fossilization.

Similar, Lalonde et al. (2005) demonstrated that *S. azorense* (grown as a H_2-oxidizer) produced a protein-rich biofilm when exposed to increasing silica concentrations and that this biofilm was rich in amino functional groups thus enhancing the adsorption of silica nanoparticles onto the surfaces of *S. azorense*. From this, they suggested that microbial silicification may lead to increased rates of sinter formation, but due to the observed restricted silicification to the biofilm matrix, speculated that the studied organism had a low preservation potential.

Microbial viability during silica biomineralisation

Microorganisms living in natural hot springs that are supersaturated with dissolved silica will invariably become silicified and fossilized (Fig. 2.7) and this process is unavoidable. However, the question whether microbes actually can survive the mineralization process and continue to function with a silica coating still remains unclear.

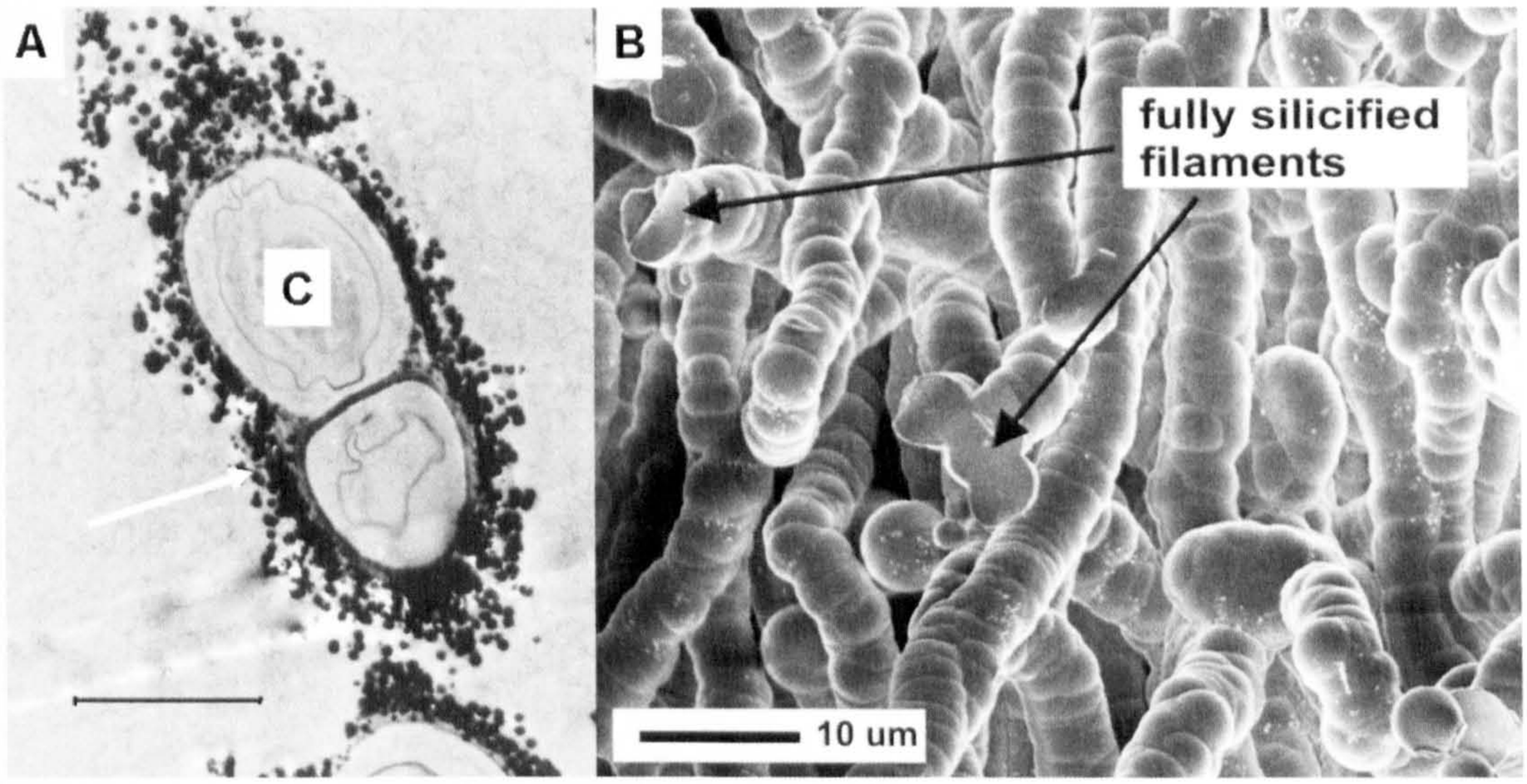

Figure 2.7: A) TEM photomicrograph of a naturally silicified microorganism (probably cyanobacteria) collected from the Strokkur hot spring, Iceland (from Phoenix, 2001). The bacterial cells (C) have acted as a nucleation site/surface for the precipitation of the amorphous silica spheres (arrow). Scale bar = 5μm. B) Fully silicified filaments on slides collected after 25 months from an outflow channel at Krafla Power Station in Iceland (this study).

Previous studies (Schultze-Lam et al., 1995; Konhauser and Ferris, 1996) focussing on the silicification of cyanobacteria suggested that if mineralization would occur inside the microbial cell this would initiate cell lysis by disrupting metabolic processes, whereas mineralization restricted to the microbial surface (i.e., cell wall, EPS sheath) may not be detrimental. However, as soon as the cell lyses, silicification will also proceed intracellularly. The decay of filamentous cyanobacteria starts quite rapidly, only a few days after cell death (Bartley, 1996). Thus, cyanobacterial trichomes and sheaths will only be preserved if silica mineralization is rapid and occurs while cells are still alive or shortly after their death (Jones et al., 1998). It follows that the style of silicification of microbes in hot springs waters is a function of the rates of silica precipitation, secondary precipitation and organic matter decay. In addition, the availability of nucleation sites and the constant new delivery of monosilicic acid to the surface of microbes or nanoparticles (all controlled by the degree of supersaturation in the fluid; e.g., Gunnarsson and Arnorsson, 2000; Jones et al., 2001) will strongly influence the textures and preservation mode of the silicified microbe in the sinter deposit. Ferris et al. (1988) proposed that iron-loaded bacterial cells may be better protected against cell wall degradation in the presence of metal cations due to the inhibition of autolytic activity (cell walls degradation by the microbe's own lytic enzymes). As a result, preservation of intact cellular structures is better maintained if

microbes display a "metal coating" before they get silicified. These results were later confirmed by Urrutia and Beveridge (1994).

Phoenix et al. (2000) applied autofluorescence analyses and measurements of the rate of photosynthesis to determine whether cyanobacterial cells (i.e., *Calothrix*) remained viable once silicified. They showed that intact, healthy cells exhibited only extracellular mineralisation (Fig. 2.7A) and that mineralised cyanobacteria remained both intact and functioning while encrusted in an extensive (~5μm) crust. However, unhealthy and damaged cells were silicified also intracellularly (Phoenix et al., 2000) suggesting that sheaths can play a vital role for the microbe to survive in hot spring environments subjected to extensive silicification. This correlates well with other experimental work by Benning et al. (2004a, b) which showed that the sheath of *Calothrix* when exposed to silica rich media increase in thickness prior to silicification.

Some studies (e.g., Merz, 1992; Verrecchia et al., 1995; Phoenix et al., 1999) argued that biomineralization (both calcite and silica) is restricted to the surface of healthy microbial cells due to metabolic processes (e.g., photosynthesis) of the microbial cell. In addition, Phoenix et al. (1999) showed that the sheath of certain cyanobacteria can act as a diffusion barrier for particles $\geq$ 11nm, thus inhibiting internal mineralization.

Despite silicification being detrimental to the microbial cell, it has been shown (e.g., Phoenix et al. 2001a, b) that prior to full silicification, the silica crusts can provide some advantages for microorganisms inhabiting hostile environments such as silica saturated hot springs. A thin layer of silica can protect microorganisms against high intensity light (UV light, Fig. 2.8; Phoenix, 2001; Phoenix et al, 2001) and predation and intrusion by other microorganisms but also prevent them from dehydration (the amorphous silica matrix is highly hydrated). Simply by acting as a viable site for mineral nucleation, microorganisms may passively allow the formation of their own siliceous shield. This process has also been proposed to have aided the survival of microorganisms in the silica-enriched shallow-water environments in the Archean era where high levels of UV radiation prevailed (Phoenix, 2001; Phoenix et al, 2001).

Based on these findings, Phoenix et al. (2000) and Benning et al. (2005) developed a silicification model (Fig. 2.8) where the accumulation of silica nanoparticles is restricted to the outer surface of the sheath due to the impenetrability of the sheaths to larger particles. The model also indicates that the accumulating silica colloids will protect the microbial cell from damaging UV light, while the photosynthetically active radiation (PAR) can still penetrate through the layer to ensure the perpetuation of photosynthesis.

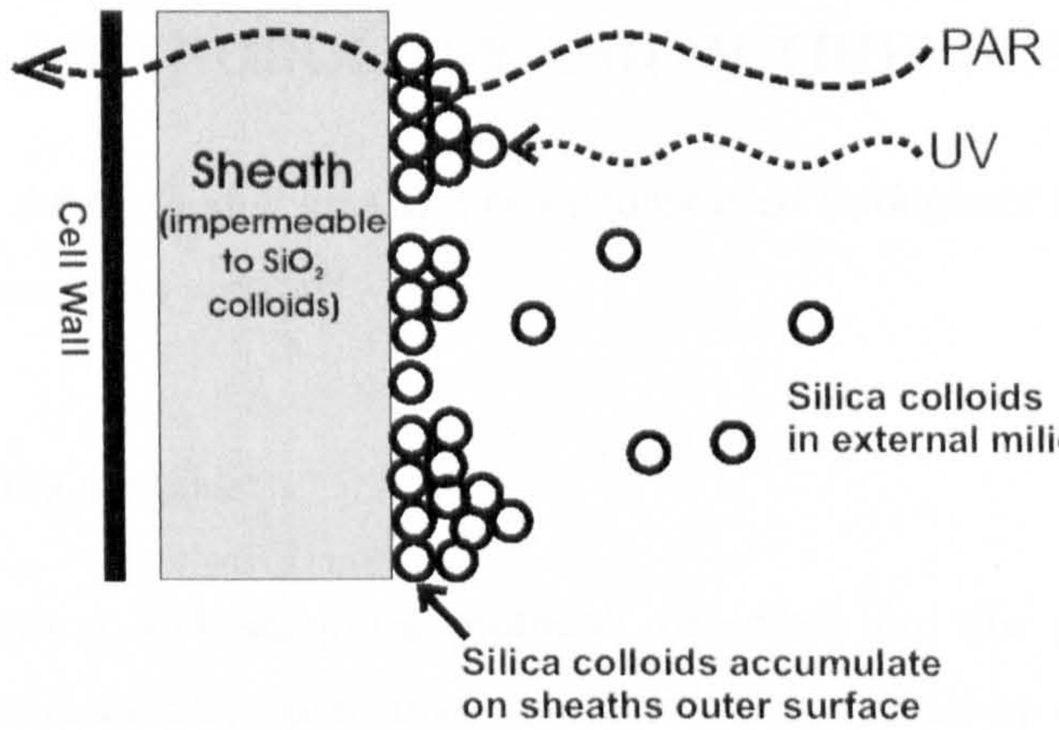

Figure 2.8: Silicification model illustrating the advantages of the microbial sheath (see text) to silicification (Benning et al., 2005).

Finally, biosilicification is also very important in the formation of siliceous microstromatolites as microbes act as nucleation and growth sites but also provide the growing microstromatolite with structural integrity and thus longevity (Konhauser et al., 1999, 2001). All these advantages are quite similar to the function of the EPS sheath thus indicating that the sheath and the precipitated silica crust may work together to protect microorganisms within the hostile conditions prevalent in hot springs (Benning et al., 2005).

3 METHODOLOGY AND METHOD DESIGN

This chapter details the methodologies and procedures used throughout the course of this study and is divided into two main sections:

(i) Field sampling methods:

a. Silicification and sampling protocol; describes on site pH, T, and flow rate measurements, collection of geothermal waters, and set-up of *in-situ* sinter growth experiments.

b. Characterization of geothermal waters; details analyses carried out on collected geothermal waters and describes the geochemical modelling applied to evaluate the silica saturation state within each studied water.

c. Characterization of *in-situ* grown sinters; sinter texture and structure were analysed using scanning electron microscopy (SEM) and sinter mineralogy was determined with X-ray diffraction (XRD).

d. Molecular techniques; describes extraction of bacterial and archaeal DNA from sediments and the subsequent analyses to determine the microbial diversity.

(ii) Laboratory methods

a. Synthesis of silica nanoparticles; details analytical methods to prepare a supersaturated silica solution and describes the procedures to initiate silica polymerisation.

b. Experimental designs; experimental set-ups employed to monitor initial steps of nucleation and growth of silica nanoparticles from a supersaturated fluid.

c. Analysis of aqueous solutions; spectrophotometric methods used to determine dissolved SiO_2 and carbohydrates.

d. Optical characterisation of solid phases; details a suite of microscopic methods applied to image synthesised silica nanoparticles.

e. Dynamic Light Scattering (DLS); describes the DLS theory and details the specifics of DLS measurements and data processing.

f. Synchrotron-based Small Angle X-ray Scattering (SAXS); gives an introduction into synchrotron radiation and SAXS theory; details the station configuration used at ESRF (Grenoble, France) and SRS (Daresbury, UK); specifies the protocols used for data reduction and analysis and describes two kinetic models employed for the interpretation of the SAXS data.

Many of the details described below are in part repeated in the results chapters in order for the chapters to be clearer and self-contained.

3.1 Field sampling methods

3.1.1 Silicification and sampling protocol.

In September 2005 short- and long-term *in-situ* sinter growth experiments were set up in five geothermal areas in Iceland: Geysir, Hveragerdi, Reykjanes, Svartsengi and Krafla (see Fig. 4.1). Prior to each silicification experiment, the temperature and pH of the geothermal waters were determined *in-situ* using a KT-thermocouple (±0.2) and a Hanna pH meter with a NIST pH electrode (±0.05, calibrated at temperature). The lateral water flow rates were determined at each site by measuring the time for a floating object (e.g., leaves, paper) to pass a certain distance (usually at least 2-7 m). Subsequently, 150 ml samples of spring or drain water were filtered through a sterile single-use 0.2 µm polycarbonate filter unit for cation (acidified on site with concentrated HNO_3, ratio 1:50) and for anion (non-acidified) determination. The polycarbonate filter papers were stored in 15 ml tubes for later analysis of suspended particulates > 0.2 µm. Additionally, 50 ml were filtered through the 0.2 µm polycarbonate filter unit for monosilicic acid (acidified on site with concentrated HNO_3, 1:10 ratio) and total silica (concentrated NaOH added on site, 1:10 ratio) analysis. All solution samples were stored in the fridge at ~4°C.

At each site a teflon tray holding 20 microscope glass slides (surfaces sterilised with 70% ethanol) was immersed into the geothermal water either within an outflow channel or close to a pool rim. Each tray contained four rows with five 25x75mm slides. They were placed in such a way that the top section of each slide (max. 1cm) was partially exposed to air. Over a time period between 30 min and 25 months, usually sets of five slides were collected at specific time intervals and analysed. For each site, the relative time steps for the collection of slides were estimated from the visible amounts of sinter deposited within and along the outflow channels or pool rims.

At each sampling interval, immediately after removal from the trays, individual slides were transferred into sterile 50ml tubes and subsequently stored in the fridge at ~4°C. Three out of five collected slides (at each sampling step) were used to determine precipitation rates after drying in an oven at 60°C (to constant weight) and weighing. The difference in weight between sinter covered and uncovered slides provided an average sinter growth rate and standard deviation in kilograms of precipitate per year and per square meter. The remaining two slides were fixed *in-situ* (in the field) with filtered 2.5 % glutaraldehyde solutions and used for the SEM characterization of biological material.

3.1.2 Characterization of geothermal waters

For cation analysis, prior to analysis, acidified samples were diluted with deionised water (DIW) to yield element concentrations within the range of the quantification method. Total concentrations of Al, B, Ca, Fe, K, Li, Mg, Mn, Na and Sr were determined using Inductively Coupled Plasma Optical Emission Spectroscopy (ICP-OES, Thermo Jarell Ash IRIS spectrophotometer). The estimated error (2%) of the measurements was calculated as twice the standard deviation from certified standard solutions.

For total anion content (i.e., Cl^-, F^-, NO_3^- and SO_4^{2-}), filtered, non-acidified waters were also diluted and analysed by ion chromatography (IC) using a Dionex DX-600 ion chromatograph with an EDS50A UVD 17OU detector, an Ionpac AS16 column and KOH as eluent. The estimated error (4%) of the measurements was calculated as twice the standard deviation from the mean of 3 repeat measurements.

Total and monomeric silica (i.e., monosilicic acid) were analysed with the spectrophotometric molybdate yellow method (Greenberg et al., 1985) which is described in more detail in section 3.2.3.

Geochemical modelling

To calculate the saturation state of silica within each geothermal system studied, the major chemical constituents, temperature and pH of the geothermal waters were used as inputs for geochemical modelling using the geochemical code PHREEQC (version 2.13.3; Parkhurst and Appelo, 1999) and the wateq4 database (Ball and Norstrom, 1992) with the amorphous silica data updated using the values from Gunnarsson and Arnórsson (2000). The saturation indices, $SI = \log (IAP/K_{sp})$, were determined for each geothermal system, with IAP being the ionic activity product and K_{sp} the solubility product and where $SI>0$ represents supersaturation and $SI<0$ undersaturation.

3.1.3 Characterization of *in-situ* grown sinters

Upon return to the laboratory the glutaraldehyde fixed slides were washed once with a phosphate buffer (pH 7) and then continuously dehydrated using a series of ethanol exchange steps (30%, 50%, 70%, 90%, 100%). In addition, at Reykjanes and Svartsengi, the untreated sterile filters used for the water collection were analysed for particulates.

Field Emission Gun (FEG) Scanning Electron Microscopy (SEM)

For microscopic imaging and qualitative elemental analysis, slides or filters were dried and placed on a sticky carbon pad covering an aluminium stub, then coated with a 3 nm platinum layer and analysed using a Field Emission Gun Scanning Electron Microscope (FEG-SEM, LEO 1530) equipped with an Oxford Instruments energy dispersive X-ray (EDX) detector and INCA software. Images were collected at 3 kV and a working distance of 4 mm, while for EDX analysis the working distance was increased to 8mm and the accelerating voltage to 15kV. More information on scanning electron microscopy is given in section 3.2.4.

To determine the silica particle size distribution on the slides from Svartsengi and Reykjanes, high-resolution SEM photomicrographs were imported into CorelDraw® and the diameter of individual silica colloids was measured by drawing an appropriately sized square around each of the particles and converting the width of the squares into real dimensions. For both sites, about 140 nanoparticles each were measured and a mean particle diameter and the polydispersity (i.e., standard deviation) were calculated.

X-ray Diffraction (XRD)

The mineralogical composition of the fresh precipitates that formed on the slides at each sampling site was analysed using X-ray powder diffraction (XRD). XRD is a non-destructive technique for textural and structural characterisation (e.g., crystal orientation, crystallinity, crystal defects) of crystalline materials. Diffraction occurs when penetrating radiation, i.e., X-rays, that interacts with a crystalline substance is scattered due to the orientation of the crystal lattice. Diffraction peaks are produced by constructive interference of a monochromatic beam scattered from each set of lattice planes at specific angles. The peak intensities are determined by the atomic arrangements within the lattice planes. Consequently, an XRD pattern can be looked upon as a fingerprint of the periodic atomic arrangements in a given material (Evans and Radosavljević-Evans, 2004).

About 200 mg of precipitate was carefully scraped off the unfixed glass slide, the materials were dried and ground to a fine powder and deposited on a silicon sample holder. Analyses were carried out with a Philips PW1050 diffractometer and scans were acquired from 5 to 70°2θ at 1°/min with a step size of 0.02° (total scan length of ~1 hour) and operating conditions of 40kV and 30mA using CuKα radiation. Data was analysed and compared to published data for standard minerals in the JCPDF files (International Center for Diffraction Data®).

3.1.4 Molecular techniques

DNA extraction and PCR amplification

DNA extractions were carried out from water-saturated sediments using the FastDNA®SPIN Kit for soils (Qbiogene; according to the manufacturer's instructions). This DNA kit is designed efficiently to isolate bacterial and archaeal as well as fungal, plant and animal genomic DNA from soil and other environmental samples. Samples were placed into sterile 2.0 ml tubes containing a lysing matrix together with irregularly shaped garnet particles and a single ceramic sphere to break up hard samples such as bones or seeds. Following lysis, samples were centrifuged to pellet debris and the lysing matrix. The supernatant was purified using a silica-based gene cleaning procedure along with SPIN filters. The eluted DNA was used for polymerase chain reactions (PCR, Fig. 3.1) and the selective amplification of bacterial and archaeal 16S rDNA (small-subunit ribosomal Deoxyribonucleic Acid).

PCR is a molecular genetic technique for making multiple copies of a DNA template (Fig. 3.1A) and consists of three basic steps which are repeated several times (Fig. 3.1B). First, the target genetic material must be denatured, i.e., the DNA helix must be unwound and separated by heating to 90-96°C. The second step involves hybridization or annealing, in which the primers (known DNA sequences from the beginning and end of the gene of interest) bind to their complementary bases on the now single-stranded DNA (Fig. 3.1B, Step 2). The third step is the synthesis of a complementary DNA strand by a DNA polymerase. Starting from the primer, the polymerase can read a template strand and match it with complementary nucleotides resulting in one new strand which forms a helix with the template (Fig. 3.1B, Step 3). This way each helix is composed of one of the original strands plus its newly synthesised complementary strand.

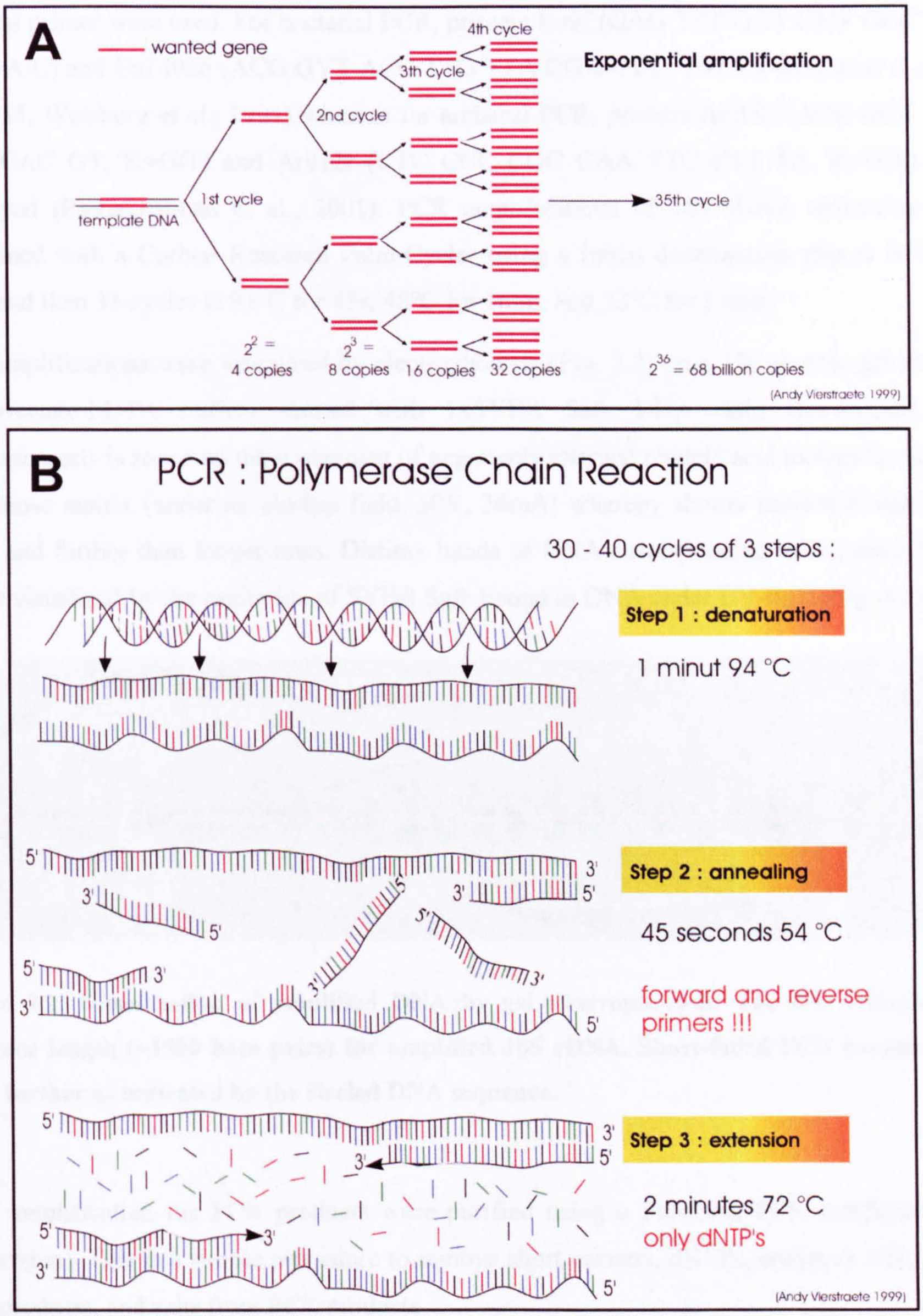

Figure 3.1: A) The exponential amplification of the gene during PCR, and B) the three basic steps of PCR (both pictures taken from http://users.ugent.be/~avierstr).

For this study, PCR reaction mixtures (50µl) contained 1x*Taq* PCR buffer (10xNH_4 Buffer), 1U *Taq* DNA Polymerase and 1.5mM MgCl2 (all included in BIOTAQ™ DNA Polymerase product purchased from BIOLINE), 5xenhancer (BIOLINE), 100uM dNTP (i.e., deoxyribonucleotide triphosphate), 1ng of extracted DNA and 0.5uM of a specific bacterial or

archaeal primer were used. For bacterial PCR, primers Eu9f (GAG TTT GAT CMT GGC TCA G, M=A/C) and Eu1492b (ACG GYT ACC TTG TTA CGA CTT, Y=T/C) were used (Lane et al., 1985; Weisburg et al., 1991) whereas for archaeal PCR, primers Ar109f (ACK GCT CAG TAA CAC GT, K=G/T) and Ar912r (CTC CCC CGC CAA TTC CTT TA, K=G/T) were employed (Ramakrishnan et al., 2001). PCR amplifications of 16S rDNA sequences were performed with a Corbett Research Palm-Cycler using a initial denaturation step at 94°C for 5min and then 33 cycles at 94°C for 45s, 48°C for 1min, and 72°C for 2 min.

PCR amplifications were visualised by electrophoresis (Fig. 3.2) on a 1% agarose gel in TAE (Tris-Acetate-EDTA buffer) stained with 1xSYBR Safe DNA stain (Invitrogen). Gel electrophoresis is based on the movement of negatively charged nucleic acid molecules through an agarose matrix (under an electric field; 80V, 30mA) whereby shorter molecules can move faster and further than longer ones. Distinct bands of DNA corresponding to sequence length can be visualized by the excitation of SYBR Safe bound to DNA under UV-light (Fig. 3.2).

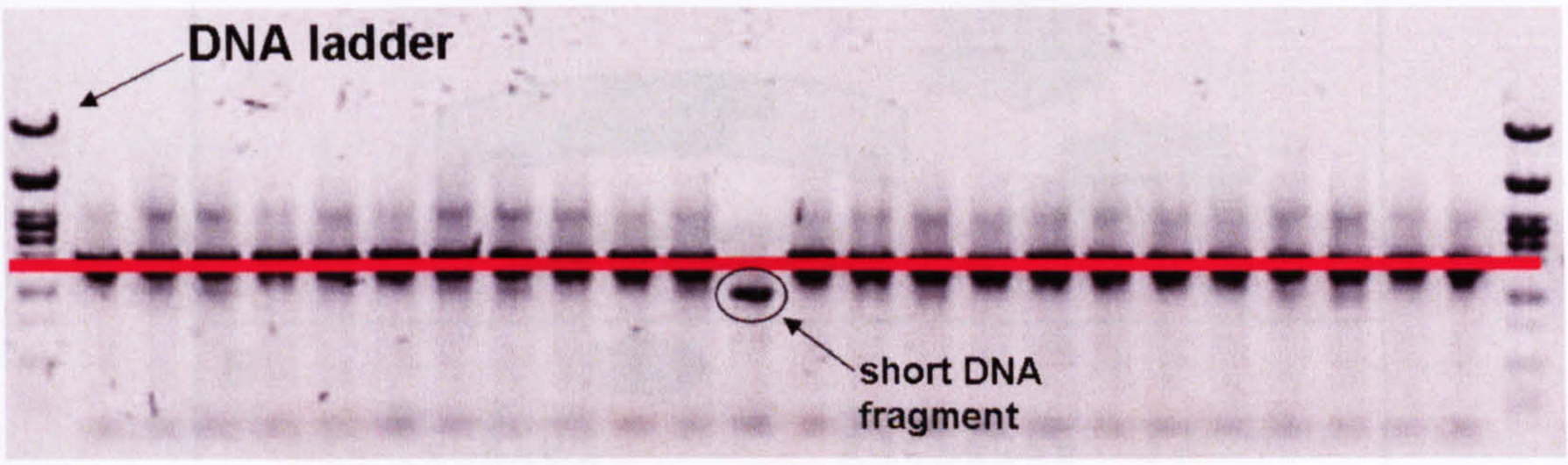

Figure 3.2: Visualisation of amplified DNA by gel electrophoresis. The line indicates the sequence length (~1500 base pairs) for amplified 16S rDNA. Short-failed PCR products will move further as indicated by the circled DNA sequence.

After amplification the PCR products were purified using a PureLink PCR Purification Kit (Invitrogen). This is a simple procedure to remove short primers, dNTPs, enzymes, short-failed PCR products, and salts from PCR products.

It should be noted that PCR can produce artefacts including chimeric sequences and DNA polymerase copy errors. A chimeric sequence is a sequence comprised of two or more phylogenetically distinct parent sequences. Chimeras are thought to occur when a prematurely terminated amplicon reanneals to a foreign DNA strand and is copied to completion in the following PCR cycles. DNA polymerase copy errors normally result in single base changes which will only have significance at the genus level.

Producing clone libraries

Cleaned up PCR products from bacterial isolates were cloned using the TOPO TA Cloning Kit (Version S) vector (pCR2.1-TOPO, Fig. 3.3) and host Escherichia coli strains (Mach1™-T1R strain, Invitrogen).

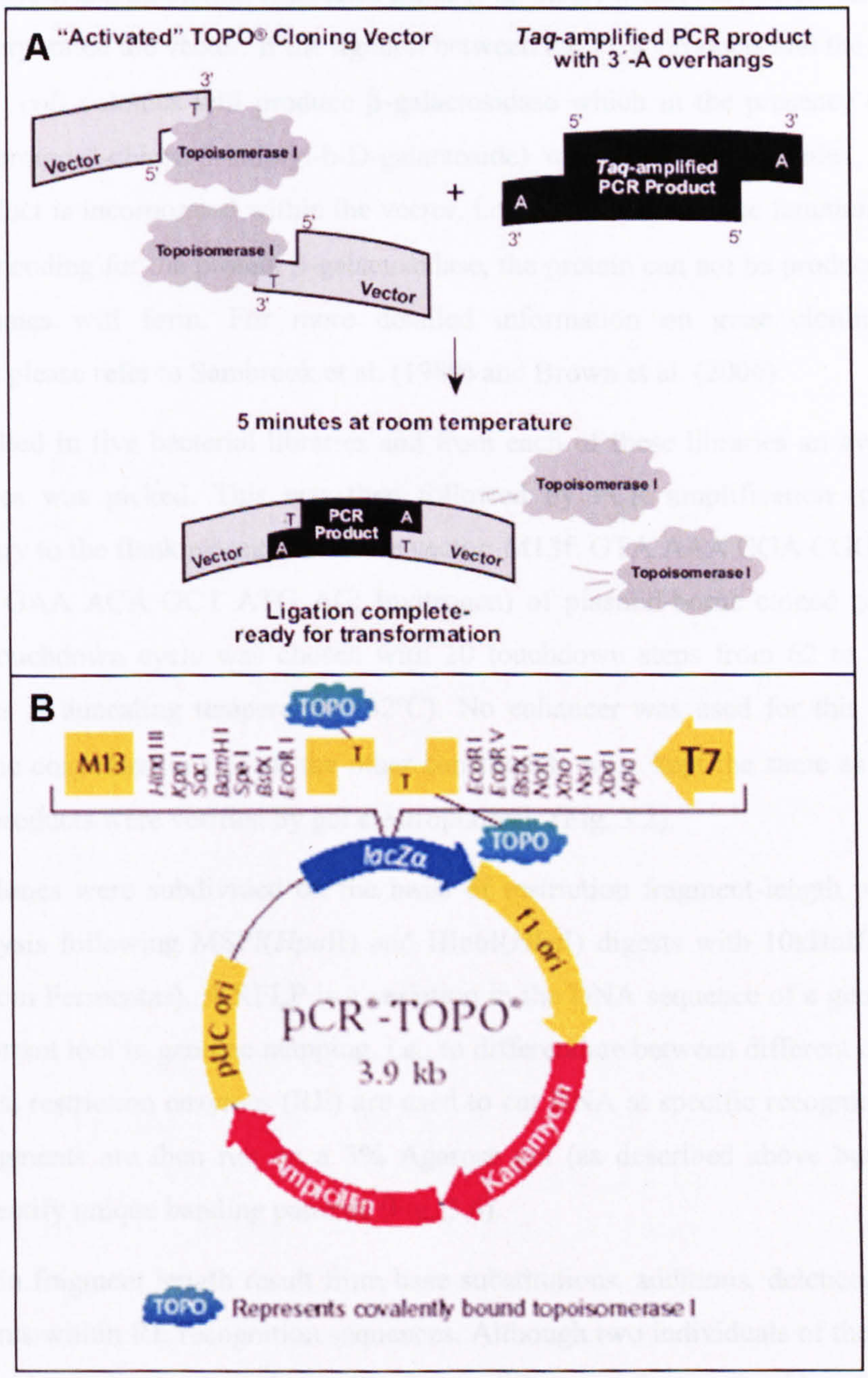

Figure 3.3: A) Mechanisms of TOPO TA cloning. B) The pCR2.1-TOPO vector showing position where Taq-amplified PCR products are inserted (both pictures were taken from www.invitrogen.com).

The key to TOPO TA Cloning is the enzyme, DNA topoisomerase I, which functions both, as a restriction enzyme (cuts only double-helical segments that contain a particular nucleotide sequence) and as a ligase (to join together DNA fragments). Furthermore, it enables the direct ligation between Taq-amplified PCR products equipped with 3′-A overhangs and the linearized TOPO TA Cloning® vectors provided with 3′-T overhangs (Fig. 3.3A). The vectors also include kanamycin and ampicillin resistance genes (Fig. 3.3B) which only select for *E. coli* cells that have incorporated the vector. If the ligation between the PCR products and the vector is not successful, *E. coli* colonies will produce β-galactosidase which in the presence of the X-gal substrate (5-bromo-4-chloro-3-indolyl-b-D-galactoside) will form blue colonies. However, if the PCR product is incorporated within the vector, i.e., inserted within the functional lacZ gene (Fig. 3.3B) encoding for the protein β-galactosidase, the protein can not be produced and white *E. coli* colonies will form. For more detailed information on gene cloning and PCR amplification please refer to Sambrook et al. (1989) and Brown et al. (2006).

Cloning resulted in five bacterial libraries and from each of these libraries an average of 100 white colonies was picked. This was then followed by PCR amplification (primers were complementary to the flanking regions on the vector; M13f: GTA AAA CGA CGG CCA G and M13r: CAG GAA ACA GCT ATG AC; Invitrogen) of plasmid-borne cloned gene from the isolates. A touchdown cycle was chosen with 20 touchdown steps from 62 to 55°C and 15 further cycles at annealing temperature (52°C). No enhancer was used for this reaction mix (50µl) and the concentrations of all the other constituents were kept the same as above. Once again, PCR products were verified by gel electrophoresis (Fig. 3.2).

Groups of clones were subdivided on the basis of restriction fragment-length polymorphism (RFLP) analysis following MSPI(*Hpa*II) and Hin6I(*Hha*I) digests with 10xBuffer Tango (all purchased from Fermentas). A RFLP is a variation in the DNA sequence of a genome and it is thus an important tool in genome mapping, i.e., to differentiate between different organisms. To detect RFLPs, restriction enzymes (RE) are used to cut DNA at specific recognition sites. The resulting fragments are then run on a 3% Agarose gel (as described above but run at 40V, 30mA) to identify unique banding patterns (Fig. 3.4).

Differences in fragment length result from base substitutions, additions, deletions or sequence rearrangements within RE recognition sequences. Although two individuals of the same species have almost identical genomes, they will always differ at a few nucleotides. Some of these differences will produce new restriction sites (or remove them) which will affect the banding pattern on the gels. Therefore, the less related the individuals, the more divergent their DNA sequences and the more likely it is to find a RFLP.

Figure 3.4: RFLP-pattern of 13 clones detected in sediments collected at Svartsengi based on HIN61 restriction. 8 different RFLP patterns (i.e., phylotypes, nr. 1 - 8) were identified among these 13 clones. Nr. 5 appears to be the most abundant clone sequence (i.e., 6 clones with identical pattern).

Based on results from the RFLP analysis, selected subgroups from each sample were sent to the Center for Genomics, Proteomics, and Bioinformatics Research Initiative (CGPBRI), University of Hawaii at Manoa (Honolulu, USA) for sequencing (ABI 3730XL capillary-based DNA sequencers). In DNA sequencing, the order of the nucleotide bases (i.e., adenine, guanine, cytosine, and thymine) in a DNA strand is determined. For more information on DNA sequencing please refer to Graham and Hill (2001).

All molecular work described above was carried out in the Wairakei Analytical Laboratory at GNS Science, Taupo, New Zealand.

Rarefaction analysis

Rarefaction is used to standardise and compare species richness / diversity between clone libraries with different sizes. For this, rarefaction curves are constructed in which the number of expected richness (e.g., RFLP patterns) is plotted against the number of individual clones subsampled from the clone library. If the curve exhibits a steep slope (i.e., increase in richness), a large fraction of the species diversity is not sampled and more clones need to be sequenced. However, if the curves approach a flat plateau, a sufficient number of clones were analysed and more intensive sampling will probably only yield a small number of additional species. In this study, rarefaction curves were generated using a programme written by Bailly et al. (2007).

Sequence assemblage and phylogenetic analysis

Contiguous sequences were assembled using Sequencher 4.7 (Gene Code Corporation) and then uploaded into the ribosomal database project (RDP-II; Cole et al., 2006 and references therein) in which all sequences were aligned and tested for sequence anomalies (e.g., chimeric artefacts). Closest relatives were found using the RDP-II Sequence Match and phylogenetic trees were constructed by the Weighbor weighted neighbor-joining (Weighbor) algorithm using the RDP-II Tree Tool. Weighbor is a distance-based phylogeny reconstruction method where the evolutionary distances between every two species is estimated. This results in a "distance matrix" which can then be used to reconstruct a phylogenetic tree that best fits the matrix. The Weighbor criterion for choosing a pair of taxa to join takes into account that errors in distance estimates are exponentially larger for longer distances (Bruno et al., 2000).

3.2 Laboratory methods

3.2.1 Synthesis of silica nanoparticles

Nucleation and growth of silica nanoparticles was determined in aqueous solutions with initial SiO_2 concentrations ranging from 320 to 1600ppm and ionic strengths (IS) from 0.02 to 0.22 M. The chosen range of SiO_2 and IS represents the concentrations most often found in geothermal waters and fluids of geological importance (e.g., seawater, brines). Stock solutions of aqueous SiO_2 were prepared by dissolving specific amounts of $Na_2SiO_2{\cdot}5H_2O$ and NaCl (Analar grade reagents) in deionised water (DIW) producing an alkaline (pH ~ 12) silica solution in which all silica was present as monosilicic acid ($H_4SiO_{4(aq)}$). Silica polymerisation and silica nanoparticle formation were induced either by lowering the pH to 7 (with 1M HCl, at 30°C) where silica solubility is lowest (Fig. 2.4) or by fast cooling a high temperature (230°C), near- neutral pH (pH 7-8) and silica supersaturated solution to temperatures between 30 and 60°C.

To determine the impact of specific organic molecules on the process of silica polymerisation and silica nanoparticle formation, a few experiments were carried out in the presence of organic compounds (representing microbial cell envelope functional groups; chapter 6 and 8). The organics used were glucose[1], glutamic acid[2] and xanthan gum[3] and were prepared by dissolving

---

[1] glucose ($C_6H_{12}O_6$) is a monosaccharide (pKa at 0.94 and 6.11; McElroy and Glass, 1951).

[2] glutamic acid ($C_5H_9NO_4$) is an acidic amino acid (pKa at 2.13, 4.31 and 9.67; Weast, 1972).

[3] xanthan gum is a complex anionic polysaccharide produced by the bacterium *Xanthomonas campestri* (Sutherland, 1994).

specific amounts of Analar grade reagents in DIW. The concentrations of the organics used were comparable with the biomass used in batch silicification experiments (e.g., Phoenix et al., 2003) but were also restricted by the low solubility of xanthan gum in water.

3.2.2 Experimental designs

The kinetics and mechanisms of the nucleation and growth of silica nanoparticles in inorganic and organic/biological systems were quantified in two systems; (1) via neutralisation of a high pH solution using a continuously stirred low temperature flow-through set-up (Fig. 3.5 and 3.6) that ensured complete mixing and homogeneity, and (2) a high-temperature system (Fig. 3.7) that was designed to mimic the polymerisation processes as they occur in natural geothermal environments where polymerisation is induced by a sudden temperature drop.

Low temperature flow through set-up

The continuous flow set-ups for SAXS and DLS are illustrated in Fig., 3.5 and 3.6. The experiments were carried out with polymerising silica solutions that were prepared in a plastic beaker (see section 3.2.1) just prior to commencement of the data collection. Note that a pH between 7 and 8 was reached in less than 30 s but a stable pH reading of 7.0 usually needed 2 - 3 minutes. The pH adjusted solutions were circulated via a peristaltic pump through a quartz capillary for the SAXS measurements (Fig. 3.5) or through a plastic cuvette for the DLS measurements (Fig. 3.6) and back into the beaker in which the solutions were continuously stirred. In contrast to SAXS measurements, the constant flow of solution in and out of the plastic cuvette affected the DLS data acquisition. As a consequence, the continuous flow was temporarily stopped during DLS measurements (5 min / pattern and 30 s delay time in between to exchange solution) and the solution in the cuvette was replaced in between measurements. The pH of the solutions in both measurement types were monitored every 5 minutes to make sure that no significant changes occurred. For most experiments an increase of about 0.5 pH units was observed (over ~ 3 hours), however, this shift was ignored during data processing as pH fluctuations between 7 and 8 hardly affect the silica polymerisation rate (Iler, 1979).

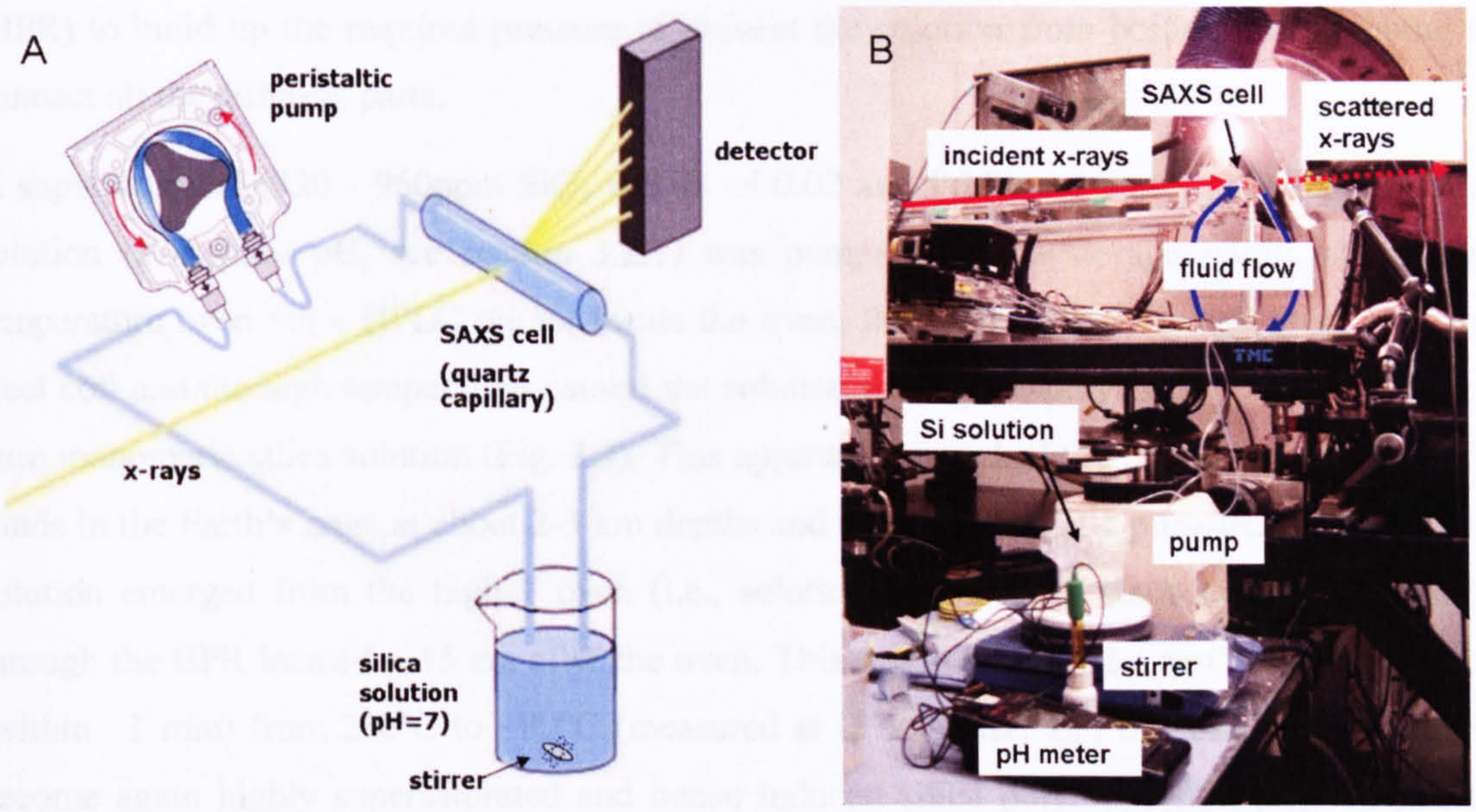

Figure 3.5: A) Schematic diagram of low temperature flow-through system used for SAXS experiments and B) experimental set-up at station 6.2m at SRS, Daresbury Laboratory, UK.

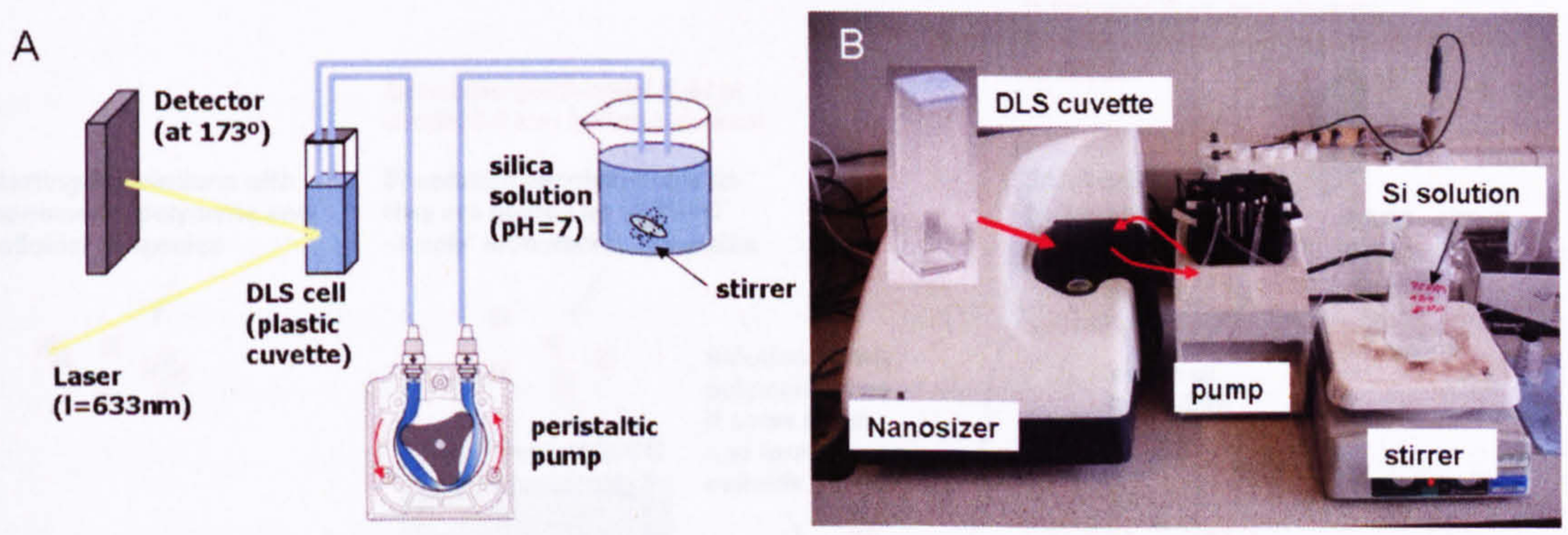

Figure 3.6: A) Schematic diagram of low temperature flow-through system used for DLS experiments and B) experimental set-up using a Malvern Zetasizer Nano ZS at Leeds University.

High-temperature, simulated geothermal system

In a second procedure, a flow-through geothermal simulator was designed to mimic the polymerisation process as it occurs in natural geothermal environments (Fig. 3.7). The system consists of a) a storage bottle that contains the experimental solutions (at 25°C), b) a HPLC pump to maintain a continuous flow of the solution at high pressures (p = 750psi), c) a high-temperature oven (kept at 230°C) with a 6m stainless steel coil, d) a backpressure regulator

(BPR) to build up the required pressure to prevent the solution from boiling and e) tubing to connect all the different parts.

A supersaturated (320 - 960ppm SiO_2 and IS of 0.02 and 0.11) and partly polymerised silica solution (at neutral pH, see section 3.2.1) was pumped from a storage bottle into a high temperature oven via a HPLC pump. Inside the oven, the fluid passed through a 6m stainless steel coil and the high temperature caused the solution to fully de-polymerise thus producing a pure monomeric silica solution (Fig. 3.7). This approach mimicked the conditions of silica-rich fluids in the Earth's crust at about 2-3 km depths and under hydrostatic pressures. After the hot solution emerged from the high-T oven (i.e., solution immediately starts to cool), it passed through the BPR located ~ 15 cm after the oven. This distance assured a fast temperature drop (within ~1 min) from 230°C to ~80°C (measured at BPR outlet) and this caused the silica to become again highly supersaturated and hence induced silica polymerisation (Fig. 3.7). This rapid cooling process simulates the conditions when a supersaturated hot spring fluid is discharged at the Earth's surface and polymerisation of the monomeric silica and thus the nucleation and growth of silica nanoparticles is initiated.

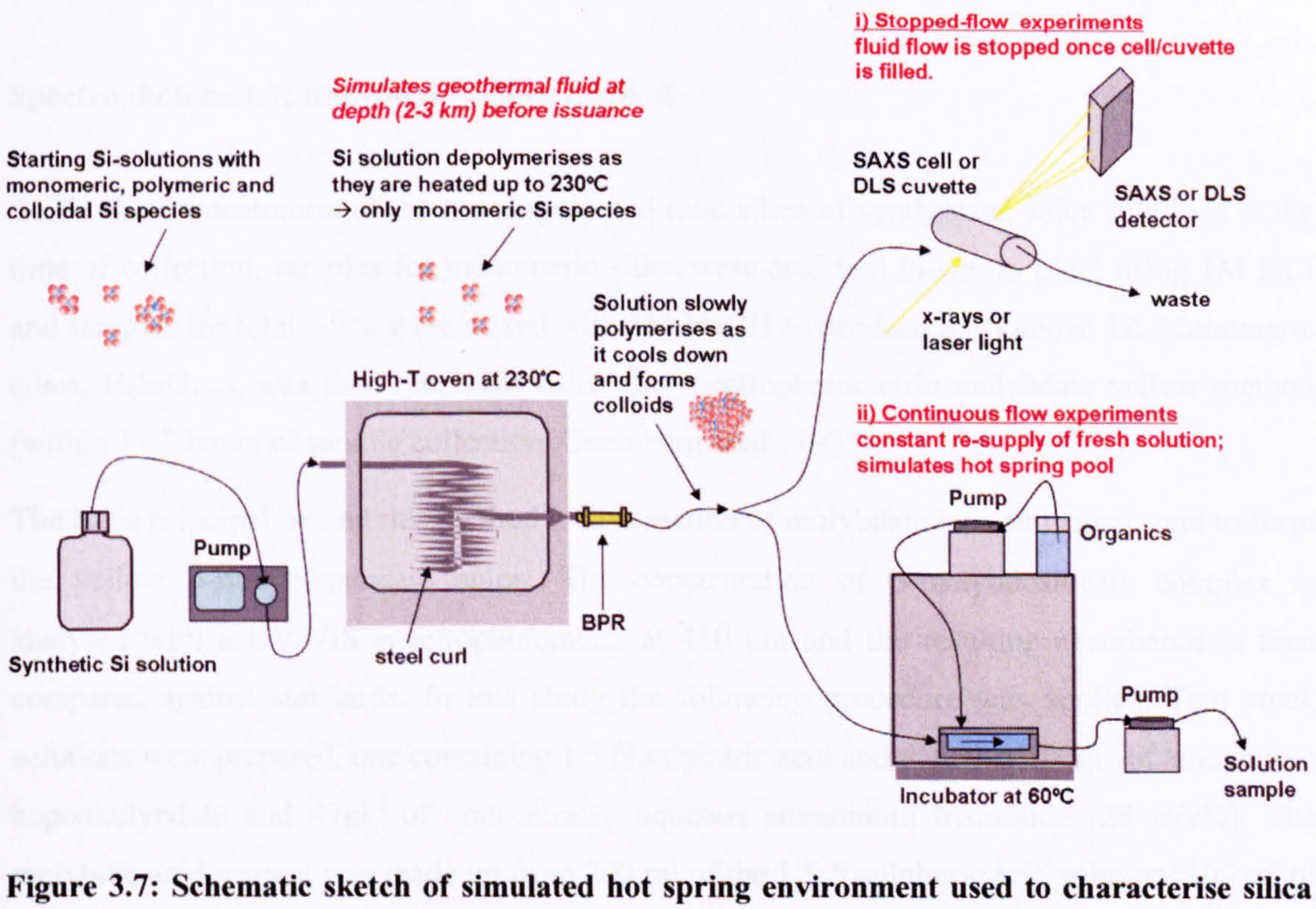

Figure 3.7: Schematic sketch of simulated hot spring environment used to characterise silica nanoparticle formation (modified from Benning and Mountain, 2004).

This high temperature set-up was used for two different sets of experiments (Fig. 3.7):

(i) Stopped-flow experiments where the initial steps of nucleation and growth of silica nanoparticles were monitored and quantified *in-situ* and time-resolved as a function of SiO_2 and IS using SAXS and DLS (chapter 7). For this, the SAXS cell or DLS cuvette were first filled with polymerising solution and then disconnected from the high-T system for subsequent data acquisition.

(ii) Continuous flow experiments where the size and polydispersity of silica nanoparticles were monitored under constant re-supply of fresh silica solution (various tested SiO_2, IS and T) and added organics (glucose and xanthan gum) in a tray placed within the incubator (for 30-42 hours, at 58 and 33°C respectively). Silica polymerisation and silica nanoparticle formation were quantified using spectroscopic and microscopic techniques (chapter 8).

3.2.3 Analysis of aqueous phase

Spectrophotometric molybdate yellow method

To fix the concentration of the monomeric and total silica of synthesised silica solutions at the time of collection, samples for monomeric silica were acidified *in-situ* to pH 2 using 1M HCl and samples for total silica were mixed with 1M NaOH to produce a pH above 12. Monomeric silica, $H_4SiO_{4(aq)}$, was then measured using the spectrophotometric molybdate yellow method (within 1 - 2 hours of sample collection, Greenberg et al., 1985).

The basic principal behind this method is the reaction of molybdate ions and silicic acid to form the yellow β-molybdosilicate anion. The concentration of β-molybdosilicate complex is analysed with a UV/VIS spectrophotometer at 410 nm and the resulting absorbance is then compared against standards. In this study the following procedure was applied. Two stock solutions were prepared, one containing 1.5 *N* sulphuric acid and the other $100gl^{-1}$ of ammonium heptamolybdate and $47gl^{-1}$ of concentrated aqueous ammonium hydroxide (28 w/v%). The molybdic acid reagent was made up from 200 ml of the 1.5 *N* sulphuric acid solution, 100 ml of the molybdate stock solution and 500 ml of distilled water. To analyse a sample, 20 ml of this reagent were mixed with less than 5 ml of a sample (SiO_2 content no higher than 20ppm) and diluted to 25 ml with deionised water. After equilibration for 10 minutes, the absorbance of each sample was measured at 410 nm on a CECIL 3041 UV/VIS spectrophotometer. The resulting values were compared with standards (8, 12, 16 and 20ppm) prepared using $Na_2SiO_3 \cdot 5H_2O$. The

final concentrations of the samples were calculated from the calibration curve (regression coefficient, $R^2 \sim 0.998$) as defined by the four measured standards and the blank. The estimated error of this method, i.e., twice the relative standard deviation of the mean (6%), was evaluated from repeated analyses of standards.

Determination of total carbohydrate – the phenol-sulphuric acid method

To determine the amount of sugars (e.g., glucose, xanthan gum) within the experiments, a colorimetric method based on the Molisch test (Molisch, 1886) for carbohydrates was applied. This method is based on the hydrolysis of polysaccharides to monosaccharides and their susequent dehydration by sulfuric acid to produce an aldehyde. This product then condenses with a colour developer (aromatic amine or phenol) to form a yellow-orange complex which is subsequently analysed with a spectrophotometer.

The method used in this thesis was developped by Dubois et al. (1956) and its reagents consist of a 5% (w/v) phenol solution and concentrated sulphuric acid (>95%). The procedure involves the following steps: into glass test tubes 1 ml of sample containing the equivalent of 20-100 µg glucose and 1 ml of phenol solution were mixed. In a second step, 5 ml of concentrated sulphuric acid were added to the solution in a way to ensure fast and complete mixing. The solutions were left for 10 minutes, shaken and left for another 20 minutes before measuring the adsorbance at 488 nm on the CECIL 3041 UV/VIS spectrophotometer. For comparison a set of glucose standards as well as a blank were prepared with each set of sample analysis. These standards (10, 20, 30, 40 and 50ppm) along with the blank defined a calibration curve ($R^2 \sim 0.999$) with which final concentration were calculated. Similar to the molybdate yellow method, the estimated error of this method (~6% for both glucose and xanthan gum) was determined from repeated analysis of standards.

3.2.4 Optical characterisation of solid phase

Field Emission Gun (FEG) Scanning Electron Microscopy (SEM)

The basic principle behind scanning electron microscopy is the detection of secondary electrons that are released when an electron beam is scanning the surface of a specimen. The secondary electrons are detected by a scintillation material that produces flashes of light which are subsequently amplified by a photomultiplier tube.

The main difference between SEM and FEG-SEM is the electron emitter type. For conventional SEM imaging, a thermionic emitter is used (a Tungsten filament is heated up by electrical

currents to a point where electrons can escape) while for FEG-SEM, electron emission is induced by applying a electrical potential gradient to a small tip radius (~ 100 nm) of a filament (e.g., Tungsten). The advantages of FEG-SEM over conventional SEM include higher spatial resolution (~ 3 or 6 times better) as well as cleaner images with less electrostatic distortions.

For elemental analysis of imaged surfaces, an EDX (Energy Dispersive X-ray) analyser was used. EDX is based on a high voltage electron beam (10-20keV), which causes X-rays specific to the elements under examination to be emitted from the scanned specimen.

Samples of synthesised silica nanoparticles were prepared by filtering a few millilitres of polymerising solution through 0.1 or 0.2μm polycarbonate filters. The filter papers were subsequently washed with DIW to remove remaining salt and silica solution and left to dry at ambient temperature. The filter papers were placed on SEM Al-stubs using sticky carbon pads and then coated with 3 nm of platinum. Analyses were done on a LEO 1530 FEG SEM equipped with an Oxford Instruments EDX detector and INCA software using a working distance of 3mm and an accelerating voltage of 3kV. For EDX analysis, the working distance was increased to 8mm and the accelerating voltage to 15kV.

Transmission Electron Microscopy (TEM)

In the TEM electrons are emitted at the top of the microscopic column (under vacuum) and are focussed by electromagnetic lenses to produce a very thin beam, which is then passed through the specimen to produce an image on the fluorescent screen placed at the bottom of the microscope.

Similar to the FEG-SEM a field emission gun can be incorporated into the TEM to produce a brighter, more coherent electron beam (thus allowing higher resolution) as well as an EDX system allowing highly spatially resolved elemental analysis and nano-diffraction of the material under consideration.

TEM samples of synthesised silica colloids were prepared by placing a droplet of diluted polymerising solution on a formvar coated copper grid which was then dried in air to form a thin film. TEM grids were analysed with a Philips CM10 TEM using an accelerating voltage of 80kV.

CRYO – TEM

To test for artefacts (e.g., shape distortions, aggregation) caused by sample dehydration or the high vacuum of standard SEM and TEM analytical approaches, some samples were also imaged

using a cryo-TEM combined with an ultra-rapid freezing technique. Cryo-TEM allows the imaging of materials suspended in a solution *in-situ* in their native environment with minor artefacts from sample handling (Hansen and Slavin, 1993).

In order to prepare the cryo-TEM samples, 5 μL of the reacting solutions were deposited on a TEM grid and specimens were flash-frozen in liquid ethane (maintained at liquid nitrogen temperatures; Egelhaaf et al., 2000) using a standard guillotine plunging device (vitrobot) that instantaneously (< 1 sec) vitrified the samples and avoided ice formation. Ethane was used as a cryogen due to its high thermal conductivity and its large heat capacity at low temperatures, which in turn prevents the formation of ice and microbubbles around the sample. The vitrified specimens were transferred at -180°C onto a Gatan 626 cryo-holder and into a FEI T20FEG TEM operated at 200 kV. After an equilibration time of 1 hour (until no apparent drift was observed), the specimens were examined at -180°C and low dose images were recorded on a 4k x 4k Gatan CCD camera.

Particle size analysis

To determine the particle size distribution of silica particles imaged by both SEM and TEM, photomicrographs were imported into CorelDraw® and the diameter of individual silica nanoparticle was measured by drawing an appropriately sized square around each of the particles. The widths of the squares were converted into real dimensions using the pixel:real size ratio of the scale bar at the bottom of the photomicrographs. To obtain a size distribution with reasonably high precision, about 100 - 200 particles were measured in each image and the mean particle diameter (i.e., mean value) and the polydispersity (i.e., standard deviation) were calculated.

3.2.5 Dynamic light scattering (DLS)

DLS is a well-established, non-intrusive technique to probe the size and polydispersity of spherical, colloidal particles. DLS is effective in the size range 0.6 nm - 6 μm (Fig. 3.8, (http://www.malvern.com/LabEng/products/zetasizer/zetasizer; May 2008) and allows the *in-situ* investigation of the particle growth process (i.e., nucleation, growth and aggregation) in a single experiment. However, at particle sizes smaller ~10 nm, the % errors of individual DLS measurements can be as large as 50% (see chapter 6 and 7).

DLS measures particle growth by tracing changes in the scattering pattern of laser light caused by the Brownian motion of the particles (Brownian motion of larger particles is slower than for

smaller particles). The particle size can be calculated from the translational diffusion coefficient, D, using the Stokes-Einstein equation:

$$d(H) = KT / 3\pi\eta D \quad \text{(Eq. 3.1)}$$

where $d(H)$ is the hydrodynamic diameter (refers to how a particle diffuses within a fluid), K is the Boltzmann constant ($1.38\times10^{-23}m^2kgs^{-2}K^{-1}$), T is the absolute temperature in Kelvin, and η is the viscosity of the fluid. Note that the DLS assumes particle sphericity.

All DLS measurements were performed with the Malvern Zetasizer Nano ZS (Malvern Instruments) equipped with a He-Ne laser (λ=633nm) and a backscatter detector at a fixed angle of 173°. The instrument recorded the intensity autocorrelation function, which was then transformed into volume functions using various algorithms to obtain size information.

DLS measurements allow easy data acquisition and fast data processing, however, compared to SAXS (see below) the accuracy of DLS measurements is far lower especially in the size range studied here (Fig. 3.8, 1 to 10nm). Therefore, this method was mainly used to verify and corroborate the SAXS results.

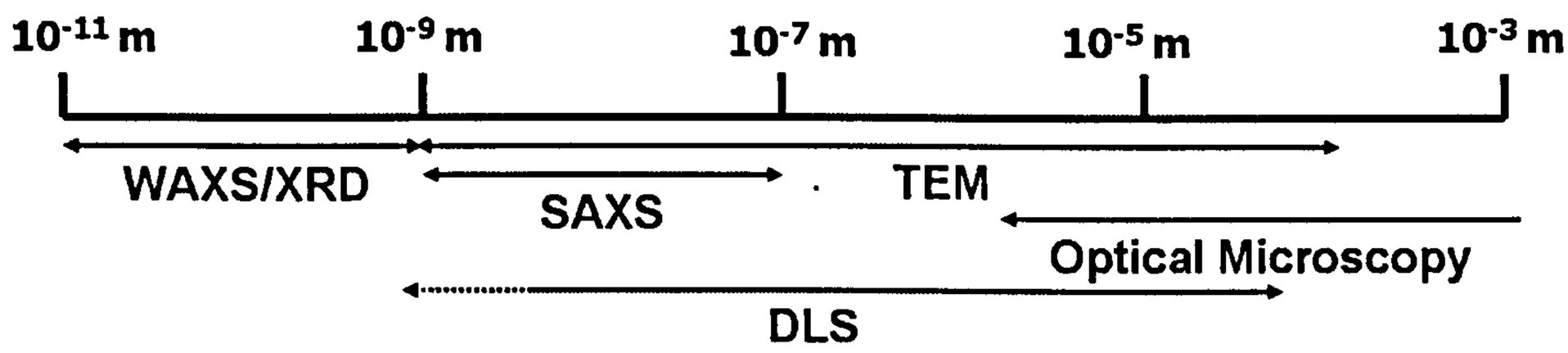

Figure 3.8: Resolution limits for some microscopic and spectroscopic methods. The dotted line indicates that DLS measurements at these small sizes are characterised by large errors.

3.2.6 Synchrotron-based Small Angle X-ray Scattering (SAXS)

Small Angle X-ray Scattering (SAXS) is a non-intrusive, time-resolved and *in-situ* method to monitor nucleation and growth of crystalline as well as non-crystalline particles suspended in solution with dimensions typically between 1 and 100nm (Fig. 3.8). SAXS can be universally applied to studies of nanostructures and it can provide (among others) information about particle size, shape and polydispersity.

Synchrotron radiation

The X-ray beam used for SAXS can have different sources. In this study, SAXS experiments were carried out using synchrotron light which has several advantages over laboratory sources including high flux and brightness as well as low divergence thus allowing SAXS measurements to be collected at low angles (~0.05˚). This results in high quality data that can be acquired at very fast time steps (<10ms) and thus the processes and kinetics of particle formation can be quantified *in-situ* and in realtime.

Synchrotron light, i.e., X-rays, are produced by accelerating electrons around a storage ring close to the speed of light (Fig. 3.9A). The electrons are generated by an electron gun and are first accelerated in a linear accelerator (Linac) and the booster ring where they reach their final speed (99.9% speed of light). They are then injected into the storage ring where they circulate (forced by powerful electromagnets), producing synchrotron radiation, but without gaining further energy. The radiation is projected at a tangent to the electron storage ring and captured by beamlines (Fig. 3.9A).

Beamlines are positioned at bending magnets marking the "corners" of the storage ring or at insertion devices (wigglers or undulators, both periodic magnetic structures forcing the electrons to undergo oscillations and radiate) which are located in the straight sections of the storage ring (Fig. 3.9A). The front of the beamline houses the optical devices (i.e., slits, attenuators, crystal monochromators and mirrors; Fig. 3.9B) to control the bandwidth, photon flux, beam dimensions, focus, and collimation of the X-rays, while the end of the beamline consists of the experimental hutch, where X-rays are focussed onto the samples, and the control cabin (Fig. 3.9B).

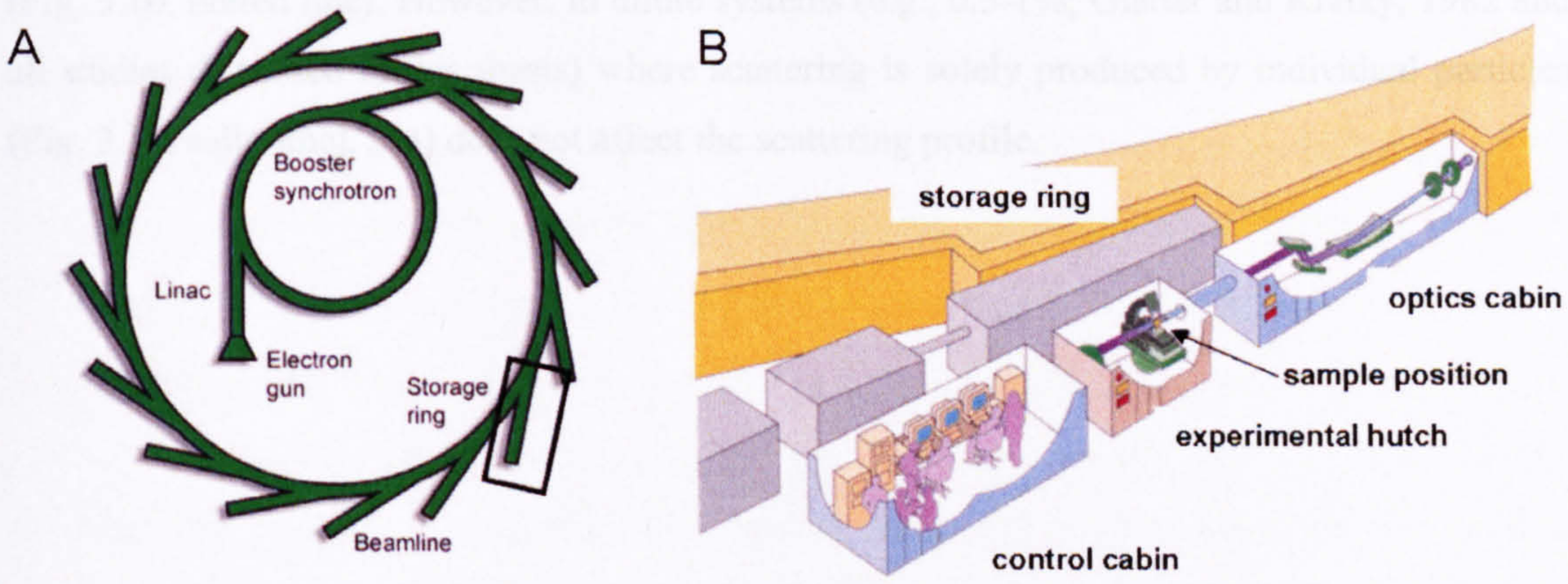

Figure 3.9: A) Schematic sketch of a synchrotron (www. diamond.ac.uk) and B) close-up of a beamline (rectangle in A) consisting of the optics cabin, the experimental hutch and the control cabin (www.esrf.eu).

SAXS theory

Using a synchrotron source, SAXS is performed by focusing an intense, monochromatic and collimated photon beam with wavelengths between 0.8 and 1.4 A (5 - 9 keV) onto a sample and observing a coherent scattering pattern that arises due to the differences in electron density between the solute and the solvent (Fig. 3.10).

Bragg's law, $d = \lambda/(2\sin\theta)$, is the basic law that governs SAXS and it states that the dimensions, *d*, of an object are reciprocal to the angles (θ) to which the X-rays are scattered. Thus, information pertaining to nano- to colloidal-scale structures can only be obtained by measuring at very small angles (2θ<6°).

For SAXS we can consider a generalized rule that describes the behaviour of the scattered intensity as a function of the Bragg size, *d* that is observed at a given scattering angle 2θ, where $d = 2\pi/q$ and $q = 4\pi/\lambda\sin\theta$:

$$I(q) = \frac{N}{V} V_p^{\,2} (\Delta\rho)^2 P(q) S(q) \quad \text{(Eq. 3.2)}$$

The total scattering intensity (eq. 3.2) is proportional to the number of scattering elements, *N*, the irradiated volume, *V*, the volume of individual scattering entity, V_p, and the electron density contrast between solute and solvent, $\Delta\rho = \rho_p - \rho_s$. Furthermore, the intensity is proportional to a form factor, *P(q)*, and a structure factor, *S(q)*, both dimensionless parameters. *P*(q) gives information about shape and size whereas *S*(q) accounts for inter-particle scattering in non-dilute systems. Particle interactions are only expected in concentrated systems which will manifest themselves at low *q* values as a sharp increase or decrease in the scattering intensity (Fig. 3.10, dotted line). However, in dilute systems (e.g., 0.5-1%; Glatter and Kratky, 1982 and all studies discussed in this thesis) where scattering is solely produced by individual particles (Fig. 3.10, solid line), *S*(q) does not affect the scattering profile.

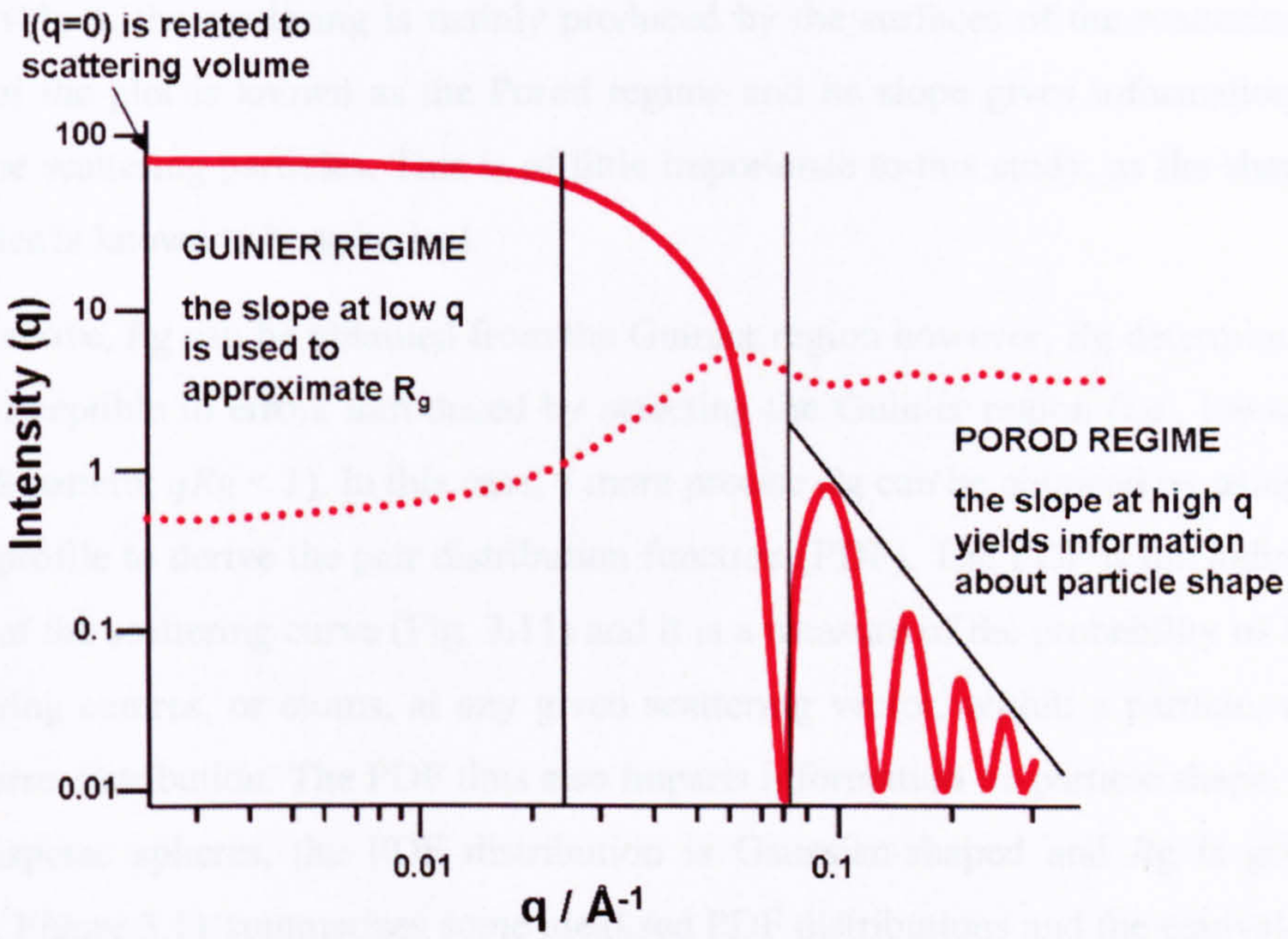

Figure 3.10: Idealized SAXS scattering profile for a dilute (solid line) and a non-dilute solution (dotted line) with monodisperse spherical particles (modified from www.ansto.gov.au).

A plot from the scattering intensity versus the scattering vector, q, provides information about two main regimes (Fig. 3.10). The area at low q angles is known as the Guinier regime. Its slope can be used to approximate the radius of gyration of the particles, i.e., the Guinier radius (Rg). Rg is basically the mechanical equivalent of the average distance inside a particle to the centre of inertia of the particle. In dilute, monodisperse systems, Rg can be determined from the following equation:

$$I(q) = I_0 e^{\frac{-q^2 R_g{}^2}{3}} \quad \text{(Eq. 3.3)}$$

where I_0 is the intensity of the scattering curve at $q = 0$ and I_0 is related to the square of the volume, V, and the electron density contrast, $\Delta\rho$, of the illuminated scattering material: $I_0 = (\Delta\rho)^2 V^2$. Using equation 3.3, Rg can be evaluated from a plot of log $I(q)$ vs. q^2, known as the Guinier plot. The slope of the linear region found in the low q range, a limit usually defined as $qR\text{g} < 1$, can be used to derive Rg. Depending on the particle shape, specific equations can be used to calculate the real particle radius. For a sphere (as in the case of silica nanoparticles) with a radius R, the following relation is valid (see Glatter and Kratky, 1982 for other shapes):

$$Rg^2 = \frac{3}{5} R^2 \quad \text{(Eq. 3.4)}$$

At high q values, the scattering is mainly produced by the surfaces of the scattering particles. This part of the plot is known as the Porod regime and its slope gives information about the shape of the scattering particles. This is of little importance to this study, as the shape of silica nanoparticles is known to be spherical.

As shown above, Rg can be obtained from the Guinier region however, Rg determined this way are very susceptible to errors introduced by selecting the Guinier region (i.e., low-q range for each SAXS pattern; $qR\text{g} < 1$). In this case, a more precise Rg can be obtained by using the entire scattering profile to derive the pair distribution function (PDF). The PDF is the indirect Fourier transform of the scattering curve (Fig. 3.11) and it is a measure of the probability of finding any two scattering centres, or atoms, at any given scattering vector, within a particle, assuming a monodisperse distribution. The PDF thus also imparts information on particle shape. In the case of monodisperse spheres, the PDF distribution is Gaussian-shaped and Rg is given by the maximum. Figure 3.11 summarises some idealised PDF distributions and the equivalent particle shapes.

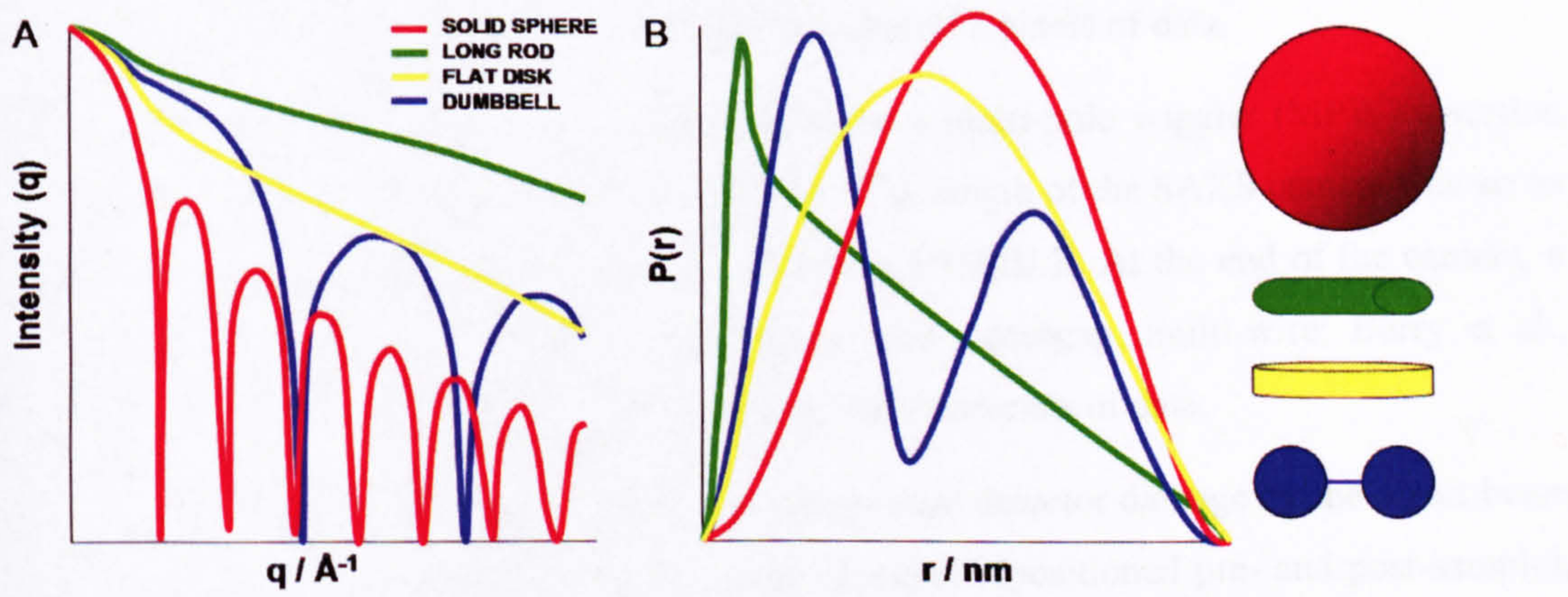

Figure 3.11: (A) Idealized SAXS scattering profiles and (B) corresponding PDF curves of various geometrical bodies as a function of particle radius (in ideal monodisperse and dilute systems; after Svergun and Koch 2003).

Another parameter of importance is the invariant, Q, defined as the integral of $I(q)$. It is related to the total scattering volume, V, produced by the shape and size of the forming particles and thus represents the total scattering power law of the sample. Q can be written as:

$$Q = 2\pi^2 (\Delta\rho)^2 V \quad \text{(Eq. 3.5)}$$

where $\Delta\rho$ is the electron density contrast (e.g., Glatter and Kratky, 1982; Bras et al., 2005). For classical growth processes (see section 2.1.2) it would be expected that the invariant continually increases with time due to continuous particle growth by monomer / oligomer addition from the

solution. However, during Ostwald ripening or coarsening (OR) (see section 2.1.2), no new material precipitates and the invariant should, therefore, remain constant.

Station configuration

All SAXS measurements were carried out either on the Dutch-Belgian (DUBBLE, BM26) beamline at the European Synchrotron Radiation Facility (ESRF), France or at station 6.2m at the Synchrotron Radiation Source (SRS), Daresbury Laboratory, UK. Here, only the parameters that affected the data collection in this study are detailed but the full configuration for DUBBLE and station 6.2m can be found in Borsboom et al. (1998) and Cernik et al. (2004) respectively.

At DUBBLE, the incident X-ray (with an energy of 12keV) was supplied by a dipole magnet and the q-range was optimized so that the final configuration used a wavelength of 1 Å and a sample-to-detector distance, i.e., camera length (evacuated camera tube), of 3.5m with an optimal derived q-range between 0.0005 to 0.223. At the end of the SAXS camera, a two-dimensional multiwire proportional detector (gas-filled and equiped with a CCD-camera - Photonic Science Xios-II) was positioned which provided 512 pixels of data.

At station 6.2m, the radiation source was provided by a multi-pole wiggler (MPW) insertion device and the energy used was 8.5 keV ($\lambda = 1.4$ Å). The length of the SAXS camera was set to 3.75 m to derive a q-range similar to the one chosen at DUBBLE. At the end of the camera, a 60° quadrant one-dimensional small-angle detector (gas microgap, multi-wire; Berry et al., 2003; Helsby et al., 2003) was positioned providing 1024 channels of data.

At both stations, a beam-stop was set such that it prevented detector damage by the direct beam and minimized the parasitic scatter. A pair of ion chambers (positioned pre- and post-sample), monitored the incoming and transmitted beam intensities, respectively. The q-axis was calibrated with the scattering pattern of wet rat-tail collagen. Images of the SAXS configuration at station 6.2 (SRS, UK) are shown in Fig. 3.12.

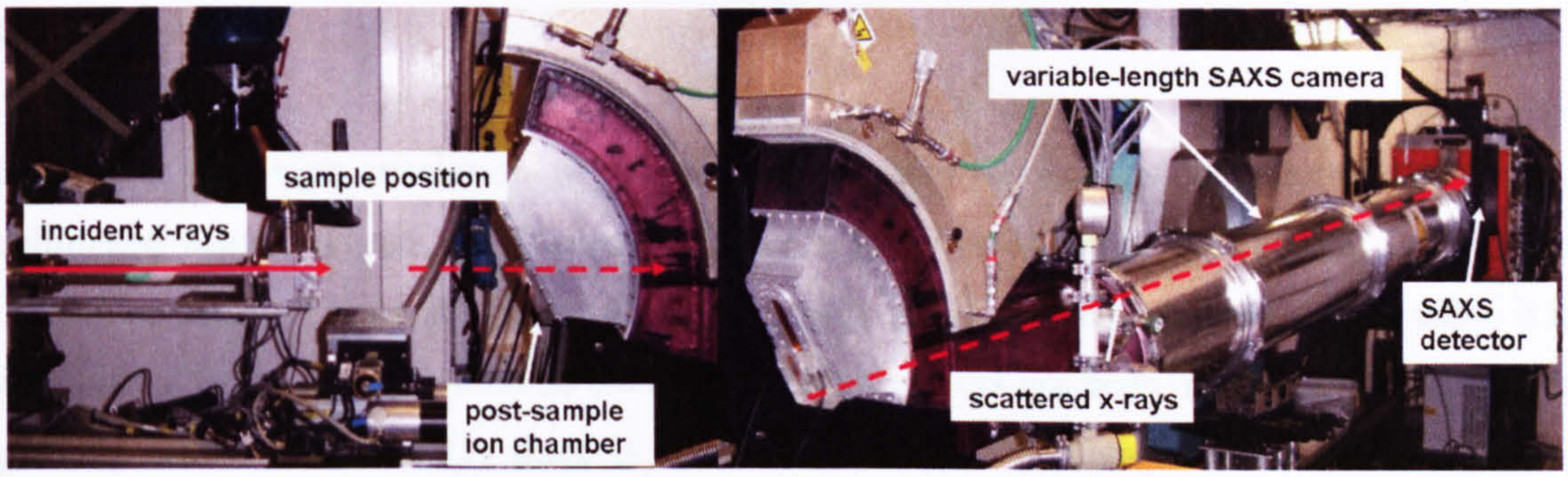

Figure 3.12: Set-up of station 6.2m at Synchrotron Radiation Source, Daresbury Laboratory, UK as discussed in the text.

Data reduction and treatment

2-D data collected at DUBBLE were first transformed to 1-D data by sector integration using BSL (a 2-D data manipulation package for image data, SRS, Daresbury). The converted DUBBLE data and the 1-D data collected at station 6.2m were then processed using the program XOTOKO (SRS software packages, Daresbury). The data were first normalised to the beam intensity (as measured by the pre-sample ion chamber) to compensate for the variation in the intensity of the incident beam flux as well as the decay of the beam current over the experimental time length. The data were then corrected for detector alinearities (i.e., each detector element does not have a uniform response to the incident X-rays) by dividing the data by a frame of fluorescence data collected from a zinc foil for station 6.2m and from a Fe^{55} source for DUBBLE respectively. Files processed this way provided ASCII file outputs that were loaded into excel for initial data analysis and to correct for scattering produced by the capillary, air, and the aqueous phase (i.e., water). These corrections are termed background subtraction. This was performed by subtracting a data set obtained for DIW (collected either before or after the experiments) from the normalised reduced scattering data.

The entire corrected intensity profiles were then read into GNOM (Svergun, 1992 and references therein), an indirect transform program for SAXS data processing. In the case of dilute and monodisperse systems, GNOM evaluates a pair distribution function (PDF) and provides an estimate for the radius of gyration, *R*g. Furthermore, GNOM extrapolates the data to $q = 0$ and thus provides a value for I_0. As mentioned earlier, the use of the entire scattering profile is more accurate than the classical Guinier approximation (see SAXS theory above) which only evaluates the slope in the Guinier regime and in chapter 6 and 7, the final reported *R*g values were thus evaluated using the GNOM code.

Data accuracy

In general, the high resolution of the SAXS detectors as well as the intense and highly collimated beam suggests small errors (<1%) for synchrotron-based SAXS data. But to date there is no standard method of determining the errors in SAXS measurements and actually, it is not unusual to see data in which no attempt to quantify errors has been made. The difficulty lies partially in the facts that (1) there is no standard way of reducing and analysing the data; background subtraction can be somewhat subjective in nature and can significantly affect the result and (2) that there is no standard methodology for SAXS measurements either. Therefore, it was necessary to replicate experimental and data reduction procedures precisely and to produce internally consistent SAXS data but also to ensure minimal errors.

In this study, the error for individual SAXS measurements was evaluated by GNOM which estimates the errors on the scattering data (usually < 3%) automatically using a polynomial smoothing procedure.

Kinetic analysis

To fit an appropriate kinetic model to the quantitative and time resolved SAXS and DLS data, the Johnson-Mehl-Avrami-Kolmogorov (JMAK) kinetic model and Thetadash kinetic model were used.

The JMAK kinetic model. The Johnson-Mehl-Avrami-Kolmogorov kinetic model (JMAK) was derived by Johnson and Mehl (1939), Avrami (1939, 1940) and Kolmogorov (1937) and it has been widely used to describe re-crystallization processes but also phase transformation processes. This model attempts to predict the fraction of crystallized material at every given point in time with the following assumptions: (1) the new phase nucleates as infinitely small, rigid, independent units that are able to overlap, (2) nucleation occurs randomly and uniformly (3) the nucleation rate is time-independent (4) the sample is of infinite size and boundary effects can be ignored, and (5) grain growth continues until impingement occurs.

The JMAK model has been applied in various studies including the growth of zeolite crystals (e.g., Thompson, 1992), polymerisation in layered phosphate salts (e.g., Cao and Mallouk, 1991), the formation of nano-zirconia (e.g., Malek et al., 1999) as well as the formation kinetics of oxyhydroxide nanoparticles (e.g., Shaw et al., 2005; Davidson et al., 2007). However, some studies (e.g., Allia et al., 1993; Illekova et al., 1996) struggled to fit the JMAK approach to their experimental data set thus indicating that similar to many other kinetics models the JMAK model may only provide a qualitative interpretation. In addition, Banfield and Zhang (2001)

suggested that the JMAK theory may not be optimal for analysis of reactions involving nanoparticles.

The essence of the model can be written as a very simple formula commonly referred to as the Avrami equation:

$$\alpha = 1 - e^{-(k(t-t_0))^n} \quad \text{(Eq. 3.6)}$$

where a is the degree of the reaction, t_0 is the induction time, k is the reaction constant and n is a constant related to the nucleation mechanisms (i.e., instantaneous, decreasing rate, or constant rate), the growth dimensionality (i.e., 1, 2, or 3-D) and the reaction mechanisms (i.e., diffusion- or surface-controlled; Table 3.1).

To obtain α, the Rg^3 values from the SAXS data were normalised using the following equation:

$$\alpha = \frac{Rg^3{}_t}{Rg^3{}_{\max}} \quad \text{(Eq. 3.7)}$$

where Rg_t is Rg at a given time, t, and Rg_{max} is Rg at the end of the reaction. Both k and n can then be determined from the intercept and slope, respectively, of a $\ln(-\ln(1-\alpha))$ versus $\ln t$ plot of the experimental data.

Table 3.1: Interpretation of the JMAK model constant, *n*, according to Hulbert (1969).

Growth dimensionality	Nucleation rate	Surface-controlled	Diffusion-controlled
3-D	constant	4	2.5
	decreasing	3 – 4	1.5 – 2.5
2-D	constant	3	2
	decreasing	2 – 3	1 – 2
1-D	constant	3	1.5
	decreasing	1 – 2	0.5 – 1.5

The Thetadash kinetic model. An alternative kinetic model is Thetadash, a population-dynamics based kinetic model developed by Hounslow et al (unpublished, University of

Sheffield). Similar to the JMAK approach, it describes the changes in volume fraction during nucleation and growth of nanoparticles. However, Thetadash assumes instantaneous and monodisperse nucleation, followed by classical growth. In a first step, Thetadash converts and normalises the experimentally obtained growth profiles (particle radius versus time) according to the degree of the reaction, α (similar to the JMAK kinetic model). In a second step, 3 different types of reaction mechanisms (chemical, surface, or diffusion controlled) and varying reaction orders are fitted to α in order to obtain the best fit in terms of the regression coefficient, R^2. For the best fit, the program also provides information about the critical nucleus size, R_0, (by extrapolating to t = 0) and the initial growth rate, G_0 (s^{-1}).

The initial growth rate obtained from Thetadash can then be used to calculate the rate constant which will allow a direct comparison to the rate constant calculated with the JMAK model (eq. 3.6):

$$k = \frac{G_0}{S_R - 1} \quad \text{(Eq. 3.8)}$$

S_R is the saturation ratio which is defined as $S_R = SI^{1/\nu}$ where SI is the saturation index and ν is the stoichiometric coefficient (i.e., the sum of the stoichiometry of the products in the solubility expression). SI is defined as:

$$SI = IAP / K_{sp} \quad \text{(Eq. 3.9)}$$

where IAP is the ionic activity product and K_{sp} is the solubility product. The SI values were calculated using the geochemical code PHREEQC (version 2.13.3; Parkhurst and Appelo, 1999) and the wateq4 database (Ball and Norstrom, 1992) with the amorphous silica data updated using the values from Gunnarsson and Arnórsson (2000).

4 SINTER GROWTH STUDIES IN ICELANDIC GEOTHERMAL AREAS

4.1 Abstract

Field *in-situ* sinter growth experiments have been carried out in five geochemically very different Icelandic geothermal areas with the aim to quantify the effects of water chemistry, [e.g., silica content (250 to 695 ppm SiO_2), salinity (meteoric to seawater), pH (7.5 to 10)], temperature (42-96°C), and microbial communities (prevalence, density, type) on the growth rates, textures and structures of sinters forming within and around hot springs. At each location, *in-situ* silica precipitation was monitored over time periods between 30 minutes and 25 months using glass slides that acted as precipitation substrates and sinter growth rates were derived.

In geothermal areas like Svartsengi and Reykjanes, subaqueous sinters developed rapidly with growth rates of 10 and 304 kg y^{-1} m^{-2} respectively, and this was attributed primarily to the near neutral pH, high salinity and medium to high silica content within these geothermal waters. The porous and homogeneous precipitates that formed at these sites were dominated by aggregates of amorphous silica but they contained few if any microorganisms. At Hveragerdi and Geysir, the geothermal waters were characterized by slightly alkaline pH, low salinity and lower silica content, resulting in undersaturated waters with low rates of sinter growth (0.2-1.4 kg $y^{-1}m^{-2}$). At these sites sinter formation was restricted to the vicinity of the air-water interface (AWI) where evaporation and condensation processes predominated, with sinter textures being governed by the formation of dense and heterogeneous crusts with well-defined spicules and silica terraces. In contrast, the subaqueous sinters at these sites were characterised by extensive biofilms, which, with time, became fully silicified and thus well preserved within the sinter edifices. Finally, at Krafla, the geothermal waters exhibited high sinter growth rates (19.5 kg $y^{-1}m^{-2}$) despite being considerably undersaturated with respect to amorphous silica. However, the bulk of the sinter textures and structure were made up of thick silicified biofilms with intermittent minor accessory minerals including albite, iron sulphides and oxides and minor traces of quartz. This suggested that in these waters, sinter growth was aided by the presence of thick biofilms which provided surfaces for the adhesion (e.g., via hydrogen bonding or entrapment within the complex structure of the exopolyssacharides) of pre-formed silica colloids. These results thus suggest that the interplay between purely abiotic processes and the ubiquitous presence of mesophilic and thermophilic microorganisms in modern silica rich terrestrial hydrothermal settings provides an excellent analogue for processes in Earth's and possibly Mars's ancient past.

4.2 Introduction

Iceland is well known for its geothermal areas which are the surface expression of the narrow belt of active faulting and volcanism caused by the Mid-Atlantic Ridge and the Greenland-Iceland-Faeroes Ridge. The geothermal areas include features such as mudpots, geysers, fumaroles and hot springs, most of which are inhabited by diverse mesophilic and thermophilic microbial life. In addition, outflow waters and condensed steam from wells and geothermal power stations created various man-made features, i.e., channels and pools (e.g., Blue Lagoon). The precipitation of silica in these systems is a well know process leading to the formation of silica sinters (e.g., Arnórsson, 1975) and the full silicification and subsequent fossilisation of microorganisms (Schultze-Lam et al., 1995; Konhauser et al., 2001). These microfossils are preserved in modern siliceous sinters and thus provide a modern analogue to fossilization in ancient siliceous terrestrial environments (Cady and Farmer, 1996; Konhauser and Ferris, 1996) and may even be important for our understanding of the siliceous sinter deposits postulated to exist in Gusev Crater on Mars (Squyres et al., 2007; 2008; Ruf et al., 2007).

The structures and fabrics of siliceous sinters deposited in and around Icelandic hot springs have been described as being partly governed by the encrustation, replacement and cementation of growing microbial mats (Schultze-Lam et al., 1995; Konhauser and Ferris, 1996). However, based on laboratory experiments and studies on natural geothermal environments (e.g., Taupo Volcanic Zone, New Zealand; Yellowstone, USA), it is evident that the mechanisms triggering silica precipitation are purely abiotic (e.g., Walter et al., 1972; Mountain et al., 2003 and references therein) and that silica saturation and precipitation is mostly induced by rapid cooling and boiling of geothermal waters or by co-precipitation with auxiliary minerals (e.g., Guidry and Chafetz, 2003; Mountain et al., 2003). Cooling seems to be the predominant process controlling the deposition of subaqueous sinter within geothermal systems. However, many silica sinters encountered in thermal hot spring areas are often formed subaerially (at or above the air-water interface, AWI) and therefore, in order to understand the formation and growth rates of silica sinters other hydrodynamic processes including wave action, capillary action, diffusion and splash must also be invoked (e.g., Mountain et al., 2003 and references therein).

Variations in silicification textures and structures have received considerable attention (e.g., Walter et al.; 1972, Ferris et al., 1986; Hinman and Lindstrom, 1996; Cady and Farmer, 1996; Schultze-Lam et al., 1995; Konhauser and Ferris, 1996; Renault et al., 1996; Jones et al., 1997, 1998; Phoenix, 2001; Konhauser et al., 2001; Mountain et al., 2003; Lalonde et al., 2005) as well as analysing the microbial diversity associated with silica precipitating springs (e.g., Pétursdóttir and Kristjánsson, 1996; Blank et al., 2002). From these studies, it follows that microorganisms play an indirect role in the silicification process as there are no metabolic

advantages to microbial silicification. However, their surfaces (e.g., cell walls, extracellular polysaccharides) provide suitable sites for the adhesion of silica particles and thus they allow different styles of silicification (governed by microbial morphology, e.g. filaments, bacillus, cocci) to develop.

Despite the plethora of silicification studies, the kinetics of sinter formation and the relationship between the inorganic precipitation rate, the sinter fabric and the associated microbiology are still poorly understood mostly due to a dearth of quantitative and *in-situ* lab and field analyses. Only few studies (e.g., Jones et al., 1999; McKenzie et al., 2001; Konhauser et al., 2001; Mountain et al., 2003; Smith et al., 2003; Handley et al., 2005, Schinteie et al., 2007) determined sinter growth rates using artificial substrates and amongst them even fewer (Mountain et al., 2003; Smith et al., 2003 and Handley et al., 2005) monitored growth rates over long time scales and characterised the structure and texture of the forming sinters at periodic time steps. Such *in-situ* field studies of sinter growth were mostly done in geothermal areas in New Zealand (e.g., Mountain et al., 2003, Handley et al., 2005) and only one short-term study was carried out at Krisuvik spring in Iceland (Konhauser et al., 2001).

Most studies related to Icelandic geothermal systems focussed on the characterization of siliceous sinters and the impact of microbes on sinter structure and texture (Schultze-Lam et al., 1995; Konhauser et al., 2001), the analysis of specific microbial assemblages and diversities in geothermal fields (e.g., Sonne-Hansen and Ahring, 1997; Kvist et al., 2007; Skírnisdottir et al., 2000), the inorganic chemistry of geothermal waters (e.g., Arnórsson et al., 1983a, b; Arnórsson, 1985; Stefánsson and Arnórsson, 2000), or silica scaling in geothermal power developments (e.g., Thordarson and Tómasson, 1989; Kristmannsdóttir 1989; Gunnarsson and Arnórsson, 2003). However, there is as yet no comparative, combined geochemical and structural study of the formation and growth rates of silica sinters in Icelandic hot spring systems.

To overcome this gap, in this study, *in-situ* sinter growth experiments were carried out in five different Icelandic geothermal discharges and hot springs (Fig. 4.1) with the main aim to quantify how pH, temperature, salinity and different microbial communities affect the growth rate and structure of silica sinters. At each location, *in-situ* growth of silica sinter was quantified based on precipitates that formed on glass slides that acted as substrates. The resulting sinter deposits were characterised using spectroscopic and microscopic methods and the effects of the various physico-chemical and microbial parameters on the growth rates and structures of sinters were assessed.

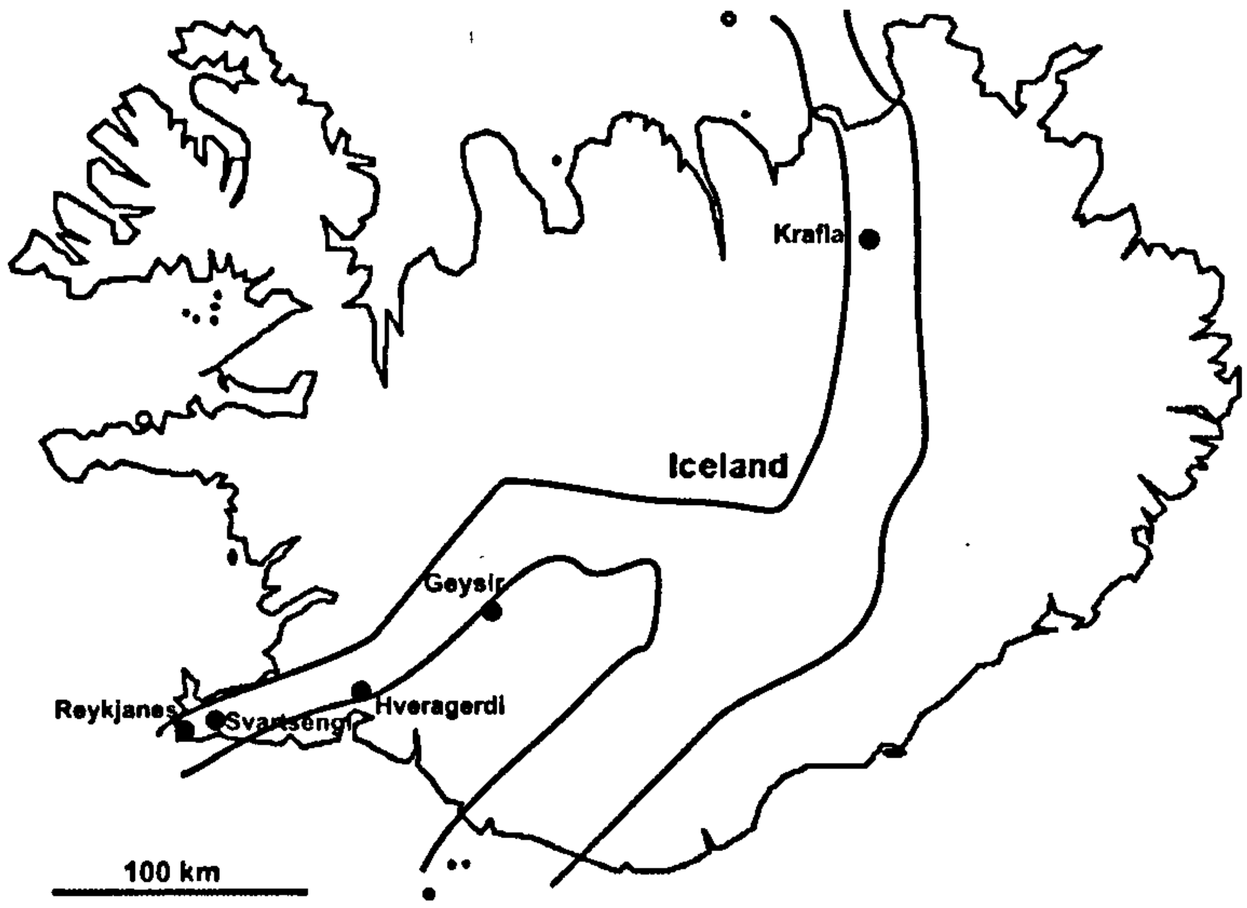

Figure 4.1: Map of sampling locations in Iceland where *in-situ* sinter growth experiments were carried out.

4.3 Methods

4.3.1 Sampling protocols

In September 2005 short- and long-term *in-situ* silica precipitation and sinter growth experiments were set up in five geothermal areas in Iceland including Geysir, Hveragerdi, Reykjanes, Svartsengi and Krafla (Fig. 4.1). Prior to each sinter growth experiment, the temperature and pH of the geothermal waters were determined *in-situ* using a KT-thermocouple (±0.2) and a Hanna pH meter with a NIST pH electrode (±0.05, calibrated at temperature). The water flow rates were determined at each site by measuring the time for a floating object (e.g., leaves, paper) to pass a certain distance (usually at least 2-7 m). Subsequently, 150ml samples of spring or drain water were filtered through a sterile single-use 0.2 µm polycarbonate filter unit for cation (acidified on site with concentrated HNO_3, ratio 1:50) and for anion (non-acidified) determination. Additionally, 50 mL were filtered through the 0.2µm polycarbonate filter unit for monomeric (acidified on site with concentrated HNO_3, 1:10 ratio) and total silica (concentrated NaOH added on site, 1:10 ratio) analysis.

At each site a teflon tray holding 20 microscope glass slides (surfaces sterilised with 70% ethánol) was immersed into the geothermal water either within an outflow channel or close to a pool rim. Each tray contained four rows with five 25x75mm slides. They were placed in such a way that the top section of each slide (max. 1cm) was partially exposed to air. Over a time

period between 30 min and 25 months, sets of five slides were collected at specific time intervals and analysed. For each site the relative time steps for the collection of slides were estimated from the visible amounts of sinter deposited within and along the outflow channels or pool rims.

At each sampling interval, immediately after removal from the trays, individual slides were transferred into sterile 50ml tubes and subsequently stored in the fridge at ~4°C. Three out of five collected slides (at each sampling step) were used to determine precipitation rates after drying in an oven at 60°C (to constant weight) and weighing. The difference in weight between sinter covered and uncovered slides provided an average sinter growth rate and standard deviation in kilograms of precipitate per year and per square meter. The remaining two slides were fixed in the field with filtered 2.5 % glutaraldehyde solutions and used for the characterization of biological material. Upon return to the laboratory the glutaraldehyde fixed slides were washed once with a phosphate buffer (pH=7) and then stepwise dehydrated using a series of ethanol exchange steps (30%, 50%, 70%, 90%, 100%). In addition, at Reykjanes and Svartsengi, the sterile filters used for the water collection were preserved and the untreated filters were analysed for particulates.

4.3.2 Characterization protocols

Solution analyses

All solution samples were stored in the fridge at ~4°C. Cations were measured by inductively coupled plasma optical emission spectrometer (ICP-OES) using a Thermo Jarell Ash IRIS spectrometer and anions were determined using a Dionex DX-600 ion chromatograph (IC) using an IonPac AS16 column and a KOH eluent. Total and monomeric silica were analysed with the spectrophotometric molybdate yellow method (Greenberg et al., 1985).

To calculate the saturation state of silica within each geothermal system studied, the major chemical constituents, temperature and pH of the geothermal waters were used as inputs for geochemical modelling using the geochemical code PHREEQC (version 2.13.3; Parkhurst and Appelo, 1999) and the wateq4 database (Ball and Norstrom, 1992) with the amorphous silica data updated using the values from Gunnarsson and Arnórsson (2000). Saturation indices, SI = log (IAP/K_{sp}), were calculated for each geothermal system, with IAP being the ionic activity product and K_{sp} the solubility product and where SI>0 represents supersaturation and SI<0 undersaturation.

Solids analyses

For microscopic imaging and qualitative elemental analyses, slides or filters were dried and placed on a sticky carbon pad covering an aluminium stub, then coated with a 3 nm platinum layer and analysed using a Field Emission Gun Scanning Electron Microscope (FEG-SEM, LEO 1530) equipped with an Oxford Instruments energy dispersive X-ray (EDX) detector and INCA software. Images were collected at 3 kV and a working distance of 4 mm, while for EDX analysis the working distance was increased to 8mm and the accelerating voltage to 15kV. To determine the silica particle size distribution on the slides from Svartsengi and Reykjanes, high-resolution SEM photomicrographs were imported into CorelDraw® and the diameter of individual silica colloid was measured by drawing an appropriately sized square around each of the particles and converting the width of the squares into real dimensions. For both sites, about 140 colloids each were measured and a mean value and standard deviation was calculated.

The mineralogical composition of the fresh precipitates that formed on the slides at each sampling site was analysed using X-ray powder diffraction (XRD). For this, about 200 mg of precipitate was carefully scraped off the unfixed glass slide, the material was dried and ground to a fine powder and deposited on a silicon sample holder. Analyses were carried out with a Philips PW1050 diffractometer and scans were acquired from 5 to 70°2θ at 1°/min with a step size of 0.02° and operating conditions of 40kV and 30mA using CuKα radiation. Data was analysed and compared to published data for standard minerals in the JCPDF files (International Center for Diffraction Data®).

4.4 Results

4.4.1 Geysir geothermal area

The Geysir geothermal area is situated on the Southern Lowlands (Fig. 4.1) at an elevation of about 120m. The geothermal activity is characterised by hot springs and geysers ranging from <20°C to 100°C. The main geothermal activity occurs within an area of only a few hundred metres across, but thermal manifestations are spread over an area of approximately 3 km^2. The waters at Geysir geothermal field are meteoric of origin (Table 4.1) and are characterised by low abundance of dissolved solids (<150 ppm Cl) with Si, Na, Cl and SO_4 being the dominant dissolved elements. Based on chemical geothermometry, the underground aquifer temperatures are >250°C and the composition with respect to major elements is considered to be controlled by equilibrium with mineral-buffer reactions at the aquifer temperature or in the upflow zone with rhyolitic and basaltic rocks (Arnórsson, 1985).

Table 4.1: Chemical composition of geothermal waters in which *in-situ* experiments were conducted.

	Krafla	GY1	GY2[a]	Hveragerdi	Svartsengi	Reykjanes
	wastewater drain	Upper spring	Sodi spring	wastewater drain	wastewater drain	wastewater drain
Date	22/09/2005	20/09/2005	20/09/2005	25/09/2005	21/09/2005	21/09/2005
pH / ° C	9.95 / 50	8.47 / 48	8.45 / 43	9.05 / 55	7.74 / 41.9	7.50 / 39.8
T (°C)	80	70-96[b]	82	66	42	75
Flow rate (m/s)	0.44	up to 0.5[b]	0.25	0.42	-[c]	-[d]
ppm						
Al	1.72	0.52	0.23	0.74	2.00	<0.1
B	0.98	0.79	1.00	0.42	6.01	5.49
Ca	3.85	1.12	1.34	3.26	1332	2550
Fe	0.08	0.09	0.12	0.05	2.80	5.90
K	39	11	13	13	1316	2314
Li	0.27	0.24	0.27	0.07	3.81	7.67
Mg	0.03	0.01	0.07	0.11	0.62	0.71
Mn	<0.005	<0.005	<0.005	<0.005	0.22	2.01
Na	269	234	242	168	8067	14657
SiO_2[e]	603	363	372	304	250[f]	695
Sr	<0.1	<0.1	<0.1	<0.1	9.0	9.4
Cl	74	114	117	120	14854	27174
F	2.08	20	15	3.24	<0.2	<0.2
NO_3	<0.2	<0.2	<0.2	0.76	23	43
SO_4	262	91	107	60	30	18
Slide collection[f]	25 months	5 d 3 months 5 months 8 months	0 (both GY2&3)	3 months 5 months 8 months 13 months	0.5 h 1 h 2 h 3 h 5 h 7.5 h	1st 3 h 6 h 19 h 24 h 5 d	2nd 4 d 7 d 11d 17 d

[a]Water chemistry at GY3 (T = 61°C) was assumed to be identical to GY2 due to their proximity (~10m)
[b]temperature and flow rate fluctuated due to frequent surges
[c]wastewater pool where water flow was minor and wave action predominated
[d]water flow rate could not be determined
[e]SiO_2 was measured from filtered water samples to which base was added
[f]d: days, h: hours

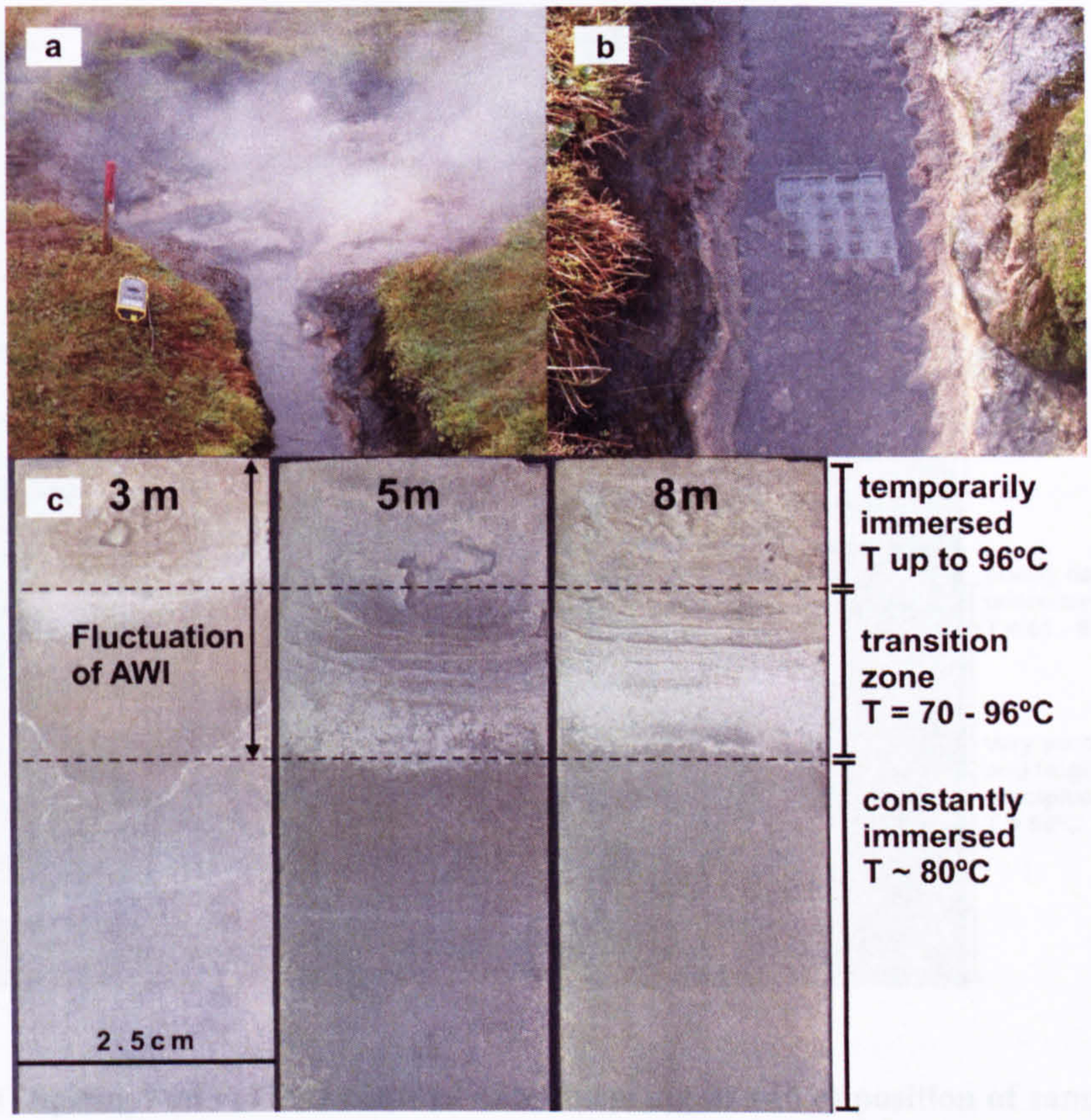

Figure 4.2: a) Spring and outflow channel of GY1, b) close up of sampling tray, and c) glass slides collected at GY1 with typical increase in silica deposits for time periods between 3 and 8 months (m).

Two different thermal features were chosen for the *in-situ* sinter growth experiments at Geysir: upper spring (thereafter called GY1, Fig. 4.2a), representing the outflow from an old borehole, and Sodi spring (Fig. 4.3a), a natural thermal spring where two different temperature regimes were studied (thereafter called GY2 and GY3, Fig. 4.3b and c). At both Geysir sites, the moderate high silica content (363 and 372 ppm SiO_2 at GY1 and GY2 respectively) and the hard and compact sinter deposits that formed within and along the outflow channels (e.g., Fig. 4.2b and 4.3b) indicated relatively low precipitation rates. XRD analyses of the newly formed sinter deposits showed opal-A, (i.e., amorphous silica) as the sole precipitating phase (Fig. 4.4; GY1-3 patterns).

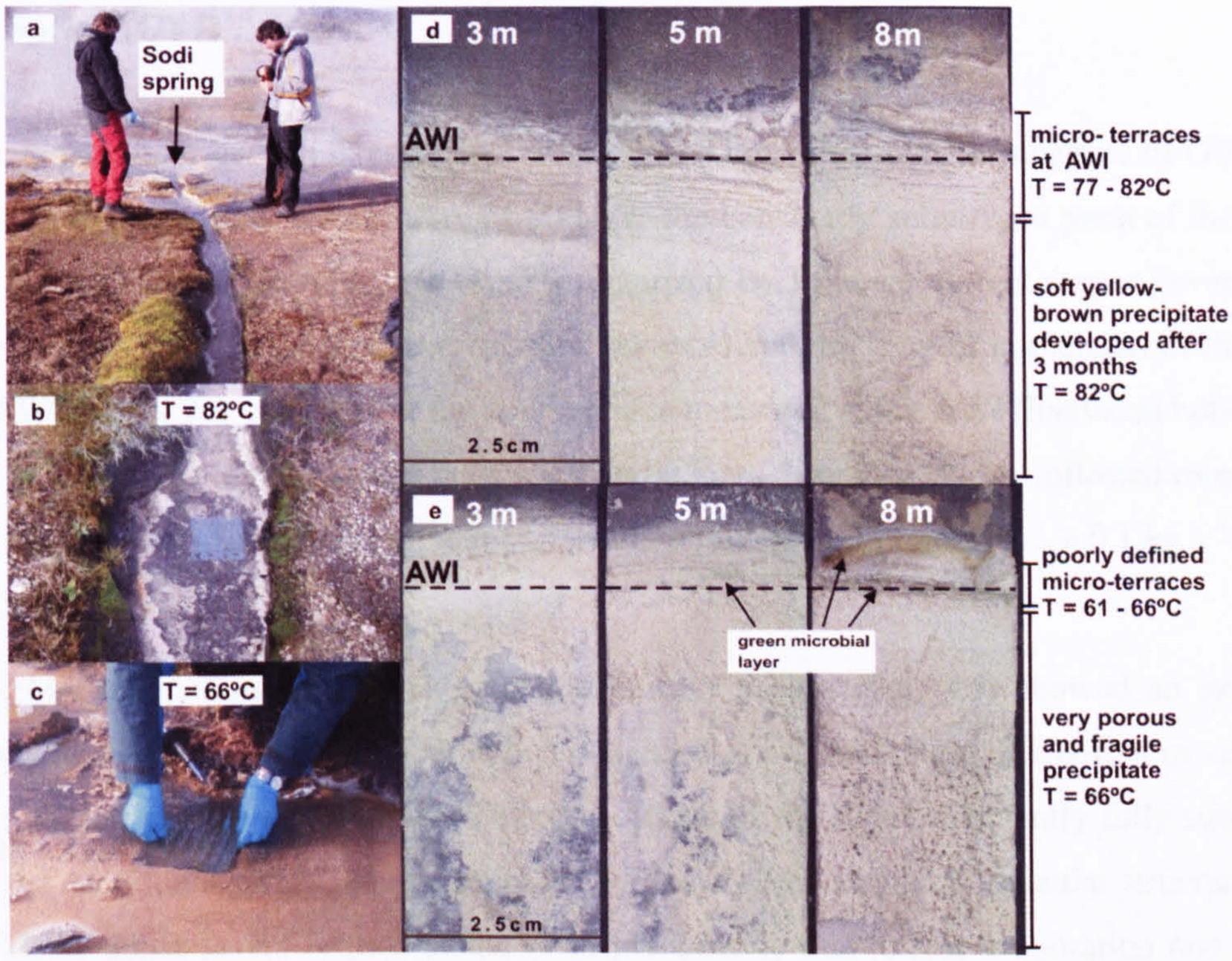

Figure 4.3: a) Spring and outflow channel of Sodi spring, b and c) position of sampling trays at GY2 and GY3 respectively, dande) slides collected from the tray placed at GY2 and GY3 respectively for a time period between 3 and 8 months (m).

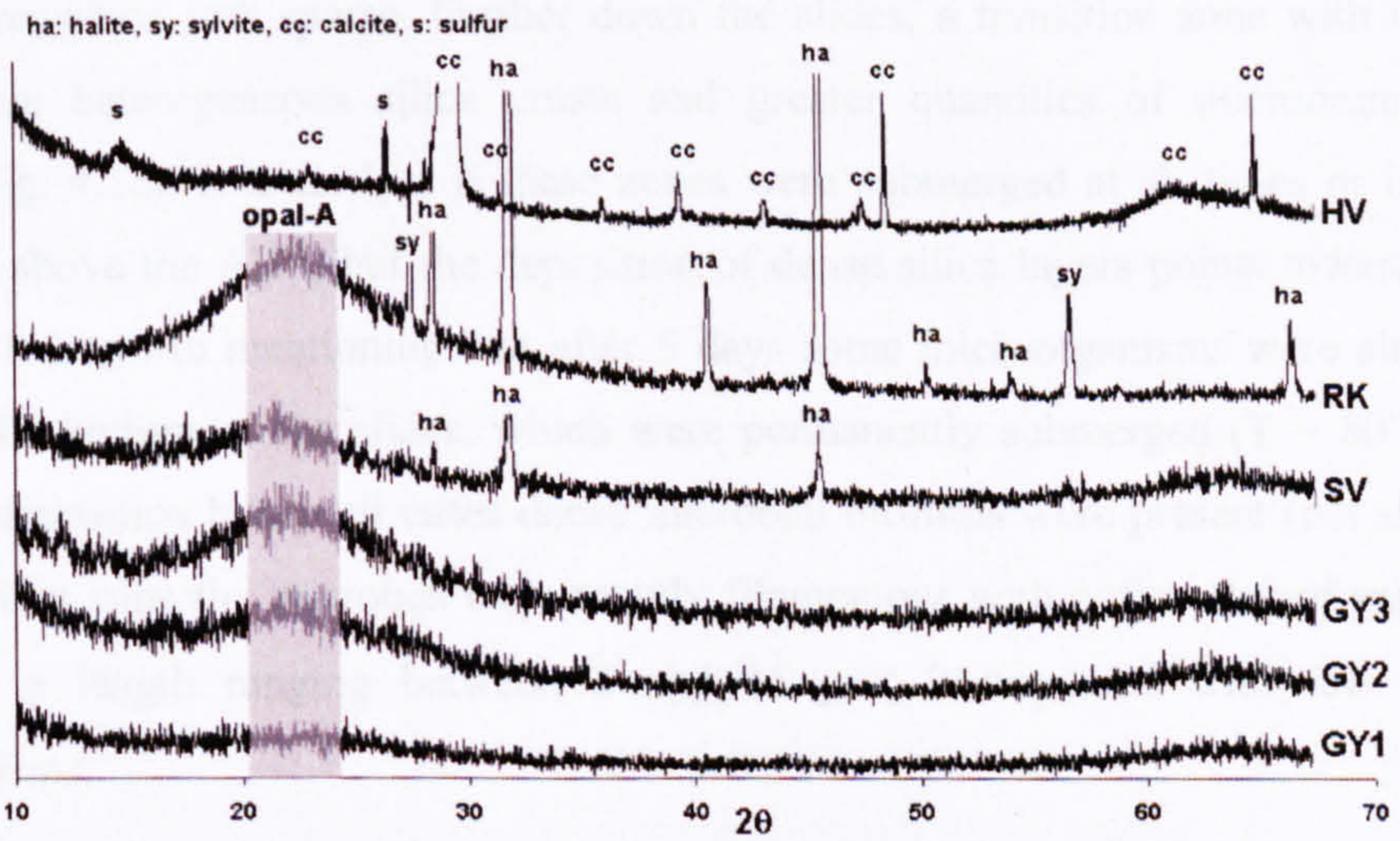

Figure 4.4: XRD pattern of precipitates from Hveragerdi (HV), Reykjanes (RK), Svartsengi (SV), and Geysir (GY1-3). Shaded area shows 2θ-range characteristic for the broad XRD peak of opal-A, i.e., amorphous silica (Herdianita et al., 1999).

Upper Spring (GY1)

Sampling and sinter growth experiments were carried out in the outflow channel of GY1 (Fig. 4.2b) at an average water temperature of 80°C (in the constantly submerged parts of the slides) and at pH 8.47 (at 48°C). This site was characterized by frequent violent surges (every 1 - 2 minutes) which affected the temperature, the flow rates and the level of immersion of the slides at the AWI (Fig. 4.2c). As a result, the temperatures measured at the AWI fluctuated between 70 and 96°C and the flow rates varied between 0 and 0.5m/s. From the slides collected over a time period of 8 months (Table 4.1, Fig. 4.2c) an average precipitation rate of 0.2 ± 0.1 kg $y^{-1}m^{-2}$ was derived.

FEG-SEM examinations of the slides collected after 5 days (Fig. 4.5) showed an extremely heterogeneous texture of the precipitate that consisted of a combination of amorphous silica and various microbial cell morphologies. The top sections of the slides, frequently fully submerged due to the occasional surges, were dominated by dense silica layers and spicular structures (Fig. 4.5a). These dense layers formed at the AWI presumably due to fast evaporation and cooling processes and consisted of silica nanoparticles that coalesced into smooth films. The spicules (defined as vertical columnar or domal structures; Handley et al., 2005 and references therein) consisted primarily of alternating layers of silica sinter and microorganisms (Fig. 4.5b). Although microorganisms were present in these upper zones, the significant temperature fluctuations were less favourable for the growth and stability of large microbial communities and the colonisation was sparse. Further down the slides, a transition zone with no spicules, thinner, more heterogeneous silica crusts and greater quantities of microorganisms were observed (Fig. 4.2c). It is unclear if these zones were submerged at all times or if they were temporarily above the AWI, but the deposition of dense silica layers points towards the latter alternative. It is worth mentioning that after 5 days some microorganisms were already partly silicified. The bottom of the slides, which were permanently submerged (T ~ 80°C), showed little silica deposition but in all cases dense microbial biofilms were present (not shown here). Overall, in this zone the microbes were mainly filamentous with a diameter of approximately 0.3μm and a length ranging between 2 and 15 μm, interspersed with few rod shaped microorganisms.

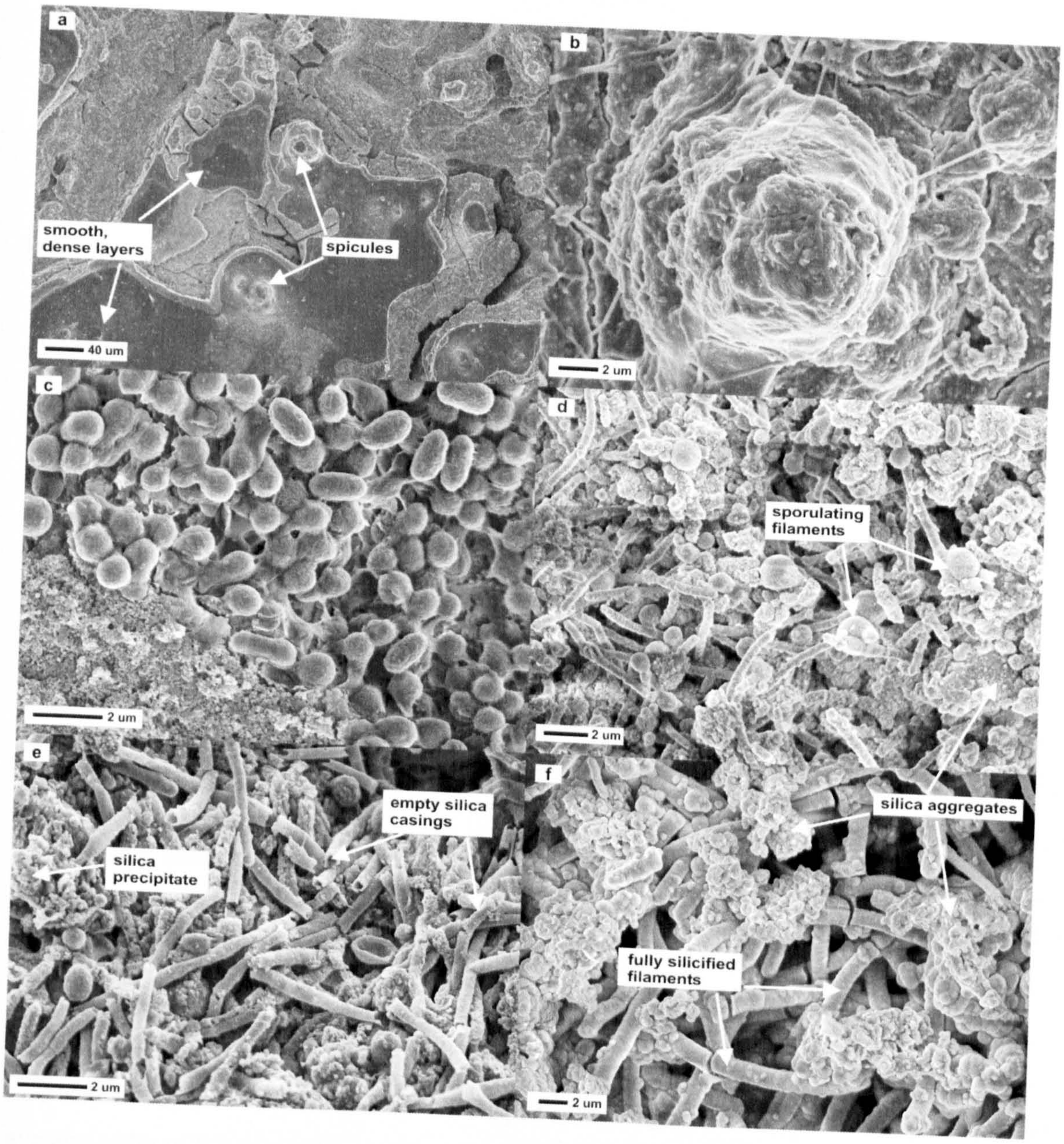

Figure 4.5: Photomicrographs of slides collected at GY1 (a-b: after 5 days, c-e: after 3 months, f: after 8 months). a) Multiple dense silica layers and spicules at the AWI, b) close-up of a single spicule, c) cocci and rod-shaped microbes found on the side of a spicule, d) microbial filaments, possibly sporulating, surrounded by silica aggregates from the transitions zone, e) empty silica casings left behind by encrusted microbial filaments, and f) mix of fully silicified microbial filaments and silica aggregates in the lower parts of the slides.

After 3 months, the slides were covered with considerably larger amounts of silica, yet the textural and structural characteristics of the precipitates were basically unchanged. However, rod-shaped bacteria as well as cocci had colonised the side of spicules (Fig. 4.5c). Further down the slides (in the transition zone, Fig. 4.5d), a few filaments were possibly sporulating.

Sporulation might have been triggered by the harsh temperature variations induced by the frequent surges. The lower parts of the slides were still covered with dense microbial mats, but after 3 months extensive silicification was observed (Fig. 4.5e). Slides collected after 5 and 8 months showed almost identical features to those observed in the 3 month slides, the main difference being the amount of silica precipitated and the degree of silicification of the microorganisms (silicified both externally and internally, Fig. 4.5f).

Sodi Spring (GY2 and GY3)

Sodi spring is located to the north-west of the main entrance to the Geysir geothermal area. Trays with glass slides were placed at two different sites within the outflow channel of Sodi spring. The first sampling site (GY2, Fig. 4.3b) was in an outflow channel ~ 5 m away from the emergence point of Sodi spring. The average water temperature was 80°C, the pH was 8.45 (at 43°C) and the flow rate was 0.25 ms^{-1}. The second tray (GY3, Fig. 4.3c) was placed in the same outflow channel but about 15 m away from the spring where the temperature was 20°C lower (T = 61°C). The goal of the two sets of experiments within the same outflow channel was to determine how sinter growth rates as well as microbial communities were affected by temperature while all other conditions were similar.

At both sites slides were removed at specific times between 5 days and 8 months (Table 4.1, Fig. 4.3d, e) from which a silica growth rate of 0.7 ± 0.3 kg $y^{-1}m^{-2}$ was estimated for GY2 and 1.4 ± 0.4 kg $y^{-1}m^{-2}$ for GY3.

At GY2, after 5 days considerable amounts of silica precipitated as layers and terraces but no spicules and only few microbes were observed in the vicinity of the AWI. The few microorganisms present were mostly rod-shaped with lengths between 1.5 to 3 μm and an average width of 0.3 μm with some already partly silicified after this short time (Fig. 4.6a). A bit further down the slides, long filaments became more abundant and they mainly covered small terraces that had formed between the various silica layers (Fig. 4.6b). In the subaqueous parts of the slides, dense biofilms consisting of very long and thin microbial filaments (width ~ 0.3 μm, 10-50 μm long) were observed (Fig. 4.6c) and hardly any silica precipitates were associated with these filamentous mats.

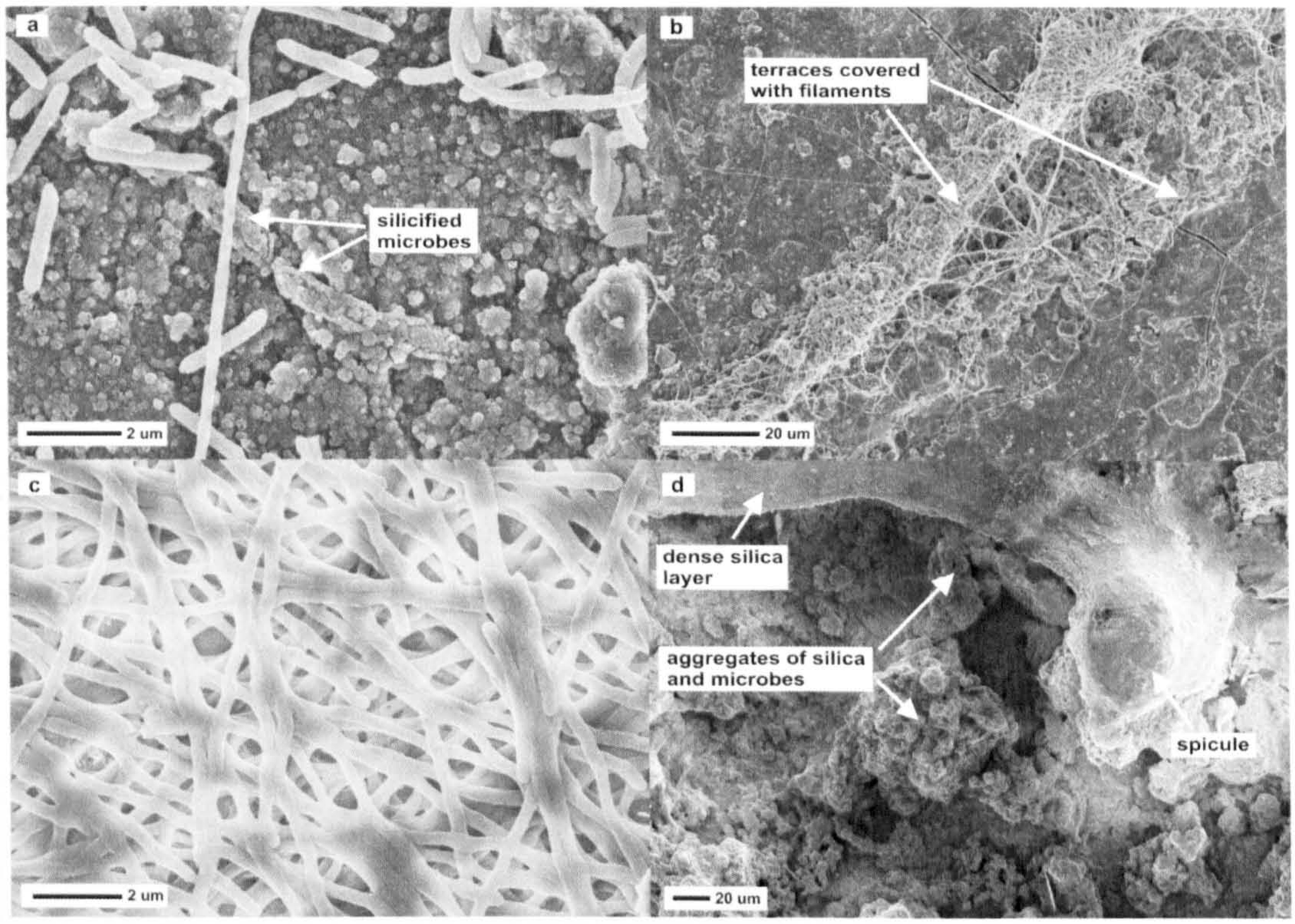

Figure 4.6: Photomicrographs of slides collected from GY2 (a-c: after 5 days, d: after 3 months). a) Unsilicified rod-shaped microorganisms, very thin and long microbial filaments as well as silicified microbes on dense silica substrate, precipitated in the vicinity of the AWI, b) terraces formed by silica layers densely populated by long, thin filaments from the middle part of the slides, c) dense microbial biofilm from the fully submerged part of the slides, and d) spicule-like structure surrounded by coarse and very porous silica aggregates at the AWI.

After 3 months, the appearance of the slides changed significantly with yellow-white precipitates covering about two third of the slides (Fig. 4.3d). In the vicinity of the AWI, distinct silica terraces (overall vertical height up to 1mm) and spicule-like structures (Fig. 4.6d) developed as a consequence of evaporation and cooling. The texture of these terraces seemed very different compared to the small terraces observed after 5 days (Fig. 4.6b) and consisted of dense layers of silica covering accumulations of partly to fully silicified microorganisms interspersed with silica aggregates (Fig. 4.6d). The heterogeneous, yellow-white precipitate covering the bottom part of the slides (Fig. 4.3d) showed very similar characteristics to the texture at the AWI, however, no dense silica layers developed. The precipitates consisted solely of a network of silicified as well as unsilicified filaments, free silica aggregates and a few diatoms. The diatoms interspersed with the silicified filaments, although not indigenous (water temperature was far too high for diatoms to survive; Brock, 1978), were probably blown into the spring as aerosols.

After 8 months, the silica terraces on the slides reached a height of up to 3 mm and far more precipitates were covering the slides; however the structure and texture of the precipitates did not change significantly during the latter 5 months of growth.

At GY3, the slides were dominated by porous and fragile precipitates (Fig. 4.3e) densely covered with microorganisms. The textures in the submerged parts of the slides were uniform regardless of the time interval at which they were collected and basically consisted of silica layers and porous silica aggregates in part intertwined with filamentous or rod-shaped microbes (both exhibiting various stages of silicification) as well as a few diatoms (Fig. 4.7a, b). The characteristics at the AWI were dominated by poorly defined silica terraces and the absence of spicules. At a closer look, the terraces consisted of silica spheres and biofilms cemented together in the form of layers (Fig. 4.7c).

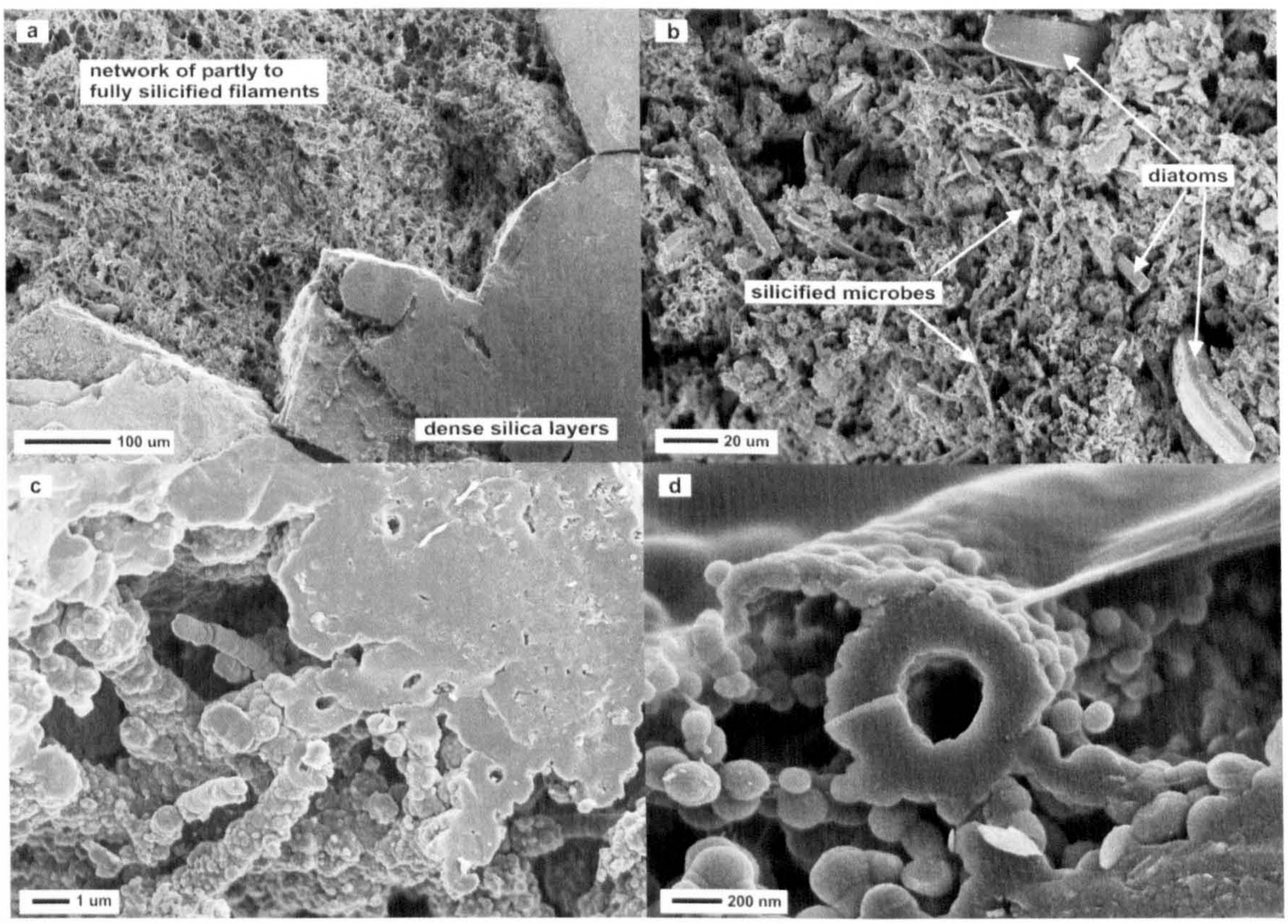

Figure 4.7: Photomicrographs of slides collected at GY3 (after 3 months). a) Compact network of microbial filaments in between dense blocks of amorphous silica, b) dense network of microbial filaments exhibiting different stages of silicification together with a few diatoms all associated with porous silica aggregates, c) silicified microbial filaments interdispersed between flat layers of amorphous silica, and d) close-up of an empty silica shell covered by silica nanoparticles that coalesce into a smooth silica layer.

After 5 months the slides at GY3 developed a thin green layer at the AWI where the temperature was about 5°C lower than within the constantly submerged part (Fig. 4.3e arrows). These green layers increased in thickness significantly over the following 3 months and their formation indicated the colonisation of the silica deposited on or above the AWI with photo-synthesising microorganisms. Interestingly, in these green layers only large accumulations of partly to fully silicified filaments, interlinked and embedded in layers of blocky silica (Fig. 4.7a, b) were observed which did not differ from the textures ad structures from the rest of the slide. The silicification of microorganisms followed the same patterns as seen in the other two Geysir sites, with silica spheres adhering to the surface of microbial cells and covering them totally (Fig. 4.7d).

4.4.2 Hveragerdi wastewater drain (HV)

The Hveragerdi geothermal area is located on the Southern Lowlands, approximately 45 km east of the capital, Reykjavik. The area is characterized by hot springs ranging from <20°C to 100°C and steam fumaroles. Several drill holes which have been sunk into the area have shown deep aquifer temperatures up to 200°C (Arnórsson et al., 1983a). The waters at Hveragerdi geothermal field are of meteoric origin (Table 4.1) and their chemistry is considered to be controlled by basalt-water interaction at >200°C and mixing with colder, shallower groundwaters. The analysed waters were characterised by low abundance of dissolved solids (<150 ppm Cl) with Si, Na, Cl and SO_4 being the dominant dissolved compounds. The increased values of NO_3 (Table 4.1) presumably developed due to the presence of nitrifying bacteria within the thick biofilms growing along and within the wastewater drain (e.g., Skírnisdottir et al., 2000; Chapter 5).

The sinter growth experiments were carried out in a wastewater drain downstream of a steam separator (Fig. 4.8a). A slide tray was placed in a channel where the flow rate was 0.4 m/s and the temperature was 66°C (Fig. 4.8b). The pH of the wastewater was slightly alkaline (pH 9.05 at 55°C) and the SiO_2 concentration was 304 ppm.

The XRD analyses of the fresh precipitates revealed calcite and small amounts of elemental sulphur as the main precipitates (Fig. 4.4; HV pattern), however, amorphous silica was clearly forming within and around the outflow channel. The precipitation of calcite within geothermal waters at Hveragerdi has been previously shown by Arnórsson (1978a). To verify the presence of amorphous silica, the crystalline calcite was removed by reacting with 10% HCl (weight loss of about 50%) and the remaining precipitate was re-analysed by XRD. This procedure exposed the characteristic broad peak of amorphous silica at 2θ of about 22.2° (Herdianita et al., 1999).

From the slides collection at Hveragerdi (Table 4.1) a silica precipitation rate of 0.7 ± 0.3 kg y^{-1} m^{-2} was estimated.

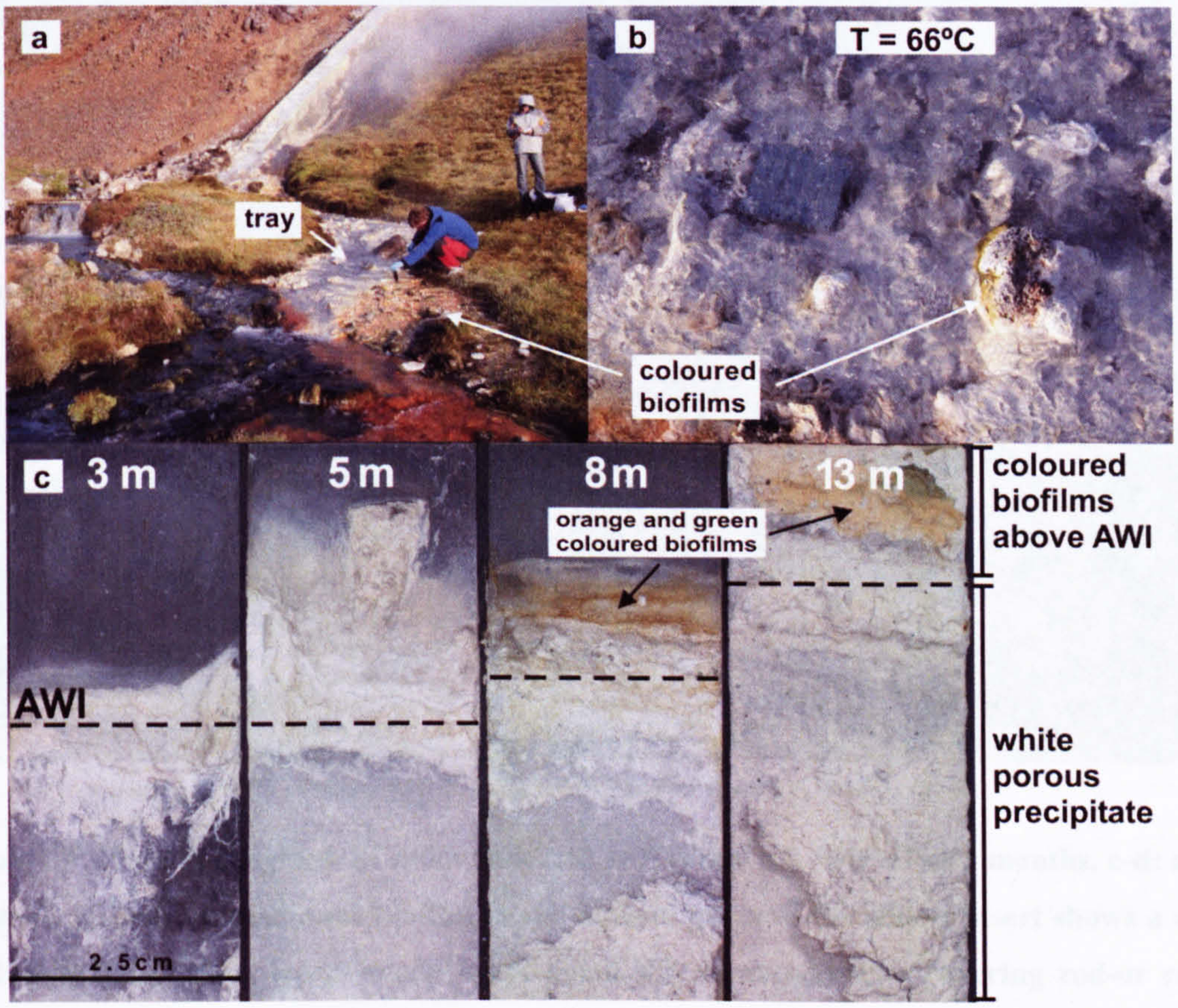

Figure 4.8: a) Outflow channel from the steam separator from Hveragerdi with marked position of the tray, b) close up of sampling tray, and c) slides collected from the tray over a time period of 13 months (m).

As expected, the amount of precipitation on the HV slides increased with time however, the position of the AWI changed over the 13 month course of the experiments (moved upwards, Fig. 4.8c). This was probably the result of increased water flow from the steam separator which then caused an increase in water depth within the outflow channel. Even though extensive silica precipitates were present in the vicinity of the AWI, no dense and well-defined terraces or spicule-like structures developed. The fabric of the precipitate was quite homogeneous from the top to the bottom of the slides and was dominated by extensive biofilms (Fig. 4.9a). These biofilms were weakly to fully silicified and frequently interspersed with amorphous silica aggregates as well as some calcite precipitates (Fig. 4.9a insert), with calcite precipitation primarily restricted to the submerged part of the slides.

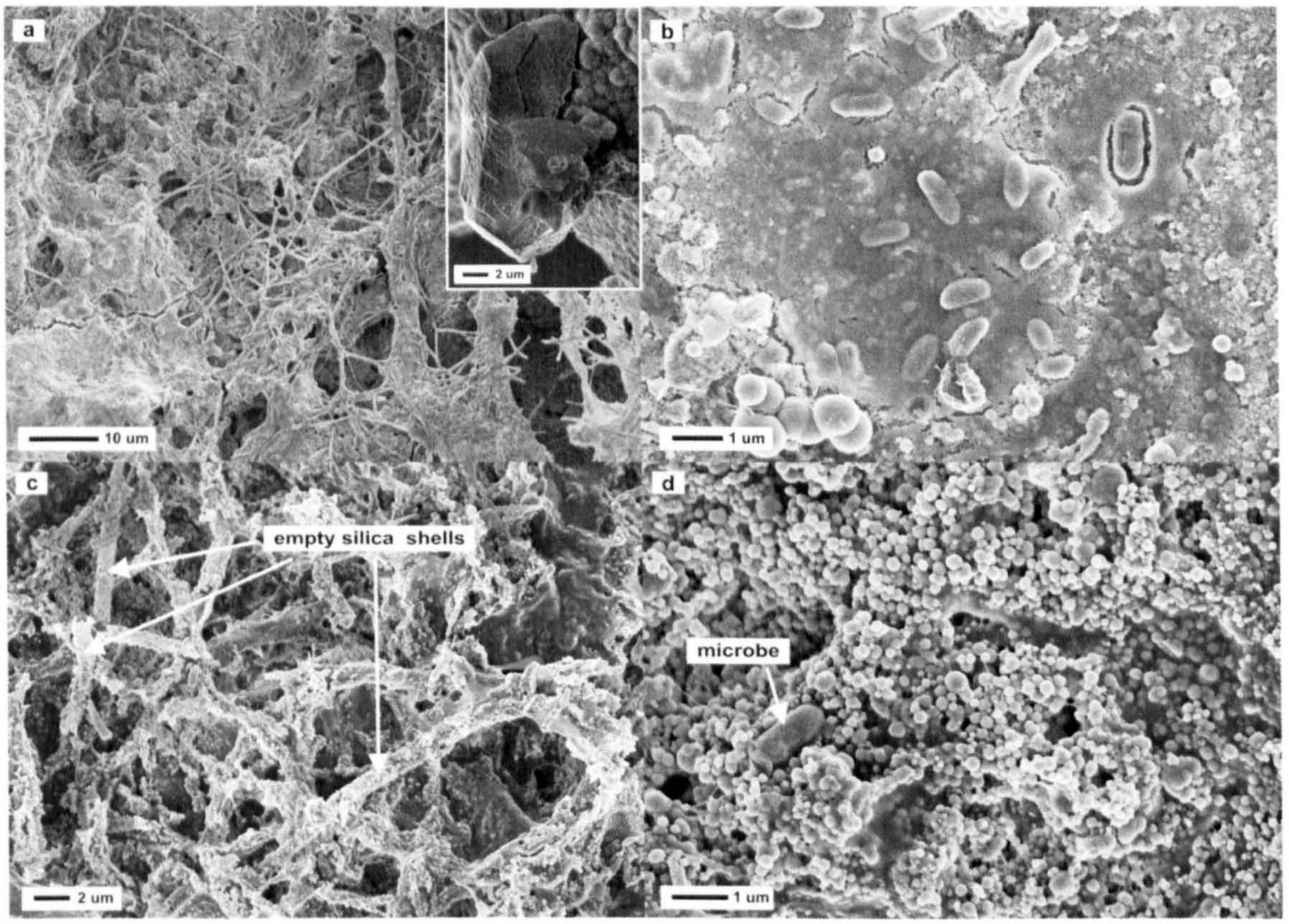

Figure 4.9: Photomicrograph of slides collected at Hveragerdi (a-b: after 3 months, c-d: after 8 months). a) Dense filamentous biofilm in the bottom parts of the slides; insert shows a calcite crystal, b) dense silica layers made up of small silica nanoparticles covering rod-or coccus-shaped microbes formed in the submerged parts of the slides, c) mix of silicified filaments, empty silica casings and silica aggregates, and d) accumulation of silica nanospheres of different sizes forming layers interspersed with microbial cells (both c and d were close to the AWI).

Similar to the processes observed at GY3, on the slides from Hveragerdi, green-yellow and bright orange biofilms developed after about 8 months suggesting the presence of photo-synthesising microorganisms (green-yellow) and orange pigmenting microbes (bright orange layer, Fig. 4.8c). These biofilms formed above the AWI where temperatures were lower (~5°C) than within the submerged parts of the slides, mimicking microbial mats that grew on sinters on the sides or within the wastewater drain (Fig. 4.8a, b). Slides collected after 3 and 5 months did not yet exhibit visible green or orange microbial layers, yet, they exhibited extensive layers of silica and calcite densely populated with mats of filamentous microorganisms (Fig. 4.9a) as well as significant amounts of rod-shaped microbes and cocci (Fig. 4.9b). The degree of microbial silicification varied substantially along the vertical length of the slides, with silicification being more pronounced in the upper parts close to the AWI. The comparison between the orange and

green layers formed on the slides after 8 months showed very similar textures and consisted primarily of a dense network of silicified filaments, empty silicified microbial cell walls and silica aggregates (Fig. 4.9c, d).

4.4.3 Reykjanes Power Station wastewater drain

The Reykjanes geothermal field is situated on the Reykjanes peninsula (Fig. 4.1). The geothermal waters are of seawater origin (Table 4.1) and have reacted with basalts at >250°C (Arnórsson, 1978b). *In-situ* sinter growth experiments were carried out in a terraced, man-made wastewater drain of a steam seperator (Fig. 4.10a). The flow rate at this site could not be determined with accuracy due to the terraced configuration of the outflow channel however, a rate of 0.5 - 0.7m/s was estimated. The temperature at the sampling site was 75°C and the pH of the wastewater was near neutral (pH 7.50 at 39.8°C). The measured SiO_2 concentration within the studied wastewater was 695 ppm.

The base and sides of the wastewater drain were covered with thick deposits of white, soft, highly hydrated and porous precipitates (Fig. 4.10a). Due to the high precipitation rate, the power station operators remove the precipitated material every few months from this drain. X-ray diffraction analysis (Fig. 4.4, RK pattern) showed that this porous material consisted of amorphous silica, with small amounts of halite and sylvite, the precipitation of which was solely due to drying of the untreated (unwashed) precipitates.

A first *in-situ* precipitation experiment was carried out for 5 days, however, after this time period the whole tray was covered with soft and porous silica precipitate (Fig. 4.10b, c) and sampling of single slides was not feasible without losing considerable amounts of material. Therefore, a second experiment with a much shorter time interval (Table 4.1) was carried out from which an average silica precipitation rate of roughly 304 ± 20 kg $y^{-1}m^{-2}$ was estimated.

The second slide series showed that already after 30 minutes a fine layer of amorphous silica formed on the slides, and within 7.5 hours the slides were covered with a 2mm thick porous layer (Fig. 4.10d). SEM analysis showed homogeneous precipitates over the full vertical length of the slides consisting of aggregates of different sized silica spheres ranging from 11 nm up to 106 nm (mean diameter 43.2 ± 20.1 nm; n=140; Fig. 4.11a).

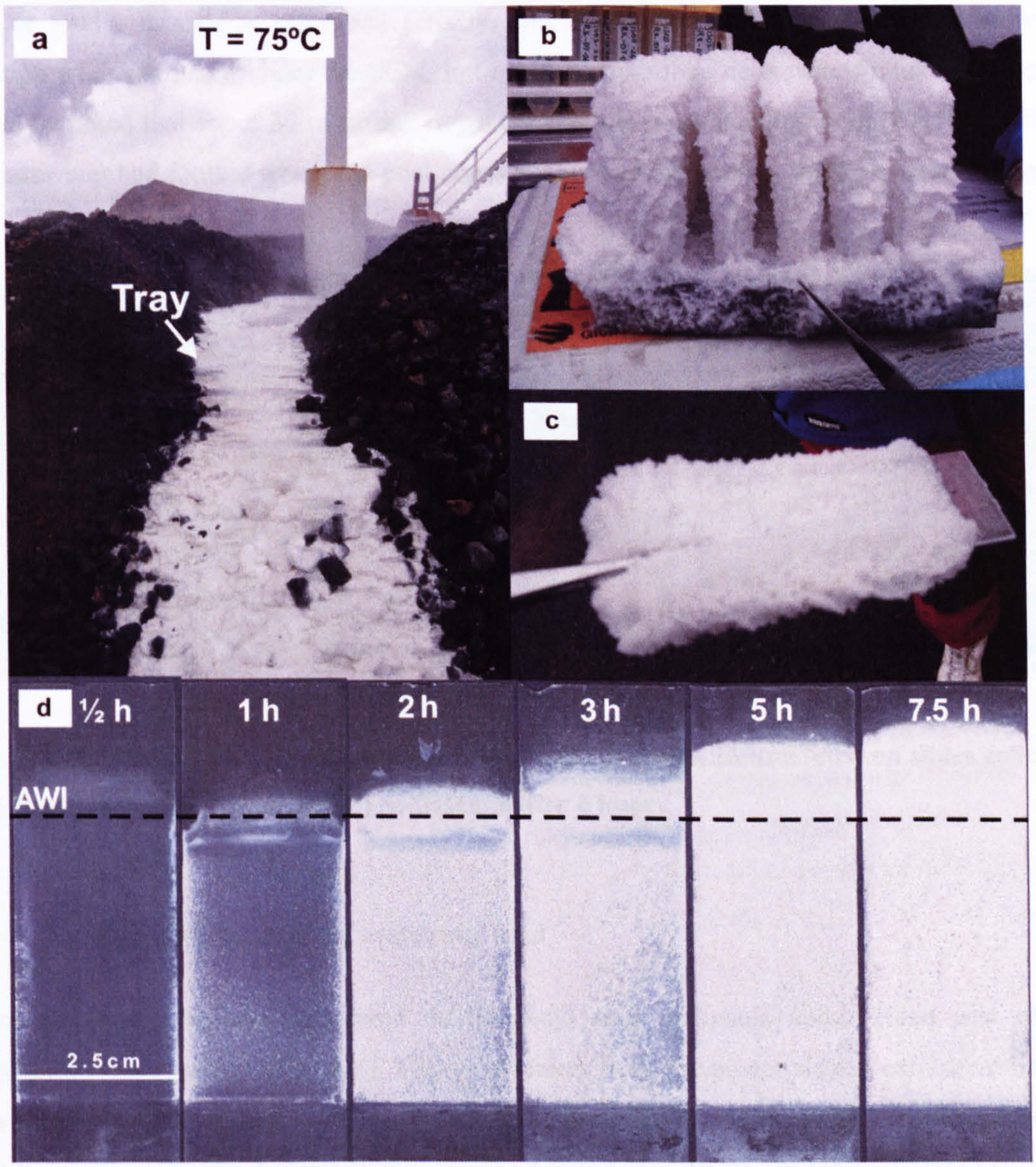

Figure 4.10: a) Outflow channel from a steam separator at Reykjanes Power Station, b) tray after 5 days, c) close up of a single slide fully covered in soft and highly hydrated amorphous silica precipitates, and d) glass slides collected from the second (short-term) experimental set as a function of time (h: hours).

Interestingly, microscopic analyses of the slides collected from this site showed a total lack of microorganisms within the porous precipitates. In addition, elemental mapping using SEM-EDX (energy dispersive X-ray) analyses also failed to reveal traces of phosphate, or carbon, which could indicate the presence of microorganisms. However, this was not surprising as the high precipitation and flow rate (i.e., constant re-supply of water from the separator) also prevented the formation of microbial features (e.g., streamers, colored mats, polysaccharides) on the sides of the wastewater drain. To further investigate whether this sampling location was

poor or totally lacking in microbial activity, single-use, sterile filter papers used for water filtration were examined under the SEM, but again no microbial cells were found. However, it should be noted that about 30 m further down the drain, a large standing pool (20x50 m, 40°C) of wastewater had formed where the pool edges exhibited some green - yellow tainted sinters.

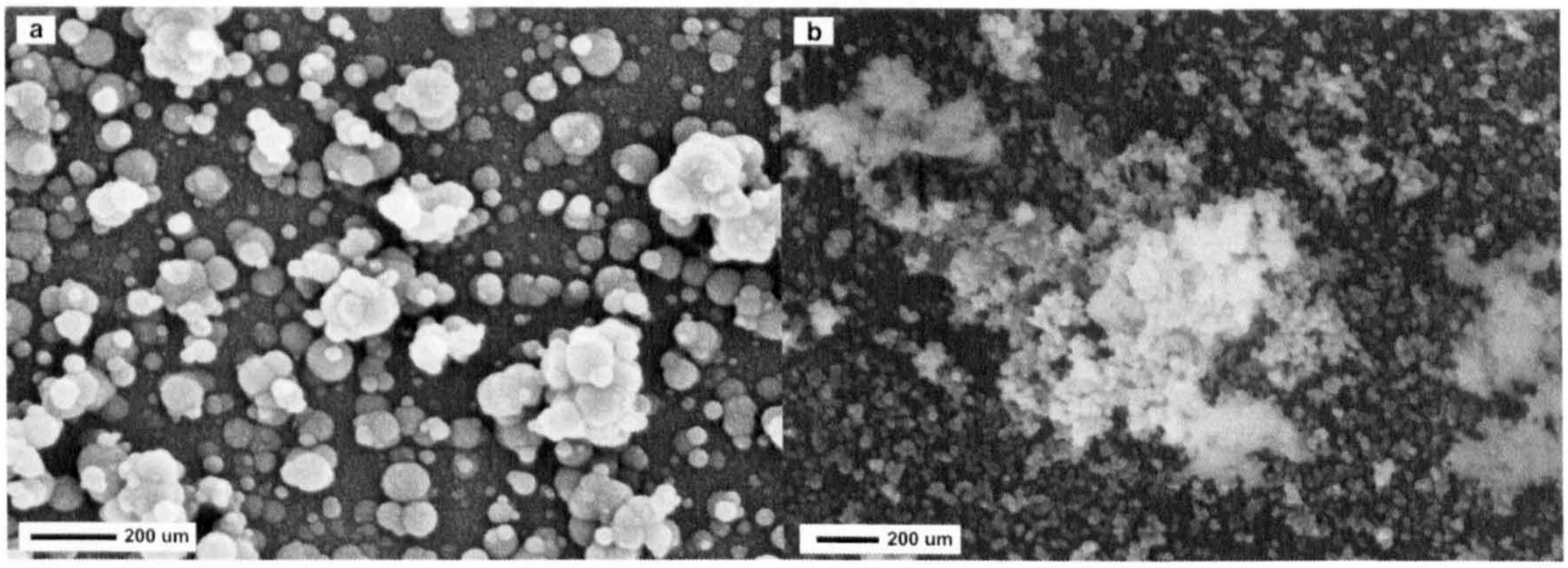

Figure 4.11: a) SEM photomicrographs of silica nanoparticles accumulated on slides collected at a) Reykjanes after 1 hour and b) Svartsengi after 6 hours.

4.4.4 Svartsengi Power Station wastewater pool

Svartsengi Power Station is located on the Reykjanes peninsula about 20km east of the Reykjanes Power Station (Fig. 4.1). The wastewaters from the power station exhibit an intense blue coloration (Fig. 4.12a) which is caused by the presence of colloidal silica suspended within the wastewater. The geothermal waters represent seawater-meteoric water mixtures (Table 4.1) with Na, Ca, K, and Cl being the most important elements.

Two sets of *in-situ* experiments (5 days, 17 days) were carried out in a pool (situated a few hundred metres downstream from a steam separator, Fig. 4.12a, b) where the water was mostly stagnant (low flow and controlled by wind and wave action). During the first set of experiments, the temperature at the study site was 42°C and the pH was 7.7 (at 42°C) while during the second set the temperature had increased to 60°C, with no change in pH. The dissolved SiO_2 concentration in the pool water was 250ppm, which was primarily a consequence of the fact that (a) the bulk of the total silica (~ 630 ppm after it leaves the steam separator; Thórdarson & Tómassson, 1989) had already precipitated in large settling tanks located close to the steam separator outflow and (b) the SV waters contained high loads of suspended colloidal silica (blue colour of the sampling pool, Fig. 12a, b) which led to a lower measured total silica concentration within the studied wastewater (colloids removed during water filtration). XRD

analysis showed amorphous silica as the sole precipitation phase with halite being present as a result of drying (<1% of total precipitate; Fig. 4.4, SV pattern).

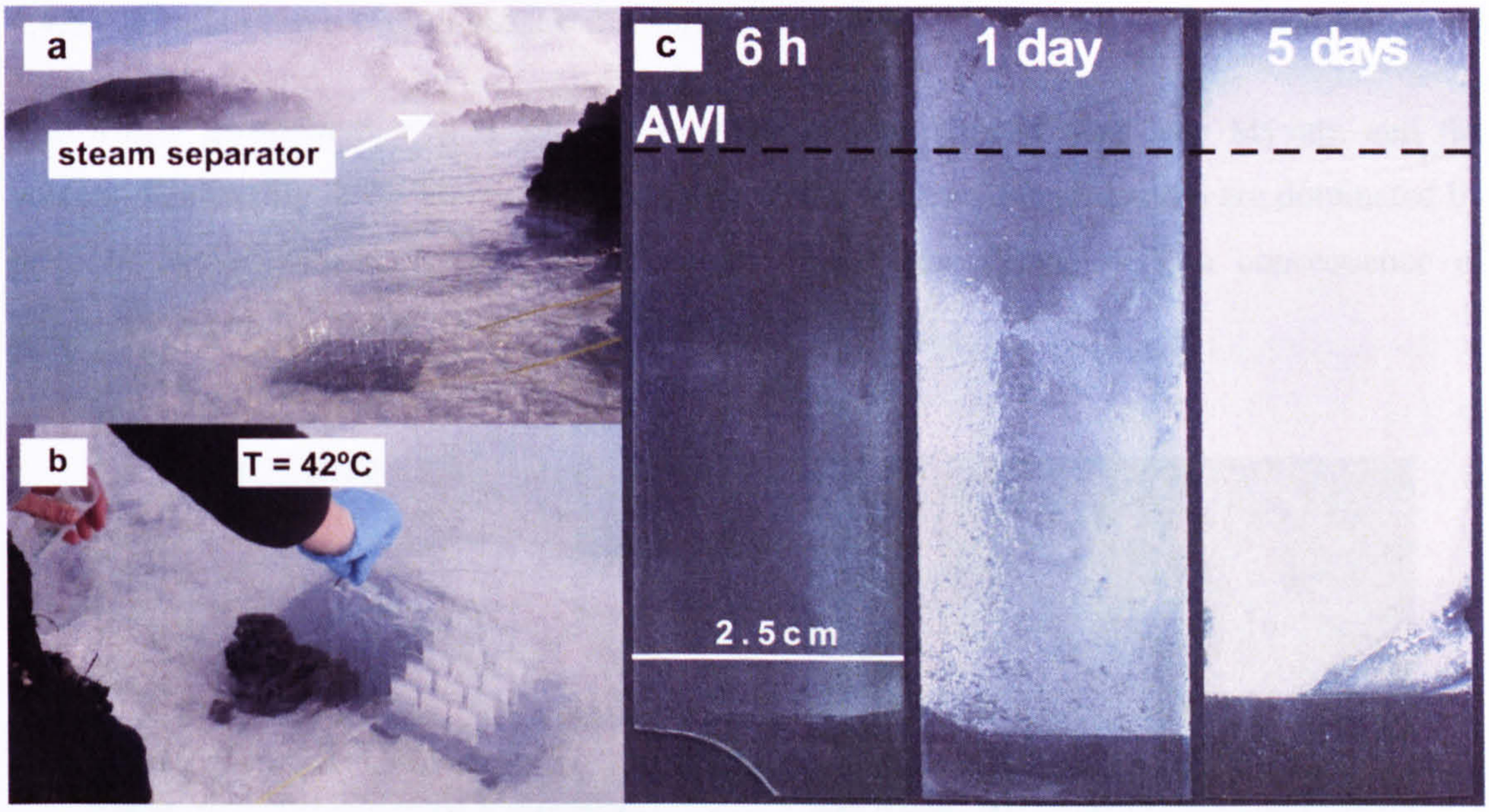

Figure 4.12: a) Blue wastewater pool at Svartsengi Power Station with sampling tray in the foreground, b) close up of trays left for 6 hours (left tray) and 5 days (right tray); note detail of sampling method; c) Slides collected from the tray over a time period of 5 days.

From the first set of *in-situ* silica growth studies (Table 4.1) an average silica precipitation rate of 9.7 ± 3.5 kg $y^{-1}m^{-2}$ was determined whereas from the second set, a slightly lower precipitation rate of 8.8 ± 3.4 kg $y^{-1}m^{-2}$ was obtained. It is important to note that the water temperature at the sampling site had increased from 42 to 60°C between the two studies. The water composition was not analysed during the second experimental period and was assumed to be equal to that in the first experimental period.

Microscopic analyses (SEM/EDX) of the precipitates on the slides revealed that they were covered with fine aggregates of silica particles (Fig. 4.11b). However, the aggregates, when compared to those from Reykjanes, were far smaller, more fragile and had an almost gel-like appearance. Individual particles exhibited diameters between 10 and 36 nm (mean 18.4 ± 4.0 nm, n=140, Fig. 4.11b). Similar to Reykjanes, the Svartsengi slides, as well as the filter paper used to collect the spring waters, revealed no traces of microorganisms. These findings were not surprising. The static nature and long residence time of the waters in the pool allowed silica to precipitate at a high rate on the slides. However, the short tenure of the slides (<17days) in the pool waters coupled with the high precipitation rate prevented microbial colonization of the

slides. In contrast, the silica-rich pool sediments were more likely to be colonized because of the static nature and longer residence time of the waters in the pool.

4.4.5 Krafla Power Station wastewater drain

The Krafla geothermal area is situated in north eastern Iceland near lake Mývatn and the volcano Krafla (Fig. 4.1). The fluids circulating within the geothermal system are dominated by meteoric water with increased concentrations of sulphate (Table 4.1), a consequence of interactions with basalts at >250°C (Arnórsson et al., 1983a).

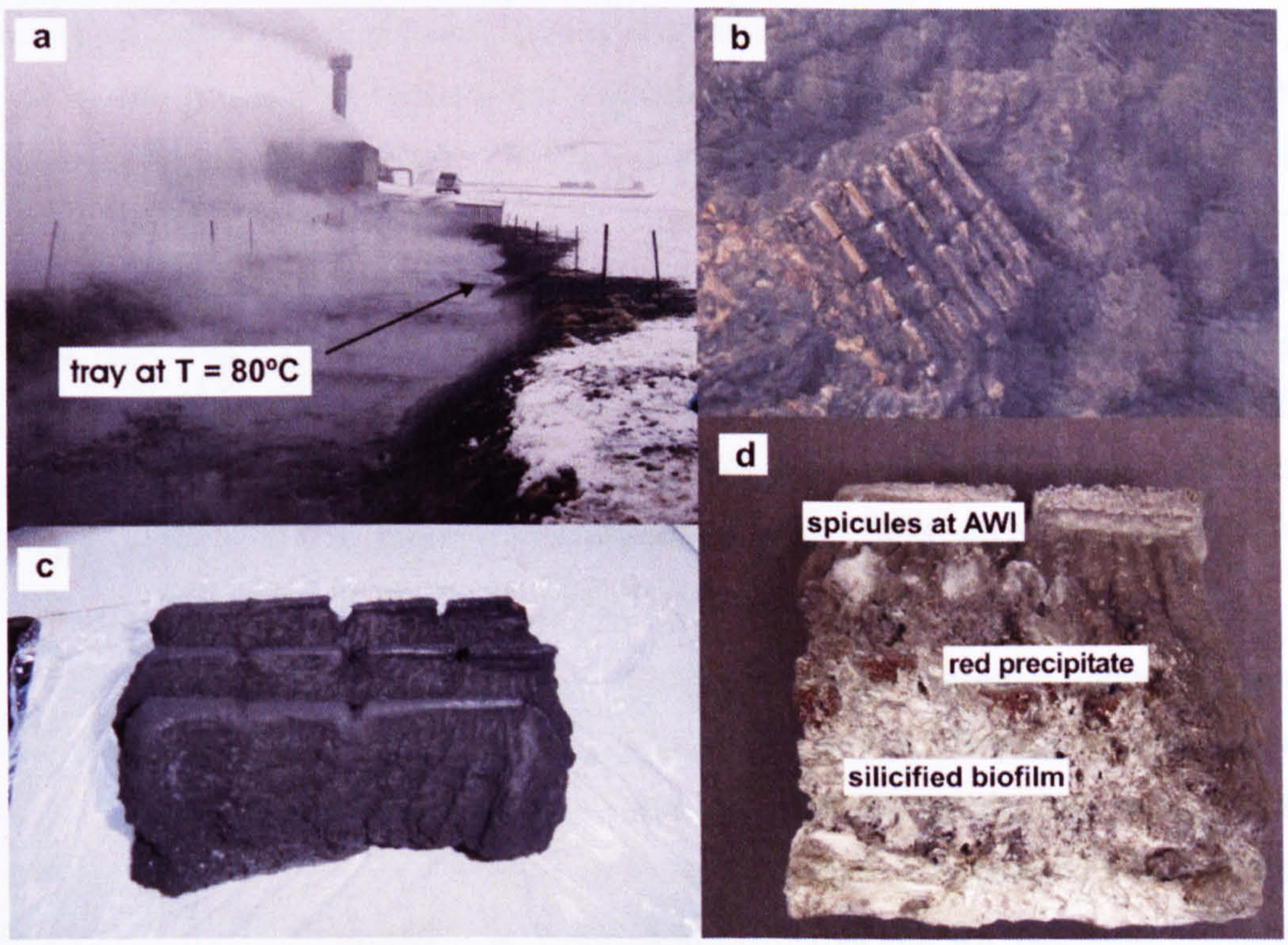

Figure 4.13: a) Steam separator and outflow channel at Krafla Power Station with location of sampling tray, b) close up of tray left for 25 months within the wastewater drain, c) coalesced slides on the tray after collection, and d) close up of 2 separated and dried slides showing a heterogeneous texture and colour.

The sampling location was situated in a wastewater drain of the Krafla Power Station where the temperature was 80°C (Fig. 4.13a). The pH was very alkaline (pH 10.0) and the SiO_2 concentration was 603ppm. Hard and compact, black-coloured sinter deposits observed along the wastewater channel indicated relatively low sinter growth rates and the *in-situ* sinter growth experiments were sampled only once after 25 months (but also as this was the most inaccessible

site). Surprisingly, the growth rate was far higher than expected and the whole tray was covered in dense, black precipitate (Fig. 4.13b, c). All slides were carefully separated and a precipitation rate of 19.5 kg $y^{-1}m^{-2}$ was estimated.

XRD examination of fresh precipitates scraped off the top (Fig. 4.14, KF-T pattern) and bottom (Fig. 4.14, KF-B pattern) of the slides revealed that amorphous silica was the main mineral phase present within the black precipitate. Interestingly, the XRD pattern of the precipitates from the constantly submerged parts of the slides revealed the presence of minor amounts of quartz (Fig. 4.14, KF-B, note small q-labelled peak above amorphous background) which could have either formed authigenically within the sinter (see discussion) or could be detrital and be brought to the surface by the circulating geothermal waters. The occurrence of quartz in aged modern geothermal sinters in New Zealand was demonstrated by Lynne et al. (2006), who reacted freshly precipitated microbe-rich amorphous silica sinters from the Wairakei Power plant drain (see also Mountain et al., 2003) in a low pH (3.5-5.5), high temperature (75-94°C) steam vent at Orakei Korako, NZ for up to 2 years. Based on changes in XRD patterns they concluded that quartz peaks developed after ~ 5 months, which could support the observations presented here where quartz peaks were observed in the subaqueous Krafla sinters (made up primarily of amorphous silica) that had reacted with the effluent solutions for 25 months (in contrast to Lynne et al., 2006 who reacted their sinter samples in steam vents). However, it is noteworthy that no quartz crystals were identified in the SEM study, yet this could be a consequence of the selective sampling and examination protocols.

The black colour of the precipitate was mainly caused by accessory minerals, including pyrrhotite, magnetite, and marcasite (Fig. 4.14, KF-T and KF-B pattern) which have all previously been identified as being in equilibrium with the geothermal waters at Krafla (Gunnlaugsson and Arnórsson, 1982). In addition, a red layer was observed in the middle part of the slides (Fig. 4.13d) consisting primarily of hematite (red colour), magnetite, marcasite and albite (Fig. 4.14, KF-R pattern). Pyrrhotite was absent within this red layer indicating a possible oxidation of the sulfides to their oxide counterparts, i.e., hematite. Albite is not a common mineral in silica sinter deposits but it has been shown to occur as an alteration product in both low and high temperatures geothermal environments (e.g., Miyashiro, 1975; Browne, 1978 and references therein). Furthermore, Stefánsson and Arnórsson (2000) demonstrated that geothermal waters are in equilibrium with low-albite at temperatures between as low as 20 to 300°C. It is important to note that the precipitation of albite, iron sulphides and oxides contributed only little (<5%) to the measured growth rate as indicated by XRD (XRD peaks of these crystalline minerals are small compared to the broad opal-A peak).

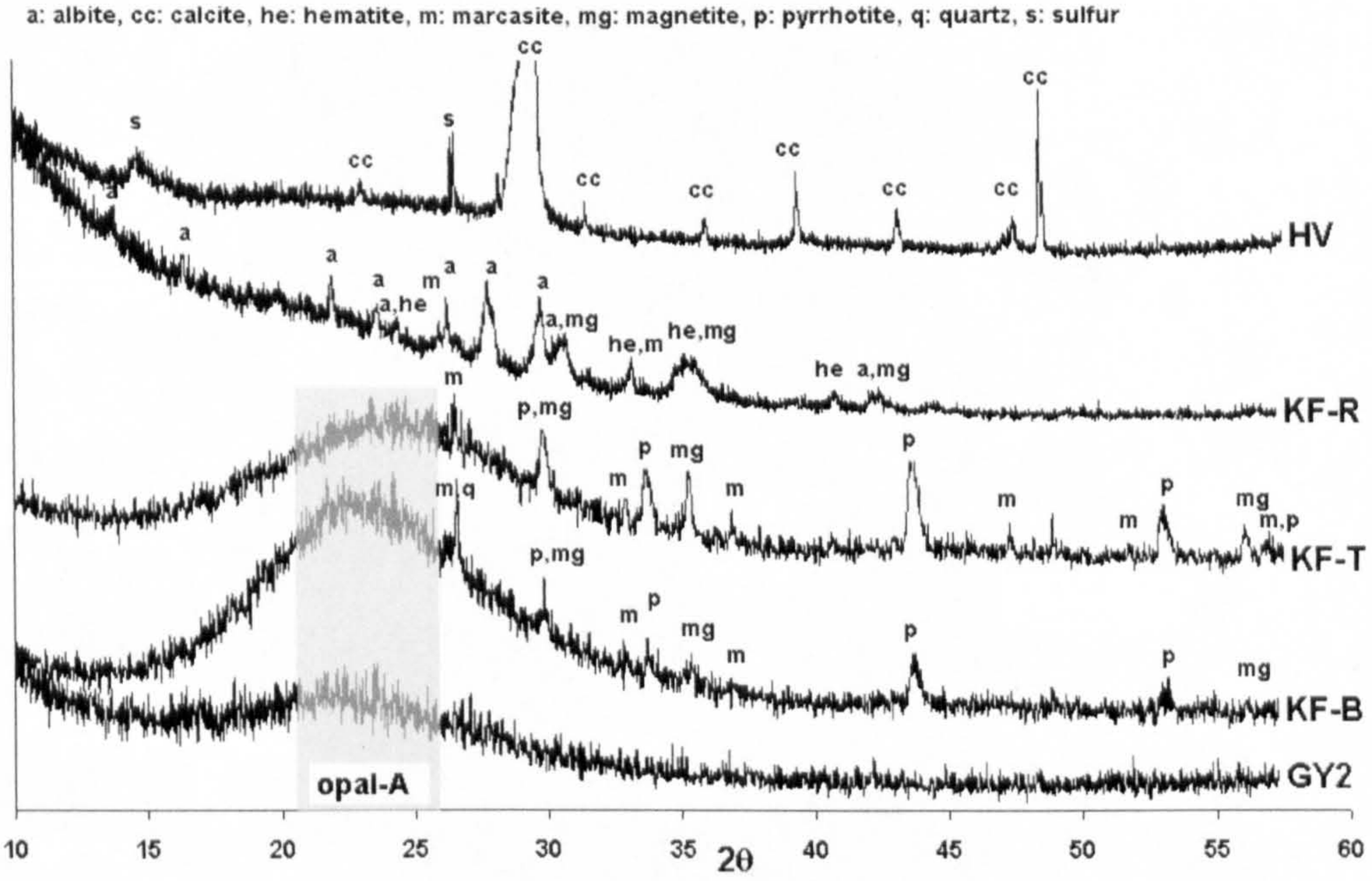

Figure 4.14: XRD patterns of precipitates scraped off different parts of the slides collected at Krafla (top of slide, KF-T; bottom of slide, KF-B; red precipitate, KF-R). For comparison, the XRD patterns from Hveragerdi (HV) and Geysir (GY2) and the position of the opal-A 2θ-range are shown.

All glass slides were covered with a 0.5 to 1cm thick layer of compact black sinter (Fig. 4.13) which made a microscopic examination of individual slides difficult and thus precipitates, scraped off close to the AWI, the middle and the bottom of the slides, were analysed. At the AWI, dense columnar textures developed consisting mainly of spherical aggregates of amorphous silica with few interspersed larger iron sulphides and oxides (confirmed by EDX and XRD; Fig. 4.14 and 4.15a) and a few rod-shaped microorganisms (Fig. 4.15a). Further down the slide, the amount of microorganisms increased but overall, the slides were dominated by perfectly smooth silica spheres that coalesced into larger aggregates (Fig. 4.15b), a few larger crystals of iron oxides, sulfides and albite (Fig. 4.15c and Fig. 4.14). In the constantly submerged parts of the slides thick silicified biofilms developed (Fig. 4.13d), consisting of long and fully silicified filaments (Fig. 4.15d) with lengths up to several hundreds of μm.

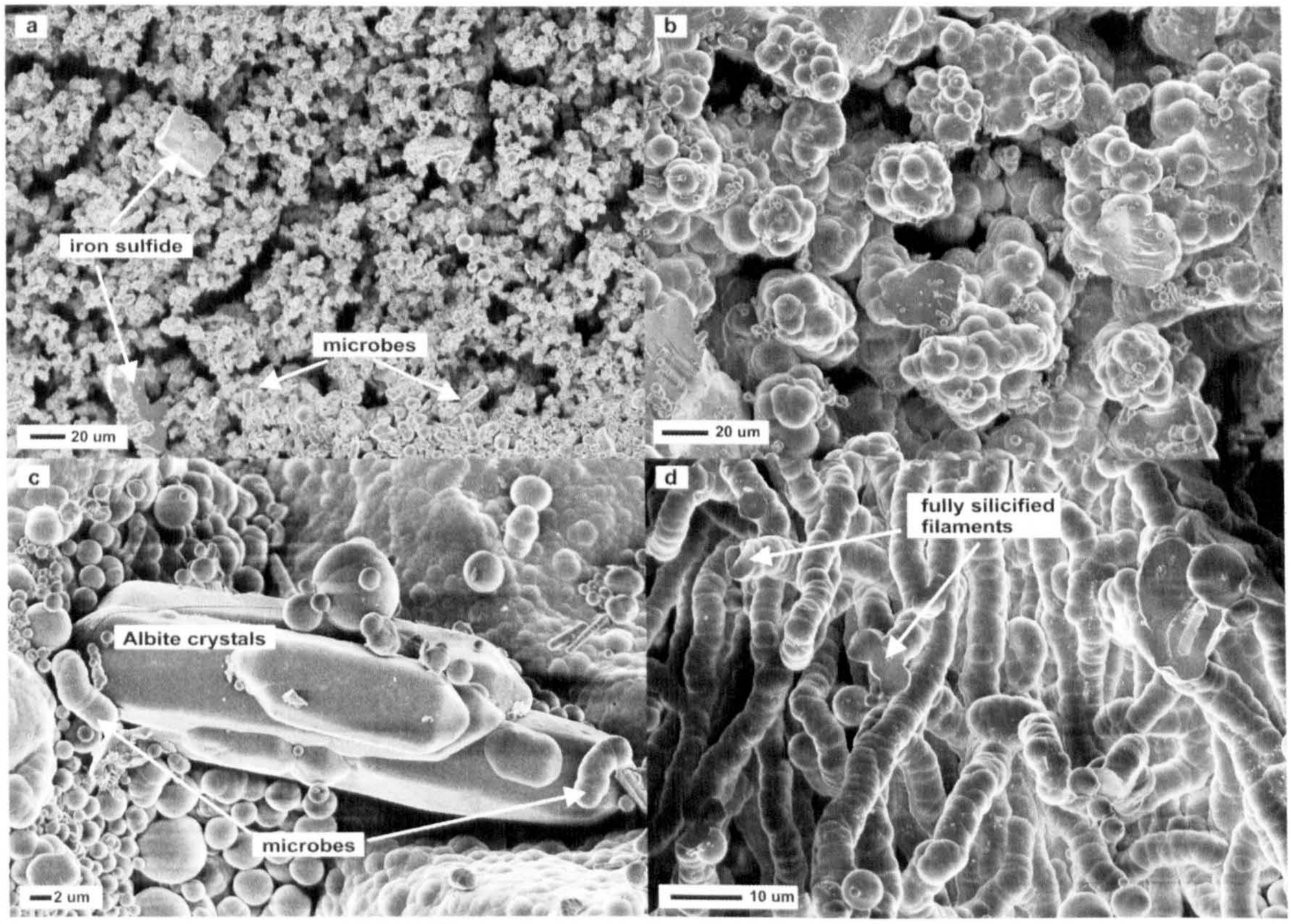

Figure 4.15: Photomicrographs of precipitate from KF after 25 months. a) Rough surface with columnar-like structures at the AWI consisting mainly of amorphous silica, iron sulphides and oxides (confirmed by EDS and XRD) interspersed with microbes and larger crystals of iron sulphides, b) aggregates of silica spheres, c) albite crystals surrounded by silica aggregates and microbes, d) dense accumulation of silicified microbial filaments in the lower parts of the slides.

4.5 Discussion

The main objectives of this study were threefold: (i) to quantify the growth rate of silica sinters as a function of temperature (42-96°C), pH (7.5-10) and geothermal water composition (specifically silica content; 250-695 ppm), (ii) to ascertain the variations in sinter structure and texture as a function of sinter growth rate and microbial communities and, (iii) to compare and contrast these features.

As mentioned previously, a few studies (Mountain et al., 2003; Smith et al., 2003 and Handley et al., 2005) have carried out similar *in-situ* sinter growth field studies in various geothermal areas in the Taupo volcanic zone in New Zealand (NZ) thus allowing a direct comparison between geothermal systems in Iceland and New Zealand. Similarly, *in-situ* growth studies (e.g., Blank et al., 2002; Spear et al., 2005; Kandianis et al., 2008 and references therein) have

been done in Yellowstone National Park, US, however, no actual sinter growth rates were determined or they concentrated on calcite precipitation, i.e., formation of travertine, thus a comparison with these studies was not possible.

4.5.1 Spring and drain water chemistry, pH and T-regimes

Within the geothermal areas at Geysir, Hveragerdi and Krafla, the spring and drain waters were characterized by low salinity and alkaline pH, wheras the geothermal waters at Svartsengi and Reykjanes were highly saline (seawater-meteoric water mixtures) with near neutral pH (Table 4.2). Temperature, one of the major controls on silica solubility, and one of the prime reasons for choosing the various experimental sites, ranged between 42 and 96°C. This was to a certain degree also mirrored by the measured silica concentrations which varied substantially between the five studied geothermal systems (695ppm to 250 ppm SiO_2) with the highest values at Reykjanes and Krafla and the lowest at Svartsengi (Table 4.2).

Table 4.2: Comparison of physico-chemical parameters of the studied geothermal waters as well as measured silica growth rate and degree of silica saturation (using PHREEQC).

Location	[a]T (°C)	[b]pH/°C	$[SiO_2]_{tot}$ ppm	[c]Salintiy %	Growth rate kg $y^{-1}m^{-2}$	Saturation Index, SI
Krafla	80	10.0 / 50	603	0.06	19.5 ± 2.4	-0.94
GY1	70 - 96	9.0 / 86	363	0.05	0.3 ± 0.1	-0.54
GY2	76 - 82	8.7 / 78	372	0.05	0.7 ± 0.3	-0.38
[d]GY3	61 - 70	9.0 / 68	[d]372	[d]0.05	1.4 ± 0.5	-0.4
Hveragerdi	66 - 74	9.1 / 71	304	0.04	[e]1.1 ± 0.4	-0.49
Svartsengi	42	7.7 / 42	250	2.56	9.7 ± 3.5	-0.09
	60	7.6 / 21	[f]-	[f]-	8.8 ± 3.4	[f]-
Reykjanes	75	7.5 / 40	695	4.67	304 ± 20	0.17

[a]temperature fluctuations over the experimental period
[b]mean value of measured pH over time period studied (variations ± 0.2 units)
[c]calculated with the ion concentrations listed in Table 1
[d]water chemistry at GY3 was assumed to be identical to GY2 due to their proximity (~10m)
[e]overall growth rate, including calcite and silica precipitation in equal amounts, was 2.1 ± 0.7 $kgy^{-1}m^{-2}$
[f]solution composition during the second experimental period was assumed to be equal to that in the first experimental period.

The main factor governing silica precipitation from geothermal waters is the silica solubility (i.e., degree of silica saturation) which is a function of pH, temperature, salinity and silica concentration (Fig. 4.16; see section 2.1.3 for more details). It follows that the degree of silica

saturation, i.e., silica precipitation rates, are highest in near-neutral, saline, low-temperature geothermal waters with high silica concentrations (Fig. 4.16).

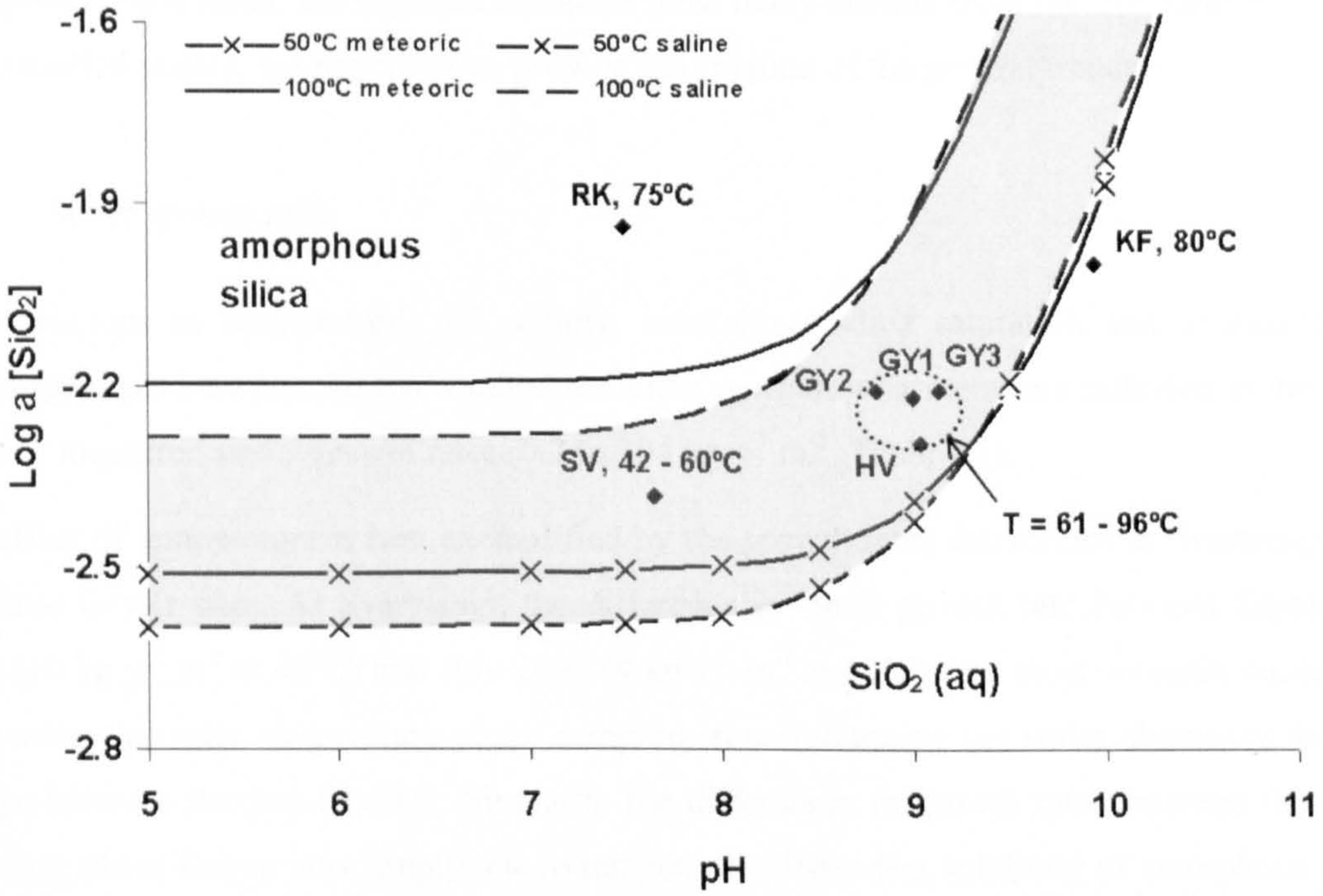

Figure 4.16: Diagram of log activity (log a) of silica as a function of pH, showing the effects of temperature and salinity. Also plotted are the pH - SiO_2 – conditions representing the five studied geothermal systems. The full lines depict the solubility of amorphous silica in meteoric waters at 50 and 100°C whereas the shaded area represents the 50 - 100°C silica solubility region in highly saline waters (contain ~ 0.7M NaCl, represents salinity of geothermal waters at Reykjanes). Data from geochemical modelling using PHREEQC (see methods, Table 4.2).

As illustrated in Figure 4.16, the surface waters sampled at Geysir, Hveragerdi and Krafla appeared to be undersaturated with respect to amorphous silica (Table 4.2, $SI_{SiO2}<0$ and Fig. 4.16 points below the stability line between amorphous silica and $SiO_{2(aq)}$) while the saline waters at Reykjanes were supersaturated (Table 4.2, $SI_{SiO2}>0$ and Fig. 4.16, RK is significantly above the stability line). Despite its low temperature and near-neutral pH, the geothermal water at Svartsengi seemed slightly undersaturated with respect to amorphous silica (Table 4.2, $SI_{SiO2}\sim0$), which was due to the fact that most silica precipitation had occurred in the settling tanks located a few hundred meters upstream. Although the waters at the experimental site were close to equilibrium with amorphous silica, the total silica concentration may have been underestimated due to removal of suspended silica particulates by filtration.

In general, the calculated SI values are representative for equilibrated systems and this assumption is only partly valid for the studied waters. Furthermore, SI values can be substantially different if calculated with another geochemical code and a different database (data not shown). As a result, the reported SI values most likely deviate from the true saturation state of the studied waters, but nevertheless provide information of the general trends.

4.5.2 Sinter growth rates

The variations in temperature, pH salinity, amorphous silica saturation and abundance of microorganisms between the five studied Icelandic geothermal systems are reflected in the wide range of measured sinter growth rates (0.2 to 304 kg y^{-1} m^{-2}, Table 4.2).

The effect of temperature is best exemplified by the growth rates determined at Svartsengi and the three Geysir sites. At Svartsengi, the difference in sinter growth rate between September 2005 (10 kg y^{-1} m^{-2} at 42°C) and July 2007 (9 kg y^{-1} m^{-2} at 60°C) was most certainly caused by an increase in water temperature at the sampling sites (assuming the water chemistry did not change between the two studies). Similarly, the differences in growth rates between the three sampling site at Geysir was simply due to temperature dependent solubility of amorphous silica (Iler, 1979)) because at all Geysir sites pH, silica concentration and salinity were equivalent. As a result, the highest precipitation rates were measured at GY3 (1.4 kg y^{-1} m^{-2}, T_{max} = 70°C) and the lowest at GY1 (0.2 kg y^{-1} m^{-2}), where the maximum temperature was about 26°C higher (Table 4.2). The water temperature at GY2 (T_{max}= 82°C) lead to a growth rate (0.7 kg y^{-1} m^{-2}) in between the values determined for GY1 and GY3. The findings are consistent with the degree of silica saturation at GY1 (SI = -0.54) as compared to GY3 (SI = -0.40). It has to be noted that all studied spring waters at Geysir were undersaturated with respect to silica (Fig. 4.16, Table 4.2), suggesting that subaqueous silica precipitation was inhibited. This was consistent with SEM results showing that sinter mostly grew close to the AWI due to evaporation and condensation processes. Similar observations were made by Mountain et al. (2003) in geothermal pools at Ngatamariki and Orakei Korako, NZ, in which sinter growth was also dominated by the formation of subaerial spicular structures. Note that the hydrodynamic and geochemical conditions at these sites were comparable with those in the Icelandic Geysir springs.

The geothermal waters at Hveragerdi had similar salinity, silica concentration, pH and temperature to GY3. After correction due to calcite precipitation, a sinter precipitation rate of 0.7 kg $y^{-1}m^{-2}$ was calculated which is substantially lower compared to GY3 (1.4 kg $y^{-1}m^{-2}$). This lower rate is reflected in the lower SI at Hveragerdi (SI = -0.49) when compared with GY3 (SI = -0.40, Fig. 16) and was due to the lower silica concentration in the waters at HV ($\Delta SiO_{2,\ GY3\text{-}HV}$ ~70ppm). As mentioned before, calcite precipitation was restricted to the submerged part of the

slides while silica mainly formed in the vicinity of the AWI (Fig. 9). Equivalent processes have been described in geothermal waters in New Zealand, e.g., Orakei Korako (Mountain et al., 2003) and Waikite (Jones et al., 2000; Mountain et al., 2003). At Waikite only calcite was found to precipitate subaqueously at high temperatures, while at Orakei Korako ~ 26% of the sinter growth contribution stemmed from subaqueous calcite precipitation with the remainder of the sinter growth being due to silica precipitation.

Much higher precipitation rates were observed for the saline waters at Reykjanes and Svartsengi. At Reykjanes the waters were supersaturated with respect to amorphous silica (SI = 0.18, 675 ppm $SiO_{2(aq)}$, Fig. 4.16) and the measured growth rate (304 kg y^{-1} m^{-2}) was between 200 and 1000 fold higher than at Geysir and Hveragerdi. This high rate was the result of the high dissolved silica concentration, the near neutral pH, and to a lesser extent, the high salinity of the drain waters. The Reykjanes growth rate is comparable to sinter growth rates within a wastewater drain at Wairakei Power Station, NZ (Mountain et al., 2003) where a similar growth rate (350 kg y^{-1} m^{-2}) was measured, although the drain waters at Wairakei were colder (62°C), more alkaline (pH=8.5) and less saline (meteoric water origin) thus more comparable to Geysir and Hveragerdi. The similarity in growth rates between Wairakei and Reykjanes may be primarily the consequence of the fast re-supply of highly silica saturated solutions, while salinity and temperature may play a lesser role.

At Svartsengi, the growth rates (9 kg y^{-1} m^{-2} at 60°C and 10 kg y^{-1} m^{-2} at 42°C) were a thirtieth of those at Reykjanes. Although, salinity at both sites was high, the lower total silica concentration (measured after filtration and colloid removal), i.e., degree of silica saturation (SI = -0.09, Table 2), and the slow re-supply of fresh silica-rich solution resulted in a much lower precipitation rate compared to Reykjanes. As mentioned previously, the bulk of the total silica had already precipitated in form of colloids along the outflow channels (blue colour in Fig. 12a). As a result, sinter growth at this site was mainly controlled by aggregation of the suspended silica colloids, and to a lesser extend by evaporation and cooling processes.

As discussed previously, the pH of geothermal waters has a strong effect on the solubility of amorphous silica (Fig. 4.16) and thus on sinter growth rates. As a result of this, it was not surprising to find the most undersaturated waters at Krafla (Fig. 4.16, SI = -0.94) where the geothermal water had a pH of 10. However, the precipitation rate determined for Krafla (19.5 kg y^{-1} m^{-2}) was ~ 10 times higher than within the undersaturated geothermal waters at Geysir and Hveragerdi although the waters at all these three sites were of equivalent salinity and temperature. Furthermore, the Krafla rate was twice as high as at Svartsengi where the wastewaters were only slightly undersaturated with respect to silica yet the waters were highly saline, near neutral, lower in temperature and contained high loads of suspended silica colloids.

As shown by the SEM analyses (Fig. 4.15a, b), at Krafla a large proportion of silica precipitated in the vicinity of the AWI due to evaporation and condensation processes. This was not surprising as the total silica concentration was twice as high as at Geysir and Hveragerdi, which resulted in a substantially higher polymerization and precipitation rate at the AWI. However, most silica was found in the submerged parts of the slides which were dominated by thick silicified biofilms (Fig. 4.13d, 15d). This suggests that once the slides were densely colonized by microorganisms, silica colloids that formed close to the AWI quickly adhered to the surfaces of the biofilm leading to its complete silicification (e.g., Mountain et al., 2003; Benning et al., 2004 a, b; Lalonde et al., 2005). Note that the adhesion of silica colloids most likely occurred via hydrogen-bonding as well as entrapment of colloids within the complex structure of the biofilms exopolysaccharides.

4.5.3 Comparison of sinter growth rates and structures/textures

Overall, in the five studied geothermal areas, the influence of microorganisms on the texture and structure of sinters was variable but, the sinter fabrics correlated well with the growth rates determined at each locality as well as other *in-situ* studies (e.g., Mountain et al., 2003; Handley et al., 2005, see section 2.2.4).

In spring and drain waters at Geysir, Hveragerdi and Krafla where the precipitation rates were low to high, sinter fabrics consisted of dense, weakly laminated and quite heterogeneous deposits. The sinter structures and textures were dominated by the high abundance of thermophilic microorganisms (60 to 96°C), and thick biofilms developed both in the submerged parts as well as at the AWI. At GY1, after only 5 days a dense mat of filaments fully covered the submerged part of the slides where the temperatures were consistently at ~80°C. Even at the AWI where the water temperature reached values as high as 96°C microorganisms were still present. Due to the slow precipitation rates at this sites, microbial surfaces became continuously covered with silica particles and with time these particles joined together to form dense layers. It has to be noted that this consolidation process did not happen rapidly but rather took weeks to months, leading to the full silicification of the microbial communities and the subsequent incorporation into the compact sinters (Handley et al., 2005). Nevertheless, at GY1 and GY2 after only 5 days, microorganisms were already partly silicified. Similar high silicification rates were observed in a spring outflow channel at Krisuvik, Iceland (Konhauser et al., 2001) as well as in various geothermal waters in New Zealand, e.g., Iodine Pool, Waimangu (Jones et al., 2004), Champagne Pool, Waiotapo (e.g., Jones et al., 1999; Handley et al., 2005).

The sinter structures and textures at Geysir and Hveragerdi were very similar. The texture of the precipitates in the subaqueous parts of slides varied mainly due to the presence of differently

shaped microorganisms (filaments, cocci, rod-shaped microbes, diatoms) as well as their abundance. At sites with lower temperatures, i.e., GY3 and HV, microbial mats colonized the slides faster and the range of microbial cell morphologies was significantly higher than at GY1 and GY2 (higher temperatures). This larger diversity was confirmed by 16S rDNA analysis of microbial mats from these sites (Chapter 5). On slides from GY3 and HV thick coloured biofilms also developed at the AWI (Fig. 4.8 and 4.11) whereas at GY1 and GY2 microbial mats were restricted to the submerged parts of the slides. The textures that dominated the vicinity of the AWI at GY1 and GY2 included compact silica crusts interspersed with spicules and terrace-like structures, which were sporadically covered with microorganisms. The best defined spicules were observed at GY1 which were very similar in character to those observed at Octopus Spring, Yellowstone National Park (a gently surging, near-neutral spring with T varying from <73 to >85°C, Braunstein and Lowe, 2001). A few spicules also formed on slides collected at GY2, however the dominant features at the AWI were distinct silica terraces that increased in height up to 3 mm over the time period studied (Fig. 4.6). Conversely, at GY3 and HV, microbial growth was much higher and the development of spicules and well defined terraces was inhibited. The latter two sites could be compared with Pavlova spring, Ngatamariki, NZ (pH = 7.2, T = 71°C, Mountain et al., 2003) where biofilms fully covered the slides after only 6 days and sinter development was far slower.

Interestingly, at Krafla, the textures and structures of the black sinters were similar to GY1 where the bottom parts of the slides were characterised by biofilms. However, most silica precipitated initially in the vicinity of the AWI (subaerially) and was enhanced by the presence of microbial surfaces in the submerged parts.

Lastly, at Svartsengi and Reykjanes where the precipitation rates were intermediate to very high, sinters forming within and along the wastewater drains and pools (both subaqueous and subaerially) were very porous and homogeneous. It is worth noting that particle interactions are aided by the presence of salts (i.e., interparticle bonding through cations such as Na^+; e.g., Iler et al., 1979 and refernces therein; Smith et al., 2003). This suggests that silica particle aggregation was enhanced in the highly saline geothermal waters at Svartsengi and Reykjanes which also explained the formation of the porous, gel-like precipitates in these waters. Intriguingly, the size distribution of the silica aggregates as well as of the individual silica nanoparticles differed between the two sampling locations. At Reykjanes, at higher temperature and precipitation rate, a wider size distribution was observed (11-106 nm), while at Svartsengi (far lower temperatures, slower precipitation rates and stagnant water) a very narrow distribution of the individual silica particles (10-36 nm) was observed. From this data, it is not possible to pinpoint the governing factor leading to this discrepancy and most probably more than one factor, e.g., temperature, precipitation rate as well as flow rate influences the size of the precipitating silica colloids. The

high precipitation rates as well as high salt contents at Reykjanes and Svartsengi was also not conducive to microbial colonization and SEM observation of slides or filters from both sites failed to reveal any microbial presence. However, successful DNA extraction from loose sediments collected at Svartsengi indicated that over longer time periods microorganisms actually adapted to conditions present in the studied pool. In contrast, DNA extraction at Reykjanes was not successful (chapter 5) which suggested that due to the high salinity, high temperature, high flow rate as well as high sinter growth rate (304 kg y^{-1} m^{-2}) the microbial abundance was low at this site.

4.6 Conclusions

In-situ sinter growth experiments carried out in natural geothermal areas are uniquely suited to provide data on the mechanisms and processes affecting or governing sinter formation as a function of a complex set of parameters. In this study, growth rates and the structural and textural developments of sinters from five diverse geothermal sites in Iceland were analyzed from both an abiotic and a biotic perspective. The fact that the physico-chemical conditions varied significantly between these sites allowed a realistic comparison of sinter growth rates, sinter structures and textures between the different hydrodynamic and geochemical settings. The results clearly showed that the mesoscopic and microscopic textural development of silica sinters was strongly influenced by (1) the inorganic silica precipitation rate which itself was a function of temperature, pH, salinity, silica saturation and flow rates, (2) the precipitation mechanism (subaqueously and/or subaerially) and (3) the presence of mesophilic and thermophilic microorganisms. The analysis showed that in all geothermal areas where the waters exhibited near neutral pH, moderate to high silica content and high salinity (i.e., Reykjanes and Svartsengi) silica precipitation rates were high. These physico-chemical parameters led to the growth of porous and homogeneous sinters that developed predominantly subaqueously. In addition, due to the high salt contents and high growth rates, microbial activity was very low and microbial fossilization and preservation was poor. Conversely, in the geothermal sites where the waters were undersaturated with respect to silica (i.e., Geysir, Hveragerdi and Krafla), subaqueous silica precipitation was inhibited and sinter growth was mostly restricted to the AWI where evaporation and condensation processes dominated. As a consequence, dense and heterogeneous sinters with well defined spicules and silica terraces formed in the vicinity of the AWI. Despite the temperatures being quite high in these springs, extensive biofilms mainly developed in the submerged zone, and in turn due to the low silica precipitation rates these biofilms became fully silicified (externally and internally) and were well preserved within the growing sinters. Nevertheless, they also substantiate the strong abiotic

– biotic relationship and their complementary roles in the build up of the silica sinter structures and textures. Naturally, the observed processes also emphasize the importance of *in-situ* studies in natural settings with a view towards enhancing our understanding of processes on the modern Earth, but with equivalent applications to ancient geological processes observed on the Precambrian Earth. Lastly, silica rich deposits recently described in Gusev Crater on Mars were postulated possibly to have derived from hydrothermal solutions supersaturated in silica. Although, obviously so far no microbial evidence has been documented, the preponderance and close association of microbial communities with silica sinters on Earth, make this a good analogue for future missions to Mars.

5 THE EFFECTS OF TEMPERATURE, SALINITY, PH AND SINTER GROWTH RATE ON MICROBIAL DIVERSITY IN ICELANDIC HOT SPRINGS

5.1 Abstract

The microbial ecology associated with siliceous sinters was studied in five geochemically diverse Icelandic geothermal systems (described in chapter 4) and analysed in terms of variations in geochemical conditions (i.e., T, pH, salinity and sinter growth rate). The diversity of microbial communities was investigated by polymerase chain reaction (PCR) amplification of 16S rDNA gene sequences from DNA extracted from sediments of each study site, followed by molecular cloning and sequencing. Both bacterial and archaeal DNA was retrieved from sediments at the two Geysir sites (GY1 and GY2), Hveragerdi (HV) and Svartsengi (SV) while only bacterial DNA was detected at Krafla (KF). No microbial DNA was found at Reykjanes (RK) suggesting that the physico-chemical conditions at this site, i.e., high salinity (≥ 4.7%), high temperature (≥ 75°C) and high sinter growth rates (≥ 300 kg y^{-1} m^{-2}), were too challenging (i.e., too extreme) for the development of thermophilic microbial communities. Findings from the other sites indicated that the detected bacterial phylotypes fall mainly into the same phylogenetic classes (i.e., *Aquificae*, *Deinococci*, *γ – Proteobacteria*). *Aquificae* (mostly closely related to *Thermocrinis*) was ubiquitous at GY1 (site with the highest temperature) but also occurred at all other high-T sites, i.e., GY2, HV and KF, while close relatives of the *Deinococci* (*Thermus* species) were restricted to GY2 and HV. *γ – Proteobacteria* were the predominant class at KF and SV but a few clones were also found at GY1 and HV. The observed phylogenetic diversity (i.e., number and composition of detected phylotypes) is argued to be strongly related to the geochemical regime of the studied geothermal waters showing a decrease in bacterial diversity with an increase in T, salinity, sinter growth rates and more alkaline pH.

5.2 Introduction

The study of extreme environments and the organisms that inhabit them, i.e., extremophiles, has made the search for extinct and extant life in the ancient Earth as well as on other planets more plausible. Amongst terrestrial extreme environments, geothermal hot springs and the associated silica sinters are well known analogues for early Earth (e.g., Cady and Farmer, 1996; Konhauser, 2000; Cady, 2001; Toporski, 2002 and references therein) and early Mars (e.g., Walter and Des Marais, 1993; Farmer and Des Marais, 1994; Farmer, 1996) conditions and the

silicification and preservation of microorganisms in these systems have thus been the focus of extensive research (see section 2.2.5 for more details). Furthermore, a plethora of studies have characterised the microbial communities found in various hot springs and analysed their metabolic pathways and how they adapted to these extreme conditions (see section 2.2.3 for more details). However, the parameters controlling the diversity of such microbial communities (i.e., the potential for microbial fossilisation and preservation) as well as the links between community diversity and geochemical/ hydrodynamic regimes prevalent in hot springs are still poorly understood.

Here we present results from phylogenetic analyses of microbial diversity in five geochemically diverse (T, pH, salinity, sinter growth rate) Icelandic geothermal systems where silica precipitation leads to the preservation/fossilization of microbial biomarkers. At each location, T, pH, salinity and water chemistry were analysed and sinter growth rates were monitored *in-situ* using glass slides that acted as precipitation substrates (chapter 4). Standard molecular techniques that targeted both bacterial and archaeal 16S rDNA were employed and five bacterial clone libraries were derived. The majority of the sequences were closely (>96%) related to currently known sequences, but representatives of new divisions were also found. The diversity of bacterial communities was determined for each site and subsequently analysed in terms of how four major geochemical factors (temperature, pH, salinity and sinter growth rate) affect the microbial community structure. The data were compared with other molecular studies on the bacterial diversity in Icelandic and other hot springs.

5.3 Methodology

At all sites (except GY3) sediments were sampled aseptically in sterile vials from the same sampling sites as described in chapter 4. The characterisation of the physico-chemical conditions (i.e., T, pH, salinity and water chemistry) and the *in-situ* determination of the sinter growth rates at these sites were described in section 4.2.

Full details of the molecular techniques are given in section 3.1.4. Briefly, DNA was extracted from the collected sediment samples using the FastDNA®SPIN Kit for soils (Qbiogene). This was followed by amplification of 16S rDNA using both bacterial and archaeal specific primer sets: Archaea Ar109f - Ar912r, Bacteria Eu9f - Eu1492b. PCR products were run on a 1% Agarose gel to identify bacterial and archaeal bands. Thereafter, PCR products were purified using PureLink PCR Purification Kit (Invitrogen).

The bacterial PCR products were cloned using a TOPO TA cloning kit (Invitrogen) according to the manufacturer's instructions which resulted in five bacterial clone libraries (see section 3.1.4

for more details). Plasmid DNA from single colonies (~100 colonies per library) was isolated and amplified using M13f and M13f primers. Groups of clones were subdivided on the basis of restriction fragment-length polymorphism (RFLP) analysis following MSPI(HpaII) and Hin6I digests. Digests were run on a 3% Agarose gel to identify unique banding patterns and based on these results, subgroups were sent off for sequencing. Returned contiguous sequences were assembled using Sequencher 4.7 (Gene Code Corporation), uploaded into the Ribosomal Database Project - II (RDP-II; Cole et al., 2006 and references therein) in which all sequences were aligned and tested for sequence anomalies (e.g., chimeric artefacts). Closest relatives were found using RDP-II Sequence Match and phylogenetic trees were constructed with the Weighbor weighted neighbor-joining algorithm using the RDP-II Tree Tool.

5.4 Results

The six sampling sites, i.e., Geysir1, Geysir2, Hveragerdi, Krafla, Svartsengi and Reykjanes (chapter 4) were characterised by relatively large variations in geochemical parameters (near-neutral to alkaline spring waters, temperatures ranging between 40-90°C, low to high salinity; Table 5.1) and where siliceous sinter deposits were observed at the side of outflow channels of hot springs and steam separators.

5.4.1 Community structure analysis

Archaeal and bacterial DNA was successfully extracted and amplified from both Geysir sites (GY1 and GY2), Hveragerdi (HV) and Svartsengi (SV), while only bacterial DNA could be amplified at Krafla (KF). At Reykjanes (RK), despite multiple attempts neither archaeal nor bacterial DNA could be extracted from the collected sediments suggesting that at this site microbial activity is very low.

Bacterial PCR products from all extractions were pooled and bacterial clone libraries were constructed for GY1 (61 clones), GY2 (89 clones), HV (81 clones), KF (46 clones) and SV (95 clones). The archaeal PCR products were not further analysed due to time constraints. The biodiversity patterns found at each sampling site are summarised in Table 5.1, while a more specific inventory including the phylogenetic affiliation, the closest RDP match with accession number, percentage similarity to the RDP data, and the number of clones related to this sequence (i.e., screened by RFLP patterns) are given in Table 5.2 and 5.3.

Table 5.1: Physico-chemical conditions, sinter growth rate and class - level diversity of bacterial communities found at each study site.

	Geysir 1 (GY1)	Geysir 2 (GY2)	Hveragerdi (HV)	Krafla (KF)	Svartsengi (SV)	Reykjanes (RK)
T (ºC)	70 - 96	76 - 82	66 - 74	80	42	75
salinity (%)	0.05	0.05	0.04	0.06	2.56	4.67
pH	9	8.7	9.1	10	7.7	7.5
sinter growth ($kg\ y^{-1}\ m^{-2}$)	0.3 ± 0.1	0.7 ± 0.3	2.1 ± 0.7	19.5 ± 2.4	9.7 ± 3.5	304 ± 20
phylogenetic classes (number of clones)	*Aquificae* (58) *γ-Proteobacteria* (1) *Bacilli* (2)	*Deinococci* (51) *Aquificae* (26) *Bacilli* (7) *β-Proteobacteria* (1) unidentified (2)	*Deinococci* (45) *Aquificae* (20) *γ-Proteobacteria* (4) *β-Proteobacteria* (3) *Nitrospira* (4) *Bacilli* (1) unidentified (4)	*γ-Proteobacteria* (21) *Actinobacteria* (9) *Flavobacteria* (8) *Aquificae* (4) *α-Proteobacteria* (3) *β-Proteobacteria* (1)	*γ-Proteobacteria* (70) *α-Proteobacteria* (10) *Flavobacteria* (4) *Cyanobacteria* (4) *Sphingobacteria* (3) *β-Proteobacteria* (2) unidentified (2)	none

Table 5.2: Summary of bacterial 16S rDNA gene sequencing results at GY1, GY2 and HV. For each analysed clone, the % identity (based on RDP-II Sequence Match), the closest RDP match with accession number, class - level affiliation, and the number of clones related to the RDP match (i.e., screened by RFLP patterns) are given.

ID %	Access	Closest database match	Phylogenetic class	# clones
GY1 (total number of clones = 61)				
100	AF255599	*Aquificales* str. SRI-48	*Aquificae*	58
100	AM749791	*Geobacillus* sp. K8	*Bacilli*	2
99	AF188300	*Acinetobacter johnsonii*	*γ - Proteobacteria*	1
GY2 (total number of clones = 89)				
93-100	Y18411	*Thermus antranikianus* str. HN3-7T	*Deinococci*	51
99-100	AF255599	*Aquificales* str. SRI-48	*Aquificae*	26
99-100	DQ108401	*Bacillus* sp. Tibet-S2a2	*Bacilli*	4
99	AB055093	*Bacillus* sp. KSM-KP43	*Bacilli*	3
99	EF554889	*Ralstonia* sp. HI3	*β - Proteobacteria*	1
<85	-	unidentified	unidentified	4
HV (total number of clones = 81)				
88-99	AF255590	*Thermus* sp. SRI-96	*Deinococci*	33
97-99	AF255591	*Thermus* sp. SRI-248	*Deinococci*	4
95-99	AF407742	*Thermus* sp. B70-05	*Deinococci*	2
93	AF020205	*Thermus scotoductus* SA-01	*Deinococci*	2
91-99	L09661	*Thermus* sp. L09661	*Deinococci*	3
98	AF407746	*Thermus* sp. Y55-10	*Deinococci*	1
89-97	AF027045	*Candidate division OP1* clone OPB14	*Aquificae*	11
90-99	AM778960	*Sulfurihydrogenibium kristjanssoni*	*Aquificae*	8
86	AF255598	*Aquificales* str. SRI-40	*Aquificae*	1
89-99	DQ862553	*Stenotrophomonas maltophilia* PTB2063	*γ - Proteobacteria*	4
93-99	AF255603	*Nitrospira* sp. SRI-9	*Nitrospira*	3
92	AF255602	*Nitrospira* sp. SRI-237	*Nitrospira*	1
90-99	EF111105	*Variovorax* sp. RBE1CD-35	*β - Proteobacteria*	2
99	AB245358	*Variovorax ginsengisoli* Gsoil 3165	*β - Proteobacteria*	1
100	AM749791	*Geobacillus* sp. K8	*Bacilli*	1
<88	-	unidentified	unidentified	4

Table 5.3: Summary of bacterial 16S rDNA gene sequencing results at KF and SV. For each analysed clone, the % identity (based on RDP-II Sequence Match), the closest RDP match with accession number, class - level affiliation, and the number of clones related to the RDP match (i.e., screened by RFLP patterns) are given.

ID %	Access	Closest database match	Phylogenetic class	# clones
KF (total number of clones = 46)				
99-100	AF058286	*Pseudomonas mandelii* (T)	*γ - Proteobacteria*	18
98-99	DQ628970	*Gamma proteobacterium* SOC A20	*γ - Proteobacteria*	2
99	DQ257426	*Acinetobacter johnsonii* strain CAI-6	*γ - Proteobacteria*	1
99-100	AJ551154	*Arthrobacter* sp. An16	*Actinobacteria*	9
99-100	DQ515962	*Flavobacterium* sp. WB3.4-82	*Flavobacteria*	8
99-100	AF255599	*Aquificales* str. SRI-48	*Aquificae*	4
99	AJ227789	*Caulobacter* sp. DSM 6811	*α - Proteobacteria*	2
100	AY315163	*Glacier bacterium* FXI13	*α - Proteobacteria*	1
100	EF554889	*Ralstonia* sp. HI3	*β - Proteobacteria*	1
SV (total number of clones = 95)				
88-100	AB166980	*Marinobacter* sp. NT N31	*γ - Proteobacteria*	66
99-100	DQ270762	*Marinobacter* sp. B-3091	*γ - Proteobacteria*	4
99-100	AY690679	*Sphingomonas* sp. GC14	*α - Proteobacteria*	5
93-100	AJ309862	*Oceanicaulis alexandrii* C116-18	*α - Proteobacteria*	3
92	EF061106	*Mesorhizobium amorphae* CCBAU	*α - Proteobacteria*	1
96	DQ486495	*Oceanicaulis* sp. DG1255	*α - Proteobacteria*	1
98	AJ440996	*Flavobacterium gelidilacus* str. LMG21619	*Flavobacteria*	4
91	AM709630	*Microcoleus chtonoplastes* PCC 7420	*Cyanobacteria*	2
91	DQ460703	*Chroococcus turgidus* HUW 799	*Cyanobacteria*	1
91	AY032933	*Symploca* sp. VP642b	*Cyanobacteria*	1
99	DQ836305	*Fulvivirga kasyanovii*	*Sphingobacteria*	1
91	AM411964	*Spingobacterium* sp. P-7	*Sphingobacteria*	1
99	Y08957	*T.rossianum* str. SC-1	*Sphingobacteria*	1
99	AY328846	drinking water bacterium MB16	*β - Proteobacteria*	1
94	DQ486503	*Limnobacter* sp. DG1290	*β - Proteobacteria*	1
<88	-	unidentified	unidentified	2

Rarefaction analysis helps to compare species richness and diversity between clone libraries having different sizes. Furthermore, this method provides information on whether the bacterial libraries were adequately sampled (i.e., the true total bacterial phylogenetic diversity within these systems has been analytically determined) which is indicated by a plateau-shaped curve. For this study, rarefaction analysis was carried out using a programme written by Bailly et al. (2007) and results are illustrated in Figure 5.1. The rarefaction curves show that the bacterial clone library for KF, and almost for GY1 and GY2, was adequatley sampled (i.e., a plateau was reached). However, this was not the case for the HV and SV clone libraries (i.e., plateau was not fully reached). It is thus likely that at these sites additional sampling of clones may have resulted in a larger number of species detected. Note that a valid comparison of species richness / diversity between study sites can only be done if all bacterial libraries are fully saturated. However, despite incomplete sampling (at HV and SV), the rarefaction curves indicate that the bacterial diversity was significantly lower at the high temperature sites (i.e., GY1, GY2 and KF) than at the low-T sites (i.e., SV and HV; Fig. 5.1). This is in good agreement with previous studies (e.g., Skirnisdottir et al., 2000; Blank et al., 2002; Fouke et al., 2003; Meyer-Dombard et al., 2005) which showed that a higher number of phylotypes is observed at lower temperatures.

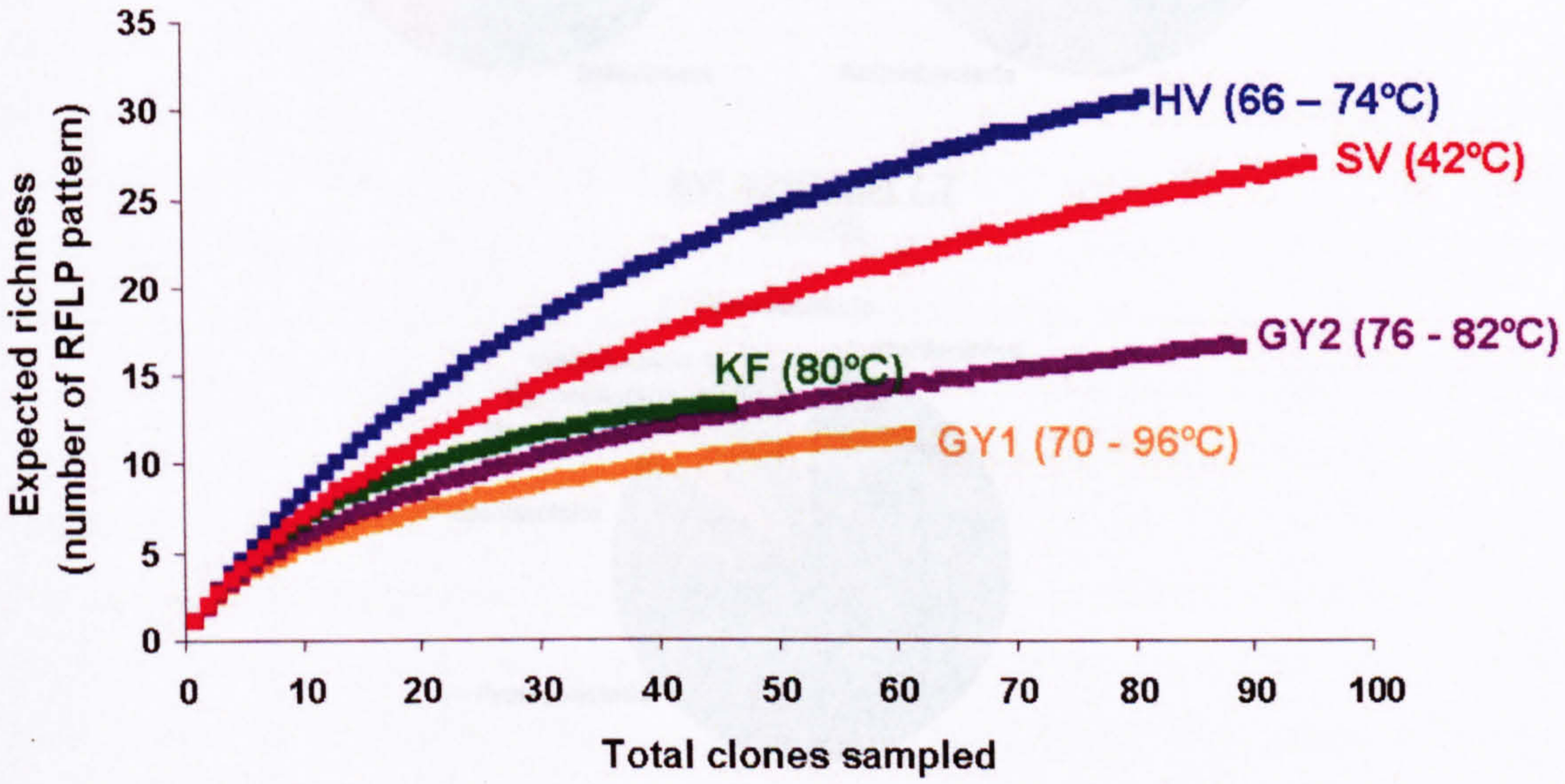

Figure 5.1: Rarefaction curve for the five bacterial 16S rDNA libraries. The cumulative number of species (i.e., expected richness) was plotted against the cumulative number of individuals (i.e., clones) analysed.

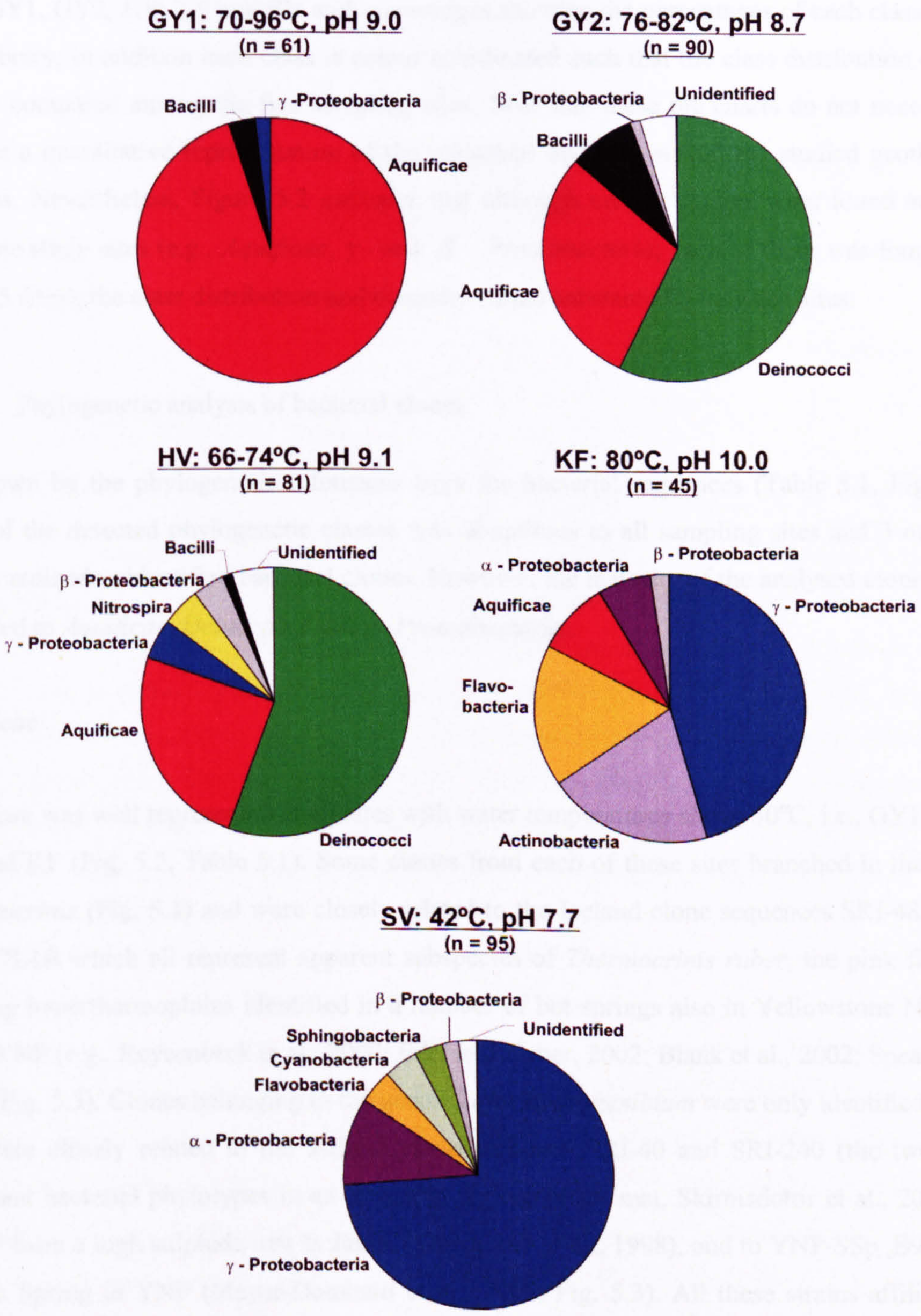

Figure 5.2: Class-level distribution and diversity of partial 16S rDNA sequences within bacterial clone libraries for both Geysir sites (GY1 and GY2), Hveragerdi (HV), Krafla (KF) and Svartsengi (SV). For reference, the total number of analysed clones (n) as well as the T-pH regime for each site are also given.

The class-level diversity and distribution of the partial 16S rDNA bacterial sequences identified at each site is illustrated in Figure 5.2. The five pie charts represent the bacterial clone libraries

from GY1, GY2, HV, KF and SV with pie-wedges showing the percentages of each class in the total library; in addition each class is colour coordinated such that the class distribution can be readily compared among the five sampling sites. Note that these pie charts do not necessarily provide a quantitative representation of the microbial diversity within the studied geothermal systems. Nevertheless, Figure 5.2 indicates that although certain classes were found at more than one study sites (e.g., *Aquificae*, γ- and β - *Proteobacteria*; each of them was found at 4 out of 5 sites), the class distribution and diversity varied substantially between sites.

5.4.2 Phylogenetic analysis of bacterial clones

As shown by the phylogenetic inferences from the bacterial sequences (Table 5.1, Fig. 5.2), none of the detected phylogenetic classes was ubiquitous to all sampling sites and 3 out of 5 sites contained unidentified bacterial clones. However, the majority of the analysed clones were affiliated to *Aquificae*, *Deinococci* and γ- *Proteobacteria*.

Aquificae

Aquificae was well represented at all sites with water temperatures above 50°C, i.e., GY1, GY2, HV and KF (Fig. 5.2, Table 5.1). Some clones from each of these sites branched in the genus *Thermocrinis* (Fig. 5.3) and were closely related to the Iceland clone sequences SRI-48, pIce1 and H7L1B which all represent apparent subspecies of *Thermocrinis ruber*, the pink filament forming hyperthermophiles identified in a number of hot springs also in Yellowstone National Park, YNP (e.g., Reysenback et al., 2000; Eder and Huber, 2002; Blank et al., 2002; Spear et al., 2005; Fig. 5.3). Clones belonging to the genus *Sulfurihydrogenibium* were only identified at HV and were closely related to the Iceland clone sequence SRI-40 and SRI-240 (the two most dominant bacterial phylotypes in an Icelandic high sulphide mat, Skirnisdottir et al., 2000), to NAK9 from a high sulphide mat in Japan (Yamamoto et al., 1998), and to YNP-SSp_B90 from Sylvan Spring in YNP (Meyer-Dombard et al., 2005, Fig. 5.3). All these strains affiliated to *Sulfurihydrogenibium kristjanssoni*, a hydrogen and sulfur-oxidizing thermophile isolated in Iceland (Flores et al., 2008). Clones from HV were also similar to strains found by other studies (OPB14 and a2b008, Fig. 5.3) that may represent a new phylotype within *Aquificae*. However, for a more definite placement of this outgroup within the *Aquificae*, new cultivable representatives are needed.

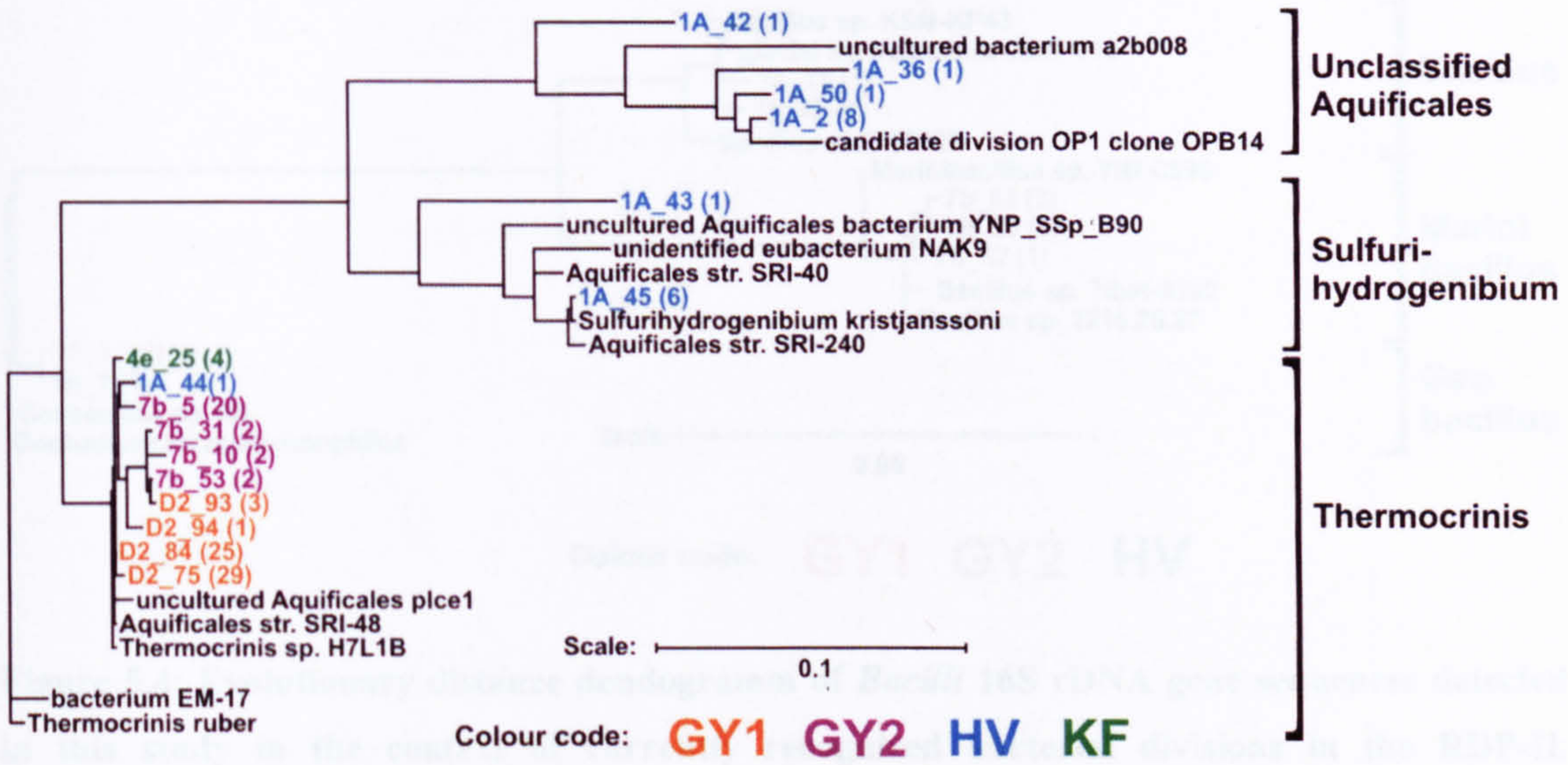

Figure 5.3: Evolutionary distance dendogramm of *Aquificae* 16S rDNA gene sequences detected in this study in the context of currently recognized bacterial divisions in the RDP-II. *Thermocrinis ruber* was used as an outgroup. Sequences designated SRI are from a high sulphide mat in Iceland, pIce1 from Haegindi and Fluidir Springs in Iceland, H7L1B from a mud hole at Hveragerthi in Iceland, EM from Octopus spring in Yellowstone National Park (YNP), OPB14 from Obsidian Pool in YNP, YNP-SSp_B90 from Sylvan Spring in YNP, a2b008 from a hydrothermal sediments in the Guaymas Basin, and NAK9 from a high sulphide mat in Japan. The scale bar is in nucleotide substitution per sequence position.

Bacilli

Similarly to *Aquificae*, clones related to *Bacilli* were only found at the high-temperature sites, i.e., GY1, GY2 and HV (except KF, Fig. 5.2, Table 5.1). GY2 clones branched in the genus *Bacillus* and *Marinibacillus* and were most closely related to KSM-KP43 (an alkaliphilic *Bacillus* strain from Japan) and to Tibet-S2a2 (an alkaliphilic psychrotolerant strain from the Qinghai–Tibet Plateau) respectively (Fig. 5.4). In contrast, *Bacilli* clones identified at GY1 and HV belonged to the genus *Geobacillus* and were most closely related to *Geobacillus* sp. K8 (Fig. 5.4), an isolate from geothermal soils in New Zealand.

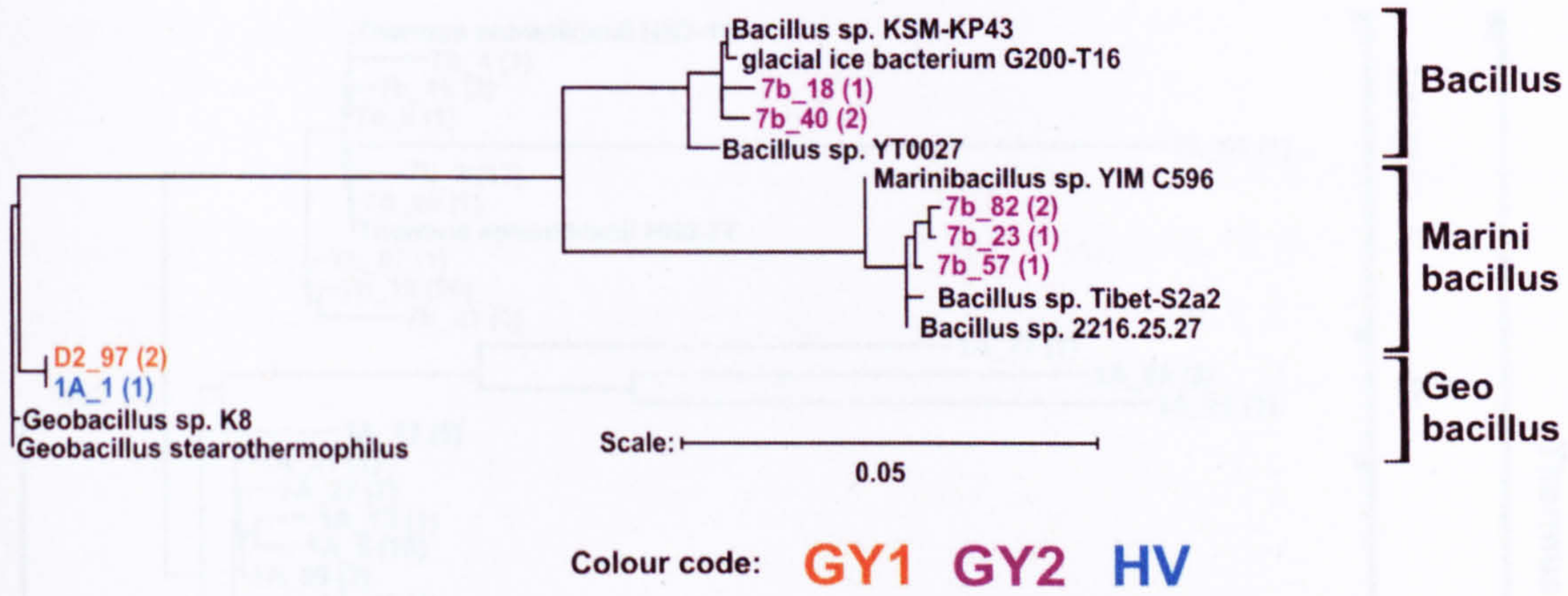

Figure 5.4: Evolutionary distance dendogramm of *Bacilli* 16S rDNA gene sequences detected in this study in the context of currently recognized bacterial divisions in the RDP-II. *Geobacillus stearothermophilus* was used as an outgroup. Sequences designated KSM-KP43, Tibet-S2a2, and YIM C596 are all alkaliphilic *Bacillus* strains from Japan, the Qinghai–Tibet Plateau and China respectively. *Geobacillus* sp. K-8 is an isolate from geothermal soils in New Zealand and sequence 2216.25.27 is from a sub-seafloor sediment core from the southwestern Sea of Okhotsk. Origin of strain YT0027 is unknown. The scale bar is in nucleotide substitution per sequence position.

Deinococci

Interestingly, *Deinococci* representatives were only found at GY2 and HV (Fig. 5.2, Table 5.1) and all clones clustered in the genus *Thermus* (Fig. 5.5). This indicated that the alkaline spring waters (pH ~9) and high temperatures (66 - 82°C) that characterised these sites were most favourable for the growth of *Thermus* species. GY2 clones had the closest database match to *Thermus antranikianii* HN3-7T and HN3-10 (branch A in Fig. 5.5), two Icelandic isolates that grow in alkaline waters (up to pH 10) and at temperatures around 80°C (Chung et al., 2000).

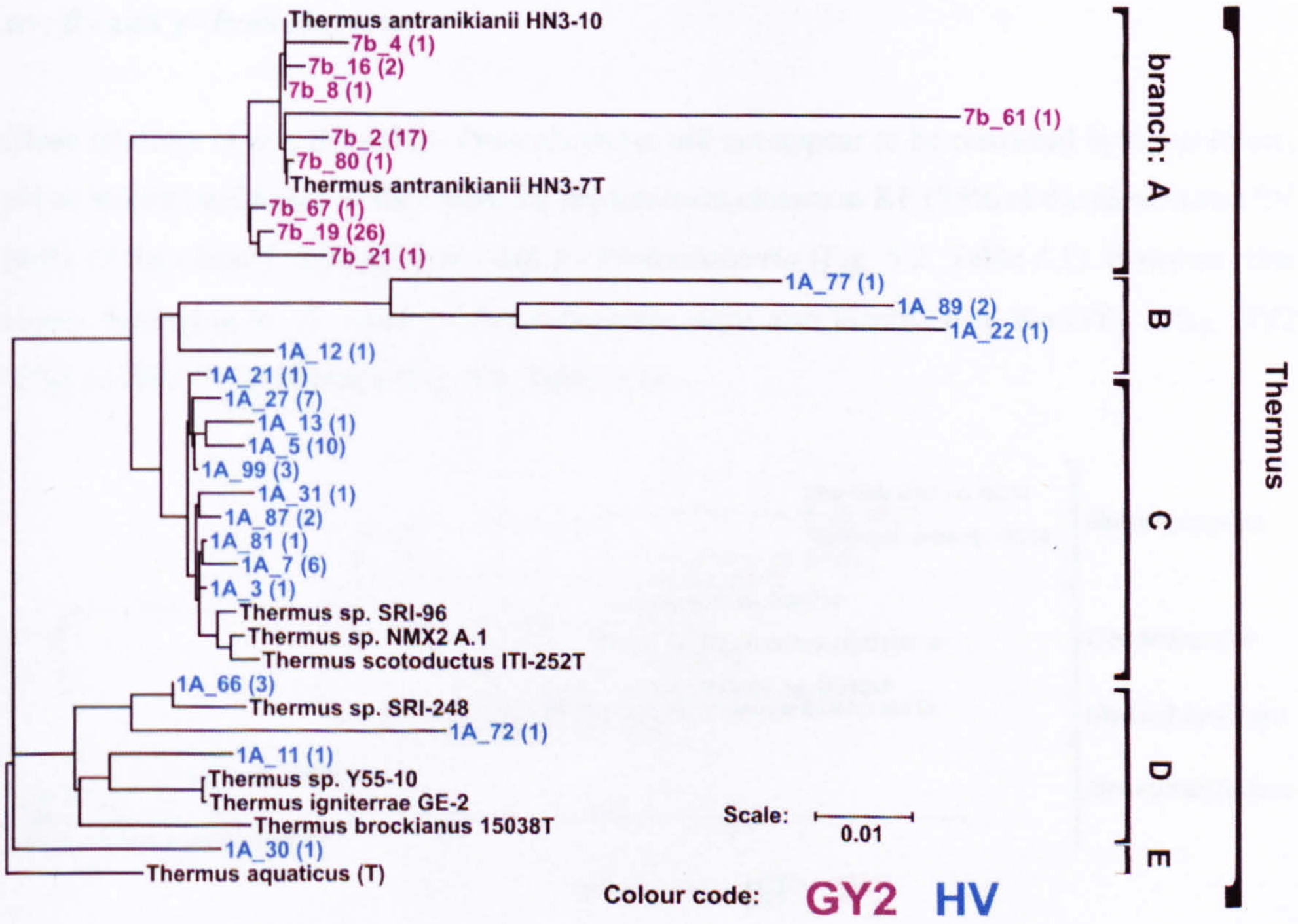

Figure 5.5: Evolutionary distance dendogramm of *Deinococci* 16S rDNA gene sequences detected in this study in the context of currently recognized bacterial divisions in the RDP-II. *Thermus aquaticus* was used as an outgroup. Sequences designated SRI are from a high sulphide mat in Iceland, strains *T. igniterrae* GE-2, *T. brockianus* 15038T, *T. scotoductus* ITI-252T, *T. antranikianii* HN3-7T and HN3-10 were isolated from hot springs in eastern and southeastern Iceland and Y55-10 from the Great Artesian Basin of Australia. Origin of NMX2 A.1 is not known. The scale bar is in nucleotide substitution per sequence position.

In contrast, *Thermus* clones found at HV were far more diverse and affiliated with 4 different lineages within the *Thermus* genus (branch B to E in Fig. 5.5). Most HV clones belonged to the C branch and were closely related to the Icelandic strain SRI-96 (identified in a high sulphide mat, Skirnisdottir et al., 2000) and to *T. scotoductus* (detected in Iceland hot springs by Chung et al., 2000). Most clones belonging to branch D (Fig. 5.5) were very similar (>97%) to SRI-248 (same origin as SRI-96), while one clone (1A_11) was more closely related to *T. igniterrae* and *T. brockianus* (isolated from Icelandic hot springs; Chung et al., 2000). The three clones constituting branch B (Fig. 5.5) and strain 1A_30 (i.e., branch E) may represent novel lineages within the genus *Thermus* as indicated by the absence of any close relatives.

α-, *β*- and *γ*- *Proteobacteria*

Close relatives of *α*-, *β*- and *γ*- *Proteobacteria* did not appear to be restricted by temperature, pH or salinity and together they were the predominant classes at KF (55% of the clones) and SV (86% of the clones), especially *α*- and *γ*- *Proteobacteria* (Fig. 5.2, Table 5.1). However, few clones belonging to *β* - and *γ*- *Proteobacteria* were also identified in the GY1 (2%), GY2 (1%) and HV (9 %) libraries (Fig. 5.2, Table 5.1).

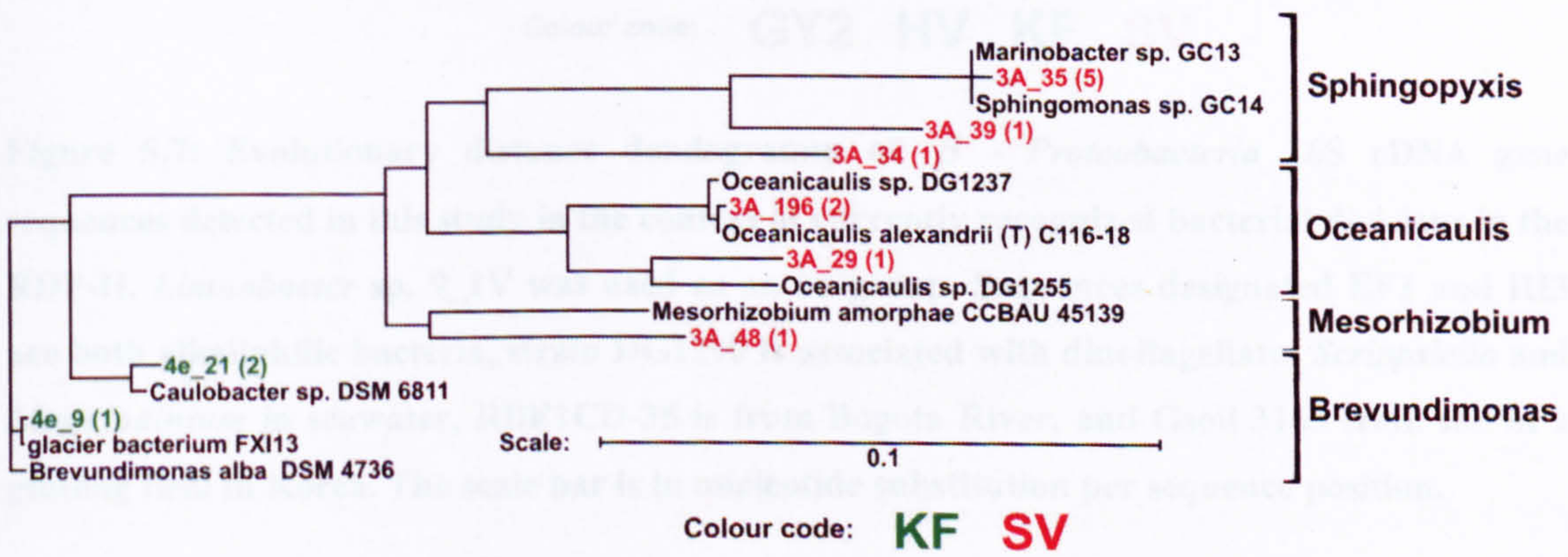

Figure 5.6: Evolutionary distance dendogramm of *α*- *Proteobacteria* 16S rDNA gene sequences detected in this study in the context of currently recognized bacterial divisions in the RDP-II. *Brevundimonas alba* was used as an outgroup. Sequences designated GC are from rhizosphere soil of salt marshes in Korea, DG1237 and DG1255 is associated with dinoflagellates *Scrippsiella* and *Lingulodinium* in seawater, DSM 6811 is from filtered seawater, DSM 4736 and CCBAU45139 from soils, and FXI13 is from sub-glacial sediments and ice from glaciers in New Zealand. The scale bar is in nucleotide substitution per sequence position.

The bacterial sequences affiliated to *α* - *Proteobacteria* (i.e., clones from KF and SV) represented four distinct lineages (Fig. 5.6). Clones identified at KF branched within *Brevundimonas* and were most closely related to isolates from both freshwater (*Brevundimonas alba*, glacier bacterium) and saline environments (*Caulobacter*, Fig. 5.6). In contrast, SV clones were more diverse and belonged to the genus *Sphingpyxis*, *Oceanicaulis* and *Mesorhizobium*. Closest relatives included a variety of species commonly found in seawater and salt marshes (e.g., *Oceanicaulis alexandrii* (T) C116-18, *Sphingomonas* sp. GC14) and soils (*Mesorhizobium amorphae* CCBAU 45139; Fig. 5.6).

Close relatives of the *β* - *Proteobacteria* were found at GY2, HV, KF and SV (Fig. 5.7) and affiliated to the genus *Variovorax* (HV clones), *Ralstonia* (GY2 and KF clones) and

Limnobacter (SV clones, Fig. 5.7). Similar to above, the closest relatives were isolates from both freshwater, seawater and soils (Fig. 5.7).

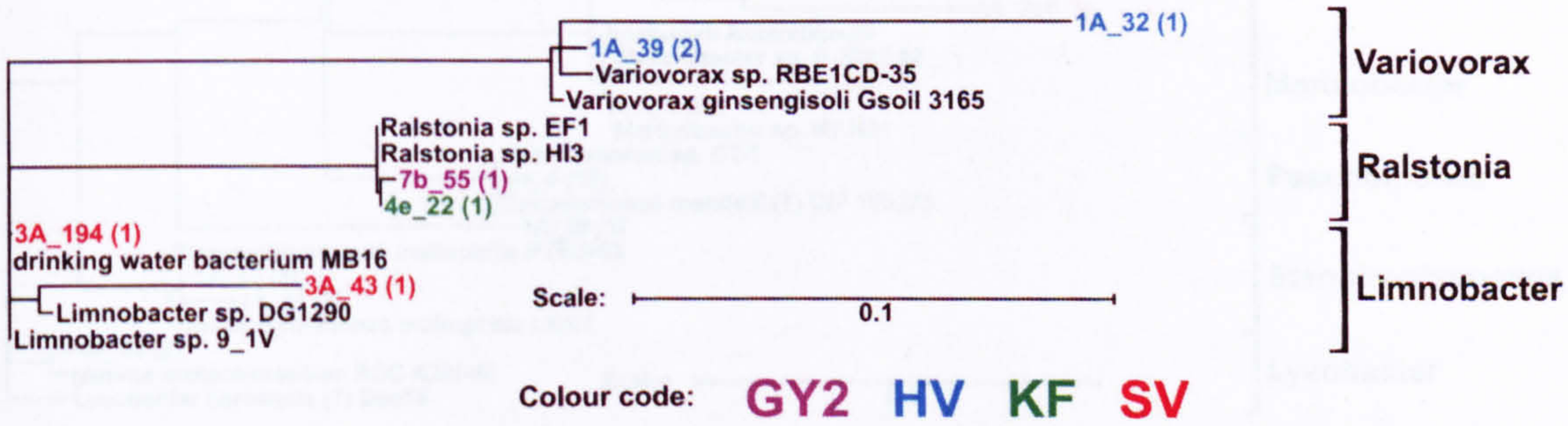

Figure 5.7: Evolutionary distance dendogramm of β - *Proteobacteria* 16S rDNA gene sequences detected in this study in the context of currently recognized bacterial divisions in the RDP-II. *Limnobacter* sp. 9_1V was used as an outgroup. Sequences designated EF1 and HI3 are both alkaliphilic bacteria, strain DG1290 is associated with dinoflagellates *Scrippsiella* and *Lingulodinium* in seawater, RBE1CD-35 is from Bogota River, and Gsoil 3165 from soil of a ginseng field in Korea. The scale bar is in nucleotide substitution per sequence position.

The γ - *Proteobacteria* clones were numerically well-presented in the KF and SV libraries but were also found at GY1 and HV (Fig. 5.8, Table 5.1). Clones that branched in the genus *Marinobacter* (i.e., genus of *Proteobacteria* found in sea water) were solely observed at SV (Fig. 5.8) which was not unexpected due to the high salinity of the SV geothermal waters and the proximity to the coast. In contrast, KF clones were most dominant in the genus *Pseudomonas* but also related to isolates within the genus *Lysobacter* and *Acinetobacter* (Fig. 5.8). The only GY1 clone that affiliated with γ – *Proteobacteria* related to *Acinetobacter*, while HV clones belonged primarily to the genus *Stenotrophomonas*. One clone from HV (1A_20) branched well outside the established *Stenotrophomonas* and may thus represent a new phylotype within the γ - *Proteobacteria* (Fig. 5.8). Note that representatives of the genus *Lysobacter* and *Marinobacter* are common inhabitants of soils and waters. Similarly, *Pseudomonas*, *Stenotrophomonas* and *Acinetobacter* have a widespread occurrence in nature (e.g., water, soil, plants) however, they also include various pathogenic strains.

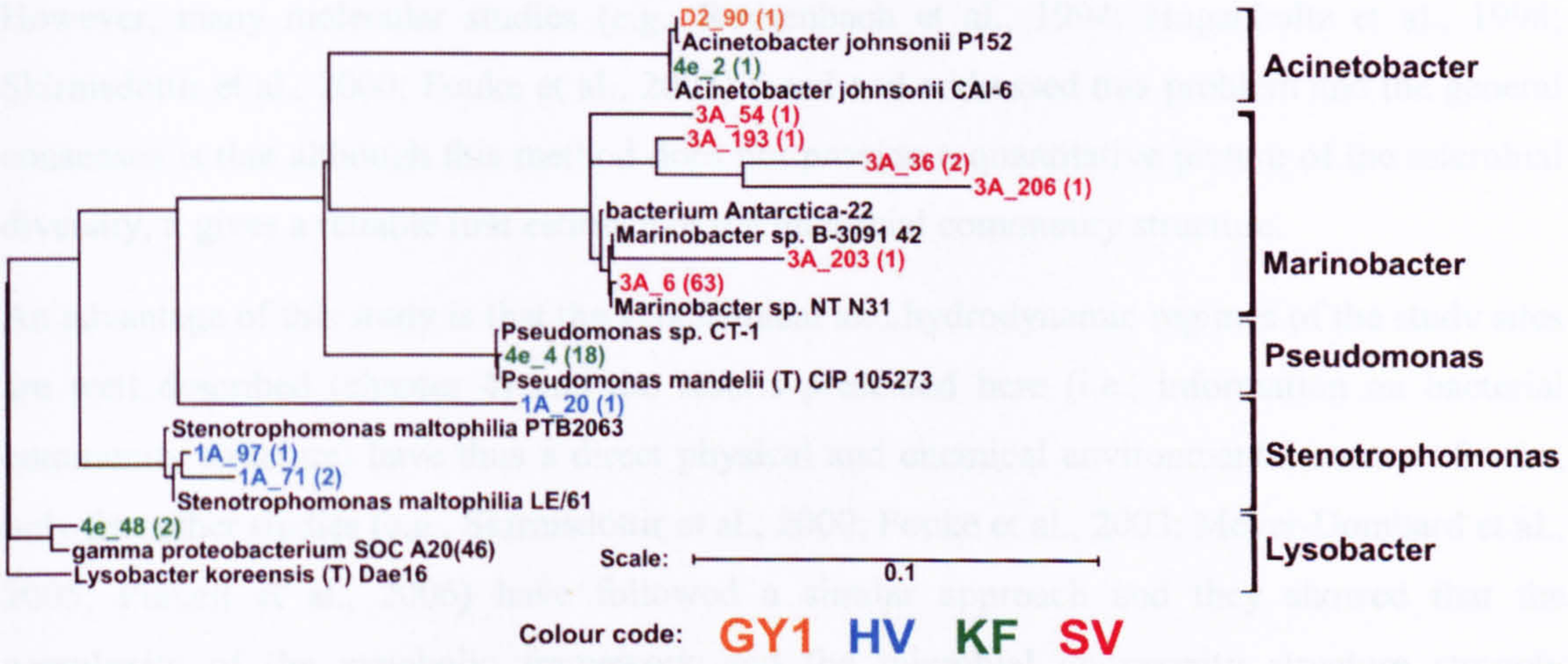

Figure 5.8: Evolutionary distance dendogramm of γ- *Proteobacteria* 16S rDNA gene sequences detected in this study in the context of currently recognized bacterial divisions in the RDP-II. *Lysobacter koreensis* was used as an outgroup. Sequence designated SOC A20(46) is from beneath a high Arctic glacier in Canada, and NT N31 is a euryhaline halophilic strain isolated from deep sea sediments. Depicted sequences belonging to the genus *Stenotrophomonas* (i.e., LE/61, PTB2063), *Pseudomonas* (i.e., CIP 105273, CT-1) and *Acinetobacter* (i.e., CAI-6, P152) are not common representative in natural environments and are thus not further described here. The scale bar is in nucleotide substitution per sequence position.

The remaining five identified bacterial classes included *Flavobacteria*, *Cyanobacteria*, *Sphingobacteria*, *Nitrospira*, and *Actinobacteria* which were mainly found at SV and / or KF (except Nitrospira at HV, Fig. 5.2). Clones belonging to these classes are included in Table 5.2 and 5.3 and more details on their phylogenetic inference are given in Appendix A.1. Similarly, the phylogenetic placement of the unidentified bacterial clones found in the GY2, HV and SV Fig. 5.2) bacterial clone libraries are not discussed here but illustrated in Appendix A.2.

5.5 Discussion

The molecular phylogenetic approach applied in this study is well known and increasingly used to describe microbial diversity in various natural environments, thus by-passing the requirement for cultivation. However, it is worth mentioning that this technique has potential bias (e.g., PCR-bias such as preferential amplification, different susceptibility to cell lysis, analysis of non-indigenous strains; e.g., Sambrook et al. 1989; Ward et al., 1997; Hurst et al., 2002; Fouke et al., 2003) which need to be kept in mind during data interpretation. Also, the microbial diversity of the studied environment are often not fully represented within the constructed clone library (see rarefaction curves above), mainly because this technique is time consuming and expensive.

However, many molecular studies (e.g., Reysenbach et al., 1994; Hugenholtz et al., 1998; Skirnisdottir et al., 2000; Fouke et al., 2003) faced and addressed this problem and the general consensus is that although this method does not provide a quantitative picture of the microbial diversity, it gives a reliable first estimate of the microbial community structure.

An advantage of this study is that the geochemical and hydrodynamic regimes of the study sites are well described (chapter 4) and the results presented here (i.e., information on bacterial community structure) have thus a direct physical and chemical environmental context. So far, only few other studies (e.g., Skirnisdottir et al., 2000; Fouke et al., 2003; Meyer-Dombard et al., 2005; Purcell et al., 2006) have followed a similar approach and they showed that the complexity of the metabolic framework and the microbial community structure strongly correlates with the geochemical and hydrodynamic regime of the studied geothermal waters. However, these studies also demonstrated that due to the high degrees of variability amongst hot springs (in terms of physico-chemical conditions), many more similar studies are needed to obtain a full understanding of the diversity of microbial communities in such environments.

5.5.1 Effects of abiotic variables on bacterial diversity

The bacterial diversity within sediments from six different geothermal waters was studied (Table 5.4). The archaeal diversity was not analysed in this study but PCR amplification using archaeal specific primers showed that archaeal species (i.e., archaeal DNA) were present at GY1, GY2, HV and SV but not at KF.

Table 5.4: Summary of physico-chemical conditions and microbial diversity at each site.

	GY1	GY2	HV	KF	SV	RK
physico-chemical conditions						
T / °C	70 - 96	76 - 82	66 - 74	80	42	75
salinity	low	low	low	low	medium	high
sinter growth rate	low	low	low	medium	medium	high
pH	~9	~9	~9	10	7.7	7.5
bacterial diversity						
# phylogenetic classes	3	4	6	6	6	-
# unidentified	-	1	4	-	2	-
# RFLP patterns	15	22	43	17	38	-
archaeal presence	yes	yes	yes	no	yes	no

No bacterial nor archaeal DNA was detected at RK suggesting that the physico-chemical conditions at this site, i.e., high salinity, high T and high sinter growth rates, were too challenging (i.e., too extreme) for the development of thermophilic microbial communities.

Each of the remaining five study sites (i.e., GY1, GY2, HV, KF and SV) was characterised by a distinct bacterial community structure each being dominated by one phylogenetic class which represented between 47 to 97% of the total clone library (Table 5.1): *Aquificae* was most abundant at GY1, *Deinococci* at GY2 and HV and $\gamma-$*Proteobacteria* at KF and SV (Fig. 5.2). Despite the apparent similarities in class distribution and diversity between some sites (e.g., GY2 & HV and between KF & SV), the compositions and relative ratios of the dominant organisms were very different (Table 5.2 and 5.3).

The geochemical parameters that varied most between the five geothermal sites were temperature, pH, salinity and sinter growth rate (Table 5.1 and 5.4) and the observed differences in bacterial diversity between sites can in part be explained by these variations. It is known that the availability and composition of energy sources (e.g., total sulfide concentration, dissolved H_2) and organic substrates is another key factor that can affect the microbial community structure within hot springs (e.g., Spear et al, 2005; Meyer-Dombard et al., 2005 and reference therein). However, these properties were not quantified in this study and their impact on the bacterial diversity observed at the study sites could thus not be assessed.

The effect of temperature

The effect of temperature on microbial diversity and phylogenetic inference is best exemplified by comparing the bacterial clone libraries for GY1, GY2 and HV. All these sites were characterised by pH ~ 9, low salinity and low sinter growth rates. The main difference between these sites was water temperature (Table 5.4). The highest bacterial diversity (i.e., greatest number of RFLP patterns) was found at HV (43) and the smallest at GY1 (15), where the maximum temperature was about 20°C higher than at HV. The water temperature at GY2 (76 - 82°C) lead to 22 different RFLP patterns indicating that the bacterial diversity at GY2 was slightly higher than at GY1 but significantly smaller than at HV. These findings indicated that the observed differences in phylogenetic diversity between GY1, GY2 and HV may be simply due to temperature differences. This confirmed previous observations (see rarefaction curves, Fig. 5.1) which showed that a higher number of phylotypes was found at lower temperatures.

As illustrated in Fig. 5.2 and Table 5.3, temperature appeared to also affect the phylogenetic inference of the bacterial communities at these sites. Despite some common traits in class - level diversity, distinct differences were observed. Close relatives of the *Aquificae* were numerically

well represented at all three sites but were most dominant at GY1 (97% of total analysed clones). Species belonging to *Aquificae* are mainly obligatory chemolithotropic, aerobic bacteria using molecular hydrogen or reduced sulfur compounds as energy donors (Skirnisdottir et al., 2000). Furthermore, *Aquificae* belong to one of the earliest branching orders of the domain *Bacteria*. GY1 and GY2 clones all branched in the genus *Thermocrinis* whereas HV clones affiliated to three different lineages, *Sulfurihydrogenibium*, *Thermocrinis* and a new phylotype not yet classified. This revealed a higher diversity of the *Aquificae* clones at HV but also suggested that species belonging to *Sulfurihydrogenibium* and to the novel phylotype were confined to temperatures ≤ 74°C (i.e., max. temperature at HV). Again, this showed that temperature is a key discriminating factor (assuming that all other parameters were equal).

The dominant bacteria at GY2 and HV belonged to *Thermus*, a genus of *Deinococci*, which was absent at GY1. *Thermus* species are aerobic, heterotrophic thermophiles that are ubiquitous to most hot springs with neutral to alkaline pH (max. pH ~ 9.5) and temperatures up to 85°C (Alfredsson and Kristjansson, 1995). This also explained the absence of these bacteria at GY1 as the frequent temperature fluctuations (from 70 to 96°C in 1 min) at this site were probably too high for their growth.

Note that all three sites were also occupied by the aerobic, heterotrophic *Bacilli* species, while close relatives of β - and γ–*Proteobacteria* as well as representatives of the nitrite-oxidizing *Nitrospira*-Group were mostly restricted to HV.

The effect of pH

The potential effect of pH on bacterial diversity is best analysed by comparing the bacterial clone library at GY2 and KF as the geothermal waters at both sites have similar salinities and temperatures (Table 5.4) and only differ in pH (pH 9 vs. 10 respectively) and sinter growth rate.

The class – level diversity at KF was higher than at GY2 (6 *vs.* 4 phylogenetic classes), but the overall bacterial diversity detected at KF was lower than at GY2 (17 *vs.* 22 RFLP patterns, Table 5.4). This suggested that the higher pH and sinter growth rate might have restricted bacterial diversity at KF. This was further demonstrated by the absence of archaeal DNA at this site. However, it should be noted that the higher sinter growth rate at KF was partly due to the presence of thick biofilms (EPS enhances silica aggregation, section 4.4.2) thus indicating that the higher sinter growth rate was probably not the discriminating factor at this site.

The variations in geochemical conditions between GY2 and KF also resulted in substantial differences in the bacterial community structure. At both sites, close relatives of *Aquificae* and β - *Proteobacteria* were found, however, most other phylotypes identified at KF were

significantly different to GY2 (Table 5.2 and 5.3). The key differences included the absence of *Deinococci*, i.e., *Thermus* species, and the dominance of $\gamma-$ *Proteobacteria* (e.g., *Pseudomonas*) within the KF clone library. The lack of *Thermus* clones was probably a result of the higher pH as these species are know to grow best at pH 7 to 9 (Alfredsson and Kristjansson, 1995) while the abundance of *Pseudomonas* is not necessarily related to the variation in pH. The remaining bacterial phylotypes that were identified at KF belonged to *Flavobacteria*, *Actinobacteria*, α- and β - *Proteobacteria*. It should be noted that most KF clones closely related to species extracted from various natural environments (e.g., freshwater, soils, glaciers, plants, Table 5.3), however their occurrence could not be linked to the geochemical / hydrodynamic regime present at this site. Furthermore, there is no known study that described similar strains in other hot spring environments and a comprehensive evaluation of these clones was thus not possible. These differences might be partly explained by the nature of the KF sample. At KF, DNA was extracted from hard sinter sediments (i.e., older sinters) collected from the bottom of the channel (close to the channel rim which was covered with snow) while at all other sites (e.g., GY2) DNA was obtained from loose sediments. The close relationship of KF clones to species extracted from soils, glaciers, etc. might thus be best explained by "contamination" from the surrounding field (e.g., channel rim sediments, snow, plants, blown in microorganisms, contaminants from animals and humans).

The effect of salinity

SV was characterised by near-neutral pH, high salinity, low temperatures and medium high precipitation rates (Table 5.1). These were substantially different to all other sites (Table 5.4) thus making a comparison difficult. Overall, the bacterial diversity identified at SV (39 RFLP patterns, 42°C) was almost twice as high as at GY1, GY2 and KF (15 – 22 RFLP patterns, 70 - 96°C, Table 5.4) which agreed with the findings that phylogenetic diversity is enhanced at lower T. However, despite the lower temperature, the microbial diversity identified at SV was slightly lower than at HV (43 RFLP patterns, 66 - 74°C). This suggested that other parameters, i.e., high salinity, near-neutral pH and medium high sinter growth rates, may have limited the microbial diversity at this site. The near-neutral pH is unlikely to be a discriminating factor (e.g., Skirnisdottir et al., 2000; Meyer-Dombard et al., 2005; Purcell et al., 2006) and similarly, the sinter growth rate was not expected to play a key role at this site. This assumption was based on observations at KF where sinter growth rates were almost twice as high as at SV and these did not seem to have affected the microbial diversity at KF. As a result, the high salinity was probably the most important parameter that was different at SV. The bacterial community structure at SV confirmed this hypothesis as most detected bacterial clones were related to

species isolated from marine environments, saline soils and coastal hot springs (i.e., close relatives of α -, β - and γ-*Proteobacteria* and *Sphinobacteria*, Table 5.3). This is important because similar halophilic species were not identified at any other study site. The remaining SV clones were related to *Flavobacteria* and *Cyanobacteria*. Identified close relatives of *Flavobacteria* were similar to KF clones while clones belonging to *Cyanobacteria* were only found at SV. This was not unexpected as *Cyanobacteria* preferentially grow at temperatures below 70°C (Madigen et al. 1997) and were thus absent at all other study sites (Table 5.4).

In summary, it has been shown that the presence and absence of bacteria appears to be directly controlled by the geochemical and hydrodynamic regime of the studied geothermal environment, which included parameters such as T, pH, salinity and sinter growth rate. However, despite substantial variations in physico-chemical conditions between sites (Table 5.3), it was not possible to identify a single parameter that had a more profound effect on microbial diversity than all others. Instead, it emerged that the combination of T, pH and salinity may control the biodiversity pattern observed at each site while sinter growth rate is only an important parameter in ecosystems where the rates are as high as 300 kg y^{-1} m^{-2}. This is nicely illustrated with results obtained at RK and KF. No microbial traces were found at RK, a site which is characterized by high temperatures, high salinity and high sinter growth rates, while high microbial diversity was detected at KF, exhibiting similar temperatures but higher pH, lower salinity and medium high sinter growth rates (Table 5.4). In this case, the higher salinity (RK: 4.7% *vs.* KF: 0.1%) and the more then 10 times higher sinter growth rate (RK: 304 *vs.* KF: 20 kg y-1 m^{-2}) at RK resulted in a far more extreme environment than at KF, i.e., prevented microbial colonization of the growing sinters.

5.5.2 Comparison to bacterial communities identified in other Icelandic hot springs

While a few studies on microbial ecology have been carried out at Svartsengi and Geysir (e.g., Petursdottir and Kristjansson, 1996, Chung et al., 2000), none have been done at Krafla and Reykjanes. Several investigations have analysed the archaeal and bacterial diversity of microbial mats from the Hengill area (i.e., includes Hveragerdi and other surrounding geothermal fields like Grensdalur). For example, Skirnisdottir et al. (2000) analysed the bacterial diversity of a sulphur mat hot spring (T = 67°C, pH 6.7) from the riverbank in Grensdalur and found almost exclusively *Aquificae* (sequences designated SRI in Fig. 5.3) and low percentages of clones that affiliated with *Deinococci*, *Nitrospira* and *Thermotogales*. These observations agree well with the results at HV, GY1 and GY2 although in this study *Deinococci* clones were numerically better represented than *Aquificae* (except at GY1 where *Deinococci* were absent, Fig. 5.2). In addition, clones related to *Nitrospira* were also found at HV however,

close relatives of the *Thermotogales* were absent at all three sites (Fig. 5.2). It should be noted that compared to the sulphur mat hot spring (T = 67°C, pH 6.7), both temperature and pH were higher at the two Geysir sites (T = 70 - 96°C, pH ~9), whereas HV featured very similar temperatures but also a higher pH (T = 66 - 74°C, pH~9). Another difference between the results of Skirnisdottir et al. (2000) and the HV findings (from this study) was that the DNA from the sulphur mat hot spring was extracted from microbial mats and the DNA analysed here (i.e., GY1, GY2 and HV) was extracted from loose sediments. The variations in community structures between these sites are thus best explained by the difference in T - pH regime and the origin of the samples, although even small geographical variations should be considered (Hjorleifsdottir et al., 2001).

From comparison to other molecular studies on microbial communities, Skirnisdottir et al. (2000) concluded that the composition of the *Aquificae* clones is influenced not only by temperature but also by varying sulphide concentration. They showed that close relatives of the genus *Thermocrinis* are more dominant in high -T (84 – 88°C) and low sulphide springs (0.2 – 1.7 ppm) while *Sulfurihydrogenibium* affiliated clones are abundant in low - T (52 – 72°C) and high sulphide (3 - 12 ppm) springs. Note that sulphide concentrations were not evaluated in the present study. However, the presence of elemental sulphur in *in-situ* grown sinters at HV (section 4.3.2) suggested higher dissolved sulphide values at HV (low – T) than at GY1 and GY2 (high – T, where no sulphur minerals were observed). In this study, all *Aquificae*-related clones at GY were close relatives of the genus *Thermocrinis* while HV clones related to both genus *Sulfurihydrogenibium* and *Thermocrinis* thus agreeing with the interpretations of Skirnisdottir et al. (2000).

The microbial community structure of filamentous mats in the Hengill area was also characterised by Hjorleifsdottir et al. (2001), who selected a hot spring in Olkelduhals which had a temperature of 85 to 88°C, pH 6.9 and abundant filamentous mats. They found that all detected bacterial phylotypes belonged to *Aquificae* and *Deinococci*. The most dominant phylotype was closest related (99%) to the Icelandic *Aquificales* clone sequences SRI-48 (Skirnisdottir et al., 2000) and pIce1 (Takacs et al., 2001) and also clustered with EM17, the most dominant clone sequence detected in filamentous mats from Octopus spring, Yellowstone National Park (Fig. 5.3). Note that EM17 was later isolated from Octopus spring and described as *Thermocrinis ruber* (Huber et al. 1998). These findings fit well with observations made at GY1 and GY2 (Fig. 5.3) which featured very similar temperatures (T= 70 - 96°C) to the Olkelduhals hot spring. The two *Thermus* phylotypes described by Hjorleifsdottir et al. (2001) were identical to *Thermus scotoductus* NMX2.A.1 and to *Thermus* str. SRI-248 respectively. Similarly, about 73% of the *Thermus* clones identified at HV (in this study) affiliated with *T. scotoductus* (Fig. 5.5, C branch) but significantly less (~9%) to strain SRI-248 (Fig. 5.5, D

branch). Most of the remaining HV clones that belonged to the genus *Thermus* suggested new phylotypes (Fig. 5.5, E and B branch).

Thermus clones identified at GY2 branched well outside the *Thermus* clades represented by the HV clones and closely related to *T. antranikianii* which was isolated from hot springs in eastern and south-eastern Iceland by Chung et al. (2000). In addition to *T. antranikianii*, Chung et al. (2000) isolated one other *Thermus* species, *T. igniterrae* and also detected two new species of *T. brockianus* and *T. scotoductus* respectively, which were all closely related to the HV clones in the present study (Fig. 5.5).

Findings from this study and observations from other molecular studies from Iceland, Yellowstone NP, USA and New Zealand (e.g., Brock and Freeze, 1969; Kristjansson and Alfredsson, 1983; Hudson et al., 1987; Kristjansson et al., 1994; Reysenbach et al., 1994; Williams et al. 1995; Hugenholtz et al., 1998; Skirnisdottir et al., 2000; Reysenback et al., 2000; Chung et al., 2000; Hjorleifsdottir et al., 2001; Eder and Huber, 2002; Blank et al., 2002; Spear et al., 2005) thus indicate that *Thermus* spp. and *Thermocrinis* spp. are abundant in many hot springs with temperatures between 75-92°C and ~pH 8-9. *Thermus* species including *T. scotoductus*, SRI-248 and *T. antranikianii* are particularly common in Icelandic hot springs (e.g., Chung et al., 2000; Skirnisdottir et al., 2000; Hjorleifsdottir et al., 2001 and this study) while *T. aquaticus* was so far only found in Obsidian Pool, YNP (e.g., Brock and Freeze, 1969; Hugenholtz et al., 1998) and *T. filiformis* seems (so far) strictly confined to New Zealand (e.g., Hudson et al., 1987; Williams et al. 1995). In contrast, *Thermocrinis* species are common to many terrestrial hot springs in Iceland (e.g., Chung et al., 2000; Skirnisdottir et al., 2000; Hjorleifsdottir et al., 2001 and this study) and Yellowstone NP, US (e.g., Reysenbach et al., 1994; Blank et al., 2002; Eder and Huber, 2002; Reysenbach et al., 2005; Spear et al., 2005).

Several other studies analysed the microbial communities in Icelandic hot springs including sites at Hveragerdi, Geysir and Svartsengi (e.g., Kristjansson and Alfredsson, 1983; Hollocher and Kristjansson, 1992; Petursdottir and Kristjansson, 1996; Sonne-Hanson and Ahring, 1997; Chung et al., 1997). However, these mostly employed culture-based techniques and the detected diversity in these studies was thus far lower (most microorganisms identified by genetic techniques can currently not be cultured). It should be noted however, that culture-based studies provide essential information on the metabolism and function of the isolated species within the microbial communities which in molecular-based studies can only be inferred from the phylogenetic inference. Therefore, to obtain a comprehensive assessment of the microbial diversity within natural environments, a combination of culture- and molecular-based techniques is probably necessary (Chandler et al., 2000).

5.6 Conclusions

The microbial community was investigated in water-saturated sediments from six different Icelandic geothermal sites and analysed in terms of variations in geochemical and hydrodynamic conditions.

Five 16S rDNA bacterial clone libraries were derived for the two Geysir sites (GY1 and GY2), Hveragerdi (HV), Krafla (KF) and Svartsengi (SV) while no microbial DNA was detected at Reykjanes (RK):

(1) *Aquificae* (mostly related to Thermocrinis) was ubiquitous at GY1 (site with the highest temperature) but also occurred at all other high-T sites, i.e., GY2, HV and KF.

(2) *Deinococci* (*Thermus* species) dominated the GY2 and HV bacterial clone libraries but were not observed at any other site.

(3) $\gamma-$*Proteobacteria* was most abundant at KF (mostly freshwater and soil genera) and SV (primarily marine genera) but few clones were also found at GY1 and HV.

The high site-specific distribution of bacterial 16S rDNA gene sequences observed in this study is argued to be strongly related to changes in T, pH, salinity and sinter growth rate. Even relatively minor differences in T (±10°C) correlated with the immense differences in bacterial community structure. Overall, observations indicate that the phylogenetic diversity (i.e., number and composition of detected phylotypes) decreased with increasing T, more alkaline pH, increasing salinity, and higher sinter growth rates. However, it was not possible to single out one parameter that affected the microbial community structure more than the others. This led to the conclusion that the biodiversity patterns determined at each site were controlled by a combination of these parameters. In this study, the most extreme habitat seemed to be defined by high temperatures (≥ 75°C), high salinity (≥ 4.7%) and high sinter growth rates (≥ 300 kg y^{-1} m^{-2}) and neither bacteria nor archaea were found (i.e., RK). Higher diversity was detected at all other less extreme conditions. These results further indicated that the physico-chemical conditions defining the precipitation of amorphous silica (i.e., sinter growth rates, chapter 4) may also be the dominant controls on microbial ecology and distribution. Similarly, Fouke et al. (2003) showed that the composition of bacterial communities is distinctively partitioned between travertine depositional facies (that are characterised by specific water chemistry, travertine chemistry and travertine morphology) in the surface drainage system of Spring AT-1 at Angle Terrace, Mammoth Hot Springs, Yellowstone National Park.

The comparison to other molecular studies on bacterial diversity in hot springs showed that the dominant phylotypes fall mainly into the same phylogenetic classes (i.e., *Aquificae*, *Deinococci*,

γ−Proteobacteria). Furthermore, some phylotypes (e.g., *Thermus* spp, *Thermocrinis* ssp,) were found in a variety of hot springs indicating that they can adapt to different geochemical / hydrodynamic regimes. However, these studies also demonstrate that the parameters controlling the diversity of these phylotypes are still not well understood and future studies should thus focus more on the correlation of community diversity and geochemical variation in hot springs.

6 QUANTIFICATION OF INITIAL STEPS OF NULCEATION AND GROWTH OF SILICA NANOPARTICLES: AN IN-SITU SAXS AND DLS STUDY

6.1 Abstract

Here we present results from an *in-situ* time-resolved study providing quantitative information on the initial steps of silica polymerisation and silica nanoparticle formation. The experiments were carried out in near neutral pH (7 – 8) solutions with initial silica concentrations of 640 and 1600 ppm SiO_2 and ionic strengths (IS) of 0.02, 0.05, 0.11 and 0.22 M. The polymerisation reactions were induced by neutralising a high pH silica solution (from pH 12 to 7) and monitored by the time dependent depletion in monosilicic acid over time. The accompanied nucleation and growth of silica nanoparticles (i.e., change in particle size over time) was followed *in-situ* and time-resolved using synchrotron-based Small Angle X-ray Scattering (SAXS) and conventional Dynamic Light Scattering (DLS) combined with scanning and (cryo-) transmission electron microscopy (SEM / cryo-TEM).

The critical nucleus diameter was quantified (1.4 – 2 nm) and results from SAXS and DLS showed that over 3 hours the particle diameter increased to a final size of ~ 8 nm. SEM and TEM photomicrographs verified SAXS and DLS data and confirmed the spherical and hydrous structure of the forming silica nanoparticles. Furthermore, fractal analysis (i.e., fractal dimension, D_m ~2.2) indicated that the formed particles consisted of open, polymeric, low-density structures.

A kinetic model for the nucleation and growth of silica nanoparticles was derived suggesting a 3 stage growth process: (1) homogeneous and instantaneous nucleation of silica nanoparticles, (2) 3-dimensional, surface-controlled particle growth following 1st order reaction kinetics and (3) Ostwald ripening and particle aggregation.

6.2 Introduction

Silica polymerisation and the subsequent formation of silica nanoparticles occur in many modern terrestrial environments (e.g., hot springs, brines, deep reservoirs) but they have also played an important role in ancient geological settings (e.g., most Archean fossils were preserved in silica cherts; e.g., Barghoorn and Tyler, 1965; Knoll, 1985; Carson, 1991; Monty et al., 1991; Westall and Walsh, 2000). Furthermore, these processes are believed to have been

crucial to the formation of silica-rich deposits recently observed on Mars (Squyres et al., 2007, 2008; Ruf et al., 2007).

The processes and mechanisms controlling silica precipitation are essential to the understanding of natural processes such as sinter formation (e.g., Guidry and Chafetz, 2002; Mountain et al., 2003), biosilicification (e.g., Jones et al., 1996, 2001; Konhauser et al., 2003, 2004), silica diagenesis (e.g., Rimstidt and Barnes, 1980; Williams and Crerar, 1985; Williams et al., 1985; Hinman, 1990), formation of diatoms (e.g., Kröger et al., 2001; Perry and Keeling-Tucker, 2000 and references therein) and silica scaling in geothermal power developments (e.g., Gunnarsson and Arnorsson, 2003). The formation of silica nanoparticles is also important in industrial processes and applications (e.g., computer, biotechnology, catalysis and chromatography) where the specific structural properties of silica nanoparticles (e.g., swelling capacity, strength, durability, thermal stability) make them highly desirable nanomaterials. As a result, the synthesis of highly monodisperse, spherical silica particles through techniques such as the Stöber method (the base catalysed hydrolysis and condensation of silicon alkoxides in low-molecular-weight alcohols; Stöber, 1968) are well established. The mechanisms and kinetics underlying these processes have been the subject of extensive laboratory investigations. Multiple techniques such as Small Angle X-Ray Scattering (SAXS), Dynamic and Static Light Scattering (DLS, SLS), ^{29}Si NMR, Raman spectroscopy and Transmission Electron Microscopy (e.g., Matsoukas and Gulari, 1988; Bogush et al., 1988; van Blaaderen et al., 1992; Bailey and Mecartney, 1992; Boukari et al., 1997, 2000; Pontoni et al., 2002; Green et al., 2003a,b) have been applied to derive models that describe the formation of alkoxide based silica particles and their growth under a variety of reactants and catalysts concentrations. Despite the plethora of research for industrial applications, the Stöber method is not representative of silica nanoparticle formation in natural environments and the derived models are not transferable.

In natural systems, the mechanisms of silica polymerisation and silica nanoparticle formation have also been widely investigated (e.g., Alexander, 1954; Goto, 1956; Baumann, 1959; Kitahara, 1960; Iler, 1979; Crerar et al., 1981; Rothbaum and Rhode, 1979; Weres et al., 1981; Carroll et al., 1998; Icopini et al., 2005, Conrad et al., 2007; Table 6.1). Overall, it is accepted that silica polymerisation and silica nanoparticle formation follows a 3-stage process where (1) silica polymerization and nucleation of silica nanospheres is followed by (2) particle growth and / or ripening and (3) particle aggregation. In the first stage, silica monomers polymerise via dimers, trimers etc. to cyclic oligomers which then form three-dimensional internally condensed nanospherical particles. During the second stage the particles grow by further accretion of silica oligomers and / or by Ostwald ripening. However, in most natural cases colloidal silica particles are not stable within the polymerising solution and they tend to aggregate (stage 3) before

completion of the ripening process (e.g., Iler, 1979; Perry, 2003; Benning et al., 2005; Icopini et al., 2005).

In the last few decades a range of reaction kinetic models have been derived from the measurements of the time dependent decrease in monosilicic acid concentration with reaction orders ranging between 1 and 5 (Table 6.1). A more detailed discussion of these studies is given in section 2.1.4.

Table 6.1: Summary of reported experimentally derived kinetic models for the decrease in monosilicic acid during the process of silica polymerisation.

Study	pH	T (°C)	SiO_2 (ppm)	max. reaction time (h)	[1]Reaction order, n
Alexander (1954)	1 - 6	1.9	6000	170	3 for pH<3.2 2 for pH>3.2
Goto (1956), Okamoto et al. (1957)	7-10	22.3	200 - 900	144	3
Baumann (1959)	0.5 - 9	30	400 - 4000	7	1 to 5
Kitahara (1960)	3 - 10	0 - 100	500 - 800	5	2 for pH<7.5 3 for pH>7.5
Bishop and Bear (1972)	8.5	25 - 45	300	200	2
Rothbaum and Wilson (1977)	7.8 - 8.7	50 - 120	500 - 1000	1000	5 to 8
Rothbaum and Rhode (1979)	7-8	5 - 180	300 - 1300	1200	4
Markrides et al. (1977, 1980)	4.5 - 6.5	75 - 105	700 - 1200	22	[3]0
[2]Peck and Axtmann (1979)	4.5 - 8.5	25 - 95	400 - 1000	-	1
[4,5]Weres et al. (1981)	2.5 - 8	50 - 100	500 - 1200	1.5	1 for $S>S_t$ 5 for $S<S_t$
Crerar et al. (1981)	7	25	1000	22	1
Icopini et al. (2005), Conrad et al. (2007)	3 - 11	25	250 - 1250	3000	4

[1]Reported rate laws were derived via the equation $-dC / dt \sim k(C-C_e)^n$ following the method described by Goto (1956).
[2]Peck and Axtmann (1979) analysed experiments reported by Makrides et al. (1980) and Rothbaum and Wilson (1977).
[3]Makrides (1977, 1980) postulated that particle growth preceeding the induction and nucleation phase was linear with time.
[4]Weres et al. (1981) used the same model as proposed by Makrides et al. (1977, 1980) and Peck and Axtmann (1979).
[5]Weres et al. (1981) proposed a 5th order rate law up to a certain silica concentration, S_t (unknown), and a 1st order rate > S_t.

The parameters that influence the mechanisms and kinetics of silica polymerisation and silica precipitation include temperature, pH, ionic strength and silica concentration (i.e., degree of silica saturation; e.g., White et al., 1956; Baumann, 1959; Iler, 1979; Rothbaum and Rhode, 1979; Marshall and Warakomski, 1980; Weres et al., 1981; Marshall and Chen, 1982; Gunnarsson and Arnórsson, 2003; Icopini et al., 2005, Conrad et al., 2007). An induction period can precede the polymerisation reaction during which little or no silica polymerisation takes place. The length of this induction period is controlled by the same factors that determine silica polymerisation (i.e., T, pH, IS and silica concentration) and it decreases with increasing degree of supersaturation (e.g., White et al., 1956; Iler, 1979; Rothbaum and Rhode, 1979; Gunnarsson and Arnórsson, 2003; Icopini et al., 2005; Conrad et al., 2007).

So far few attempts were made to image and quantify the size of the nanoparticles forming within the polymerising solution. Rothbaum and Rhode (1979) determined the relative size of silica nanoparticles at different temperatures using chromatography, viscosity measurements and light scattering and concluded that with increasing temperature (5 to 180°C), the average molecular weight of the polymers formed increased from approximately 10^5 to 10^9 (in Daltons). Makrides et al. (1980) used light scattering to follow the polymerisation process and proposed a size of the primary nuclei in the order of a few angstroms which towards the end of the reaction reached several nm in size. More recently, Icopini et al. (2005) and Conrad et al. (2007) used Atomic Force Microscopy (AFM) to image the nanoparticulate silica fraction grown for 12h and suggested that the primary particles were about 3nm in diameter. These data supported previous results by Iler (1979) who postulated that at pH 2 to 7 the silica particles are unlikely to grow larger than 2 - 3nm.

However, none of these studies provide any direct evidence for the mechanisms and kinetics of silica polymerisation and little to no quantitative or time-resolved data on the size of the nanoparticles forming within the polymerising solution. In addition, despite the wide-ranging research efforts to elucidate the reaction mechanisms and rates of silica polymerisation (Table 6.1), a molecular level mechanistic understanding of the nucleation and growth of primary silica particles in natural aqueous solution is still lacking.

Here we present the first direct quantification of the initial steps of silica polymerisation and silica nanoparticle formation in inorganic solutions that mimicked natural waters. The reaction progress (i.e., nucleation and growth of silica nanoparticles) was followed *in-situ* and in real-time using synchrotron-based Small Angle X-ray Scattering (SAXS) and conventional Dynamic Light Scattering (DLS) combined with electron microscopic techniques (Scanning and Transmission Electron Microscopy, SEM / TEM). A series of experiments were carried out at a range of silica concentrations and ionic strengths and a kinetic model was developed for the

growth of silica nanoparticles divided into 3 stages: (1) nucleation of critical nuclei, (2) particle growth and (3) particle coarsening and aggregation.

6.3 Methodology

6.3.1 Silica nanoparticle synthesis

The nucleation and growth of silica nanoparticles was followed in aqueous solutions with initial silica concentrations (SiO_2) of 640 and 1600ppm and ionic strengths (IS) of 0.02, 0.05, 0.11 and 0.22 (i.e., concentrations most often found in geothermal systems; e.g., Arnórsson et al., 1983). High pH stock solutions (~pH 12) of aqueous SiO_2 at the desired ionic strength were prepared by dissolving specific amounts of $Na_2SiO_2{\cdot}5H_2O$ and NaCl in deionised water. Silica polymerisation and silica nanoparticle formation was induced by adjusting the high pH solution to 7 with 1M HCl. Data acquisition started immediately after the pH stabilized at 7 (usually within 5 minutes) and all reactions were carried out at 30 ± 2° C. The length of each experiment varied between 1 and 3 hours. The pH of the reacting solution was automatically recorded (at 5 min time intervals) via a pH meter (Orion 710 with a gel electrode) interfaced with a computer. In all experiments, the pH increased by 0.5 to 0.8 pH units.

Concomitant with the polymerisation process, the decrease of monosilicic acid was analysed over a time period of 3 hours. A few millilitres of the reacting solution were removed after specific time steps and each aliquot was analysed for monomeric and total silica using the spectrophotometric molybdate yellow method (Greenberg et al., 1985).

6.3.2 Small Angle X-ray Scattering (SAXS) procedure

All SAXS measurements were carried out on the Dutch-Belgian beamline (DUBBLE) BM26 at the European Synchrotron Radiation Facility (ESRF), Grenoble, France. Here, we only detail the parameters that affected the data collection in this study and the full DUBBLE configuration can be found in Borsboom et al. (1998). A wavelength of 1 Å and a sample-to-detector distance of 3.5m were used. Data were collected with a 2-dimensional multiwire proportional detector (gas-filled and equiped with a CCD-camera - Photonic Science Xios-II) and a pair of ion chambers (positioned pre- and post-sample) that monitored the incoming and transmitted beam intensities, respectively. The q-axis was calibrated with the scattering pattern of wet rat-tail collagen.

SAXS experiments were carried out in flow-through mode to ensure that the solutions were well mixed at all times (Fig. 6.1A). The initial high pH (~pH 12) silica solutions were prepared in a plastic beaker that was connected to both ends of a quartz capillary SAXS cell (1.5 mm OD and 10 mm walls) via Teflon tubing. The solution in the beaker was continuously stirred and just prior to commencement of the SAXS data acquisition the pH of the initial solution was adjusted to 7 (max. 5 min). The pH adjusted solutions were circulated via a peristaltic pump from the beaker through the quartz capillary of the SAXS cell and back into the beaker (Fig. 6.1A).

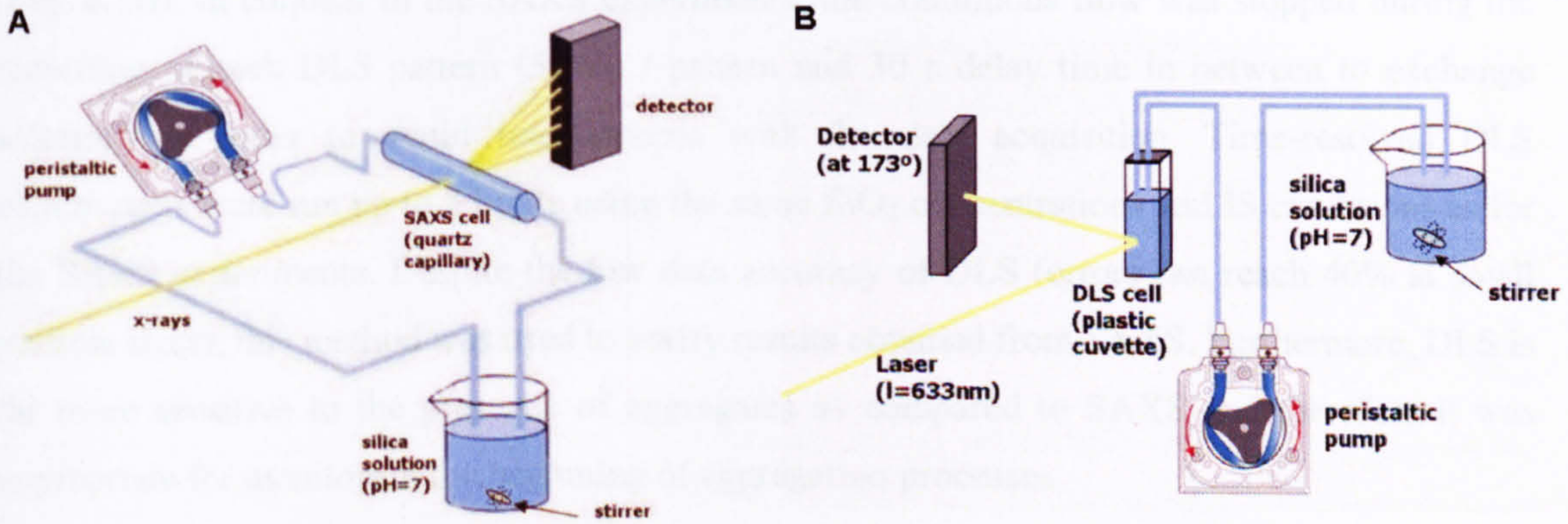

Figure 6.1: Low temperature flow through set-up of (A) SAXS and (B) DLS experiments.

Time-resolved SAXS spectra from the polymerising silica solution were collected every 5 minutes over time periods between 1 and 3 hours. Data-reduction (i.e., correction for detector alinearities, decaying ion beam - using the post-sample ion chamber values, and background scattering) as well as sector integration to convert the 2D to 1D SAXS patterns were carried out using XOTOKO and BSL (SRS software packages, Daresbury) respectively. The reduced data were analysed using GNOM, an indirect transform program for SAXS data processing (Svergun, 1992). In the case of a dilute, monodisperse system GNOM evaluates a pair distribution function (PDF) and provides an estimate for the radius of gyration, *R*g. For spherical particles, the PDF should be Gaussian-shaped (Svergun and Koch, 2003) and *R*g is given by the maximum. GNOM also calculates I_0 which is the intensity at q=0 (i.e., a direct measure of the electron density contrast and the total scattering volume; Glatter and Kratky, 1982) and an error of the fit (<0.1 Å for *R*g).

6.3.3 Dynamic Light Scattering (DLS)

All DLS measurements were done with a Zetasizer Nano ZS (Malvern Instruments) equipped with a He-Ne laser (λ=633nm) and a backscatter detector at a fixed angle of 173°. The

instrument recorded the intensity autocorrelation function, which was transformed into volume functions to obtain size information. All DLS results presented below are shown as volume distributions.

DLS experiments were carried out using a flow through system (Fig. 6.1B) similar to the one described above for the SAXS experiments. Teflon tubing was connected to a disposable plastic cuvette (stationary in the DLS instrument) and to a plastic beaker from which the constantly stirred and pH adjusted solutions were pumped through the cuvette using a peristaltic pump (Fig. 6.1B). In contrast to the SAXS experiments, the continuous flow was stopped during the recording of each DLS pattern (5 min / pattern and 30 s delay time in between to exchange solution) in order to avoid interferences with the data acquisition. Time-resolved DLS experiments were run up to 3 hours using the same SiO_2 concentrations and IS conditions as for the SAXS experiments. Despite the low data accuracy of DLS (errors can reach 40% at small particle sizes), this method was used to verify results obtained from SAXS. Furthermore, DLS is far more sensitive to the presence of aggregates as compared to SAXS and therefore it was appropriate for monitoring the beginning of aggregation processes.

6.3.4 Electron Microscopy

Silica nanoparticles were imaged using field emission gun scanning electron microscopy (FEG-SEM), transmission electron microscopy (TEM) and cryo-TEM. For FEG-SEM, samples were prepared by filtering a few millilitres of the polymerising solution at specific time intervals through 0.1μm polycarbonate filters, which were immediately washed with deionised water to remove the remaining salt and silica solution and left to dry at ambient temperatures. The filter papers were placed on SEM Al-stubs, coated with 3 nm of platinum and analysed with a LEO 1530 FEGSEM using a working distance of 3mm and a beam intensity of 3kV. TEM samples were prepared by depositing a droplet of the reacting solutions on formvar coated copper grids. The grids were air dried and imaged using a Philips CM10 TEM at an accelerating voltage of 80kV.

One sample was also imaged using cryo-TEM combined with an ultra-rapid freezing technique. In order to prepare the cryo-TEM samples, 5 μL of the reacting solution was deposited on a TEM grid which was then flash-frozen in liquid ethane (Egelhaaf et al., 2000) using a standard guillotine plunging device (vitrobot) that instantaneously vitrified the sample and avoided ice formation. The vitrified specimen was transferred at -180°C onto a Gatan 626 cryo-holder and into a FEI T20FEG TEM operated at 200 kV. After an equilibration time of 1 hour (until no apparent drift was observed), the specimen was examined at -180°C and low dose images were recorded on a 4k x 4k Gatan CCD camera.

The size distributions of the silica particles were determined from the recorded images (both SEM and TEM). To obtain a size distribution with reasonably high precision, about 100 - 200 particles were measured in each image and the mean values and standard deviations were calculated.

6.3.5 Kinetic data analysis

For the kinetic analysis of the nucleation and growth of silica nanoparticles, the time-resolved SAXS data were tested against two particle nucleation and growth models: (a) the Thetadash kinetic model (Hounslow et al. unpublished) and (b) the Johnson-Mehl-Avrami-Kolmogorov (JMAK) kinetic model (Kolmogorov, 1937; Avrami 1939, 1940; Johnson and Mehl 1939).

Thetadash kinetic model

Thetadash is a population-dynamics based kinetic model which converts and normalises the experimentally obtained growth profiles (particle radius versus time) according to the degree of the reaction, α (i.e., $0 < \alpha \leq 1$ with $\alpha = 1$ denoting the end of the reaction). In a second step, 3 different types of reaction mechanisms (chemical, surface, or diffusion controlled) and varying reaction orders are fitted to α in order to obtain the best fit in terms of a regression coefficient, R^2. From the best fit, information about the critical nuclei radii, R_0, (by extrapolating to $t = 0$) and the initial growth rate, G_0 (s^{-1}), can be obtained.

For a direct comparison to the JMAK kinetic model (see below), the initial growth rate (G_0) was used to determine the reaction rate constant using the equation $k = G_0 / (S_r - 1)$ (eq. 3.8 in section 3.2.6) where S_R is the saturation ratio which is defined as $S_R = SI^{1/\nu}$ where SI is the saturation index and ν is the stoichiometric coefficient (i.e., the sum of the stoichiometry of the products in the solubility expression). The SI values were calculated using the geochemical code PHREEQC (version 2.13.3; Parkhurst and Appelo, 1999) and the wateq4 database (Ball and Norstrom, 1992) with the amorphous silica data updated using the values from Gunnarsson and Arnórsson (2000).

The JMAK kinetic model

The JMAK model is based on the Avrami equation (Avrami, 1939): $\alpha = 1 - e^{-(k(t-t_o))^n}$ (eq. 3.6 in section 3.2.6) where α is the degree of the reaction, t_0 is the induction time, k is the reaction constant and n is a constant related to the nucleation mechanism (i.e., instantaneous, decreasing

rate, or constant rate), growth dimensionality (i.e., 1, 2, or 3-D) and reaction mechanism (i.e., diffusion- or surface-controlled; Hulbert, 1969). Note that in a surface-controlled mechanism the reactions are limited by the amount of interface available whereas a diffusion-controlled mechanism is limited by the rate of transport of reactants through the matrix to the particle surface.

To obtain α, Rg values (i.e., radius of gyration) from the SAXS data were normalised using the following equation: $\alpha = Rg^3_t / Rg^3_{max}$ (eq. 3.7 in section 3.2.6) where Rg_t is Rg at a given time t, and Rg_{max} is Rg at the end of the reaction. Both k and n can be determined from the intercept and slope, respectively, of a $\ln(-\ln(1-\alpha))$ *vs.* $\ln t$ plot of the experimental data. Note that calculated JMAK rate constants are only conditional rate constants as they imply several processes occurring simultaneously (e.g., dissolution, nucleation, growth; Lasaga, 1998).

6.4 Results

6.4.1 Time evolution of monosilicic acid concentration

The decrease of monosilicic acid, [SiO_2(aq)], was monitored over 3 hours in aqueous solutions with 640 and 1600 ppm SiO_2 and varying ionic strengths, IS (Fig. 6.2). In the experiments with high initial silica concentration (Fig. 6.2, open symbols), about 80% of [SiO_2(aq)] (with respect to silica solubility at 30°C; dotted line in Fig. 6.2) polymerised within the first 5 minutes, whereas only 15% of [SiO_2(aq)] was removed at the lower concentration (640 ppm SiO_2, Fig. 6.2, full symbols). This showed that the initial silica concentration and the degree of silica supersaturation respectively had a major impact on the rate of silica polymerisation, i.e., on the time length to establish steady state (silica solubility at 30°C; Fig. 6.2). In contrast, ionic strength seemed to have had less of an effect on the overall decrease of [SiO_2(aq)] over time (were within errors of each other), nevertheless solutions with higher IS consistently exhibited slightly higher polymerisation rates. In all data sets, a steady state close to the saturation level was obtained after only 3 hours.

Note that after five minutes, for all experiments with high initial SiO_2 concentration (1600 ppm), the monosilicic acid concentration had dropped significantly lower (~25%) than in the experiment at lower concentration (i.e., 640ppm SiO_2, Fig. 6.2). It is only after approximately 60 minutes that similar [SiO_2(aq)] values were established for all studied SiO_2 and IS conditions. The fact that [SiO_2(aq)] values are not identical between the different tested concentrations indicates that the polymerisation reaction cannot be described by a simple

chemical kinetic model, i.e., reaction rate is not solely governed by silica concentration but also affected by other parameters (e.g., surface area of forming particles, pH).

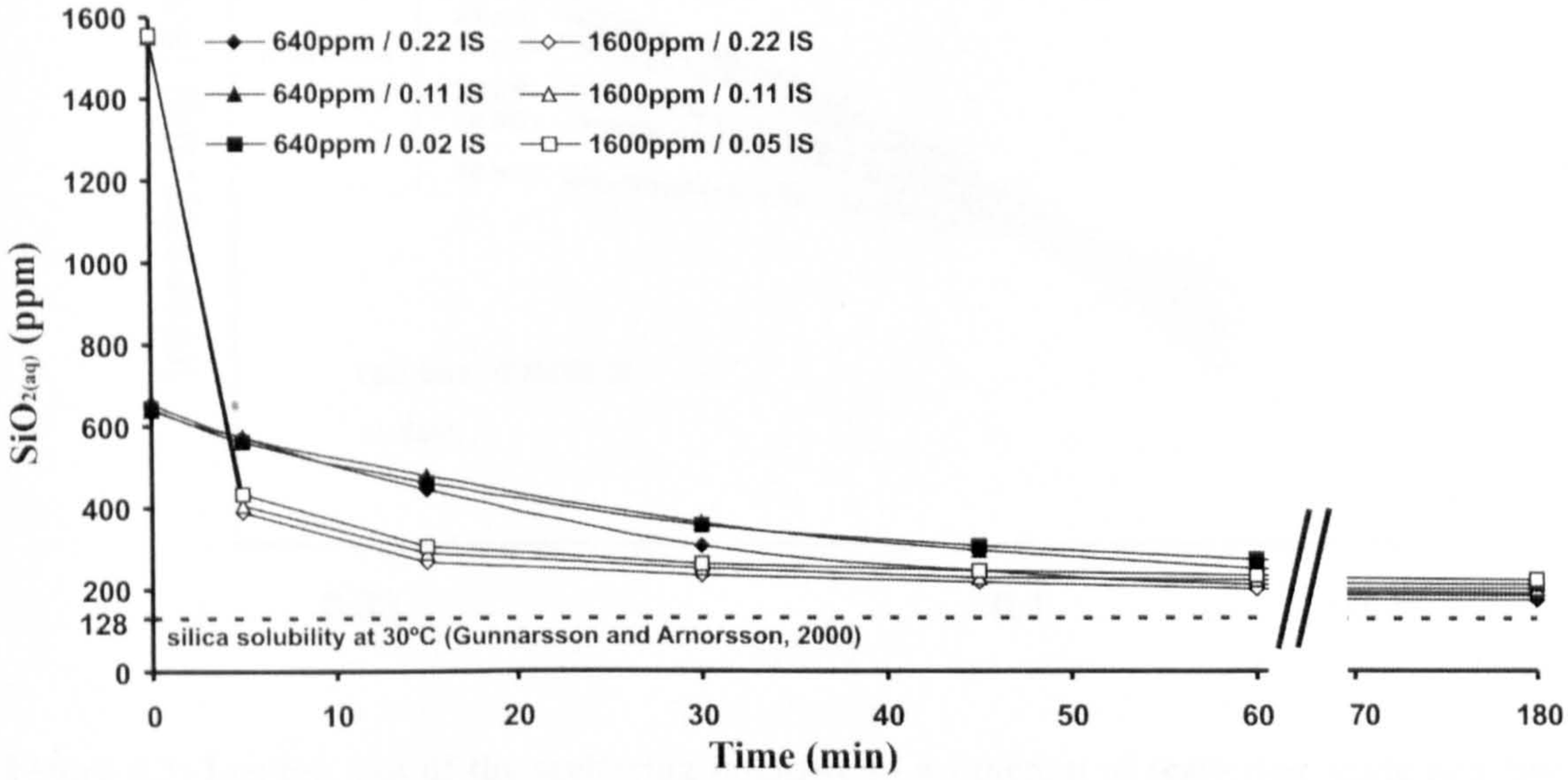

Figure 6.2: Decrease of monosilicic acid, [SiO_2(aq)], in solutions with 640ppm and 1600ppm SiO_2 and IS of 0.02, 0.05, 0.11 and 0.22 (at pH 7, T = 30°C). Errors on individual data points are <6%.

6.4.2 SAXS

In Figure 6.3, the log-log plot of a typical time-resolved SAXS profile from an experiment with 640ppm SiO_2 and IS=0.11 is shown. Note that in this experiment SAXS patterns were collected every 5 minutes over a time length of 155 minutes but for clarity only a few profiles were plotted. The solid lines depict the GNOM fits, demonstrating both the quality of the SAXS data and the suitability of the GNOM model applied to the current data. The two dominant features in these plots were (i) the change in scattering intensity, $I(q)$ with time and (ii) the increase in the slope at low q (i.e., Guinier region with $qR_g < 1$; Guinier, 1939). The increase in scattering intensity at low q is related to a change in electron density contrast between the matrix and the newly formed particles and a change in the total scattering volume (i.e., increase in particle volume or number) whereas the increase in the slope indicates an increase in the particle size with time.

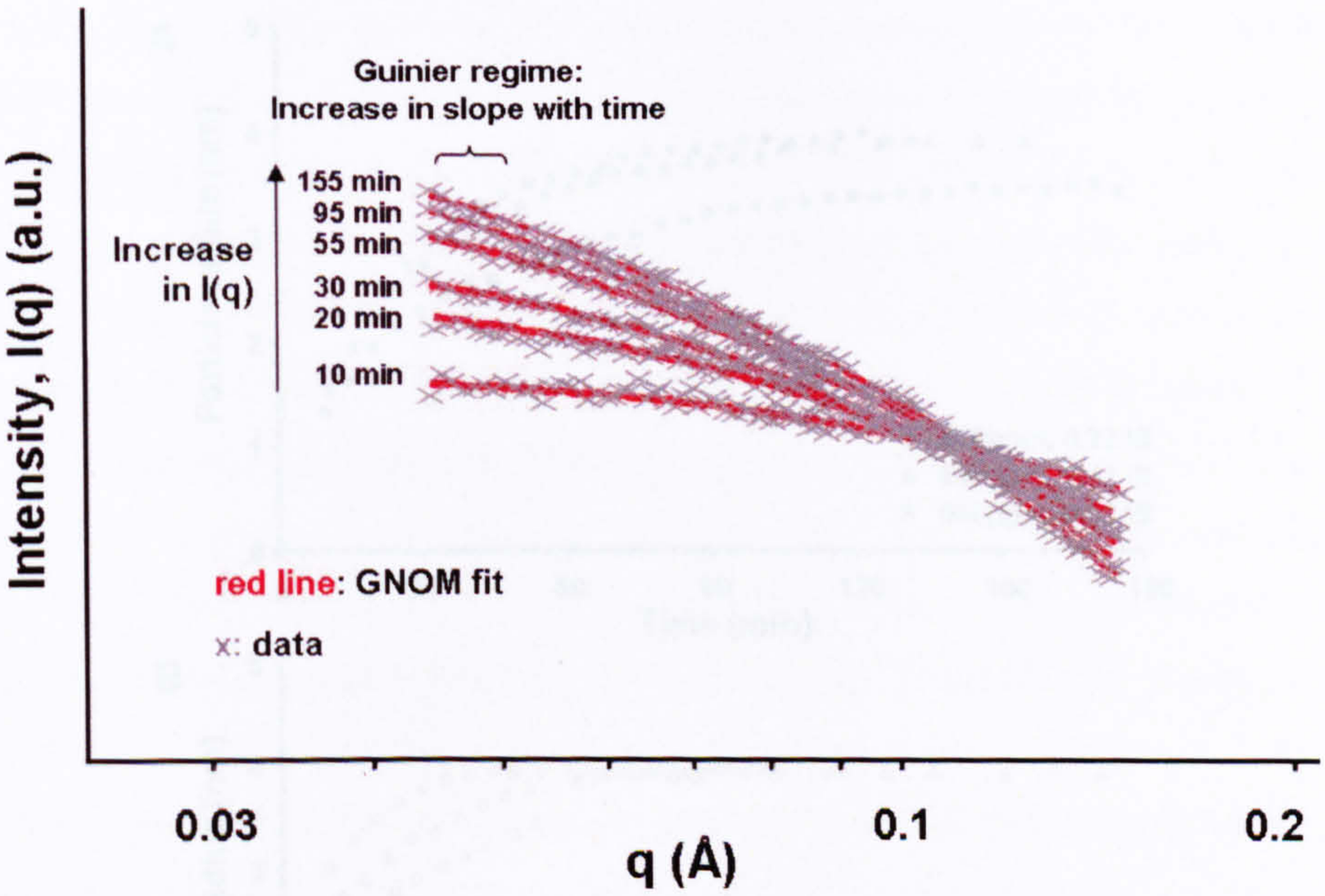

Figure 6.3: Log-log plot of the scattering intensity as a function of scattering angle and time (640ppm SiO_2, 0.11 IS). Note that SAXS profiles for the other data sets (i.e., low/high SiO_2 or low/high IS) exhibited similar characteristics. Solid lines depict GNOM fits. For clarity, the errors for individual SAXS measurements (<3%) are not shown.

The log-log plot also showed that the chosen system was sufficiently dilute (i.e., to make the analysis described above appropriate for the data), as indicated by the absence of a sharp increase or decrease in the scattering intensity at low q (i.e., the scattering profiles did not exhibit a structure factor, Glatter and Kratky, 1982; Fig. 6.3).

The radius of gyration, Rg was evaluated from the full scattering pattern using GNOM and the assumption of a monodisperse distribution of spherical particles (GNOM fits shown in Fig. 6.3). Note that under these assumptions (i.e., low polydispersity) Rg values extracted from the time dependent SAXS profiles represent average values. The real particle radius, R, was then evaluated from the following equation (valid for a sphere with a radius R; Guinier, 1939)

$Rg^2 = \frac{3}{5}R^2$ (eq. 3.4 in section 3.2.6).

The time evolutions of the radius of a spherical silica particle, R, as a function of different SiO_2 and IS are shown in Figure 6.4A and 6.4B. In these plots, time = 0 minutes denotes the point where silica polymerisation was initiated (i.e., pH adjusted to 7). It should be noted that no SAXS data could be obtained for the initial 10 minutes due to the experimental set-up (i.e., ~ 5 min to stabilise pH at 7, securing the hutch and start experiment) and the time needed to acquire the first data point (i.e., 5 minutes).

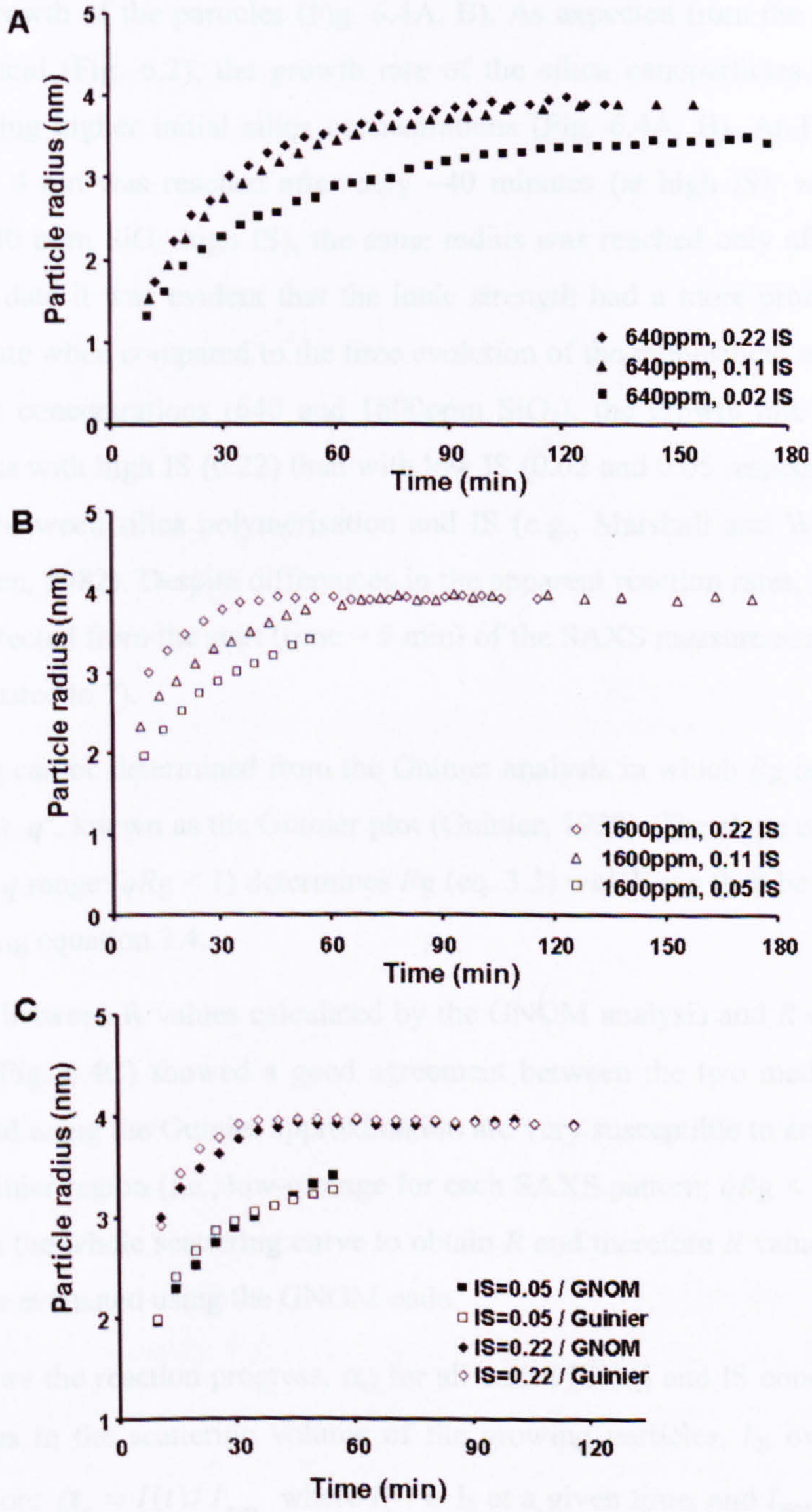

Figure 6.4: Time evolution of particle radius obtained from the GNOM analysis showing the growth of silica nanoparticles in solutions with A) 640ppm and B) 1600ppm SiO_2 at 3 different IS each. Note that the errors were typically <3%. C) Comparison of *R* obtained from the GNOM analysis and from the Guinier plot showing the agreement between the GNOM and Guinier approach (for solutions with 1600ppm SiO_2 and IS = 0.05 and 0.22).

For all tested conditions (i.e., SiO_2 and IS), the radius of the particles increased from about 1.5 (at low SiO_2) and ~ 3 nm (at high SiO_2) to ~ 4nm (both concentration regimes) over 3 hours

confirming the growth of the particles (Fig. 6.4A, B). As expected from the time evolution of the monosilicic acid (Fig. 6.2), the growth rate of the silica nanoparticles was enhanced in solutions containing higher initial silica concentrations (Fig. 6.4A, B). At 1600 ppm SiO_2, a final radius of ~ 4 nm was reached after only ~40 minutes (at high IS), while at the lower concentration (640 ppm SiO_2, high IS), the same radius was reached only after about 95 min. From the SAXS data it was evident that the ionic strength had a more pronounced effect on particle growth rate when compared to the time evolution of the monosilicic acid (Fig. 6.2). For both tested silica concentrations (640 and 1600ppm SiO_2), the growth rate was significantly higher in solutions with high IS (0.22) than with low IS (0.02 and 0.05 respectively) confirming the relationship between silica polymerisation and IS (e.g., Marshall and Warakomski, 1980; Marshall and Chen, 1982). Despite differences in the apparent reaction rates, in all experiments particles were detected from the start (time = 5 min) of the SAXS measurements (i.e., 5 minutes after pH was adjusted to 7).

Alternatively, *R*g can be determined from the Guinier analysis in which *R*g is evaluated from a plot of log $I(q)$ *vs.* q^2, known as the Guinier plot (Guinier, 1939). The slope of the linear region found in the low q range ($qRg < 1$) determines *R*g (eq. 3.3) which can then be used to determine R of a sphere using equation 3.4.

The comparison between R values calculated by the GNOM analysis and R extracted from the Guinier region (Fig. 6.4C) showed a good agreement between the two methods. However, R values determined using the Guinier approximation are very susceptible to errors introduced by selecting the Guinier region (i.e., low-q range for each SAXS pattern; $qRg < 1$). In contrast, the GNOM code fits the whole scattering curve to obtain R and therefore R values used for further calculations were evaluated using the GNOM code.

Figure 6.5A shows the reaction progress, α_r, for all tested [SiO_2] and IS conditions determined from the changes in the scattering volume of the growing particles, I_0, over time using the following equation: $\alpha_r = I(t)/I_{max}$ where I(t) is I_0 at a given time, and I_{max} is I_0 at the end of the reaction. Similar to the radius profiles (Fig. 6.4), the reactions proceeded fastest in solutions with the highest initial SiO_2 and IS, as demonstrated by the fast increase in α_r at the beginning of the reaction and the early completion of the reaction (α_r=1) at higher [SiO_2] and IS.

An example of a time-resolved PDF plot for a polymerising solution with initial SiO_2 of 1600ppm and IS=0.05 is shown in Figure 6.5B. Over time, the PDF showed an increase in both the area under the curve and a shift in the apex of the curve indicating an increase in particle size. In the case of perfect, monodisperse spheres (a valid assumption for silica nanoparticles), the shape of each individual PDF curve should be Gaussian. Despite the PDF being slightly skewed towards the right, the near-Gaussian shape of the PDF curves obtained in this study

(Fig. 6.5B) supported this assumption. The observed tail could be induced by the presence of a few aggregates or it could also indicate the presence of some degree of polydispersity. Note that the shape of the PDF curves did not differ between experiments (i.e., over the studied silica and salt concentration).

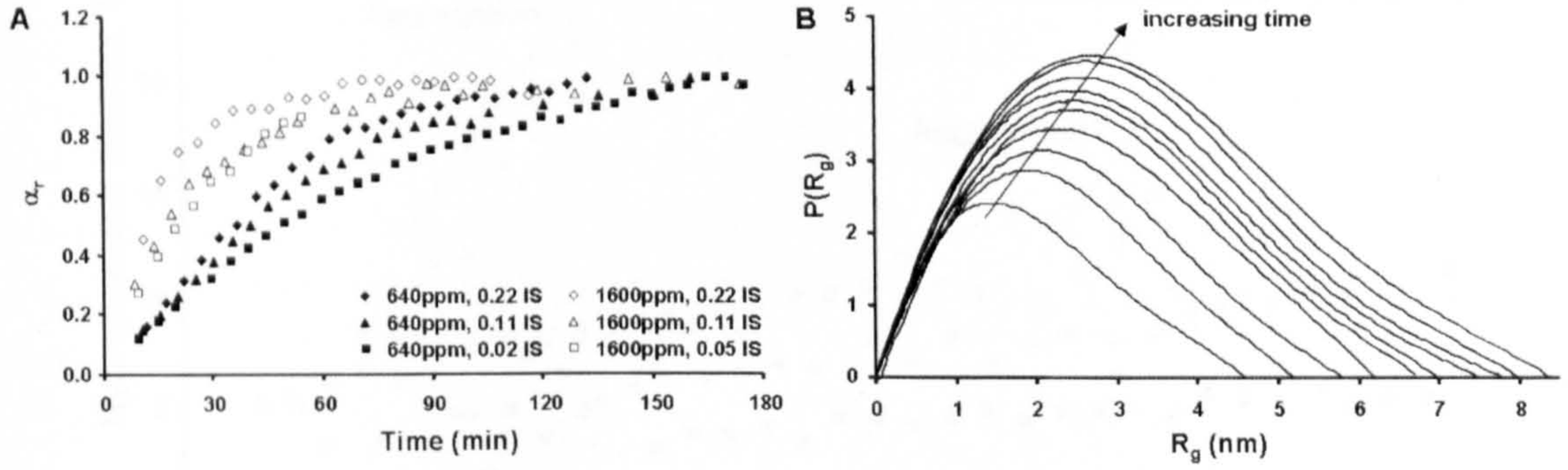

Figure 6.5: A) Time evolution of the normalised scattering intensity, α_r, in solutions with 640ppm and 1600ppm SiO_2 at three different IS each. B) PDF of scattered silica nanoparticles as a function of *R*g and time (t=10-55min with time steps of 5 min) evaluated with GNOM (1600ppm Si, 0.05 IS).

6.4.3 DLS

The time dependent growth of silica nanoparticles was monitored in 6 different solutions by DLS (Fig. 6.6, for clarity only 4 data sets are shown). Note that DLS measures the hydrodynamic diameter of the growing particles via changes in the scattering of laser light caused by the Brownian motion of the particles. In contrast to the SAXS measurements, the data showed large variations between single data points. Furthermore, due to the lower resolution of DLS at small particle sizes the average % error of DLS measurements ranged between 27 and 40 (Fig. 6.6). Despite these larger errors, overall, the trends between particle growth profiles and SiO_2 / IS were similar to those observed with SAXS. However, the DLS growth curves differed from the SAXS results in two ways: (i) the appearance of the first detectable particle was delayed at lower SiO_2 concentrations (~30 min; Fig. 6.6, full symbols) and (ii) following an initial steady growth a sudden increase in particle size was observed for higher concentrated solutions (after 30min for 1600ppm SiO_2/0.22 IS and after 120min for 1600ppm SiO_2/0.05 IS, Fig. 6.6). The observed delay at low concentrations probably represents an artefact of the lower detection limits of the DLS as compared to synchrotron-based SAXS measurements (~1 *vs.* 0.1 nm). Conversely, the dramatic increase in growth probably indicates aggregation as even a small percentage (1-2%) of larger particles in a particle suspension would dramatically increase

the overall R derived by DLS (http://www.malvern.com/LabEng/products/zetasizer/zetasizer; May 2008).

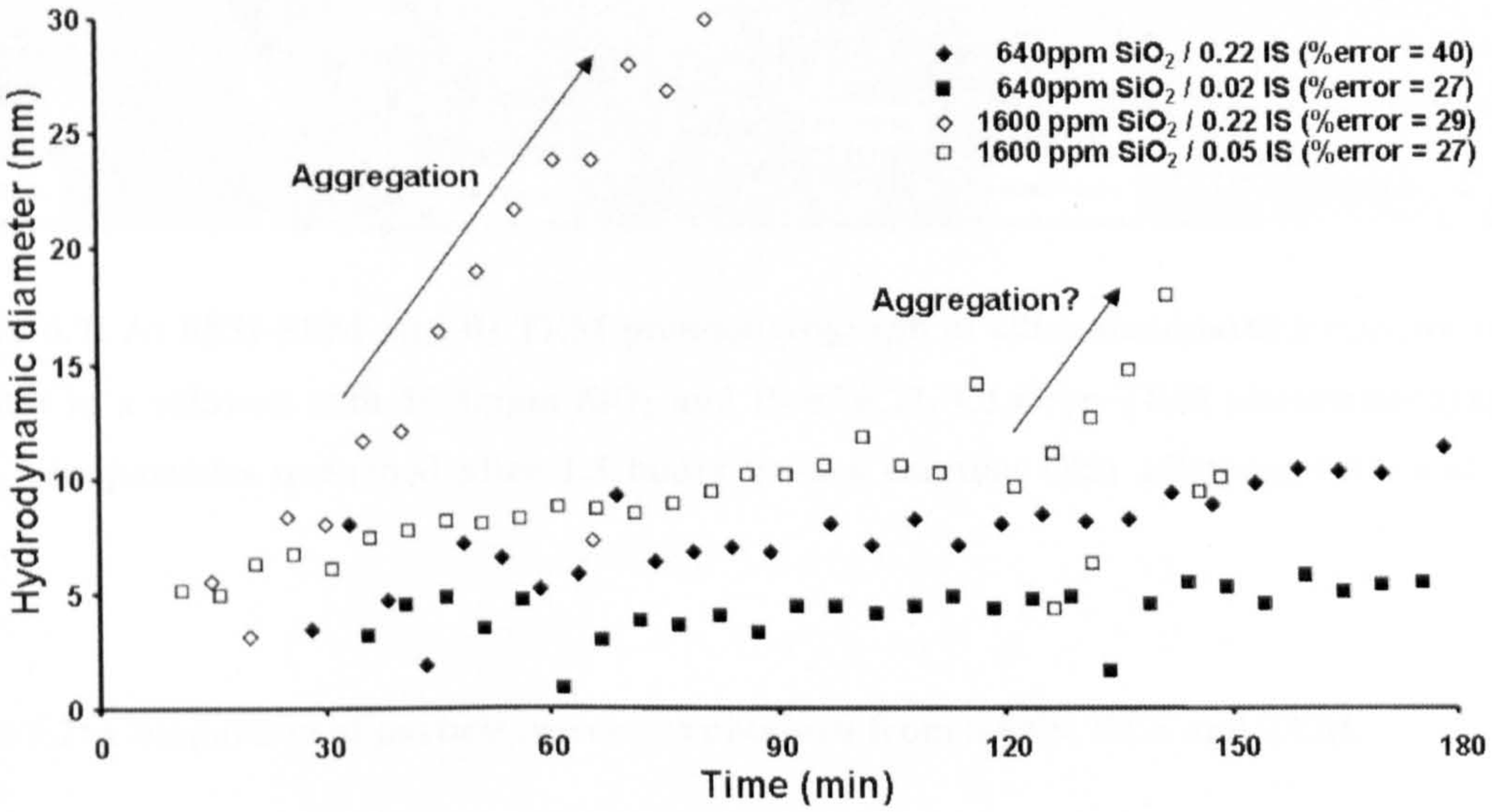

Figure 6.6: Growth of silica nanoparticles in solutions with varying SiO_2 and IS as determined by DLS. The arrows indicate the start of particle aggregation for solutions with 1600ppm SiO_2 and IS of 0.05 and 0.22; % errors are average values.

6.4.4 Electron Microscopy

To image and verify the size of silica nanoparticles evaluated with SAXS and DLS, samples of the reacting solutions were removed after specific time steps for SEM and TEM analysis. Figure 6.7A shows a FEG-SEM photomicrograph of silica nanoparticles after 1.5 hours of polymerisation in a solution with an initial silica concentration of 1600ppm SiO_2 and 0.22 IS. The particles are all aggregated but from image analyses an approximate particle size of 4 to 8 nm could be estimated for the individual particles within the aggregates.

A more accurate estimate of the particle size distributions was derived from the TEM photomicrographs (Fig. 6.7B) where the individual particles could be distinguished. The micrographs confirmed that the particles are approximately spherical and monodisperse. Using the TEM photomicrographs, the average particle diameter and the polydispersity (i.e., ± standard deviation) were determined for a variety of experimental conditions. The results are listed in Table 6.2 along with the results from DLS and SAXS (R values from SAXS are converted to particle diameter).

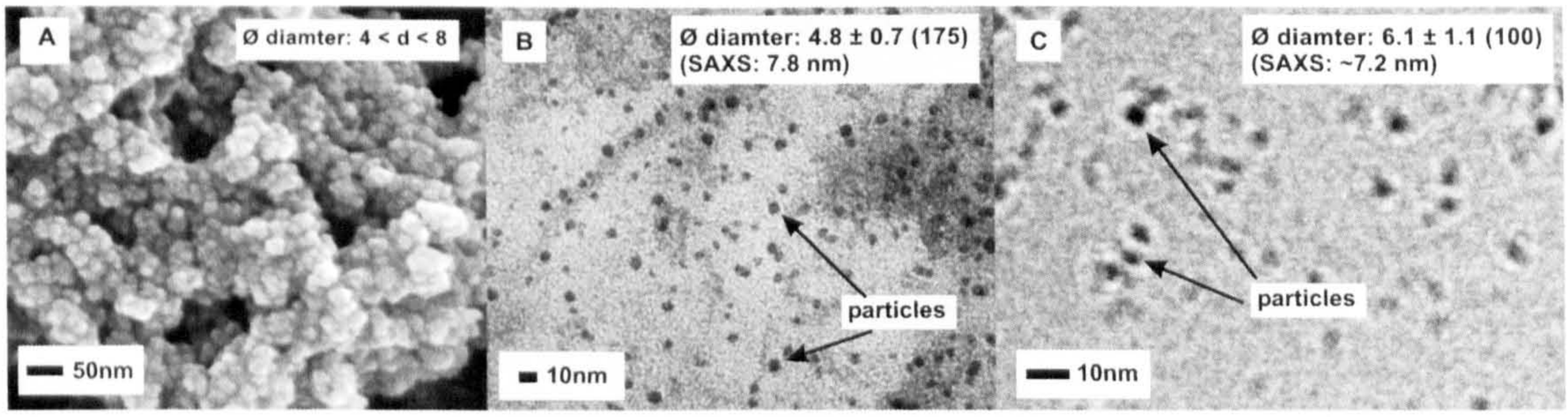

Figure 6.7: A) FEG-SEM and B) TEM photomicrograph of silica nanoparticles grown for 30 minutes in a solution with 1600ppm SiO_2 and IS of 0.22. C) Cryo-TEM photomicrograph of silica nanoparticles quenched after 1.5 hours from a solution with 1600ppm SiO_2 and IS of 0.05.

Table 6.2: Comparison of particle diameters obtained from SAXS, DLS and TEM.

SiO_2 (ppm)	IS	Time (h)	Particle diameter (nm) SAXS	DLS	TEM
640	0.02	1	5.8	4.6 ± 1.0	3.1 ± 0.4
		2	6.7	4.7 ± 1.1	3.3 ± 0.4
	0.11	1	7.0	-	-
		2	7.7	-	4.5 ± 0.7
	0.22	1	7.2	5.8 ± 1.9	5.2 ± 0.9
		2	8.0	8.0 ± 5.0	3.6 ± 0.5
1600	0.05	1	6.9	8.7 ± 2.2	-
		1.5	~ 7.2[b]	10.1 ± 3.1	6.1± 1.1[a]
		2	~ 7.5[b]	9.6± 1.8	-
	0.11	1	7.6	9.9 ± 3.5	5.4 ± 0.5
		2	7.9	Aggregation	-
	0.22	0.5	7.5	8.0 ± 1.0	5.1 ± 0.6
		1	7.9	Aggregation	6.7 ± 0.9
		2	7.9	Aggregation	-

[a]Result from cryo-TEM
[b]Estimates based on the progression of growth curves obtained from SAXS
[c]Error of SAXS < 0.3nm

Finally, to test for artefacts caused by sample dehydration and the high vacuum of standard SEM and TEM analytical approaches, cryo-TEM photomicrographs of silica particles that were flash-frozen in solution in their native state from an experiment with 1600 ppm SiO_2 and IS = 0.05 were evaluated (Fig. 6.7C). The particle diameters obtained from cryo-TEM matched those derived from the SAXS measurements better than the results from conventional TEM (Table 6.2).

6.4.5 Kinetic analysis of SAXS data

The evaluation of the reaction kinetics of silica nanoparticle nucleation and growth was carried out with the time-resolved SAXS data from the experiments with 640ppm SiO_2 and IS of 0.02, 0.11 and 0.22. The growth profiles of particles forming in the higher concentrated solutions (1600pm SiO_2) did not provide enough data points for a thorough kinetic analysis but they could be used for comparative analyses.

Nucleation

In the case of silica, a supersaturated solution is assumed to undergo homogeneous nucleation when care is taken to avoid impurities, i.e., existing surfaces, on which heterogeneous nucleation could occur. Furthermore, the goodness of fit of the data to the Thetadash kinetic model (see below; Fig. 6.8), which assumes instantaneous nucleation, indicates that particle nucleation was instantaneous. This is supported by the immediate decrease in monosilicic acid, i.e., instantaneous silica polymerisation, after the pH was lowered to 7 (Fig. 6.2).

For homogeneous nucleation, the radius of the critical nucleus, R_0^+, forming within a supersaturated solution can be expressed using the Gibbs-Kelvin equation (Gibbs, 1961): $R_0^+ = 2v\sigma / RT\ln(S+1)$ (eq. 2.2 in section 2.1.2) where v is the molar volume (27.2 cm^3; Iler, 1979), σ is the interfacial surface energy (80 erg cm^{-2}; Iler, 1973), R_c, the gas constant, and S is the supersaturation defined as $S = (C - C_s)/C_s$ with C being the actual concentration and C_s the solubility. *Cs* for amorphous silica was obtained from Gunnarsson and Arnórsson (2000).

Calculated R_0^+ values for all experiments are listed in Table 6.3. In all 640ppm SiO_2 experiments, R_0^+ varied between 1.04 (IS = 0.22) and 1.07 (IS = 0.02) while in the 1600ppm SiO_2 experiments, R_{0+} = 0.67 - 0.68 nm. Note that the effect of IS on the critical nuclei radius was only minor.

Table 6.3: Summary of the derived kinetic parameters. Critical nuclei radii, R_0^*, were calculated from the Gibbs-Kelvin equation (eq. 2.2). An independent evaluation of the critical nuclei radius, R_0, along with the initial growth rate, G_0, were obtained from the Thetadash kinetic model. The Thetadash reaction constants, k, were calculated using G_0 (eq. 3.8). Finally, the JMAK reaction constants, k* were determined with the JMAK kinetic model (eq. 3.6).

				Thetadash model		JMAK model
SiO_2 (ppm)	IS	R_0^+ (nm) Gibbs - Kelvin	[a]R_0 (nm)	G_0 ($x10^{-12}s^{-1}$)	k ($x10^{-4}s^{-1}$)	k* ($x10^{-4}s^{-1}$)
640	0.02	1.07	1.07	2.16	3.18	2.77
	0.11	1.06	1.05	3.22	4.61	3.34
	0.22	1.04	1.06	3.70	5.02	3.61
[b]1600	0.05	0.68	-	-	-	-
	0.22	0.67	-	-	-	-

[a]Using R_0, an average interfacial surface energy of 85.4 ± 1.6 erg cm^{-2} was calculated.

[b]The 1600 ppm SiO_2 experiments did not provide enough data points for Thetadash and JMAK analysis.

Growth mechanism: classical growth

In classical growth theory, particles grow by atom-by-atom or molecule-by-molecule attachment to a pre-existing surface. The growth profiles obtained from SAXS showed an initial fast and steady increase concomitant with the depletion of monosilicic acid to the point where saturation was almost reached and classical growth was no longer occurring. To test data from this initial growth phase, the SAXS data were fitted to two kinetic models, the Thetdash and the JMAK kinetics models, both of which are based on classical growth approaches.

Results from the Thetadash analysis for experiments with initial SiO_2 of 640ppm and IS = 0.02, 0.11 and 0.22 are shown in Figure 6.8. Exceptionally good fits between the data and the kinetic model were obtained using a first order rate law with a surface-controlled mechanism. Data analysis with Thetadash also provided information on the size of the critical nuclei, R_0 and the initial growth rate, G_0 which are listed in Table 6.3. While G_0 was used to calculate the rate constants, k (eq. 3.8; Table 6.2), the R_0 values were used to estimate an interfacial surface energy for amorphous silica (eq. 2.2). From these calculations a value of 85.4 ± 1.6 erg cm^{-2} was obtained which agrees exceptionally well with the value used in this study (80 erg cm^{-2}, Iler, 1973; also used by Conrad et al., 2007) and the literature data for the interfacial surface energy for amorphous silica (i.e., between 50 and 100 erg cm^{-2}, Iler, 1979 and references therein).

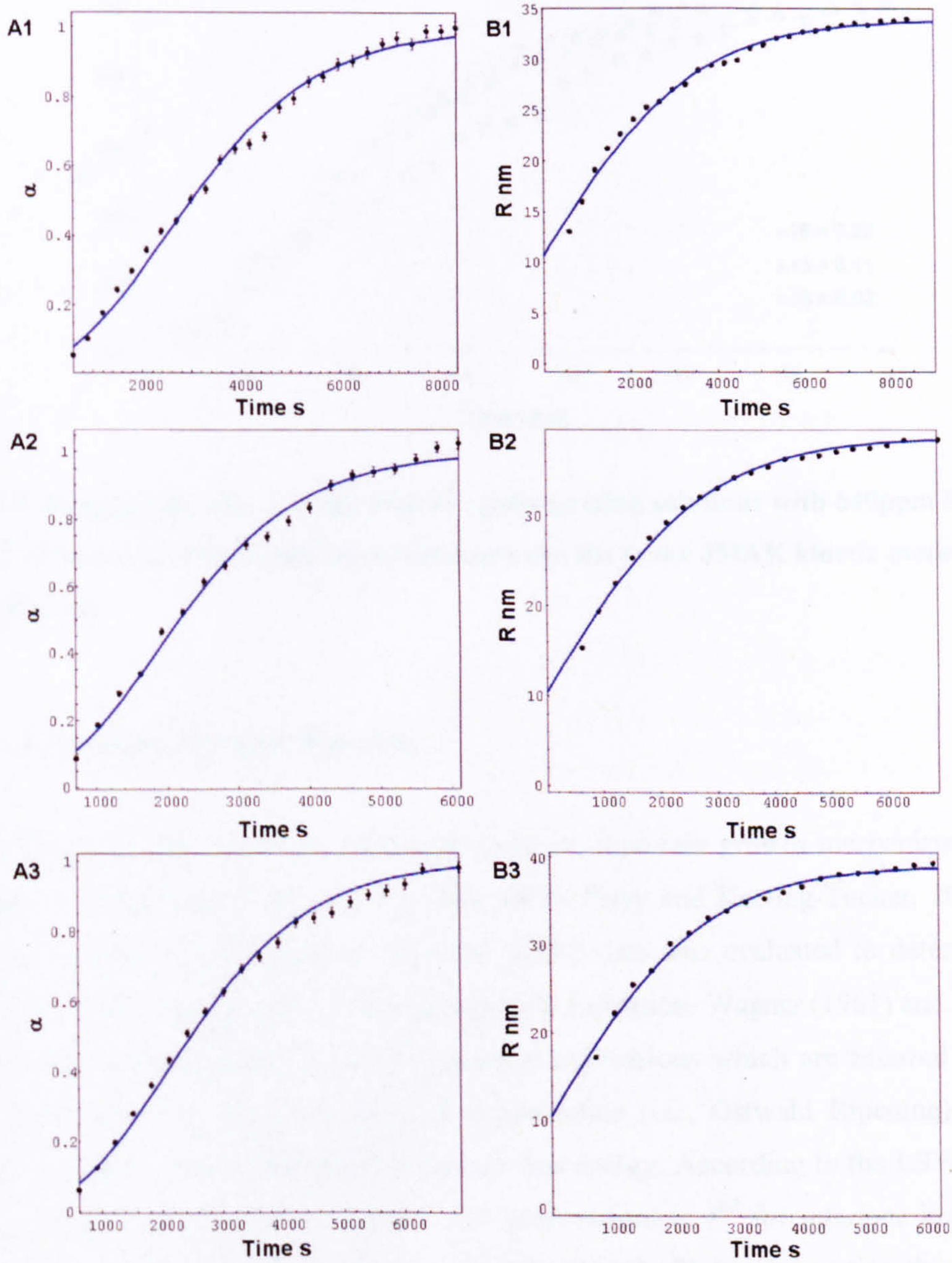

Figure 6.8: Plots showing α (A1-A3) and R (B1-B3) fits to the Thetadash model (solid line) for three SAXS experiments with initial SiO_2 of 640ppm and IS of 0.02 (A1, B1), 0.11 (A2, B2) and 0.22 (A3, B3).

For comparison with the Thetadash analysis, the 3 different data sets were also fitted to the JMAK kinetic model (Fig. 6.9) and an average exponent n of 1.7 ± 0.1 (eq. 3.6) was obtained. The fit of the SAXS data with the JMAK model is reasonably good (Fig. 6.9) suggesting that the initial steps of silica nanoparticle growth proceeded via classical growth. The rate constants determined from the JMAK analysis are given in Table 6.3.

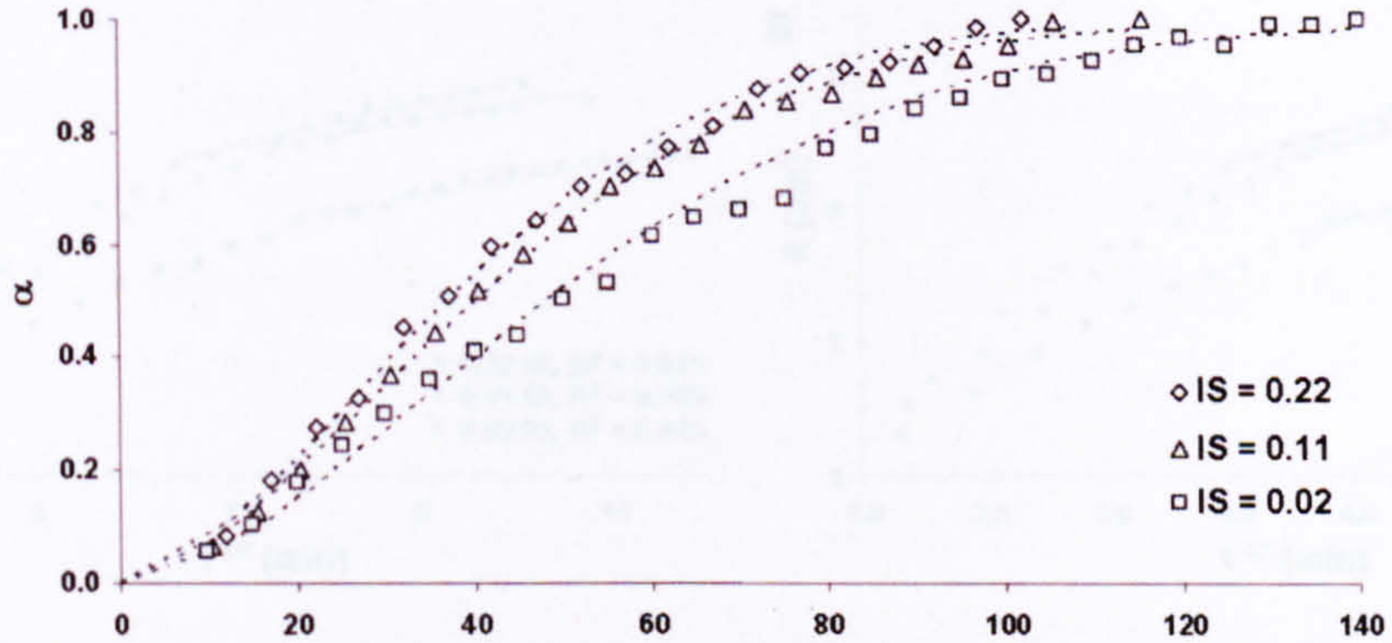

Figure 6.9: Reaction process, α, with time for polymerising solutions with 640ppm SiO_2 and IS of 0.02, 0.11 and 0.22. The dotted lines represents the fits to the JMAK kinetic model with *n* set to 1.7 and t_0=0s.

Growth mechanism; Ostwald Ripening

Ostwald Ripening (OR) has been suggested to be an important growth mechanism during the late stages of silica particle growth (e.g., Iler, 1979; Perry and Keeling-Tucker, 2000; section 2.1.2). The particle size information from the SAXS data was evaluated to determine if OR played a role in the final stages of silica nanoparticle formation. Wagner (1961) and Lifshitz and Slyozov (1961) independently derived theoretical expressions which are referred to as LSW theory. They described the coarsening of a precipitate (i.e., Ostwald Ripening) due to the tendency to minimize the total particles surface free energy. According to the LSW theory, the average particle radius follows a growth rate proportional to $t^{1/2}$ for interface kinetic limited growth, or proportional to $t^{1/3}$, for diffusion limited growth. Plots representing the evolution of the radius *R vs.* $t^{1/2}$ and $t^{1/3}$ are shown in Figure 6.10. Note that the complete growth profiles (i.e., $0 < \alpha < 1$) are shown while the trendlines were only fitted to the later growth phases, which approximately fitted a linear trend. These plots show a minimal difference in the goodness of fit (*R* squared; Fig. 6.10) between the two different growth processes thus indicating that an OR model fit in this study fails to discriminate between a surface- ($t^{1/2}$) and diffusion controlled ($t^{1/3}$) mechanism (Fig. 6.10). The discrepancy between the OR model and the SAXS data indicates that it might be problematic to use the OR model as a growth mechanism for silica nanoparticles.

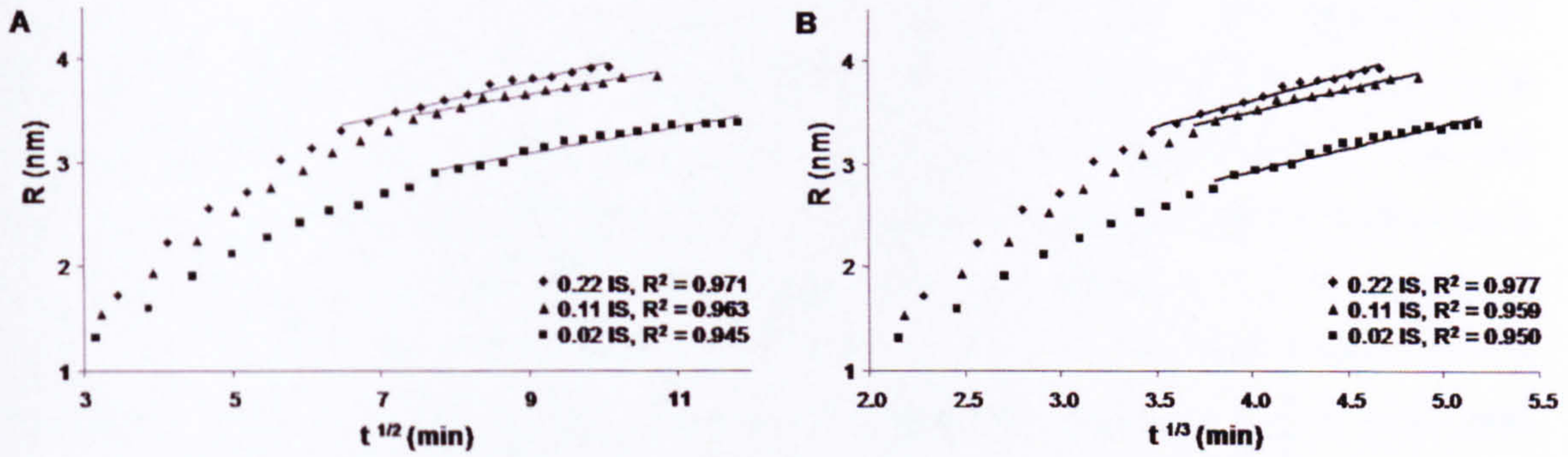

Figure 6.10: Based on the LSW theory, the average particle radius, *R*, follows the growth rate proportional to (A) $t^{1/2}$ for interface kinetic limited growth or to (B) $t^{1/3}$, where growth is diffusion limited (shown for solutions with 640ppm SiO_2 and varying IS).

Besides an increase in mean particle radius, the LSW theory also indicates that during OR the particle size distribution broadens (i.e., increase in polydispersity) and its skewness changes to the right (e.g., Eberl, 1998; section 2.1.2). This was tested with the silica particle size distribution as determined for 2 different aging times (30 and 60 minutes) in a solution with 1600ppm SiO_2 and IS of 0.22 (Fig. 6.11) using TEM photomicrographs. The results show that at 30 minutes a fairly narrow size distribution (5.1±0.6 nm, 200 particles measured) with almost Gaussian distribution was obtained. At 60 minutes, the size distribution broadened significantly (6.7 ± 0.9 nm, 200 particles measured) but no shift in skewness was observed (Fig. 6.11). Despite the absence of a shift in skewness, the increase in polydispersity supports OR, however this could also be indicative of particle aggregation.

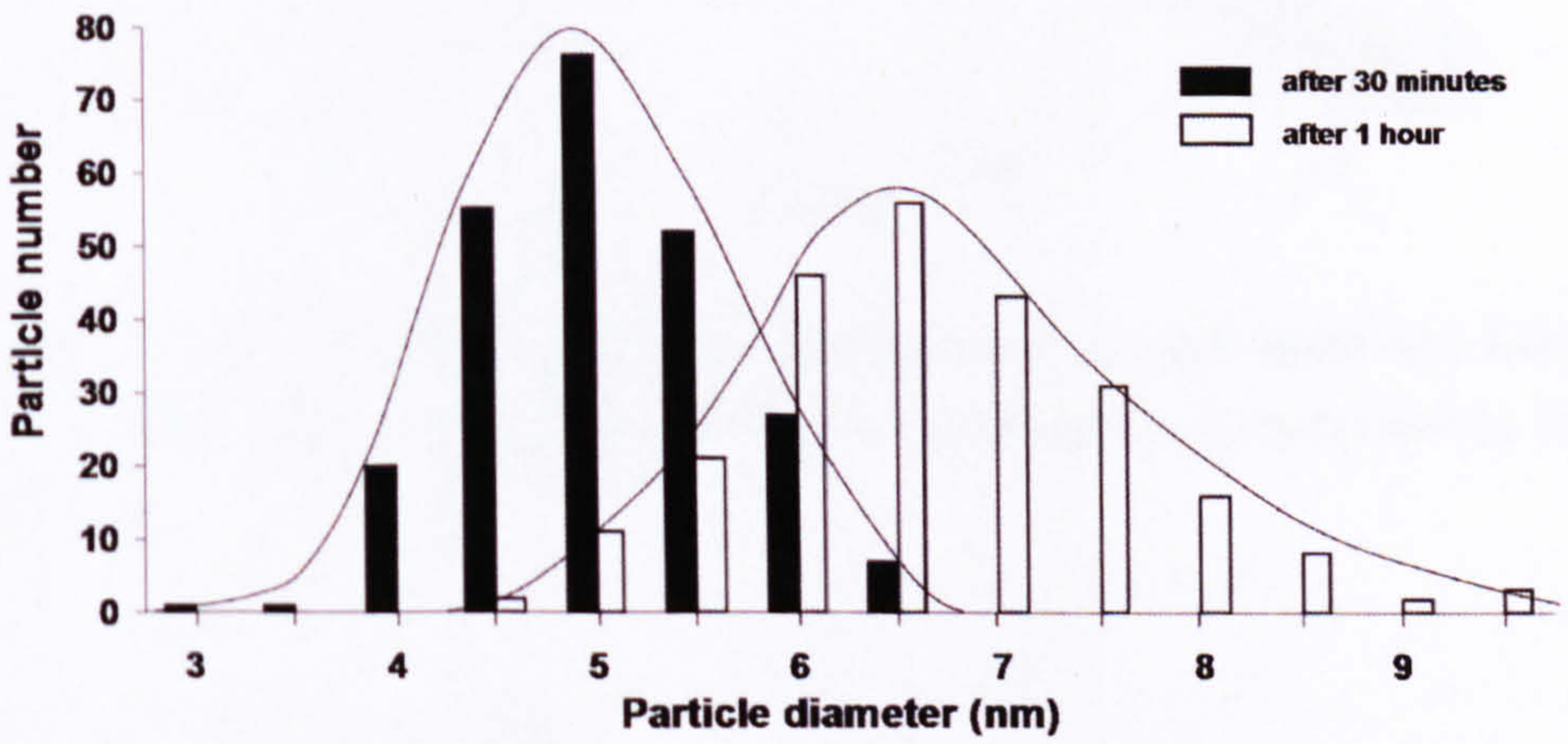

Figure 6.11: Particle size distributions for two different aging times obtained from TEM photomicrographs of samples with initial 1600ppm SiO_2 and IS=0.22 (200 particles were measured for each time step).

Finally, further support for Ostwald ripening can be derived from the time evolution of the invariant, Q, which is defined as the integral of $I(q)*q^2$ (i.e., Kratky curve, Fig. 6.12). Q is related to the scattering intensity produced by the shape and size of the forming particles and thus represents the total scattering power law of the sample. For classical growth processes it would be expected that the invariant continually increases with time due to continuous growth of the silica nanoparticles from solution. However, during OR, no new material should precipitate and the invariant should, therefore, stay constant. The invariant indicates an increase over the first 60 minutes (insert in Fig. 6.12) in the experiment with 640ppm SiO_2 and IS = 0.11 supporting classical growth for this initial fast growth phase, however, thereafter the invariant does not further increase and stays reasonably constant supporting OR for the second growth stage of silica nanoparticle growth. Note that with increasing scattering (i.e., particle growth), the scattering profiles migrate to higher q-values (Fig. 6.12) which might not be fully covered by the probed q-range. Therefore, the observed constancy of the invariant could also be due to an incomplete Kratky plot.

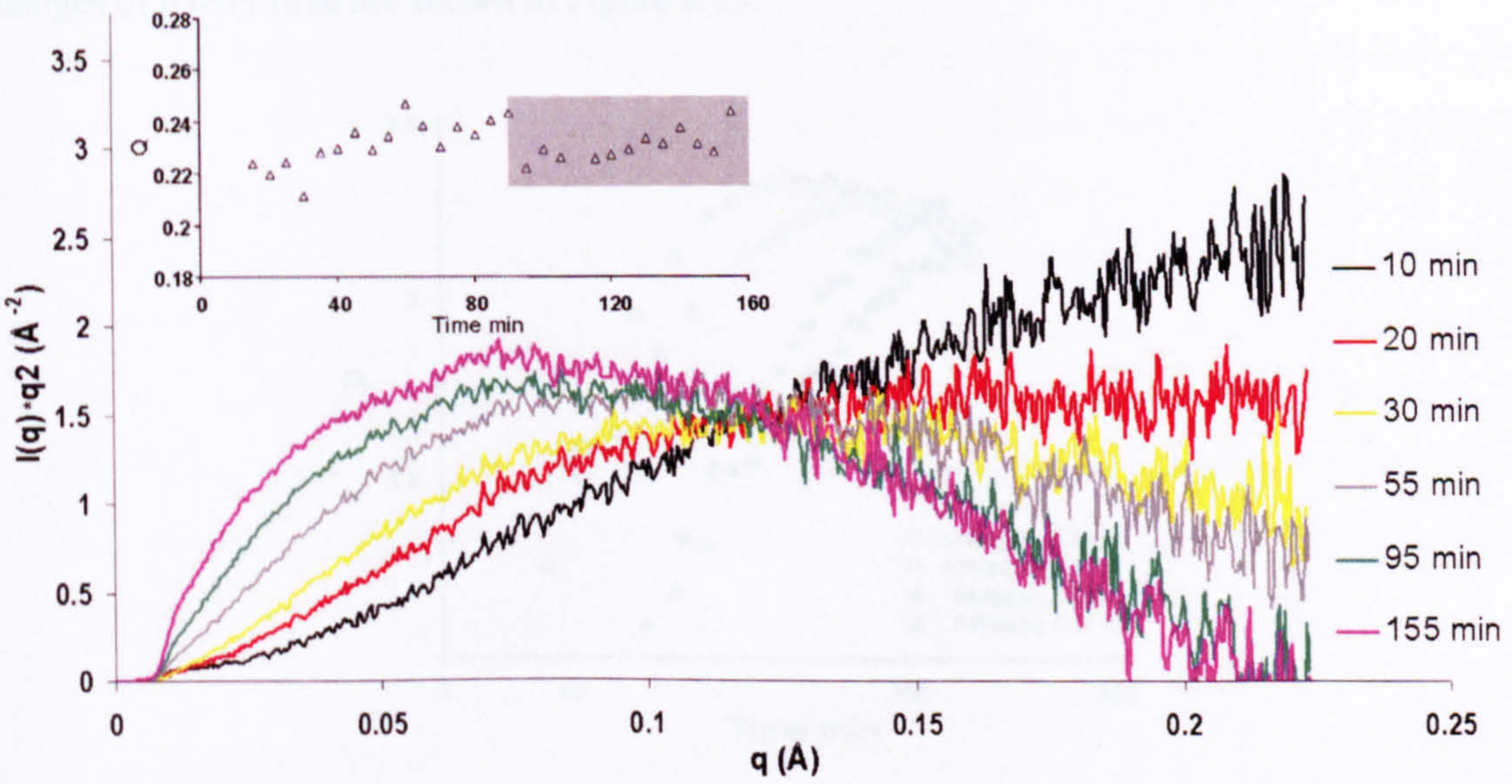

Figure 6.12: The Kratky plot of SAXS data obtained from the experiment with 640ppm SiO_2 and IS=0.11. The insert shows the time evolution of the invariant, *Q*, as derived by integrating the Kratky plot.

Growth mechanism: Aggregation

Aggregation of monodisperse nanoparticles is generally described by two main models, diffusion-limited colloid aggregation (DLCA) and reaction-limited colloid aggregation (RLCA) (e.g., Weitz and Huang, 1985; Weitz et al., 1985). The DLS and SEM/TEM results confirmed

the occurrence of aggregation processes (Fig. 6.6 and 6.7) within the latter stages of silica particle growth; however these data sets did not provide enough data points for a thorough analysis of the aggregation mechanisms.

Nevertheless, some information about the aggregates can be derived. The structure and complexity of the aggregates formed can be described by a fractal geometry concept (e.g., Pfeifer and Obert, 1989; Lin et al., 1990) in which the objects that form during particle growth and aggregation are characterised with a fractal dimension D_f. Boukari et al. (1997) employed the fractal geometry concept on alkoxide silica particle growth by analysing the power-law regime ($Rg^{-1} << q << a^{-1}$; where a is the size of the smallest unit building the fractal structure) of SAXS patterns. In this regime, $I(q) \sim q^{-p}$, where the exponent p is related to the fractal dimension. For mass fractals (D_m), which can be described as open, polymeric, low-density structures, $p = D_m$ with $1 < p < 3$ (3-D space) whereas surface fractals (D_s) have uniform cores but open surface structures, $p = 6 - D_s$ with $3 < p < 4$. The SAXS data from four experiments were least-square fitted with the power law of $I(q) \sim q^{-p}$ with p being the fitting parameter. The changes of p over time are shown in Figure 6.13.

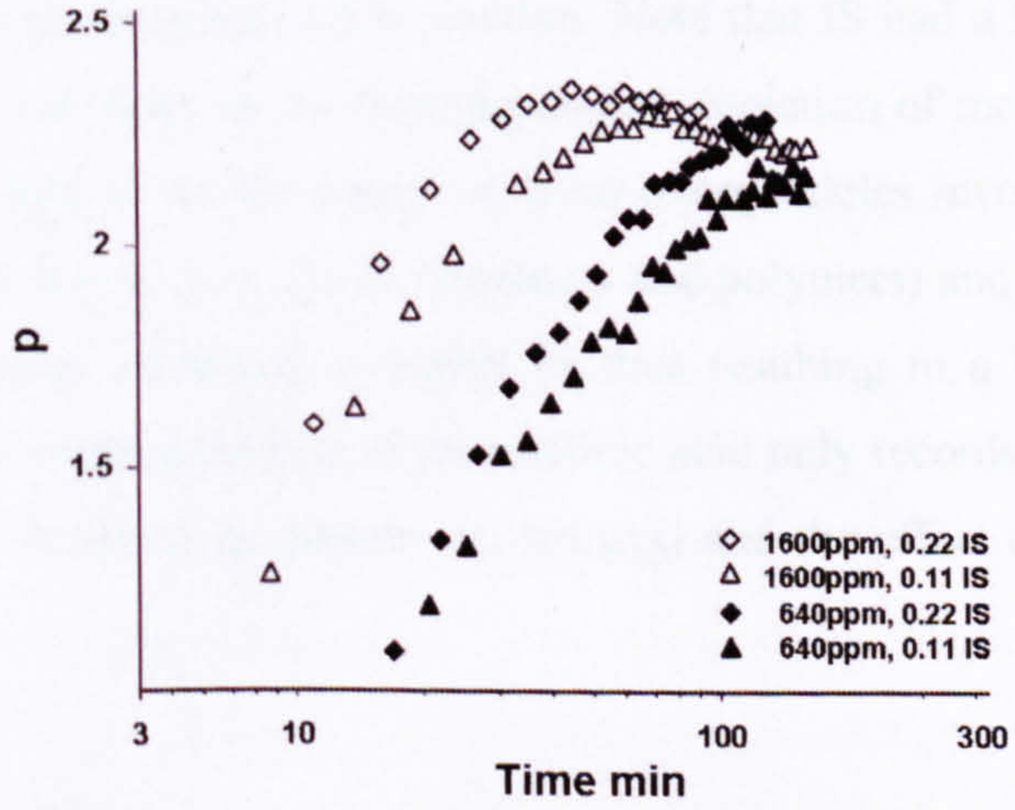

Figure 6.13: Plot of exponent *p* determined from the power law range of four SAXS profiles as a function of time.

The time evolution of p correlated well with the tested [SiO_2] and IS (i.e., the saturation state): higher saturated solutions (high SiO_2) induced fast changes in p while lower saturated solutions (low SiO_2) exhibited slower changes. Note that besides a shift in time, the trends of the p *vs.* t curves (Fig. 6.13) were identical for all fitted SAXS curves suggesting that the nucleation and growth processes did not change between experiments. This was in agreement with previous studies on silica aggregates (Boukari et al., 1997). Despite a continuous change in particle

structure, as indicated by the increase in p, all formed particles can be described as mass-fractals ($1<p<3$; Fig. 6.12) with a fractal dimension of $D_m = p$ and no transition to surface-fractal was observed.

6.5 Discussion

All experiments were conducted at neutral pH and 30°C, where silica solubility is at a minimum (Iler, 1979). The SAXS and DLS results along with the time-dependent depletion of monosilicic acid, [$SiO_{2(aq)}$], confirmed previous studies that concluded that the rate of silica polymerisation and nanoparticle formation increased with increasing ionic strength and silica concentration (e.g., Rothbaum and Rhode, 1979; Icopini et al., 2004; Conrad et al., 2007). In all experiments the reacting solutions were highly supersaturated with respect to amorphous silica and the degree of saturation invariably affected the growth rate and hence the time length for the reaction to be completed. In addition, due to the highly supersaturated state of the solutions studied, silica polymerisation occurred instantaneously during pH adjustment prior to data collection suggesting that the first silica nanoparticles (critical nuclei) formed immediately after the initiation of the silica polymerisation reaction. Note that IS had a more profound effect on particle growth (Fig. 6.4) than on the time-dependent depletion of monosilicic acid (Fig. 6.2). This was not unexpected as the formation of silica nanoparticles involves multiple steps (i.e., formation of dimers, trimers up to cyclic oligomers and polymers) and the reaction rate of each of these steps is slightly increased at higher IS thus resulting in a higher overall effect. In contrast, the time-dependent depletion of monosilicic acid only records the initial steps of silica polymerisation (i.e., formation of dimers and trimers) and the effect of IS will thus not be as pronounced.

6.5.1 Particle size analysis

Particle growth curves obtained from SAXS showed that over 3 hours the particle radii increased from about 1.5 - 3 nm (depending on the concentration regimes) to a final radius of ~4nm (Fig. 6.4). The maximum radii at the end of the initial growth were identical for all tested SiO_2 and IS conditions and thus not affected by the degree of silica saturation (i.e., SiO_2 and IS). In contrast, the first particle size probed by SAXS differed significantly between experiments as a result of the different sized critical nuclei as well as the different growth rates, particularly in higher silica saturated solutions. Due to the experimental set-up the formation of the critical nuclei could not be probed directly by SAXS or any other method applied in this study. However, the size of the critical nuclei was calculated using the Gibbs-Kelvin approach and was

also determined using data from the Thetadash analysis (Table 6.3). The agreement between these values was exceptionally well and the comparison showed that in all solutions with 640ppm SiO_2 the critical nuclei radius, R_0^+ was about 1 nm with little influence of IS. In solutions with higher silica concentrations (1600ppm SiO_2), the critical nuclei radius could only be determined via the Gibbs-Kelvin approach ($R_0^+ \sim 0.68$ nm, Table 6.3) and these values were substantially smaller than in the less concentrated solutions (Table 6.3). Note that the stability of the critical nuclei decreases with decreasing size (more energy is needed to sustain a higher surface to volume ratio). However, the nucleation process has a higher driving force in more concentrated solutions thus enabling the stabilisation of smaller nuclei. The values for the critical nuclei radius, R_0 obtained in this study were in good agreement with results from Iler (1979) who calculated that the first stable silica particle would range between 1 and 2 nm in diameter.

In order to compare SAXS results with DLS and TEM data, R values determined from SAXS were converted to particle diameter (Table 6.3). In Figure 6.14, the direct comparison between the SAXS and DLS results for the growth of silica nanoparticles in a solution with 1600ppm SiO_2 and IS of 0.05 are shown. Particularly in the initial stages of the reaction (< 60 minutes) both growth curves follow the same trends, although the errors in the DLS data are substantially larger due to the lower accuracy when compared to the SAXS data. In both data sets the diameter of the first detected particle was ~4 nm. This was followed by a steady increase in particle diameter towards a final value of 8 nm. After about 70 minutes, the DLS derived particle diameter increased to sizes > 15 nm (Fig. 6.13) while the SAXS average particle diameter stabilised at a final size of 8 nm (Fig. 6.4A, B). These differences are likely to be due to the formation of aggregates. In DLS, even 1-2% by volume of larger particles can significantly change the DLS derived particles sizes while SAXS measurements are less susceptible to the presence of larger aggregates. Note that the formation of aggregates was also shown by SEM (Fig. 6.7A) while with TEM and cryo-TEM (Fig. 6.7 B, C) only few aggregates were observed. However, it is possible that a significant proportion of the aggregates observed with SEM/TEM were induced by sample preparation (i.e., dehydration) and therefore did not provide a true picture of the proportion of the particles and aggregates within the suspension.

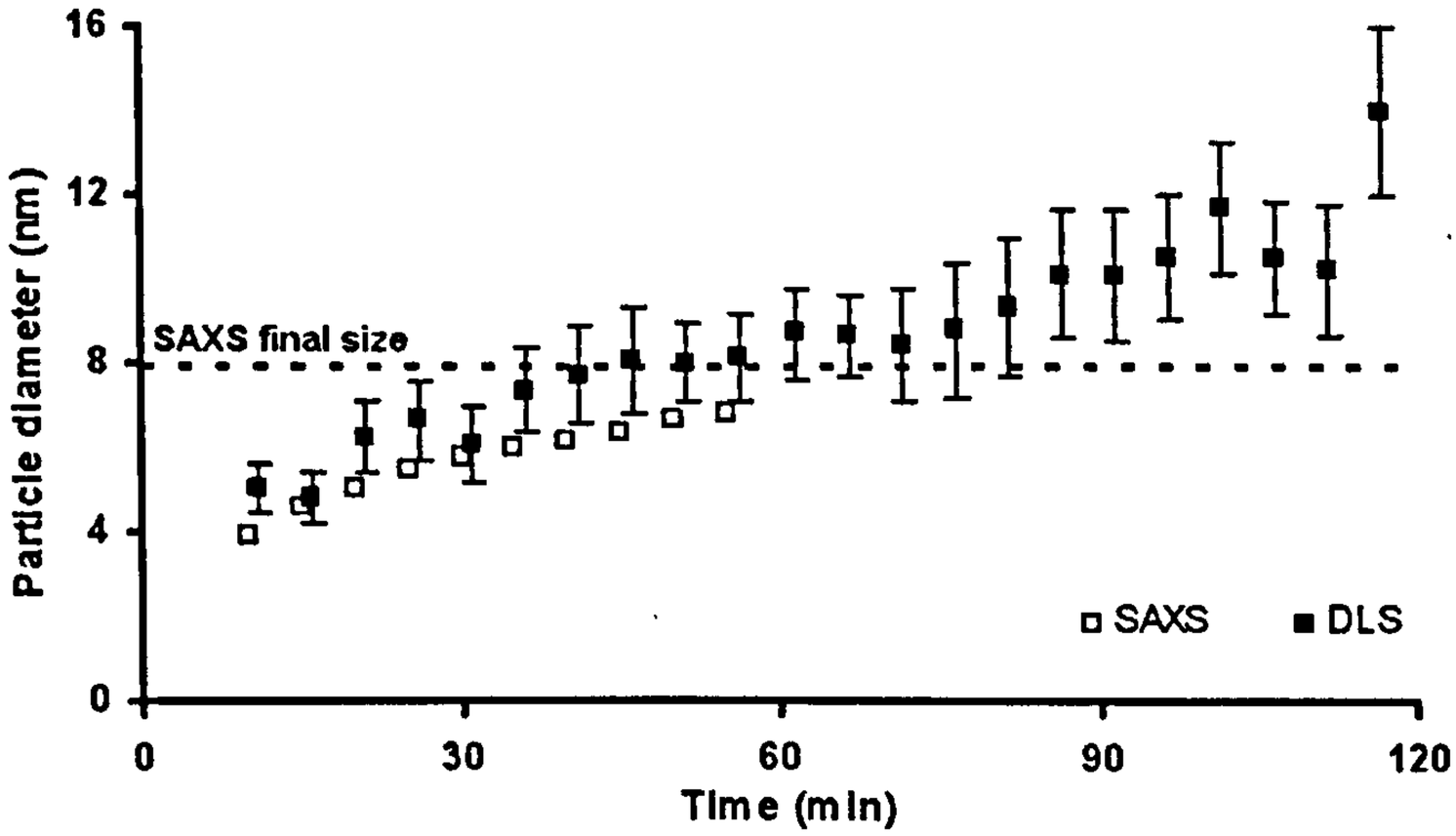

Figure 6.14: Growth of silica nanoparticles as a function of time in a silica solution with 1600ppm SiO_2 and IS of 0.05 measured by SAXS and DLS.

As shown in Table 6.3, the particle diameter obtained from SEM and (cryo-)TEM were generally smaller than DLS and SAXS. The smaller particles sizes were not unexpected as the SEM and TEM analysed samples were placed within a high vacuum and thus undergo dehydration and relaxation processes causing the highly hydrous (up to 13 wt% water; e.g., Krauskopf, 1956; Jones and Renault, 2004) and open-structured particles to collapse. Particle diameters obtained from cryo-TEM better matched the SAXS derived particle sizes because the flash-frozen particles do not dehydrate within the high vacuum of the electron microscope. The difference observed (e.g., SAXS: 7.2 ± 0.3 and cryo-TEM: 6.1 ± 1.1) most likely resulted from the lower accuracy of determining sizes from cryo-TEM.

6.5.2 Analysis of the reaction kinetics

The initial stage of silica nanoparticle formation was characterised by silica polymerisation where monosilicic acid coalescence to form dimers, then trimers up to cyclic oligomers (Perry and Keeling-Tucker, 2000, section 2.1.2). This oligomerisation process eventually led to the formation of stable nuclei having a diameter of approximately 1 - 2 nm (Table 6.3). Due to the dilute and highly supersaturated state of the silica solutions (which would enhance the diffusion of monosilicic acid to the forming nuclei), silica polymerisation was instantaneous. This suggested that particle nucleation must have also occurred instantaneous. This was further supported by the good fits of the SAXS data to the Thetadash model in which instantaneous nucleation was assumed.

The second step of silica nanoparticle formation was characterised by the fast decrease of monosilicic acid concentration and the 3-dimensional growth of silica nanoparticles (Fig. 6.15, ~5 – 100 min). The dimensionality of the growth was shown by the Gaussian-shaped PDF curves as well as SEM and TEM photomicrographs which all indicated that the particles remained spherical throughout the reaction. Further evidence was provided by the quality of the fits to the Thetadash model (Fig. 6.8), which assumes 3-D growth and where the best fit in terms of the regression coefficient was obtained using a first order rate law with a surface-controlled mechanism. For a surface-controlled, 3-D growth mechanism, following a zero nucleation rate, the JMAK model should yield a *n* value of 3 (Hulbert, 1969) however, the *n* value calculated form the particle growth data was 1.7. This might indicate a growth dimensionality < 3 or the inappropriateness of the JMAK model for the growth of silica nanoparticles. Results from this study as well as from the literature (e.g., Iler, 1979; Icopini et al. 2005; Conrad et al., 2007) have shown that silica nanoparticles are spheres and n should therefore yield a value close to 3. This suggested that the use of the JMAK model for the growth of silica nanoparticle was problematic. Similar problems were reported by Banfield and Zhang (2001) and they concluded that the JMAK theory may not be that suitable for analyses of reaction kinetics involving nano-phases and that the fitting constants should be interpreted with care. This led to the conclusion that the Thetadash model was more appropriate and the parameters and mechanisms obtained more accurate.

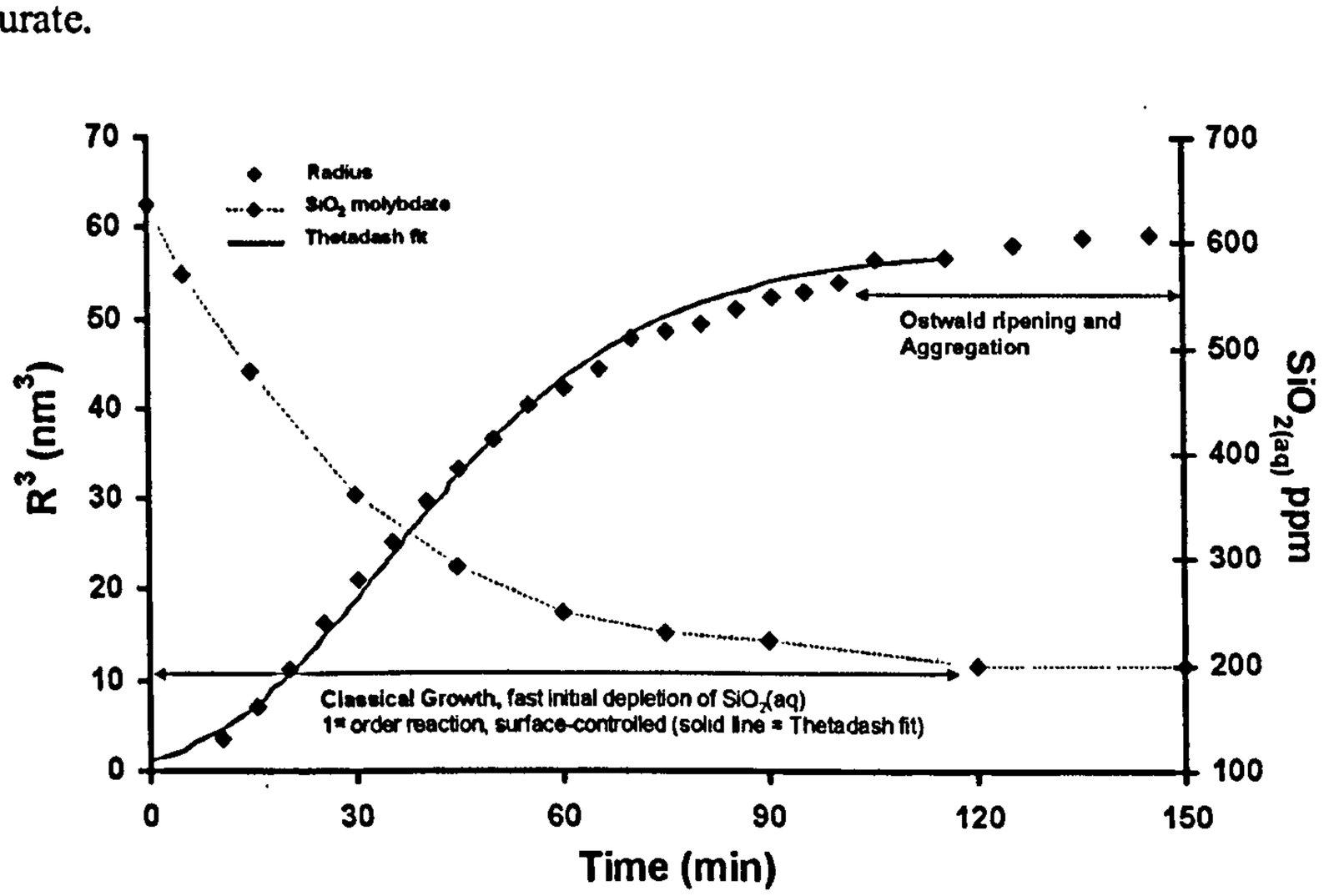

Figure 6.15: Schematic illustration of the growth stages of silica nanoparticles from supersaturated solutions. Instantaneous homogeneous nucleation occurs at t = 0min, followed by initial fast particle growth concomitant with the decrease in monosilicic acid (5 – 100 min) and by Ostwald ripening / particle aggregation at longer time scales.

Nevertheless, the calculated rate constants, regardless of the kinetic model from which they were derived, showed similar values and trends (Table 6.3). In both models, the rate constant increased with increasing IS (i.e., increasing supersaturation), with the Thetadash rate constants being larger than those obtained from the JMAK model (Table 6.3).

Rimstidt and Barnes (1980) obtained a reaction constant of 2.7×10^{-4} s^{-1} using a first order kinetic model to describe silica polymerisation (pH 7, T=25°C) which compares well with the values obtained in this study. Unfortunately, most other studies have used a reaction order >1 and the few that agreed on 1st order reaction kinetics differed in the reaction mechanisms (i.e., diffusion *vs.* surface-controlled mechanisms) making comparisons with other studies difficult. Furthermore, most previous studies followed the time-dependent decrease in monosilicic acid, i.e., the silica polymerisation process, and only inferred the reaction kinetics and mechanisms for silica nanoparticle growth. Despite silica polymerisation and silica nanoparticle growth being intimately connected, they are two very different processes (chemically-controlled polymerisation *vs.* 3-D, surface-controlled particle growth). Therefore, the reaction kinetics for the growth of silica nanoparticles can not be derived from the kinetics of the silica polymerisation process alone. The kinetic pathways seem to be further complicated by the complexity of the silica polymerisation process which to date is not well understood as indicated by the plethora of suggested reaction models for this process (Table 6.1). Furthermore, as shown by Harrison and Loton (1995) it might be necessary to divide the polymerisation process into distinct stages (e.g., dimerisation, oligomerisation) and to determine the mechanisms and kinetics for each stage in order to derive an overall mechanism of silica polymerisation in natural waters. This supports the approach employed in this study where the reaction kinetics for silica nanoparticle formation was determined by following *in-situ* and time resolved the nucleation and growth of silica nanoparticles in solution.

Ostwald ripening has been suggested by several studies to be involved in the process of silica nanoparticle growth. The fit of the SAXS data to the OR model was very poor for the initial stages of particle growth and only improved slightly for the later stages of growth as indicated by the somewhat linear trends in R *vs.* $t^{1/2}$, $t^{1/3}$ plots (Fig. 6.10), the increased polydispersity (Fig. 6.11) and the constancy of the invariant at later time points (Fig. 6.12). It seems reasonable to assume that OR did not occur within the initial stages of nucleation and growth of silica nanoparticles (within the time scale studied here), but may become more significant in the later stages of growth when the concentration of monosilicic acid approaches the solubility level and classical growth is energetically less favourable (Fig. 6.15).

6.5.3 The structure of silica nanoparticles

Analysis of the power-law regime of SAXS profiles showed that the structure of the scattering particles was continuously changing (i.e., increase in p and D_m respectively; Fig. 6.13) but that they were all mass fractals ($p < 3$) characterised by polymeric, open structures. This agrees well with previous studies (e.g., Iler, 1979, Perry and Keeling-Tucker, 2000) that have commented on the hydrous and porous structure of silica nanoparticles. A good illustration of the open nature of amorphous hydrated silica can be found in Perry and Keeling-Tucker (2000). It is not surprising, therefore that sample dehydration and exposure to high vacuum in the SEM and TEM measurements caused the particle structures to collapse, which explained the smaller particle sizes measured relative to SAXS/DLS and cryo-TEM (Table 6.2).

As shown in Figure 6.14, D_m increased from ~1 to a final size of 2.2-2.3 for the tested suspensions. This steady increase was caused by the continuous hydrolysis of the growing particles, with hydroxyl groups being removed from the particles by intra-particle densification / dehydration (Boukari et al., 1997). The establishment of the maximum D_m indicated the end of the densification process. Further growth of D_m to values > 3 which would mark the transition from mass to surface fractals (i.e., hydrolysis continues at the particle surface) was not observed. This is possibly a consequence of the short time scale probed in this study. Boukari et al. (1997) showed that depending on the saturation state of the solution as well as the physico-chemical conditions of the experiments, the transition from open, polymeric structures to smooth silica nanoparticles can take hours to weeks.

For alkoxides, Martin et al. (1990) and Lin et al. (1990) associated the fractal dimensions with an aggregation mechanism where objects that form during diffusion-limited colloid aggregation (DLCA; fast process) have low fractal dimensions (D_f = 1.7-1.8, porous aggregates) whereas during reaction-limited colloid aggregation (RLCA; slow process) compact aggregates with high fractal dimensions (D_f = 2.1-2.2) are produced. Applied to this study, the high fractal dimension, D_m = 2.2-2.3, obtained for the later stages of growth suggested slow, reaction-limited colloid aggregation. This is in good agreement with the decreased growth rates observed towards the end of silica nanoparticle growth where classical growth was no longer favourable and processes including OR and aggregation dominated.

6.5.4 Implications

Silica polymerisation and the formation of silica nanoparticles are widespread in nature and occur in many terrestrial environments (e.g., geothermal waters, brines, seawater). Silica nanoparticles are also extensively used in industry and medicine where they can be produced by

various methods to suit specific industrial applications. Regardless of the natural environment or the industrial application of silica nanoparticle formation, it is the size and structure that determines the chemical and physical behaviour (e.g., dissolution, adsorption, precipitation) of the nanoparticles. Therefore, it is essential to obtain a good understanding of the mechanisms and kinetics controlling the formation of silica particles including accurate measurements of the particle sizes and structures. The information obtained in this study demonstrated for the first time that the final diameter of silica nanoparticles precipitated from supersaturated silica solutions (~8nm from SAXS) was more than double the size cited in the literature (~3-4nm; e.g., Iler, 1979 and references therein, Icopini et al, 2005). This significant difference has a huge impact on the physico-chemical properties (e.g., specific surface area, chemical stability and reactivity) of the particles and therefore needs to be included in energetic considerations and kinetic analyses of chemical and physical processes that involve silica nanoparticles.

6.6 Summary

The time dependent decrease of monosilicic acid gave insight into the dynamics of silica polymerisation, whereas *in-situ* time-resolved SAXS and DLS measurements provided the essential tools to monitor and quantify the initial steps of nucleation and growth of silica nanoparticles in aqueous solutions. SEM and high-resolution TEM were used to image and verify results obtained by SAXS and DLS providing snap-shots of particle size and shape at specific time steps during the reaction.

Overall, the nucleation and growth of silica nanoparticle is governed by a series of processes governed by different kinetic mechanisms which can be divided into 3 main stages (Fig. 6.15):

(1) the nucleation stage characterised by instantaneous homogeneous nucleation where monosilicic acid polymerises to form stable nuclei with a diameter of between 1 and 2 nm

(2) the 3-dimensional growth of silica nanoparticles following first order reactions kinetics coupled with a surface controlled reaction mechanisms

(3) the late growth stage where classical growth ends and processes including Ostwald ripening and aggregation set in (especially at longer time scales).

Note that stage (1) and (2) are governed by the fast decrease of monosilicic acid while during the last stage the solubility level is almost established. At the end of this 3-stage process, regardless of the tested silica concentration and ionic strength, the final particle diameter was about 8nm characterised by mass fractal structure (i.e., open, polymeric structure).

6.7 Supplementary data

The initial steps of silica polymerisation and silica nanoparticle formation were also quantified in organic solutions (i.e., added glucose, glutamic acid or xanthan gum) using the same methodology as in the inorganic experiments. However, no effect on silica polymerisation and silica nanoparticle growth was observed and results were thus not further discussed here. A summary of the results is given in Appendix B.

7 THE FORMATION OF SILICA NANOPARTICLES INDUCED BY COOLING A SUPERSATURATED SOLUTION: STOPPED-FLOW EXPERIMENTS

7.1 Abstract

Stopped-flow experiments were carried out to quantify the formation of silica nanoparticles *in-situ* and in real-time with the polymerisation being induced by rapid cooling of a supersaturated silica solution. For this, a novel flow-through geothermal simulator system was designed to work on-line with a synchrotron-based Small Angle X-ray Scattering (SAXS) or a conventional Dynamic Light Scattering (DLS) detector system. The effects of SiO_2 concentration (640 *vs.* 960ppm), ionic strength (0.02 *vs.* 0.06) and temperature (30 to 60°C) on the initial steps of nucleation and growth of silica nanoparticles were determined.

Both SAXS and DLS results showed that the rate of silica polymerisation and nanoparticle formation was enhanced with increasing silica concentration while only minor changes were observed with increasing ionic strength or temperature. SAXS data showed that the size of the first detected particles ranged between 3 – 4 nm and that particles were still growing after 3 hours. Extrapolation of the SAXS growth curves suggested a final particle diameter of ~8nm.

Comparison to results from pH-drop experiments (chapter 6) showed that the mechanisms and kinetics of particle growth were unaffected by the two different methods to induce silica polymerisation (both following first order reactions kinetics coupled with a surface controlled reaction mechanism). However, the formation of silica nanoparticles from a supersaturated silica solution proceeded substantially slower if silica polymerisation was induced by fast cooling as opposed to pH-drop. This was evidenced by the occurrence of an induction period, the formation of larger critical nuclei, reduced particle growth rates and the absence of particle aggregation in the T-drop experiments. This is argued to be due to differences in (1) time length to establish supersaturation and (2) pH- and T-dependency of amorphous silica solubility.

7.2 Introduction

The precipitation of silica in active geothermal systems is a well known process leading to the silicification of microorganisms and to the formation of silica sinters. Several studies have considered the interaction processes between microorganisms and the inorganically nucleating silica particles (e.g., Ferris et al., 1988; Urrutia et al., 1992; Urrutia and Beveridge, 1994; Fein

et al., 1997, 2002; Cox et al., 1999; Phoenix et al., 2003; Yee et al., 2003, 2004; Benning et al., 2004a,b), or have studied the rates of amorphous silica nucleation in hot springs (e.g., Rothbaum et al., 1979; Weres, 1981; Carroll et al., 1998). Furthermore, a plethora of laboratory studies (e.g., Iler, 1979; Fournier, 1985; Rimstidt and Barnes, 1980; Icopini et al., 2005; Conrad et al., 2006 and chapter 6 in this study) investigated the mechanisms and kinetics of silica nanoparticle formation in solutions mimicking natural fluids, yet, silica polymerisation was usually induced by lowering the pH of a supersaturated, high-pH silica solution to near neutral values where silica solubility is at a minimum. However, in many natural systems (e.g., geothermal pools or deep-sea vents) silica polymerisation and silica colloid formation is the result of rapid cooling of a high-temperature, supersaturated near neutral fluid to ambient (geothermal) or low temperatures (deep sea) rather than a pH change.

So far, experimental challenges to simulate natural geothermal processes in the laboratory precluded the quantification of the kinetics and mechanisms of silica nanoparticles formation from cooling hot fluids. To overcome this gap, experiments were performed that aimed at elucidating the mechanisms of silica polymerisation and silica nanoparticle formation where polymerisation was induced by rapid cooling of a supersaturated silica solution. For this, a novel flow-through geothermal simulator system (modified after Benning and Mountain, 2004) was designed to work on-line with a synchrotron-based Small Angle X-ray Scattering (SAXS) or conventional Dynamic Light Scattering (DLS) cell and detector systems that permitted the *in-situ* and in real-time quantification of the nucleation and growth of silica nanoparticles. The SAXS and DLS data were complemented by electron microscopic imaging (Scanning and Transmission Electron Microscopy, SEM / TEM) to determine the size and polydispersity of the nucleating and growing silica nanoparticles. The reactions were monitored for a range of silica concentrations, ionic strengths and temperatures and results were compared to data from experiments where the polymerisation reaction was triggered by pH-drop (see chapter 6).

7.3 Methodology

7.3.1 Experimental set-up

The flow-through geothermal simulator designed to mimic the polymerisation process as it occurs in natural geothermal environments is illustrated in Figure 7.1. The system consists of a) a storage bottle that contains the experimental solutions (at 25°C), b) a HPLC pump to maintain a continuous flow of the solution at high pressures (p = 750psi), c) a high-temperature oven (kept at 230°C) with a 6m stainless steel coil, d) a backpressure regulator (BPR, set at 750psi) to

build up the required pressure to prevent the solutions from boiling and e) tubing to connect all the different parts.

A supersaturated ([SiO_2] = 640 or 960ppm, and ionic strengths of 0.02 and 0.06) and partly polymerised silica solution (at neutral pH) was pumped from the storage bottle into the high-T oven via the HPLC pump (Fig. 7.1). Inside the oven, the fluid passed through the steel coil and the high temperature caused the solution to fully de-polymerise, thus producing a pure monomeric silica solution (i.e., all silica is dissolved). This approach mimicked the conditions of silica-rich fluids in the Earth's crust at about 2-3 km depths and under hydrostatic pressures. After the hot solution emerged from the high-T oven (i.e., solution immediately starts to cool), it passed through the BPR located ~ 15 cm after the oven. This distance assured a fast temperature drop (within ~1 min) from 230°C to ~80°C (measured after BPR outlet) which caused the silica to become again highly supersaturated and hence induced silica polymerisation. This rapid cooling process simulates the conditions when a supersaturated hot spring fluid is discharged at the Earth's surface and polymerisation of the monomeric silica (i.e., monosilicic acid) is initiated.

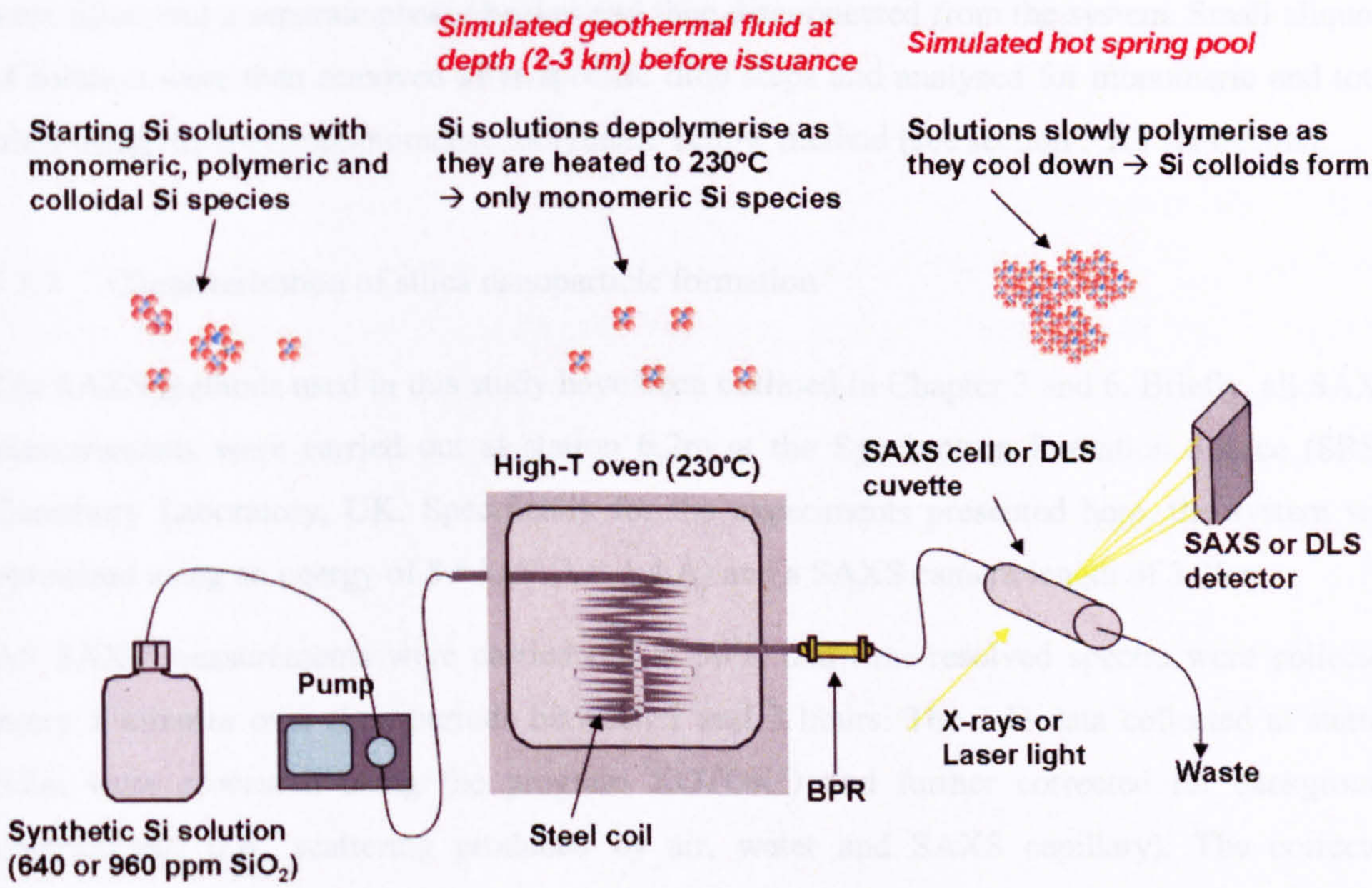

Figure 7.1: Schematic diagram of simulated hot spring system used to quantify silica nanoparticle formation induced by fast cooling of a solution saturated with silica (modified after Benning and Mountain, 2004).

This geothermal simulator allowed the *in-situ* and time-resolved monitoring of the very first steps of nucleation and growth of silica nanoparticles within the cooling polymerising solution. This was done by connecting the outlet of the BPR to a quartz capillary SAXS cell (1.5 mm OD and 10 mm walls) or a DLS cell (disposable plastic cuvette stationary placed in the DLS instrument) via Teflon tubing. Once filled, the SAXS and DLS cells were disconnected from the BPR and data acquisition was started (i.e., stopped-flow experiments; Fig. 7.1).

The initial supersaturated silica solutions were prepared by dissolving specific amounts of $Na_2SiO_2{\cdot}5H_2O$ and NaCl in deionised water. The pH of the highly alkaline solutions (~pH 12) was adjusted to 7 using 1M HCl and then filled into the storage bottle from where the solutions were pumped through the system (Fig. 7.1). During all experiments an increase of about 0.5 to 0.8 pH units was measured in the solutions emerging from the BPR. However as shown by previous studies (e.g., Iler, 1979) the rate of silica polymerisation is not affected by this pH increase and this could therefore be discounted in the data processing.

The silica polymerisation process was followed by the time-dependent decrease in monosilicic acid (up to 2 hours). For this, about 5 ml of the cooling polymerising solution (from the BPR) were filled into a separate plastic beaker and then disconnected from the system. Small aliquots of solution were then removed after specific time steps and analysed for monomeric and total silica using the spectrophotometric molybdate yellow method (see section 3.2.3 for details).

7.3.2 Characterisation of silica nanoparticle formation

The SAXS methods used in this study have been outlined in Chapter 3 and 6. Briefly, all SAXS measurements were carried out at station 6.2m at the Synchrotron Radiation Source (SRS), Daresbury Laboratory, UK. Specifically for the experiments presented here, the system was optimized using an energy of 8.5 keV (λ = 1.4 Å) and a SAXS camera length of 3.75 m.

All SAXS measurements were carried out at 30°C and time-resolved spectra were collected every 5 minutes over time periods between 1 and 3 hours. The 1-D data collected at station 6.2m were processed using the program XOTOKO and further corrected for background contributions (i.e., scattering produced by air, water and SAXS capillary). The corrected intensity files were analysed using GNOM to derive information about the size and polydispersity of the growing particles (see section 3.2.6 and 6.2.2 for details).

To corroborate SAXS results, *in-situ* dynamic light scattering (Zetasizer Nano ZS, Malvern Instruments; see section 3.2.5 for details) experiments were performed up to 3 hours using the same SiO_2 and IS conditions as for the SAXS experiments. In addition, the heating capability of

the DLS instruments (to 60°C) allowed particle growth (i.e., particle size and polydispersity) to be monitored also as a function of temperature (at 30, 40, 50 and 60°C).

Silica nanoparticles were imaged using field-emission gun (FEG) scanning electron microscopy (SEM) and transmission electron microscopy (TEM). More details of FEG-SEM and TEM sample preparation and imaging conditions are given in section 3.2.4 and 6.2.4. The size distributions of the silica particles were determined from the recorded TEM images. To obtain a size distribution with reasonably high precision, about 100 particles were measured in each image and the mean particle diameter and standard deviations (i.e., polydispersity) were calculated.

7.4 Results

7.4.1 Time course of the monosilicic acid concentration

In Figure 7.2A, the decrease in concentration of monosilicic acid, [SiO_2(aq)], is shown as a function of silica concentration (640 and 960ppm SiO_2) and ionic strength (0.03 and 0.06 IS). The plot reveals that the initial silica concentration and the degree of silica supersaturation respectively had a major impact on the rate of silica polymerisation as indicated by the fast depletion of [SiO_2(aq)] in the 960ppm SiO_2 experiment as compared to the delayed polymerisation reaction within the lower concentrated solution (640ppm SiO_2, Fig. 7.2A). In the 960ppm SiO_2 experiments (Fig. 7.2A, full and open squares), about 75% of [SiO_2(aq)] (with respect to amorphous silica solubility at 30°C; dotted line in Fig. 7.2A) polymerised within the first 20 minutes, whereas only 28% of [SiO_2(aq)] was removed at the lower concentration (Fig. 7.2A, crosses). In contrast, ionic strength had little effect on the overall decrease of [SiO_2(aq)] over time and the two data sets with 960ppm SiO_2 but with varying IS (0.03 *vs.* 0.06; Fig. 7.2A, full *vs.* open squares) were within error of each other. Note that after 2 hours, all three data sets reached a monosilicic acid concentration close to the amorphous silica solubility, indicating the end of the initial fast depletion in [SiO_2(aq)] (Fig. 7.2A).

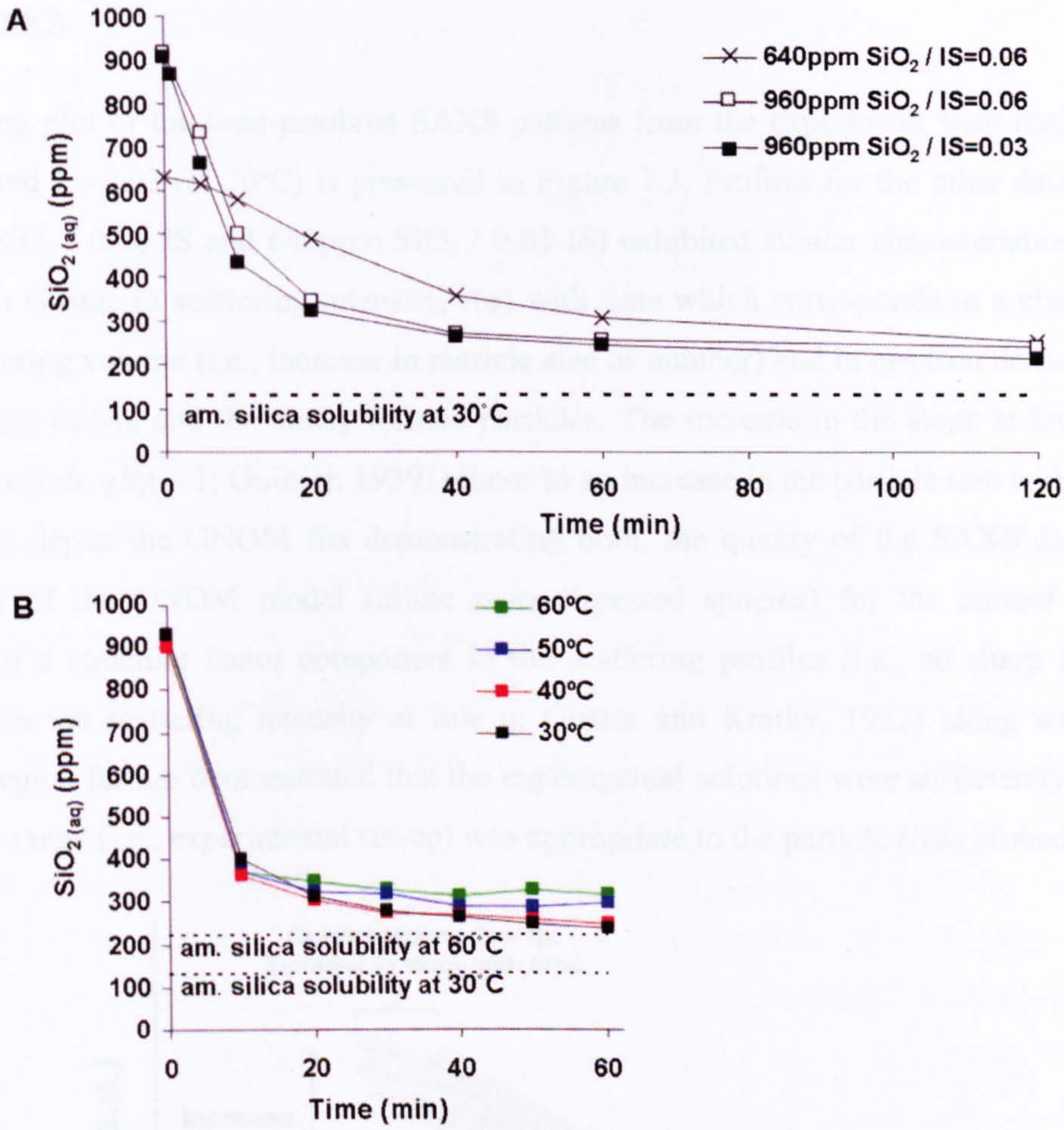

Figure 7.2: Time-dependent decrease in monosilicic acid, $SiO_2(aq)$, as a function of (A) silica concentration (640 *vs.* 960 ppm SiO_2) and ionic strength (0.03 *vs.* 0.06 IS; all experiments were carried out at 30°C) and (B) temperature (30 to 60°C) for experiments with 960ppm SiO_2 and IS=0.03. Dotted lines represent amorphous silica solubility from Gunnarsson and Arnórsson (2000).

The effect of temperature (30 to 60°C) on the polymerisation process for solutions with 960ppm SiO_2 and IS=0.03 is illustrated in Figure 7.2B. During the initial fast depletion in [$SiO_2(aq)$] (~80% with respect to silica solubility at the respective temperature, within the first 20 minutes) only small differences between the four tested temperatures were observed. Thereafter, the polymerisation process proceeded significantly faster at 30°C than at 60°C as expected from the decreased silica solubility at lower temperatures (dotted lines in Fig. 7.2B).

7.4.2 SAXS

The log-log plot of the time-resolved SAXS patterns from the experiment with initial SiO_2 of 960ppm and IS=0.03 (at 30°C) is presented in Figure 7.3. Profiles for the other data sets (i.e., 960ppm SiO_2 / 0.06 IS and 640ppm SiO_2 / 0.03 IS) exhibited similar characteristics. The plot revealed a change in scattering intensity, $I(q)$ with time which corresponds to a change in the total scattering volume (i.e., increase in particle size or number) and in electron density contrast between the matrix and the newly formed particles. The increase in the slope at low q angles (Guinier region, $qRg < 1$; Guinier, 1939) relates to an increase in the particle size with time. The solid lines depict the GNOM fits demonstrating both, the quality of the SAXS data and the suitability of the GNOM model (dilute monodispersed spheres) for the current data. The absence of a structure factor component in the scattering profiles (i.e., no sharp increase or decrease in the scattering intensity at low q; Glatter and Kratky, 1982) along with the flat Guinier region further demonstrated that the experimental solutions were sufficiently dilute and that the q-range (i.e., experimental set-up) was appropriate to the particle sizes probed.

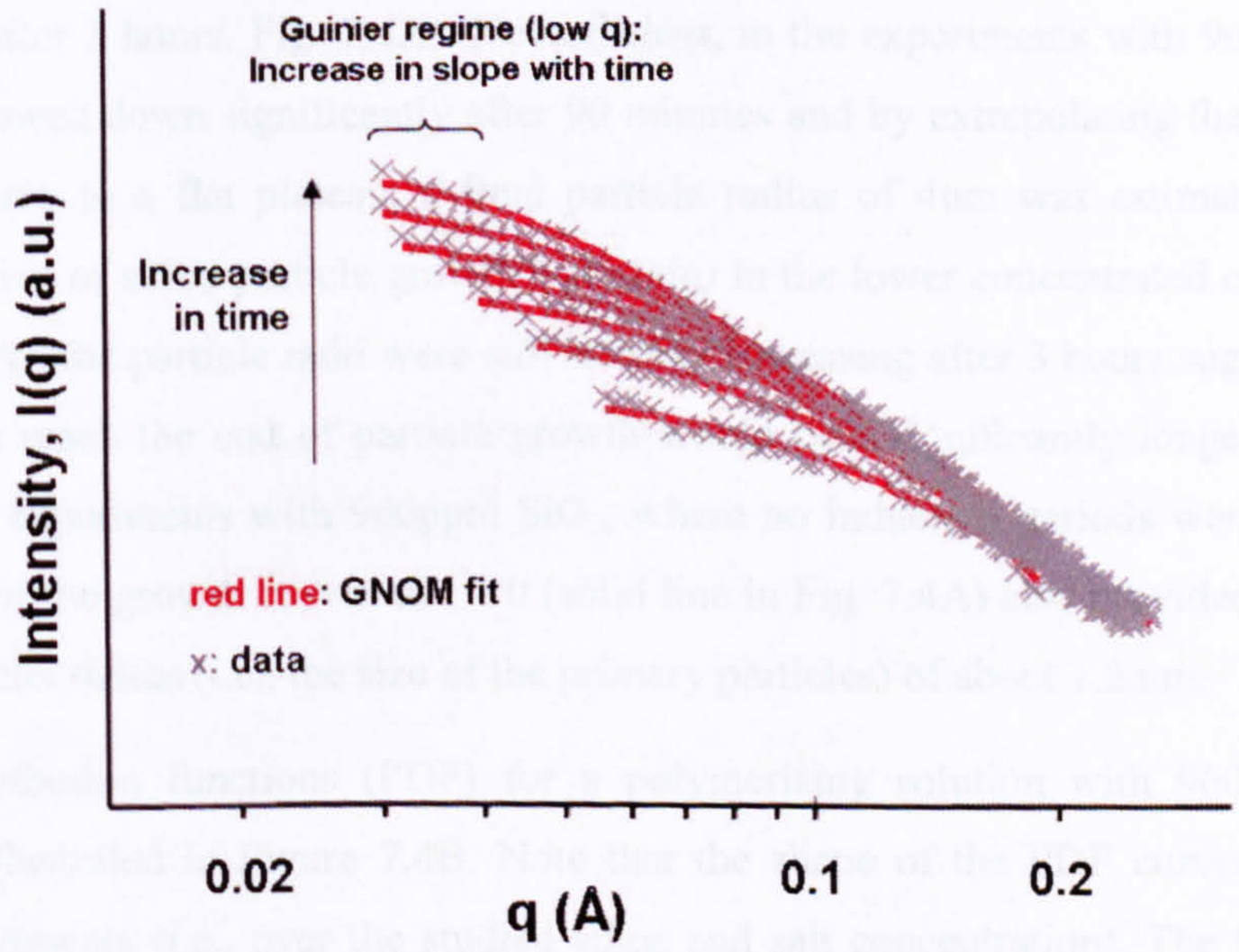

Figure 7.3: Log-log plot of the scattering intensity as a function of scattering angle and time (960ppm SiO_2, 0.03 IS, 30°C). The solid lines depict GNOM fits. For clarity, the errors for individual SAXS measurements (<3%) are not shown.

The radius of gyration, Rg was evaluated from the full scattering pattern using the GNOM code and the assumption of a monodisperse distribution (GNOM fits shown in Fig. 7.3). The real particle radius, R, was then calculated using Rg and equation 3.4 (section 3.2.5).

Figure 7.4A shows the increase in *R* over time as a function of different SiO_2 and IS. In this plot, t=0 denotes the point where the hot solutions reached the SAXS cell (i.e., about 1-2 minutes after emerging from the high-T oven). Note that no SAXS measurements could be obtained for the initial 10 minutes due to the experimental set-up (i.e., ~ 5 min preparation time to start SAXS experiments and securing the hutch) and the time needed to acquire the first data point (i.e., 5 minutes)

No differences were observed in either the particle size or the particle growth rate between data obtained for the reactions with high SiO_2 (960ppm) but different IS (0.03 *vs.* 0.06). In contrast, particle growth was significantly delayed in the lower concentrated solution (640ppm SiO_2, 0.06 IS; Fig. 7.4A crosses) with an induction time of approximately 60 min. These results agreed with the observations from the depletion of monosilicic acid over time (Fig. 7.2A) and reaffirmed that silica concentration (i.e., silica supersaturation) was the prime control for the rate of silica polymerisation and silica particle growth, while the differences in IS did not cause any deviations. Based on the observations from the depletion in monosilicic SiO_2, SAXS patterns were acquired for 3 hours, yet a final particle size was not reached (i.e., particles were still growing after 3 hours, Fig. 7.4A). Nevertheless, in the experiments with 960ppm SiO_2 the growth rate slowed down significantly after 90 minutes and by extrapolating the progression of the growth curve to a flat plateau, a final particle radius of 4nm was estimated. Due to the delayed initiation of silica particle growth (~60 min) in the lower concentrated experiment (640 SiO_2, Fig. 7.4A), the particle radii were still steadily increasing after 3 hours suggesting that the time length to reach the end of particle growth would take significantly longer (about 5 to 6 hours). In the experiments with 960ppm SiO_2, where no induction periods were observed, the extrapolation of the growth curves to t = 0 (solid line in Fig. 7.4A) also provided an estimate of the critical nuclei radius (i.e., the size of the primary particles) of about 1.2 nm.

The pair distribution functions (PDF) for a polymerising solution with 960ppm SiO_2 and IS=0.03 are illustrated in Figure 7.4B. Note that the shape of the PDF curves did not differ between experiments (i.e., over the studied silica and salt concentration). The PDF plots were slightly skewed towards the right but the near-Gaussian shape of the PDFs supported the assumption of fairly monodisperse, spherical silica nanoparticles. The observed tails could either relate to the presence of aggregates or the presence of some degree of polydispersity. The increase in both the area under the curve and the apex of the curve indicated an increase in particle size.

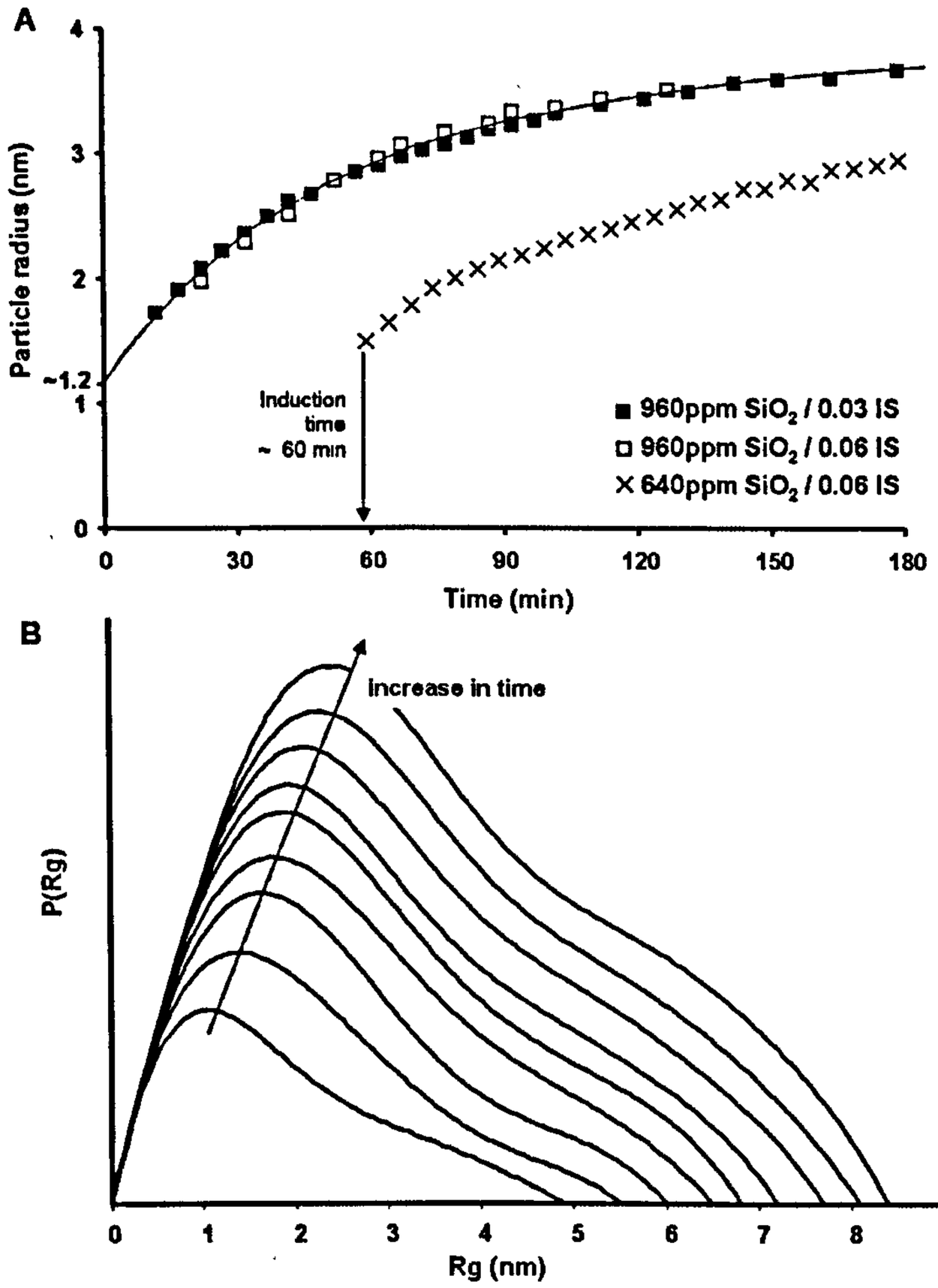

Figure 7.4: A) Time course of *R* as obtained from the GNOM analysis in solutions with 640ppm and 960ppm SiO_2 and different IS (note that the errors were typically ~3%). The solid line shows the extrapolation of the growth curve to t = 0 to estimate the critical nuclei radius (R_0 ~ 1.2 nm). B) PDF of scattered silica nanoparticles as a function of *R*g and time evaluated with GNOM (960ppm SiO_2, 0.03 IS).

7.4.3 DLS

The time-resolved DLS data are illustrated in Fig. 7.5A. Due to the lower resolution of DLS at small particle sizes, DLS data displayed substantially more scatter and the average % error of DLS experiments ranged between 27 and 56% (for clarity these errors are not shown in Fig. 7.5) as compared to the 1 - 3% error for the SAXS data. Despite these larger errors, overall, the trends between particle growth rate and SiO_2 concentration and IS respectively were similar to those observed with SAXS. While in the 960ppm SiO_2 experiments the first particles (~3 nm in diameter) were detected after 15 minutes, an induction period of about 35 minutes was observed for the first particles in the 640ppm SiO_2 experiment. Compared to the SAXS results, this

induction time was ~25min shorter, but the large scatter in the DLS data (particularly below t = 60 min) indicated that these initial data points might not be reliable. In contrast to the SAXS data, the particle diameters derived by DLS seemed less affected by SiO_2 and were within the average % error of each other. Note that this was most certainly the result of the lower resolution of DLS indicating the limitation of this method for the size analysis of nanoparticles in the range between 1 and 10 nm.

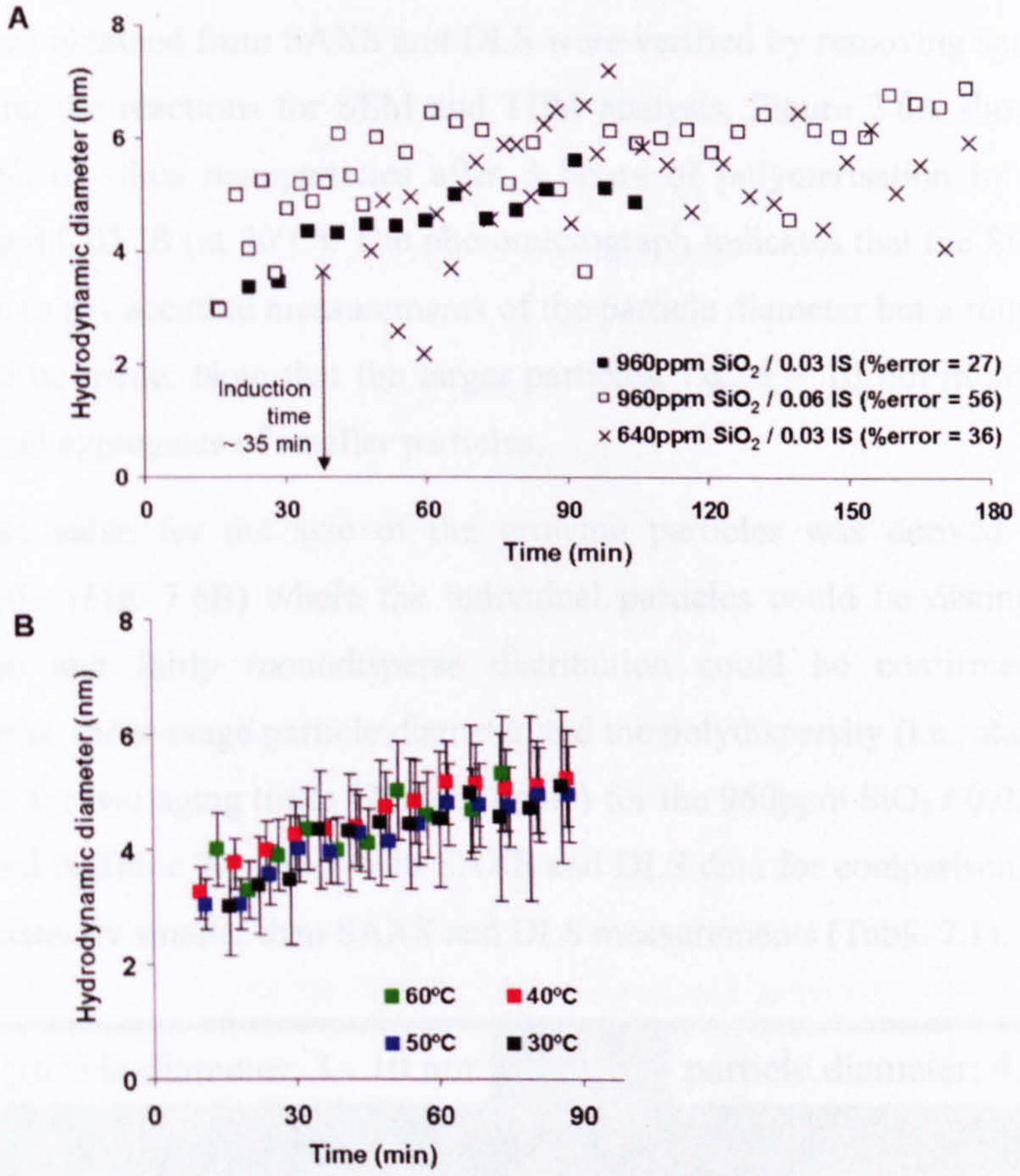

Figure 7.5: A) Growth of silica nanoparticles in solutions with varying SiO_2 and IS as determined by DLS (at 30°C). The arrow indicates the induction period (i.e., first detectable particle) for the 640ppm SiO_2 experiment (listed % errors are average values for a specific experiment). B) Growth of silica nanoparticles in solutions with 960ppm SiO_2 and 0.03 IS as a function of temperature (30 to 60°C).

In Figure 7.5B the influence of temperature (30 - 60˚C) on the growth of silica nanoparticles is shown for solutions with 960ppm SiO_2 and 0.03 IS. The plot indicates that the temperature change from 30 to 60˚C appeared to have no detectable effect on particle size and growth rate. In all growth profiles, the first detectable particles had a diameter of around 3 nm which then increased to about 5nm within the first 90 minutes. Due to enhanced silica solubility at higher

temperature, one would expect lower polymerisation rates (similar to the time-dependent depletion in monosilicic acid; Fig. 7.2) and therefore slightly different particle growth profiles. However, the substantial errors in DLS experiments indicated that even if differences in particle size and particle growth rate were present they could not have been revealed by DLS.

7.4.4 Electron Microscopy

The particle sizes obtained from SAXS and DLS were verified by removing samples at various time steps during the reactions for SEM and TEM analysis. Figure 7.6A shows a FEG-SEM photomicrograph of silica nanoparticles after 3 hours of polymerisation in a solution with 960ppm SiO_2 and 0.03 IS (at 30°C). The photomicrograph indicates that the SEM resolution is slightly too low to get accurate measurements of the particle diameter but a rough estimate of 3 to 10 nm could be made. Note that the larger particles, i.e., 5 – 10 nm in size in Fig. 7.6A, possibly represent aggregates of smaller particles.

A more precise value for the size of the growing particles was derived from the TEM photomicrographs (Fig. 7.6B) where the individual particles could be distinguished and the spherical shape and fairly monodisperse distribution could be confirmed. Using TEM photomicrographs, the average particle diameter and the polydispersity (i.e., standard deviation) was determined for two aging times (2 and 3 hours) for the 960ppm SiO_2 / 0.03 IS experiment. Results are listed in Table 7.1 along with SAXS and DLS data for comparison. Note that TEM values are consistently smaller than SAXS and DLS measurements (Table 7.1).

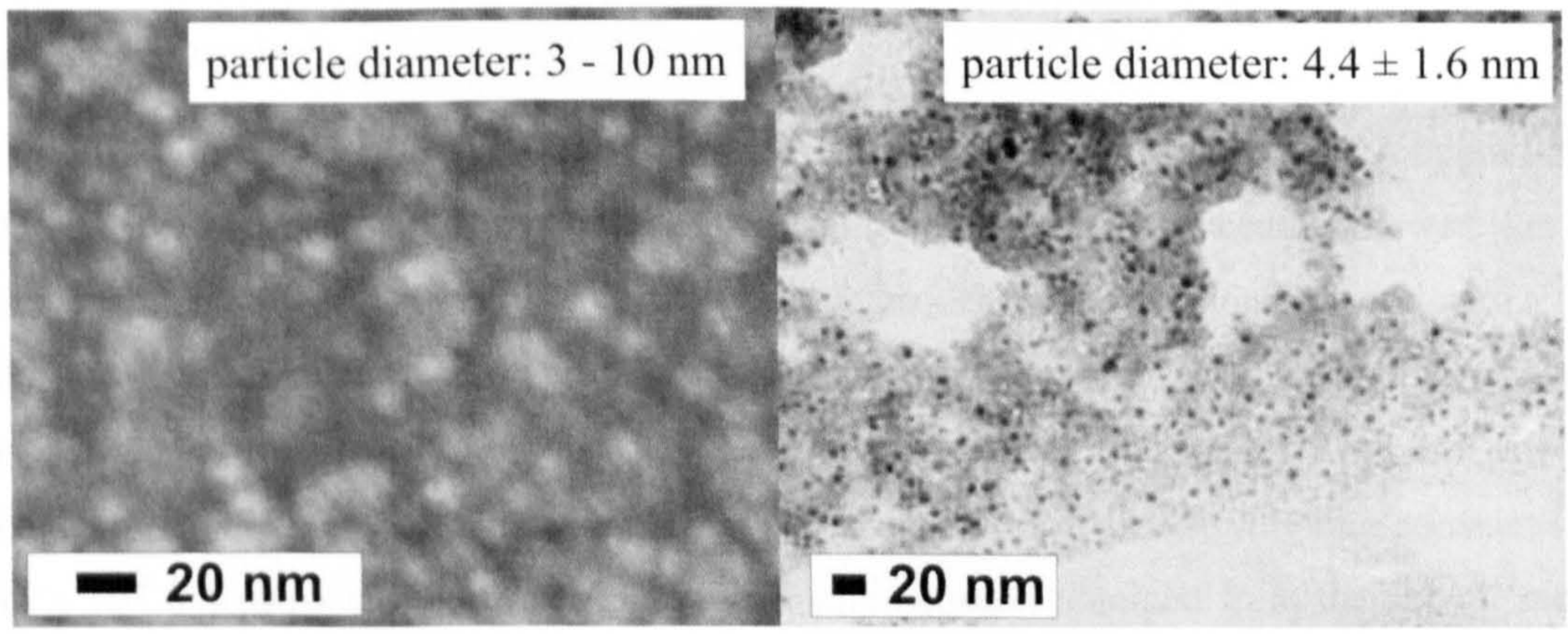

Figure 7.6: Photomicrograph of silica nanoparticles grown for 3 hours in a solution with 960ppm SiO_2 and IS of 0.03 (at 30°C) imaged by A) FEG-SEM (white spots = particles) and B) TEM (black spots = particles).

Table 7.1: Comparison of particle diameter obtained from SAXS, DLS and TEM.

SiO_2 (ppm)	IS	Time (h)	Particle diameter (nm)		
			SAXS	DLS	TEM
960	0.03	2	6.8 ± 0.2	5.7 ± 2.9	3.2 ± 0.6
		3	7.3 ± 0.2	6.6 ± 3.3	4.4 ± 1.6

7.4.5 Kinetic analysis of SAXS data

To evaluate the reaction kinetics for the formation of silica nanoparticles, the time-resolved SAXS data from the experiments with 640 and 960 ppm SiO_2 and IS of 0.03 and 0.06 were fitted with the Thetadash and the JMAK kinetic models which are both based on classical growth theory (see section 3.2.6 and 6.3.6 for details). However, the fitting of the SAXS data to these two models turned out to be problematic due to the following three reasons: 1) the final particle size was not reached within the tested time period (particularly in the 640ppm SiO_2 experiment), 2) the poor quality of the scattering pattern for the first 10 - 20 minutes in both 960ppm SiO_2 experiments (this is because >300 data points from individual scattering profiles needed to be omitted during GNOM analysis) and 3) the occurrence of an induction period in the 640ppm SiO_2 experiment (i.e., point in time where particles nucleated is unknown). As a consequence, the kinetic modelling of the SAXS data from the 640ppm SiO_2 / 0.06 IS and the 960ppm SiO_2 / 0.06 IS experiment did not yield reasonable results and were excluded in the following discussion.

In Figure 7.7, the fits to the Thetadash and to the JMAK model are shown for the 960ppm SiO_2 / 0.03 IS experiment (i.e., most complete growth profile). The fitting procedure showed that the fit between the SAXS data and the Thetadash kinetic model were exceptionally good with a first order rate law coupled with a surface-controlled mechanism (Fig. 7.7A). Data analysis with Thetadash also provided information on the size of the critical nuclei (R_0 = 1.47 nm) and the initial growth rate ($G_0 = 1.52 \times 10^{-12}$ s^{-1}). G_0 was then used to calculate the rate constant ($k = 1.46 \times 10^{-4}$ s^{-1}) using eq. 3.8 to compare to the rate constant obtained from the JMAK model (fig. 7.7B).

The fit between the JMAK model and the SAXS data was also very good (Fig. 7.7B) supporting that the initial steps of silica nanoparticle growth proceed via classical growth. The fitting procedure also provided a value for the JMAK exponent n (1.3) and the rate constant ($k^* = 2.12 \times 10^{-4}$ s^{-1}, eq. 3.6).

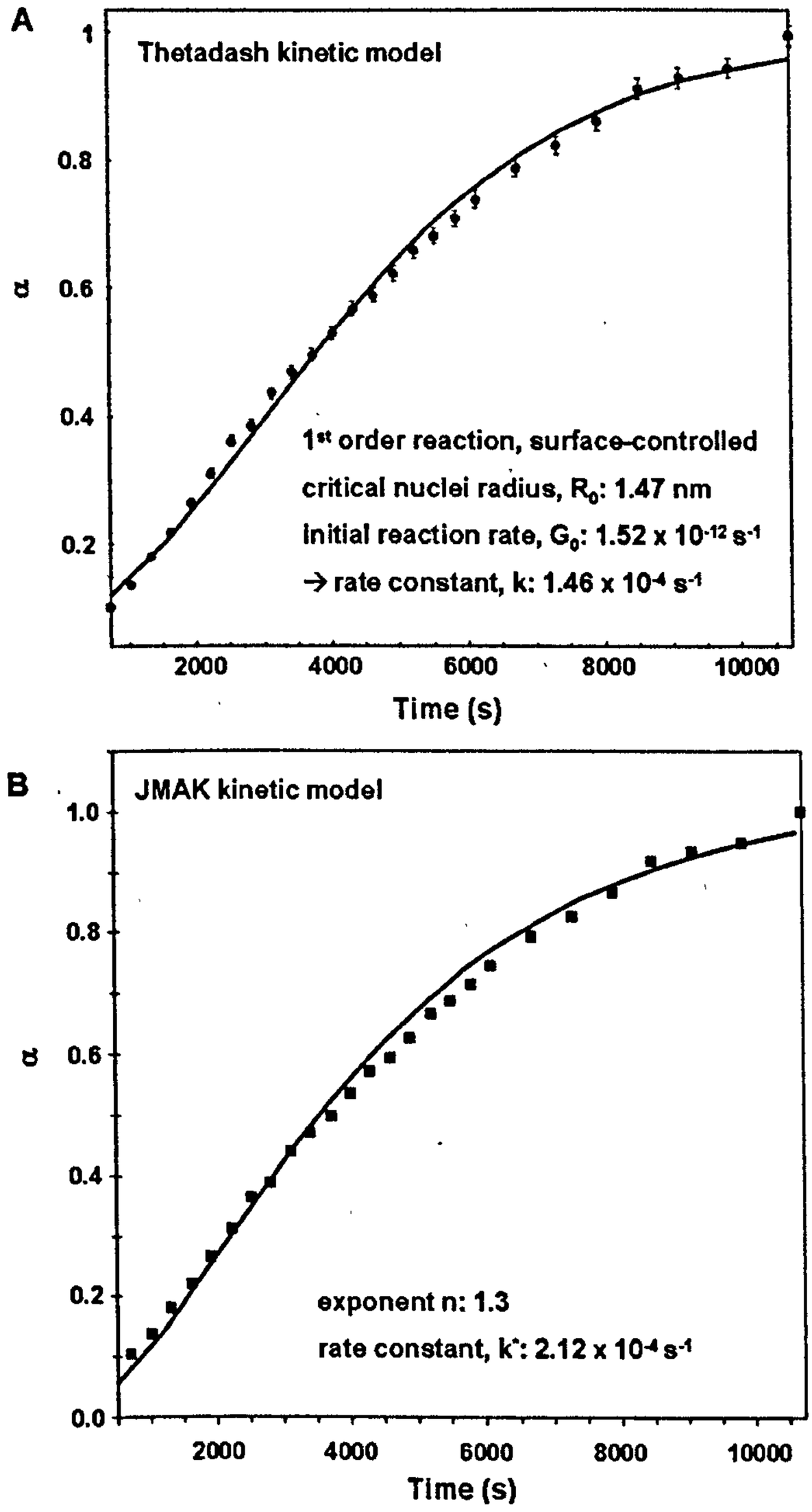

Figure 7.7: Reaction process, α (eq. 3.7), with time for the 960ppm SiO_2 / 0.03 IS experiment. The solid lines represent the fits to the (A) Thetadash and the (B) JMAK kinetic model. Also shown are the parameters that were obtained from the fitting procedure to both the Thetadash and JMAK kinetic models.

7.5 Discussion

For the first time, the nucleation and growth of silica nanoparticles was quantified *in-situ* and under simulated hot spring conditions using a flow-through geothermal simulator. All experiments were conducted at neutral pH with varying silica concentrations (640 *vs.* 960 ppm SiO_2), ionic strengths (0.03 *vs.* 0.06 IS) and temperatures (30 to 60°C). Both SAXS and DLS

results confirmed previous studies that concluded that the rate of silica polymerisation and nanoparticle formation was affected by increasing silica concentration (e.g., Rothbaum and Rhode, 1979; Icopini et al., 2004; Conrad et al., 2007). Similarly, a change in ionic strength or temperature was expected to affect the silica solubility and hence the polymerisation reaction and particle growth rate (see chapter 6). However the tested IS (0.03 *vs.* 0.06) and T (30 to 60°C) variations may have been too small to have an observable effect, i.e., the differences could not be resolved with the techniques employed.

In all experiments the reacting solutions were supersaturated with respect to amorphous silica and the degree of saturation (i.e., the silica concentration) invariably affected the growth rates and hence the time lengths for the reactions. In the 960ppm SiO_2 experiments, the polymerisation reaction did not exhibit an induction period (Fig. 7.2), i.e., the first silica nanoparticles were detected 10 min after the initiation of the silica polymerisation reaction (i.e., time required to prepare / start the SAXS experiment and to acquire the first data point, Fig. 7.4A). In contrast, the polymerisation process and particle growth was delayed in the 640ppm SiO_2 experiments (Fig. 7.2) and particles were not detected until 60 min after cooling the solution (Fig. 7.4A). Note that in the 640ppm SiO_2 experiments, although scattering patterns were recorded (from t = 10 – 55min, Fig. 7.4A), the patterns were indistinguishable from the background, i.e., no particles were detected. Nevertheless, particles might have already nucleated after about 10 to 15 minutes (at the time when polymerisation started; Fig. 7.2) but may have been unstable within the polymerising solution and re-dissolved again. Once a certain degree of polymerisation was reached (i.e., ~65% had polymerised at t = 60 min) the critical nuclei were energetically stable and started growing.

7.5.1 Particle size analysis

Particle growth curves obtained from SAXS showed that the size of the first detected particles ranged between 3 – 4 nm (depending on the concentration) and that particles were still growing after 3 hours (based on the observation of the time-dependent depletion in monosilicic acid, data acquisition stopped thereafter). Although at 960ppm SiO_2, a plateau (i.e., a final particle size) was almost reached, at 640ppm SiO_2 the particles were still increasing in size substantially after 3 hours. By extrapolating the progression of the growth curve, a final particle diameter of ~8 nm was estimated for the 960ppm SiO_2 experiments. For the 640ppm SiO_2 experiment, a similar final size was expected from the trend of the growth curve but also from previous observations which suggested that the final particle size was not affected by the degree of silica saturation (see section 6.4.1).

Although the formation of the critical nuclei could not be quantified, the radius of the critical nuclei was calculated using the Gibbs-Kelvin approach (eq. 2.2) and was also obtained from the fitting to the Thetadash kinetic model (Fig. 7.7A, Table 7.2). Furthermore, by extrapolating the growth curve to t = 0, a third estimate of R_0 could be derived (Table 7.2).

Table 7.2: Summary of evaluated critical nuclei radius, R_0 (R_0^+ was calculated using the Gibbs-Kelvin approach; R_0 was obtained from Thetadash analysis and R_0^E was estimated by extrapolating the progression of the growth curve to t=0).

Experiment	R_0^+ Gibbs – Kelvin Approach	R_0 Thetadash kinetic model	R_0^E Extrapolation of growth curve
640ppm SiO_2, 0.06 IS	1.07 nm	-	-
960ppm SiO_2, 0.03 IS	0.85 nm	1.47 nm	~1.2 nm
960ppm SiO_2, 0.06 IS	0.85 nm	-	-

The R_0^+ values obtained from the Gibbs-Kelvin approach showed that the critical nuclei radius was significantly lower (~20%) in higher concentrated silica solutions and little influenced by IS (Table 7.2). This is not surprising as the nucleation process has a higher driving force in more saturated solutions (i.e., higher concentrations) thus enabling the stabilisation of smaller nuclei (more energy is needed to sustain a higher surface to volume ratio). Only one SAXS profile could be used for the Thetadash analysis (see above) and therefore, only one R_0 value (from the 960ppm SiO_2 / 0.03 IS experiment) was evaluated to compare to the R_0^+ values calculated with the Gibbs-Kelvin approach (Table 7.2). The disagreement between theses two values, i.e., R_0 is almost twice as big as R_0^+, is probably the result of the poor quality of the SAXS data at the start of data acquisition (in both 960ppm SiO_2 experiments) and thus, R_0 obtained from Thetadash might not be as accurate. This was further supported by the critical nuclei radius obtained from the extrapolation of the full growth curves (R_0^E ~ 1.2 nm, Fig. 7.4A) which better matched the R_0^+ value calculated with the Gibbs-Kelvin approach (R_0^+ = 0.85 nm). It should be noted that the critical nuclei size obtained from the Gibbs-Kelvin approach is solely controlled by the degree of supersaturation (assuming molar volume and surface free energy remain constant) and thus does not consider any other parameters (e.g., induction time, presence of salts / organics) that could potentially influence the critical nuclei size.

To compare the SAXS results with the DLS and TEM data, the particle radii determined from SAXS were converted to particle diameters (Table 7.1). Figure 7.8 shows the direct comparison between the SAXS and DLS results for the growth of silica nanoparticles in solutions with 960ppm SiO_2 and IS of 0.06. For clarity, the errors of the DLS measurements are not shown. Both growth curves followed similar trends, although the DLS data scatter substantially more than the SAXS data due to the lower accuracy of the DLS measurements. In both data sets the diameter of the first detected particle ranged between 3 and 4 nm which then steadily grew by the addition of monomers to trimers and oligomers (e.g., Perry and Keeling-Tucker, 2000). After 3 hours they reached a size of about 6 - 7 nm (Fig. 7.8) but were still growing (although at a substantially slower rate).

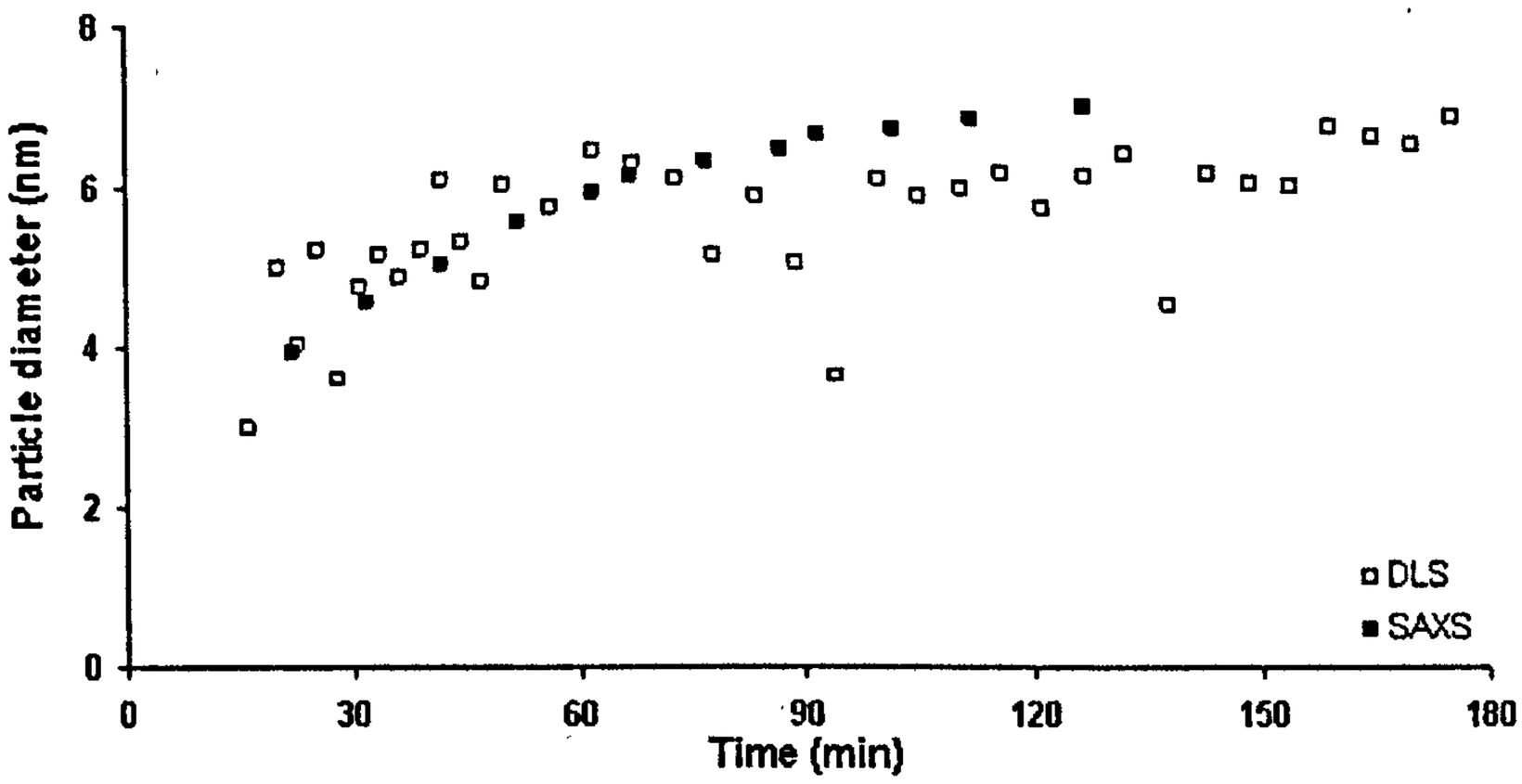

Figure 7.8: Change in particle diameter during the growth of silica nanoparticles as a function of time in a silica solution with 960ppm SiO_2 and IS = 0.06 measured by SAXS and DLS.

From previous results (chapter 6), one might expect particle aggregation towards the end of the growth process, however only few aggregates were seen with SEM and TEM. Furthermore, despite DLS measurements being highly susceptible to the presence of larger aggregates (see section 6.3.3) no indications for particle aggregation (e.g., sudden increase in particle size) were observed in any of the acquired DLS profiles. This suggests that for the tested conditions, the nucleating and growing particles were relatively stable within the polymerising solution and did not aggregate over the studied 3 hours.

The particle diameters obtained from TEM were significantly smaller (up to 50%) than those derived from DLS and SAXS (Table 7.1). This was not unexpected as for TEM analyses samples are dried and placed under high vacuum and thus they undergo dehydration and relaxation processes causing the highly hydrous (up to 13 wt% water, section 2.2.2) and open-

structured particles to collapse. Furthermore, the errors on single size measurements obtained from TEM images are in the order of 15-30% as compared to <3% for SAXS data points.

Note that so far the assumption was made that the scattering (for both DLS and SAXS) was produced by monodisperse particle suspensions. This means that all particles have the same size at all times during the reaction and that all particles nucleated at the beginning of the reaction. However, as indicated by the slightly skewed PDF distribution (Fig. 7.4B), the large average errors of the DLS measurements (Fig. 7.5) and the SEM/TEM photomicrographs (Fig. 7.6), the studied systems exhibited some degree of polydispersity.

Comparison to pH-lowering experiments (chapter 6)

Most previous experimental studies that followed silica polymerisation and silica nanoparticle growth have induced silica polymerisation by lowering the solution pH from highly alkaline pH to near neutral values where silica solubility is at a minimum (e.g., Alexander et al., 1954; Iler, 1979; see also chapter 6). Yet, in natural geothermal systems the polymerisation reaction is a result of rapid cooling of a supersaturated near neutral fluid. Naturally, one would expect that the polymerisation reaction and thus silica nanoparticle growth should be similar regardless of the method applied (i.e., pH- *vs.* T- drop) to induce silica supersaturation (assuming the tested solutions are identical). However, the comparison between results from this and the previous chapter (Fig. 7.9, Table 7.3) as well as data in the literature indicates substantial differences in polymerisation and particle growth rates between the two methods. Note that the slight difference in IS between the two illustrated data sets (Fig. 7.9; pH-drop/0.02 IS *vs.* T-drop/0.06 IS) could be neglected as demonstrated above (Fig. 7.4).

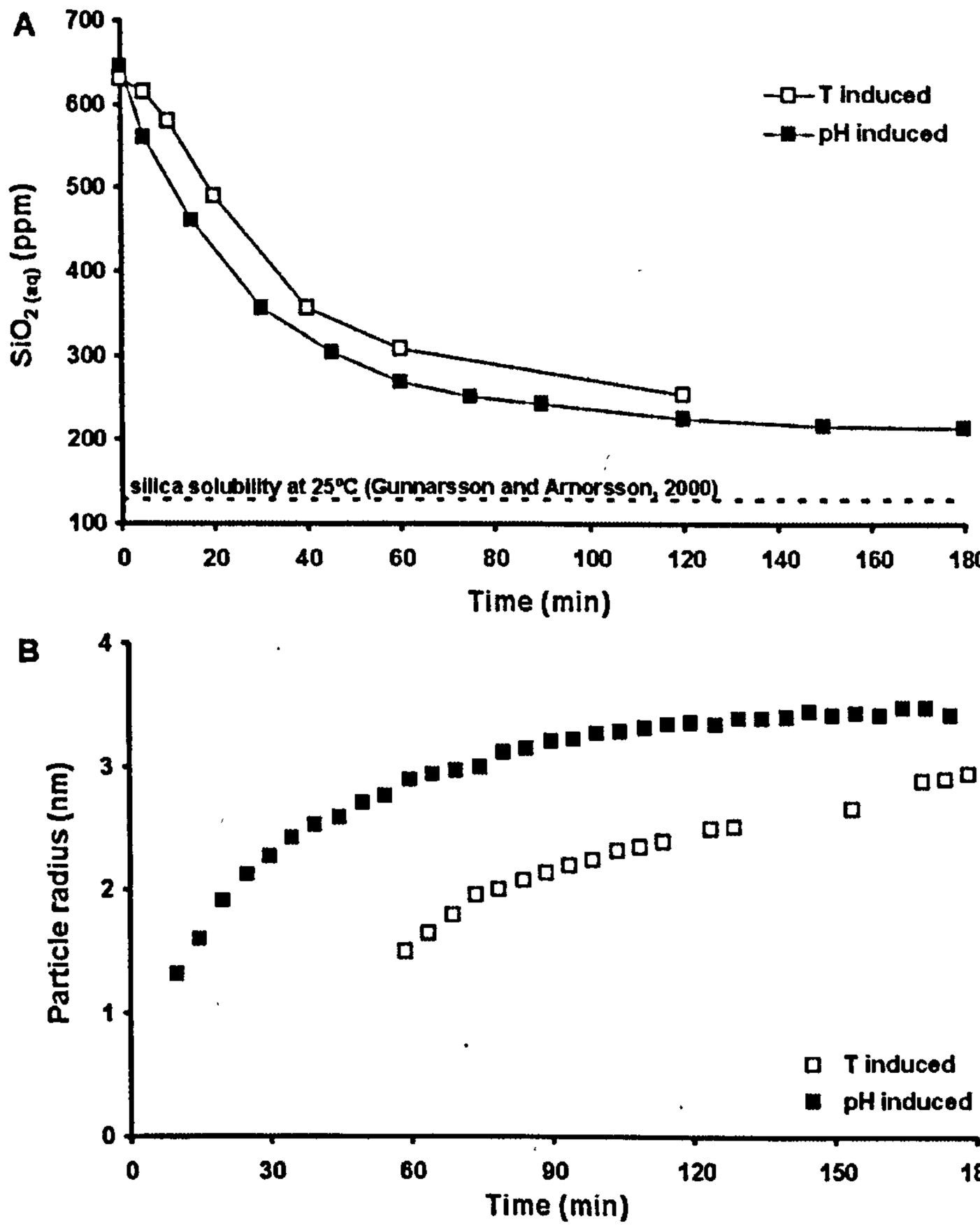

Figure 7.9: The effect of T- and pH- induced silica supersaturation on (A) the time-dependent depletion in monomeric SiO_2 and (B) the increase in SAXS particle radius over time in solutions with 640ppm SiO_2 (both experiments were carried out at 30°C).

The dominant trend observed in Figure 7.9A indicates that the polymerisation reaction proceeds faster when induced by pH-drop than by fast cooling. This is shown by the slight delay in the depletion in monosilicic acid in the T-drop experiments (~ 5-10 min) compared with the more immediate decrease in monosilicic acid in the pH-drop experiment (Fig. 7.9A). A similar trend was observed in the growth profiles (Fig. 7.9B): in the T-drop experiment, the particles started growing after ~60 minutes while growth seemed instantaneous in the pH-drop experiment (first detected particle at 10 min, Table 7.3).

Table 7.3: Comparison of reaction kinetics between pH- and T-drop experiments (see text) for solutions with 640ppm SiO_2.

	pH – drop	T – drop
	640ppm SiO_2 0.03 IS	640ppm SiO_2, 0.06 IS
Nucleation		
R_0 Gibbs-Kelvin Approach	1.07	1.07
R_0 Thetadash	1.07	1.47
Instantaneous nucleation	yes	no
Induction period	no	~ 60 min
Particle growth		
1st order reaction, surface-controlled	yes	yes
Thetadash rate constant ($x10^{-4}$ s^{-1})	3.18	1.46
JMAK rate constant ($x10^{-4}$ s^{-1})	2.77	2.12
Aggregation		
DLS	yes	no
SEM / TEM	yes	no

The discrepancy in polymerisation and particle growth rates seem to be the result of differences in time to establish supersaturation. In the pH-drop experiments, the sudden change in pH from 12 to 7 (<30 s) induces instantaneous supersaturation and thus forces the monosilicic acid to polymerise. In contrast, the "fast" cooling process of the hot fluid from 230°C to 30°C occurs over 2 to 3 minutes as a result of which supersaturation is not reached instantaneously but rather increases continuously as T decreases. Therefore, the polymerisation process is less driven and proceeds slower. In addition, the pH- and T-dependency of silica solubility differ substantially from each other (Fig. 7.10). In the case of pH, silica solubility is at a minimum around pH 6 to 9 but then increases drastically at pH > 9 (Fig. 7.10A) whereas in the case of T, the solubility does not exhibit any dramatic changes but steadily increases with increasing T (Fig. 7.10B; more details are given in section 2.1.3). This further suggests that the radical change in pH will enforce the polymerisation reaction substantially more than the change in T. Interestingly, the final particle size was not affected by these different methods and for various silica concentrations and ionic strengths (Fig. 6.4, 7.4) a final particle diameter of 7 - 8 nm was derived.

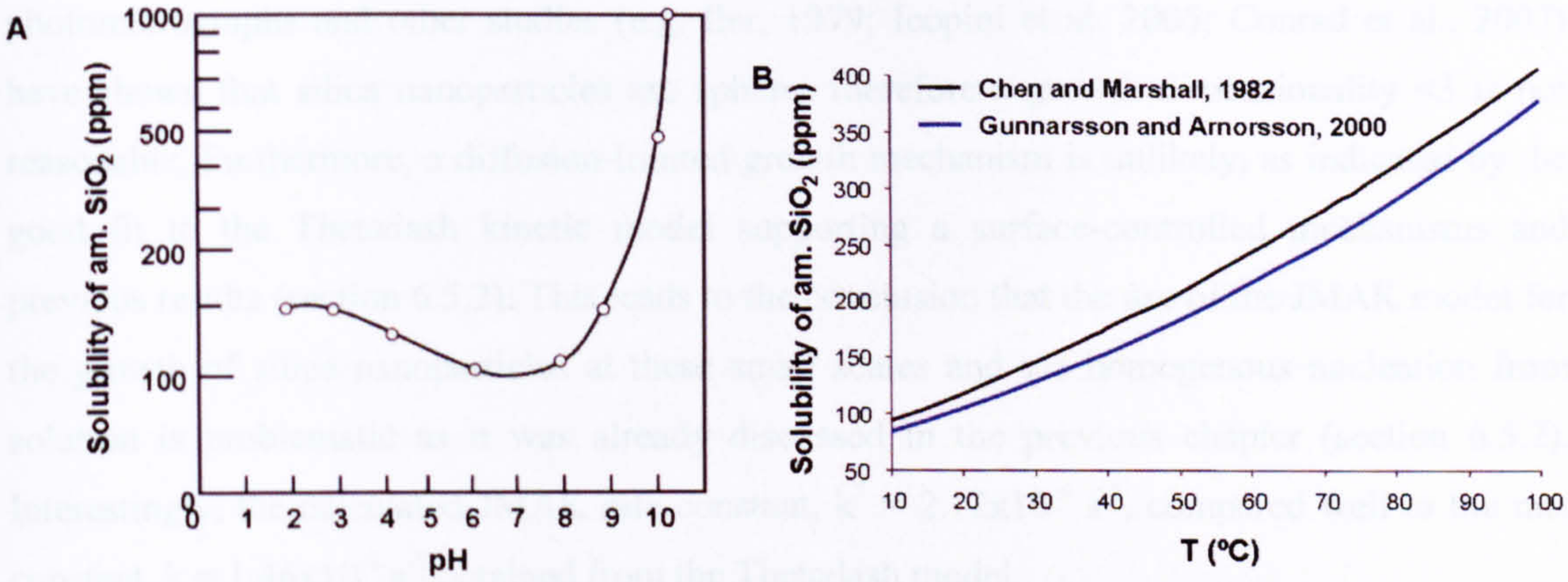

Figure 7.10: Amorphous silica solubility as a function of A) pH (Alexander et al., 1954) and B) temperature (in salt-free solutions).

7.5.2 Kinetics and mechanism of particle growth

The initial stage of silica nanoparticle formation from a supersaturated solution is characterised by silica polymerisation and the nucleation of stable nuclei with sizes around 2 – 3 nm (Table 7.2). The nucleation mechanism is assumed to be homogeneous and instantaneous (see section 6.5.2 for details). SAXS results presented here however, do not support instantaneous nucleation in the case of T-drop due to the occurrence of an induction period in the 640ppm SiO_2 experiment. In addition, the poor quality of the scattering data at the start of the 960 ppm SiO_2 experiments concealed essential particle size information for the initial 10-20 minutes. Nevertheless, the good fit of the SAXS data to the Thetadash kinetic model, which assumes instantaneous nucleation (Fig. 7.7A) suggested that in the 960ppm SiO_2 experiment, instantaneous nucleation might have occurred.

The second stage of silica nanoparticle formation is governed by the fast decrease of monosilicic acid (Fig. 7.2) and the 3-dimensional growth of spherical silica nanoparticles (Fig. 7.4A). The shape of the silica particles was verified by SEM and TEM (Fig. 7.6) but also by the near Gaussian-shaped PDF curve (Fig. 7.4B). Furthermore, the good fits to the Thetadash model (Fig. 7.7A), which assumes 3-D growth and where the best fit in terms of the regression coefficient was obtained using a first order rate law with a surface-controlled mechanism, confirmed the 3-D radial growth. The fitting procedure to the JMAK model resulted in a n value of 1.3 (Fig. 7.7B). According to Hulbert et al. (1969), for a surface-controlled, 3-D growth mechanism, the JMAK model should yield a n value between 3-4. This discrepancy might indicate 1) a growth dimensionality < 3, 2) a diffusion-controlled mechanism or 3) the inappropriateness of the JMAK model for the growth of silica nanoparticles. SEM/TEM

photomicrographs and other studies (e.g. Iler, 1979; Icopini et al. 2005; Conrad et al., 2007) have shown that silica nanoparticles are spheres therefore a growth dimensionality <3 is not reasonable. Furthermore, a diffusion-limited growth mechanism is unlikely, as indicated by the good fit to the Thetadash kinetic model supporting a surface-controlled mechanisms and previous results (section 6.5.2). This leads to the conclusion that the use of the JMAK model for the growth of silica nanoparticles at these small scales and via homogenous nucleation from solution is problematic as it was already discussed in the previous chapter (section 6.5.2). Interestingly, the calculated JMAK rate constant, $k^* = 2.12x10^{-4}$ s^{-1}, compared well to the rate constant, $k = 1.46x10^{-4}$ s^{-1} obtained from the Thetadash model.

There are no studies in the literature with similar experiments to compare the rate constants to. The kinetic studies that investigated the processes of silica polymerisation and silica nanoparticle formation looked at the time-dependent decrease in monosilicic acid and then inferred the reaction kinetics for silica nanoparticles growth from these results (see section 2.1.4). However, these are two very different processes (chemically-controlled polymerisation *vs.* 3-D, surface-controlled particle growth) and should therefore be separated for kinetic considerations (see section 6.5.2 for more details).

Ostwald ripening and particle aggregation has been suggested by several studies to dominate the later stages of silica nanoparticle growth (e.g., Iler, 1979; Perry and Keeling-Tucker, 2000). However, in the experiments discussed here (polymerisation induced by T-drop) aggregation was not observed. This could be a consequence of slower particle growth, as evidenced in the SAXS data (Fig. 7.9B) which prevented the reaction and invariably later aggregation to be fully monitored.

Comparison to pH-lowering experiments (chapter 6)

Results from this study support the first two of the three stage process for the formation of silica nanoparticles proposed in the previous chapter: (1) silica polymerisation and nucleation of silica nanospheres, (2) particle growth and (3) particle ripening and aggregation (see section 6.4.2 for details). The general mechanisms and kinetics of silica nanoparticle growth were thus not affected by the different approach to induce silica polymerisation (i.e., T-drop *vs.* pH-drop; both support 1st order, surface-controlled particle growth). However, the rate of silica polymerisation and particle growth was substantially lowered when polymerisation was induced by T-drop (i.e., occurrence of an induction period, smaller rate constants; Fig. 7.9 and Table 7.3). Furthermore, no aggregation processes were observed in this study, while several signs of particle aggregation (i.e., data from DLS, SEM and TEM) were found in the pH-drop experiments. This further confirmed that particle growth was retarded in the T-drop experiments.

This might also explain the discrepancy in critical nuclei sizes (obtained from Thetadash) between the two experiments (pH-drop: 1.07 nm *vs.* T-drop: 1.47 nm). As mentioned before, *smaller critical nuclei form (i.e. are stable) in more saturated solutions due to a higher driving force. However, as shown above this might not solely be controlled by the degree of supersaturation but could potentially be also influenced by how supersaturation is induced.* Therefore, the bigger critical nuclei determined for the T-drop experiments (using Thetadash / extrapolation of growth curves) might thus be another consequence of the slower reaction kinetics in these experiments. Equally, this could explain the differences in critical nuclei size between values determined with the Gibbs-Kelvin approach and with Thetadash (as well as the extrapolation of the growth curve) in this study (Table 7.2). The Gibbs-Kelvin critical nuclei size is only dependent on the degree of supersaturation and will not take into account that in the T-drop experiments, the overall reaction is retarded. Therefore, the extrapolation of the growth curve to t=0 (i.e. Thetadash, Table 7.2) might give a more accurate estimate of the critical nuclei size.

7.5.3 Comparison to the literature

Few studies looked at silica polymerisation and precipitation in natural geothermal waters (e.g., Rothbaum et al., 1979; Weres, 1981; Carroll et al., 1998) or have simulated natural geothermal processes within the laboratory (e.g., Rothbaum and Rhode, 1979; Carroll et al., 1998). Similar to the present study, Rothbaum and Rhode (1979) investigated the polymerisation process in near neutral solutions with varying SiO_2 and at varying T in which silica supersaturation was also induced by fast cooling. Their data showed that in solutions with 600 - 650ppm SiO_2 and at 30°C, silica polymerisation was delayed by up to 20 minutes thus supporting the T-drop data presented above (Fig. 7.9A, open symbols). In contrast, Icopini et al. (2005) and Conrad et al. (2007) showed that in pH-drop experiments using similar experimental solutions (pH 7, 750ppm SiO_2, 25°C) no induction periods were observed which confirmed the pH-drop data presented here (Fig. 7.9A, full symbols).

Rothbaum et al. (1979) examined the depletion in monosilicic acid within freshly discharged geothermal waters (polymerisation is induced by T-drop). For this, they removed freshly discharged geothermal waters from various wells from Broadllands and Wairakei (NZ) into teflon bottles which were then kept at sampling temperature (i.e., 80 – 90°C) to follow the polymerisation process up to 4 hours. Similar to Rothbaum and Rhode (1979) and the results from the present study, Rothbaum et al. (1979) showed that in geothermal waters with 570 and 620 SiO_2 an induction period delayed the polymerisation process in their experiments. It should

be noted that their experiments were carried out at a higher temperature and the observed induction periods were accordingly longer (40 - 60 minutes).

All these studies support the hypothesis that silica polymerisation is delayed in systems where silica supersaturation is induced by fast cooling (compared to pH drop). However, so far none of these studies (nor any other studies) were able to derive quantitative information on the mechanism and kinetics of silica nanoparticles formation, i.e., have monitored *in-situ* and time-resolved the nucleation and growth of silica nanoparticles. Furthermore, despite efforts to quantify the precipitation rates of amorphous silica in natural geothermal systems (e.g., Weres, 1981; Carroll et al., 1998) there is currently no data set available to compare to the kinetic data presented here. This is mainly due to different experimental set-ups used in these field and lab studies (e.g., usage of silica gels, quantifying total silica scale) as well as differences in the evaluation of the reaction kinetics (e.g., precipitation rate as a function of the Gibbs free energy of reaction).

7.6 Conclusions

The time-dependent depletion in monosilicic acid provided information on the silica polymerisation process, while *in-situ* time-resolved SAXS and DLS measurements were used to follow and quantify the initial steps of nucleation and growth of silica nanoparticles. SAXS and DLS results were supported by SEM and high-resolution TEM photomicrographs providing information on the size and shape of the growing silica particles at various stages during the reaction.

Combining the results from the pH-drop experiments (chapter 6) with data obtained in this study, it was found that the nucleation and growth of silica nanoparticles from a supersaturated silica solution proceeds substantially slower if silica polymerisation was induced by fast cooling. This was evidenced by the occurrence of an induction period at the start of both the time-dependent depletion in monosilicic acid and particle growth in the T-drop experiments. Therefore, the assumption of instantaneous homogeneous nucleation (as postulated in chapter 6) might only be valid under certain conditions (i.e., only occurs in solutions with a certain degree of supersaturation but it also depends on how supersaturation is induced / established). Furthermore, the delayed reaction kinetics in the T-drop experiments also seemed to have affected the critical nuclei size (i.e., are larger in T-drop experiments). Nevertheless, the mechanisms and kinetics of particle growth seemed unaffected by the two different methods to induce silica polymerisation as evidenced by the good fits to the Thetadash model using first order reactions kinetics coupled with a surface controlled reaction mechanism. Unfortunately, the late growth stage was not monitored in this study but in comparison with the previous

literature and the results from chapter 6, it is most probable that the late stages will be characterised by Ostwald ripening and particle aggregation.

8 THE SIZE AND POLYDISPERSITY OF SILICA NANOPARTICLES UNDER SIMULATED HOT SPRING CONDITIONS: CONTINUOUS-FLOW EXPERIMENTS

8.1 Abstract

The nucleation and growth of silica nanoparticles in geothermal waters, i.e. under constant re-supply of supersaturated silica solution, was simulated using a flow-through geothermal simulator system. The effect of silica concentration ($[SiO_2]$), ionic strength (IS), temperature and organic additives on the size and polydispersity of the silica nanoparticles formed was quantified. While the applied increase in IS did not affect the size (30 - 35 nm) and polydispersity (± 9 nm) observed at 58°C, an increase in $[SiO_2]$ notably enhanced silica polymerisation and also resulted in slightly smaller mean particle sizes. The biggest effect was observed with a decrease in temperature (58 to 33°C) or the addition of glucose; in both cases particle growth was restricted to sizes below 20 nm. Conversely, the addition of xanthan gum induced the development of a thin film that enhanced silica aggregation.

8.2 Introduction

Several studies have characterized biosilicification occurring in hot spring pools by quantifying interaction processes and mechanisms between microorganisms and silica (see section 2.2 for details). Overall, it has been shown that microorganisms play a rather passive role in the silicification process and simply provide surfaces for silica nanoparticles to adhere (e.g., Benning et al., 2004a, b, 2005; Lalonde et al., 2005; section 2.2.5). This suggests that the microorganisms might therefore not necessarily influence the kinetics of silica nanoparticle formation. However, to understand biosilicification occurring in modern hot springs, the mechanisms by which silica particles nucleate, grow and aggregate have to be quantified in the first place. Furthermore, the impact of varying geochemical conditions (e.g., $[SiO_2]$, IS, T, pH) as well as the presence of microorganisms (i.e., functional groups of microbial cell envelope) on these processes have to be assessed. Lastly, biosilicification needs to be further investigated under simulated hot spring conditions, i.e., under constant re-supply of fresh supersaturated solution and where silica polymerisation and nanoparticle formation are induced by rapid cooling (e.g., Benning and Mountain, 2004).

The aims of this study were, therefore, to elucidate the mechanisms of silica polymerisation and silica nanoparticle formation with the polymerisation being induced by rapid cooling of a

supersaturated silica solution and under constant re-supply of silica supersaturated solution. For this, a flow-through geothermal simulator system was designed to follow the formation of silica nanoparticles in both inorganic and organic solutions. The experiments were carried out with near neutral pH solutions and at a range of silica concentrations, ionic strengths and temperatures most often found in natural geothermal systems. Furthermore, the effect of specific organics (e.g., glucose and xanthan gum; representing microbial cell wall functional groups, exopolysaccharides) on the polymerisation process was tested. The silica polymerisation process was monitored by following the time dependent depletion in monomeric silica and complemented by scanning electron microscopy (SEM) and dynamic light scattering (DLS) to image and quantify the size and polydispersity of the growing silica nanoparticles at various time steps. Variations related to the different tested parameters (i.e., SiO_2 concentration, IS, T, organics) on the size and polydispersity of silica nanoparticles will be discussed.

Note that the high-temperature flow-through geothermal simulator system used here simulates processes in stagnant (water flow < 0.5 mls^{-1}) outflow pools of natural hot springs (e.g., Octopus Spring, Yellowstone National Park, US) and geothermal power plants (e.g., Svartsengi, Iceland, this study). Therefore, in part results from this study can be directly applied to field studies described in chapter 4.

8.3 Methodology

A high-temperature flow-through geothermal simulator system (Fig. 8.1, more details in section 7.2.1) was used to equilibrate a supersaturated silica solution ([SiO_2] = 320 - 960ppm; ionic strengths, IS = 0.02 or 0.11; pH 7) in a high temperature oven (at 230°C and for 2.5 h residence time) in order to achieve full de-polymerisation prior to the experiments. After passing through a backpressure regulator, BPR, the solutions were led via Teflon tubing into a Teflon tray inside an incubator (at 33 or 58°C, Fig. 8.1). This cooling simulated the conditions of a supersaturated deep fluid being discharged in a hot spring. Organics were added to the tray via an additional pump which metered out exact concentrations of glucose or xanthan gum in order to obtain the desired concentrations within the tray.

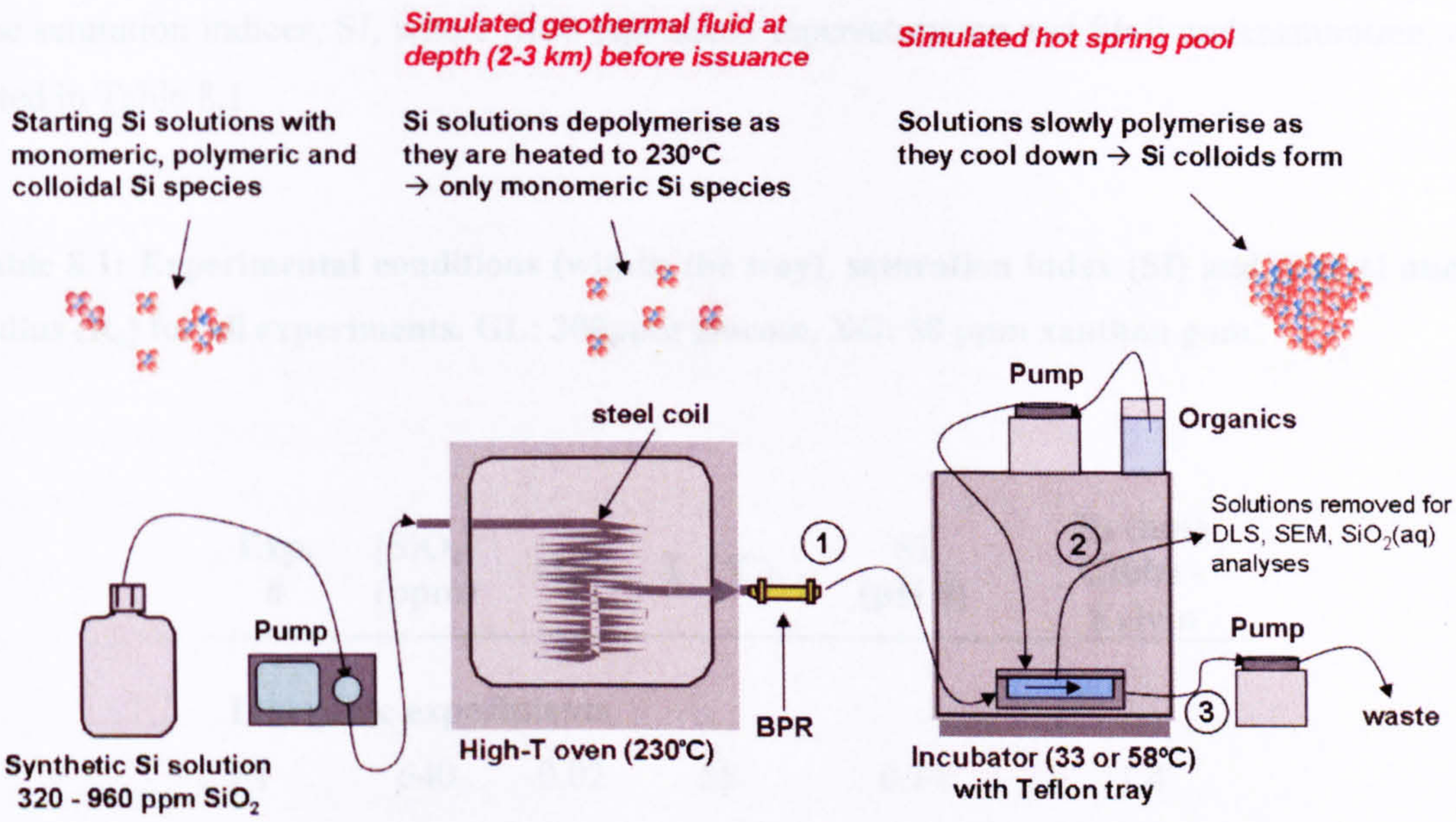

Figure 8.1: Sketch of the simulated hot spring system (modified after Benning and Mountain, 2004).

The growth of silica nanoparticles under permanent supply of fresh silica solution was monitored over 31 or 46 hours with samples removed at specific time steps from (1) the BPR outlet (T ~ 80°C; solutions cooled for ~1 min), (2) the middle of the tray (solutions polymerised for ~ 1 hour) and (3) the outlet of the tray (solutions polymerised for ~ 2 hour, Fig. 8.1). An aliquot of the sample was used for analysis of the monomeric silica, [SiO_2(aq)] and total silica concentration, total [SiO_2] (section 3.2.3; molybdate yellow method). In the experiments with organics, small aliquots of these samples were also used to determine the concentration of the added organics within the tray (section 3.2.3; the phenol-sulphuric acid method for sugars) in order to ensure a constant concentration of organics. Lastly, the remaining sample was filtered and the filter papers were analysed using a LEO 1530 FEG SEM (section 3.2.4). Changes in size distribution of silica nanoparticles (i.e., mean particle diameter and polydispersity) were derived from SEM photomicrographs (see section 3.2.4) or via direct analysis of the particles in solution using standard dynamic light scattering (DLS, Malvern Nanosizer, section 3.2.5). Note that for DLS, samples were acidified (with 1M HCl to pH 2) immediately after removal from the tray to stop the polymerisation reaction, i.e., particle growth. Before DLS analysis, samples were sonicated for 3 minutes (using an ultrasonic bath) to disperse aggregated silica particles.

To calculate the saturation state of silica (within the tray) for all experiment (except organic experiments), the parameters listed in Table 8.1 (i.e., [SiO_2], IS, T) were taken as inputs for geochemical modelling using the geochemical code PHREEQC (see section 3.1.2 for details).

The saturation indices, SI, where SI>0 represents supersaturation and SI<0 undersaturation, are listed in Table 8.1.

Table 8.1: Experimental conditions (within the tray), saturation index (SI) and critical nuclei radius (R_0) for all experiments. GL: 300ppm glucose, XG: 50 ppm xanthan gum.

Exp. #	$[SiO_2]$ (ppm)	IS	T (°C)	SI (pH 8)	R_0 (nm) Gibbs - Kelvin
Inorganic experiments					
E1	640	0.02	58	0.14	1.4
E2	320	0.02	58	-0.17	-
E3	430	0.02	58	-0.04	-
E4	960	0.02	58	0.31	1.0
E5	640	0.11	58	0.14	1.4
E6	640	0.02	33	0.33	1.1
Organic experiments					
E7	identical to E1 + GL		-	-	
E8	identical to E1 + XG		-	-	

As mentioned previously (chapter 6 & 7), the size of the critical nuclei (i.e., primary particle) can not be determined using SEM and DLS. However, in order to obtain an estimate of the size of the critical nuclei, the critical nuclei radius, R_0, was calculated using the Gibbs-Kelvin approach (eq. 2.2 in section 2.1.2). R_0 for all inorganic experiments (except undersaturated, S<0, experiments) is given in Table 8.1.

8.4 Results and Discussion

Below most results will be compared to the E1 experiment. Experiments E2 to E8 were designed in such a way that only 1 parameter was varied in comparison to E1 (either initial $[SiO_2]$, IS, T or organics; Table 8.1). Each section will therefore start with general observations from the E1 experiment, followed by the comparison and discussion of the results obtained from the other experiments.

8.4.1 The monomeric and total silica concentration

General observations

The polymerisation reaction was followed via the changes in the monomeric silica concentration, [SiO_2(aq)], while the total silica concentration, total [SiO_2] was used to verify that no silica was removed from the solution while passing through the system. In Figure 8.2 the time course of the monomeric and total silica concentrations at three different sampling positions (i.e., (1) BPR, (2) tray – middle and (3) tray – outlet; Fig. 8.1) is shown over 46 hours for the E1 experiment (Table 8.1).

The constant total [SiO_2] measured at the BPR, in the middle and at the outlet of the tray (Fig. 8.2, full symbols) demonstrated that over the entire length of the experiment no silica was removed from the solution (by adhesion to tubes or tray walls or settling of aggregates, etc.). Furthermore, [SiO_2(aq)] in solutions collected at the BPR (Fig. 8.2, open triangles) was identical to the total [SiO_2] which showed that despite the rapid cooling (~1 min) from 230 to ~80°C (i.e., T at the BPR), polymerisation was not yet initiated (i.e., no decrease in [SiO_2(aq)]). This also suggested the occurrence of an induction period which delayed silica polymerisation adequately so that the polymerisation reaction did not start until the solution reached the tray.

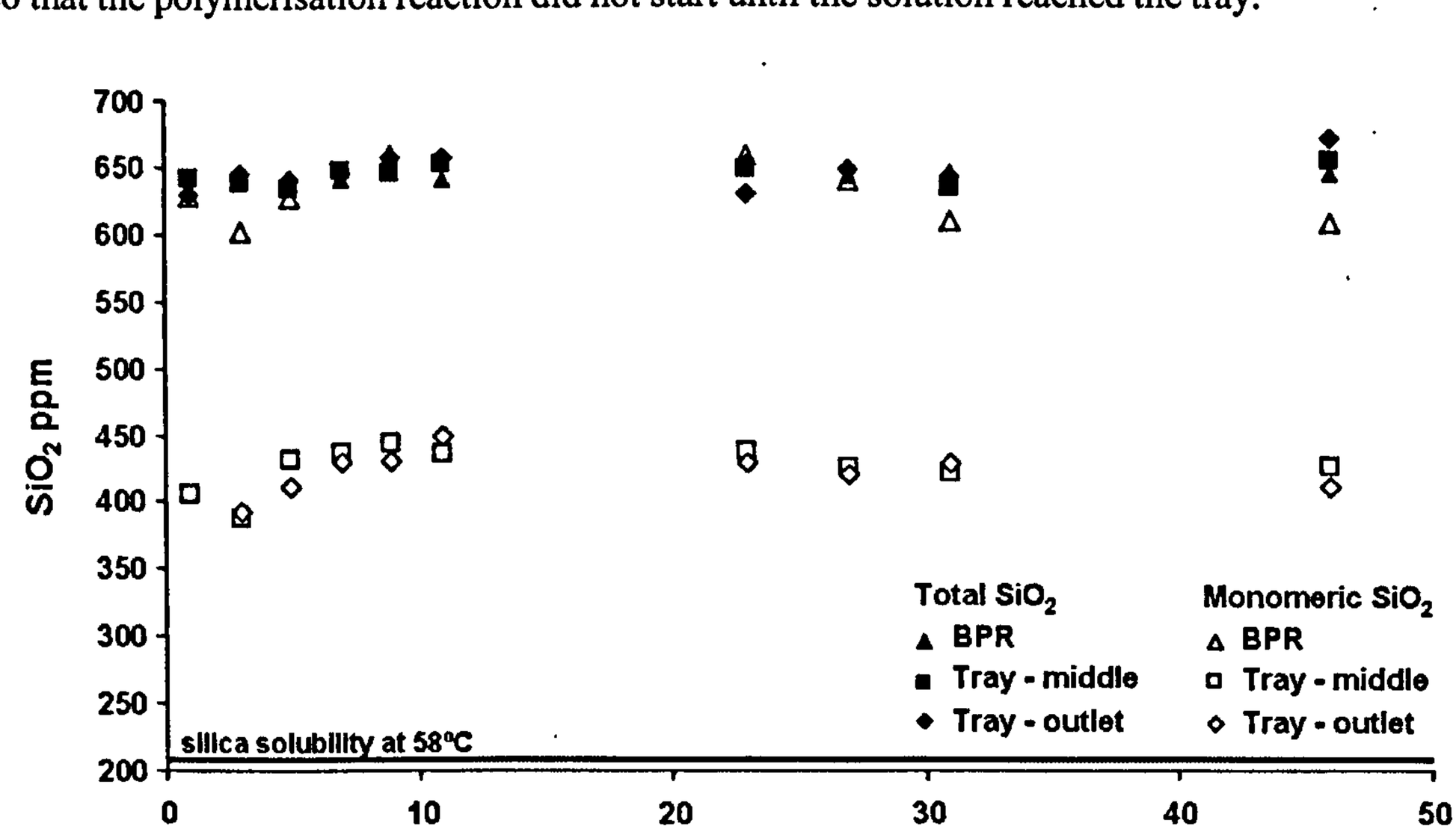

Figure 8.2: Variations in monomeric (open symbols) and total (full symbols) silica concentrations measured at three different sampling positions, i.e., BPR, tray - middle and tray – outlet, in a 640ppm SiO_2 solution (E1 experiment) over 46 hours. Errors of individual data points <6%.

[SiO_2(aq)] measured in the middle (solution polymerised for ~1h) and at the outlet of the tray (solution polymerised for ~2h) were almost identical and values were generally about 200-250ppm lower than the total [SiO_2] at the same position (Fig. 8.2). This showed that about 50% of [SiO_2(aq)] (with respect to silica solubility at 58°C; solid line in Fig. 8.2) had polymerised within the 1-2 hours the solution needed to pass through the tray. The similarity in [SiO_2(aq)] between the two sampling positions (i.e., tray-middle and –outlet) indicated that the polymerisation process was extremely slow (i.e., an additional hour of polymerisation hardly affected the monomeric SiO_2). This also confirmed that the constant re-supply of fresh silica solution maintained constant conditions in the experiments.

It is worth mentioning that during the first 9-11 hours, a 10-15 % increase in [SiO_2(aq)] was observed which correlated with the time needed to establish a steady state within the tray (Fig. 8.2). At equilibrium (t>11h), the [SiO_2(aq)] values were about twice as high (~420ppm) as the silica solubility (209ppm at 58°C; Gunnarsson and Arnórsson, 2000), confirming that the constant re-supply of new solution guaranteed a continual polymerisation reaction.

Lastly, all these results were in good agreement with the calculated saturation state for this experiment (SI = 0.14) showing that the solutions passing through the tray were oversaturated with respect to silica and polymerisation was favoured. Also, the proximity of SI to 0 (i.e., saturation) correlated with the observed low rates of silica polymerisation. However, note that the calculated SI values are representative for equilibrated systems and this assumption is only partly valid for the studied systems, nevertheless, the calculated SI values give information about the general trends observed.

For all other experiments (i.e., E2 to E8, Table 8.1) the same general trends were observed, e.g., no polymerisation at the BPR (Appendix C.1), no silica was removed from the solutions by adhesion / settling (Appendix C.2, C.3), and similar [SiO_2(aq)] values in tray and at the outlet (Appendix C.2, C.3). Therefore, the following comparison and discussion of the experiments E2 to E7 will mainly focus on the changes in [SiO_2(aq)] measured in the middle of the tray.

The effect of varying inorganic parameters

Influence of silica concentration. The influence of initial silica concentration (320 – 960 ppm SiO_2) on the polymerisation process via the changes in [SiO_2(aq)] is shown in Figure 8.3. At lower SiO_2 concentrations (E2 and E3), despite variations between individual data points, the [SiO_2(aq)] values did not differ from the total silica concentration (i.e., 320 and 430 ppm SiO_2 respectively). This showed that although fresh silica solution was continuously supplied, no silica polymerisation occurred in these experiments. This also agreed well with the saturation

indices determined for these experiments (E2: SI = -0.17, E3: SI = -0.04) showing that in both cases the solutions were undersaturated with respect to silica (specifically in E2).

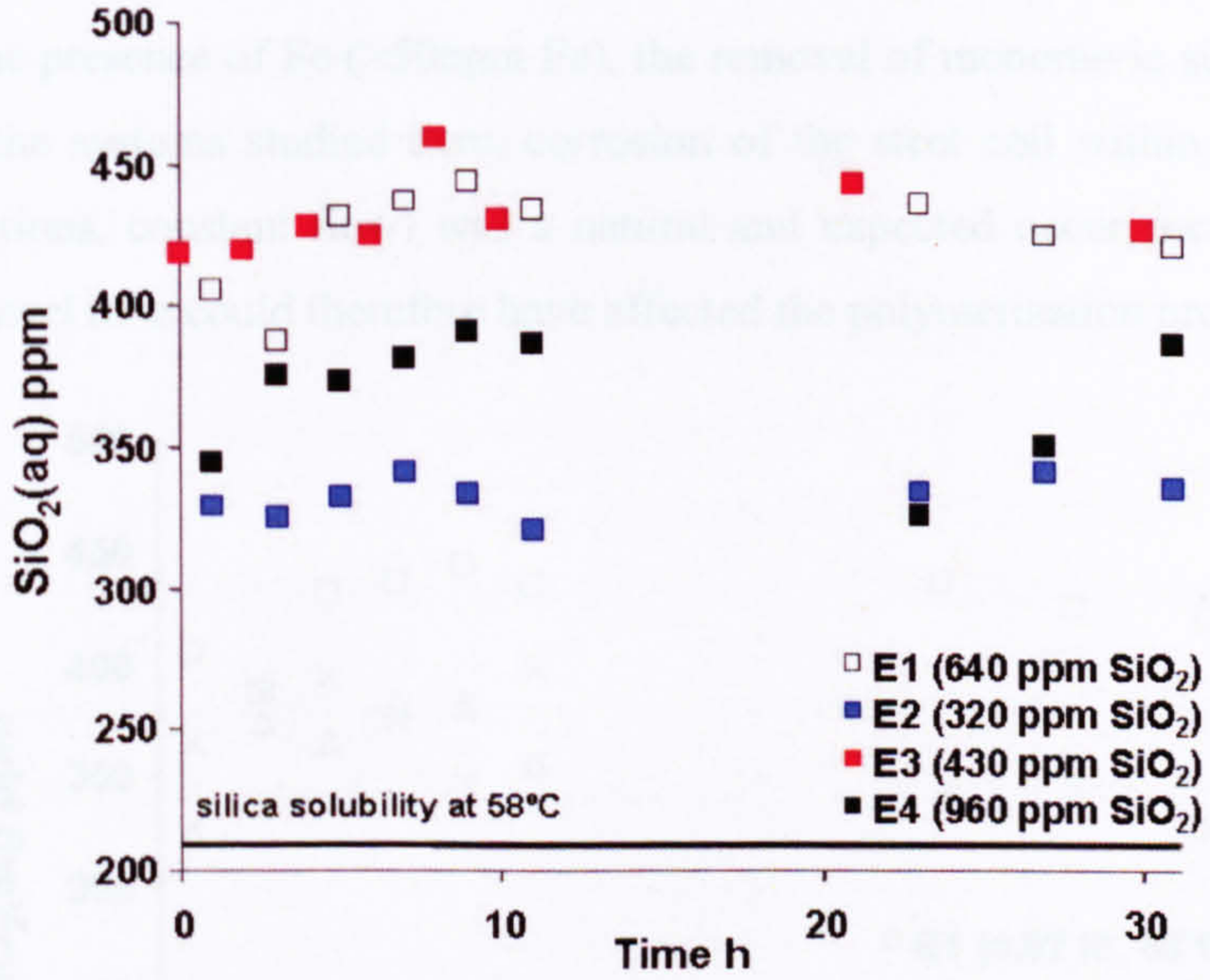

Figure 8.3: Variations in monomeric silica concentration, [SiO_2(aq)], as a function of silica concentration over 31 hours (measured in the middle of the tray).

At the highest SiO_2 concentration (E4, 960ppm SiO_2), the monomeric silica, [SiO_2(aq)], followed a similar trend as observed for E1 (640ppm SiO_2) but values were generally 20-100 ppm lower (Fig. 8.3, black *vs.* white squares). This was due to the increased degree of silica saturation (i.e., higher SiO_2) in this experiment which enhanced the polymerisation rate within the tray. This was also reflected in the higher SI obtained for E4 (SI = 0.31) when compared with E1 (SI = 0.14, Table 8.1). Note that [SiO_2(aq)] measured after 23 and 27 hours were substantially lower than after 10 hours which suggested an imbalance of the physico-chemical conditions within the tray. This could have resulted from changes in water volume or T over night. However, steady state seemed re-established again after 31 hours.

Influence of ionic strength. The influence of ionic strength (E5, 0.11 IS) on the time course of [SiO_2(aq)] is illustrated in Figure 8.4 (triangles). Note that data were only collected until t=11h due to a pressure failure of the system over night (i.e., corrosion of the stainless steel tube). The initial 9-11 hours were characterised by an increase in [SiO_2(aq)], which similar to E1 and E4 suggested the establishment of a steady state within the tray. The [SiO_2(aq)] for E5 were generally about 50-100ppm lower when compared to E1 (Fig. 8.4 open squares) indicating that the higher IS of E5 increased the polymerisation of silica. However, the SI value calculated for E5 was identical to E1 (SI = 0.14, Table 8.1) suggesting that the slight increase in IS did not

affect the saturation state of the solution (i.e., polymerisation rate) within the tray. The observed changes might therefore be related to corroding stainless steel tubes within the high-T oven (e.g., [SiO_2(aq)] removal by Fe(III) surfaces). Yee et al. (2003) and Phoenix et al. (2003) have showed that in the presence of Fe (>50ppm Fe), the removal of monomeric silica from solution is enhanced. In the systems studied here, corrosion of the steel coil within the oven (230°C, saline silica solutions, constant flow) was a natural and expected occurrence. Iron release by corrosion of the steel tube could therefore have affected the polymerisation process.

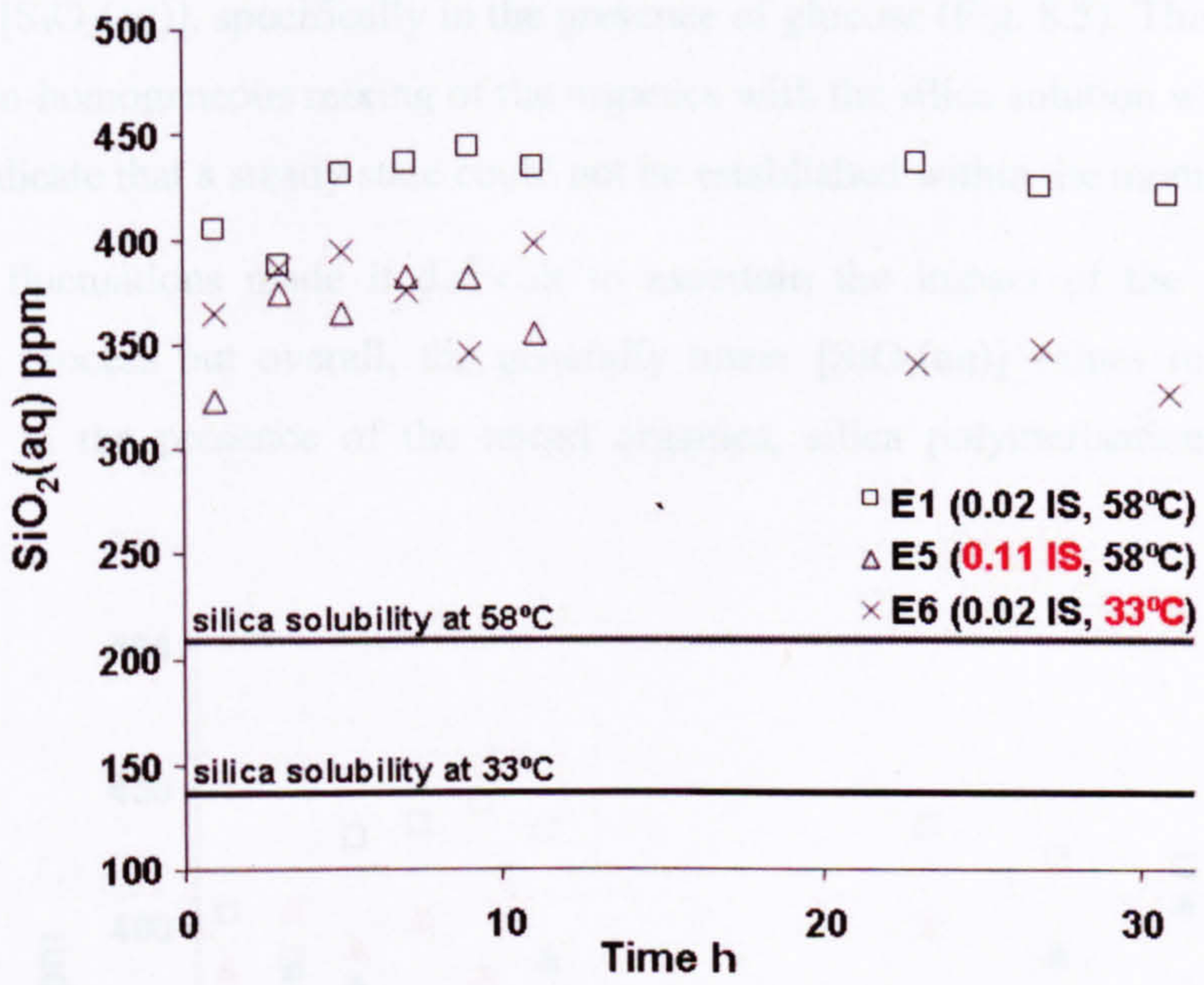

Figure 8.4: Variations in monomeric silica concentration, [SiO_2(aq)], as a function of higher ionic strength (E5, 0.11 IS) or lower T (E6, 33°C) over 31 hours (measured in the middle of the tray).

Influence of temperature. In the experiment at lower temperature (E6, 33°C), monomeric silica [SiO_2(aq)] was lower than in E1 (58°C), thus indicating that silica polymerisation was enhanced in this experiment (compared to E1, Fig. 8.4 crosses *vs.* squares). This was not surprising as silica solubility is strongly affected by T (e.g., 136ppm SiO_2 at 33°C and 209ppm SiO_2 at 58°C; Gunnarsson and Arnórsson, 2000). In addition, the degree of silica saturation was substantially higher in E6 (SI = 0.33) compared to E1 (SI = 0.14, Table 8.1). Similar to observations made above, the first 9-11 hours were dominated by substantial scatter but they showed a general increase in [SiO_2(aq)] which at t ~ 11h reached a steady state (Fig. 8.4). At steady state (i.e., t > 11h), the [SiO_2(aq)] values in E6 were still about twice as high as the silica solubility calculated for the lower temperature (i.e., 136 ppm for 33°C). This confirmed previous results that the constant re-supply of new solution guaranteed a continual polymerisation reaction.

The effect of organic additives

It should be noted that the concentration of the added organics (monitored in samples collected from both the middle and the outlet of the tray) was constant over the 31 hours (Appendix C.2). This verified that no organics were removed from the solution (e.g., adhesion to tray walls) while passing through the tray.

The experiments with added organics (glucose, E7 or xanthan gum, E8) were characterised by fluctuations in [SiO_2(aq)], specifically in the presence of glucose (Fig. 8.5). This may have been the result of non-homogeneous mixing of the organics with the silica solution within the tray but it could also indicate that a steady state could not be established within the monitored 31 hours.

The observed fluctuations made it difficult to ascertain the impact of the organics on the polymerisation process but overall, the generally lower [SiO_2(aq)] values (compared to E1) suggested that in the presence of the tested organics, silica polymerisation was somewhat enhanced.

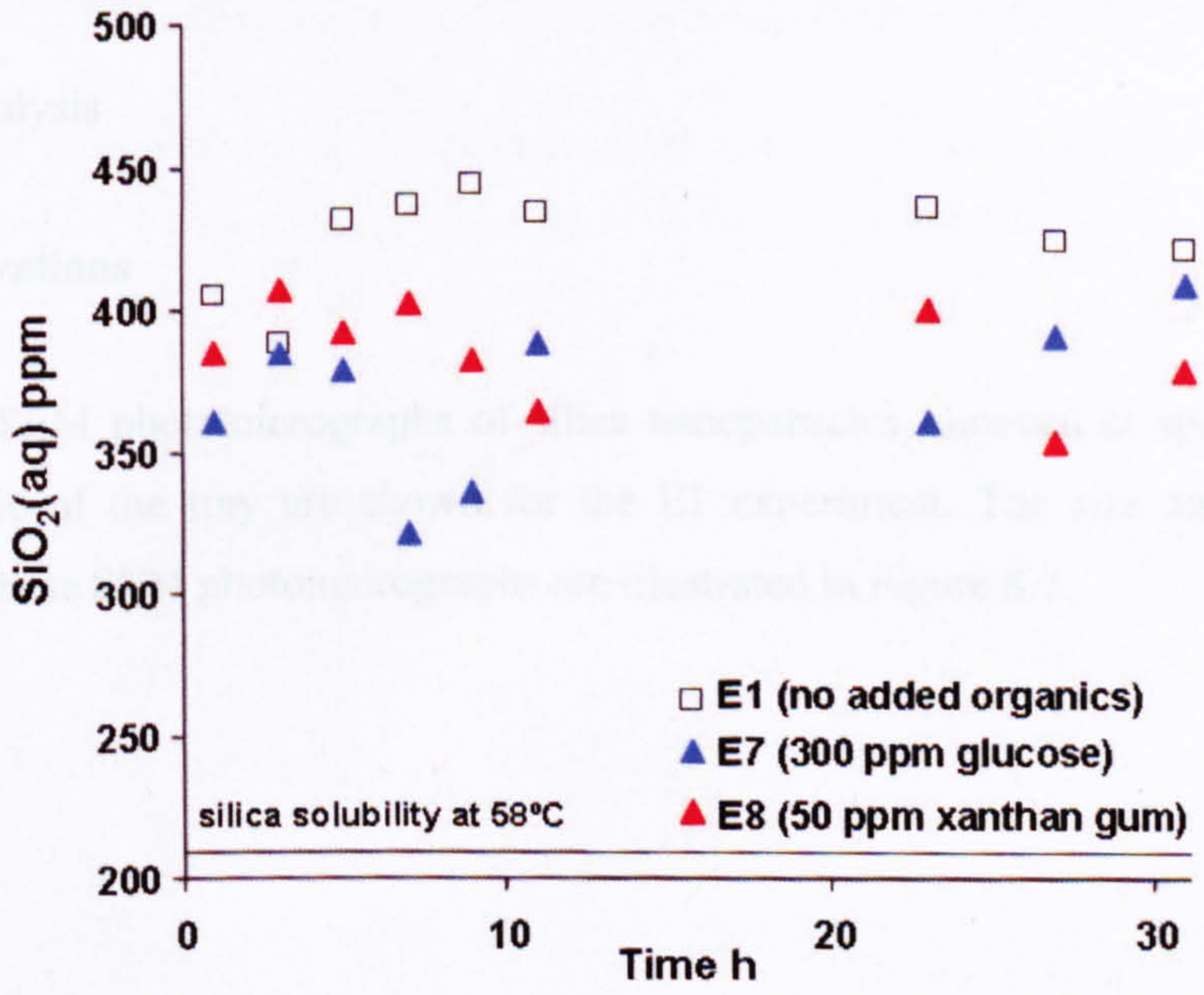

Figure 8.5: Variations in monomeric silica concentration, [SiO_2(aq)] as a function of added glucose (300ppm) and xanthan gum (50ppm) in experiments with initial 640ppm SiO_2 over 31 hours (measured in the middle of the tray).

Previous studies (e.g., Richardson, 1957; Iler, 1979; Coradin et al., 2004 and references therein) have shown that sugars, hydroxylated polymers and gelatine can interact with the molybdate reagent which will then decrease the amount of available molybdic acid to form the yellow

silicomolybdic complex. Overall, this can lead to a decrease in the amount of monomeric silica measured. However, Richardson (1957) demonstrated that 2g of sucrose (i.e., disaccharide: glucose and fructose) did not affect the analysis of 0.1mg of monomeric silica. In this study, the amount of glucose (within the analysed sample) was substantially smaller (5-10mg) and the monomeric silica content analysed was far higher (5-10 mg) compared to the study by Richardson (1957). This indicates that it was unlikely that glucose interfered with the molybdate yellow method applied in this study. In the case of xanthan gum, Richardson (1957) showed that the addition of 200mg of mannose (a structure component of xanthan gum) to a solution containing 0.1mg of silica can cause an error (in the determination) of less than <4%. In this study, the applied organic and silica concentrations (both 5 - 10 mg) again were very different. Therefore, similar to glucose, it was not expected that the lower [SiO_2(aq)] values in the xanthan gum experiments (E8) were the consequence of xanthan gum – molybdic acid interferences. This was further supported by results presented in Appendix B, where the addition of glucose and xanthan gum did not seem to affect the time-dependent depletion in monomeric silica (i.e., the analysis of monomeric silica) compared to the inorganic experiment.

8.4.2 Size analysis

General observations

In Figure 8.6, SEM photomicrographs of silica nanoparticles removed at specific time steps from the middle of the tray are shown for the E1 experiment. The size and polydispersity obtained from these SEM photomicrographs are illustrated in Figure 8.7.

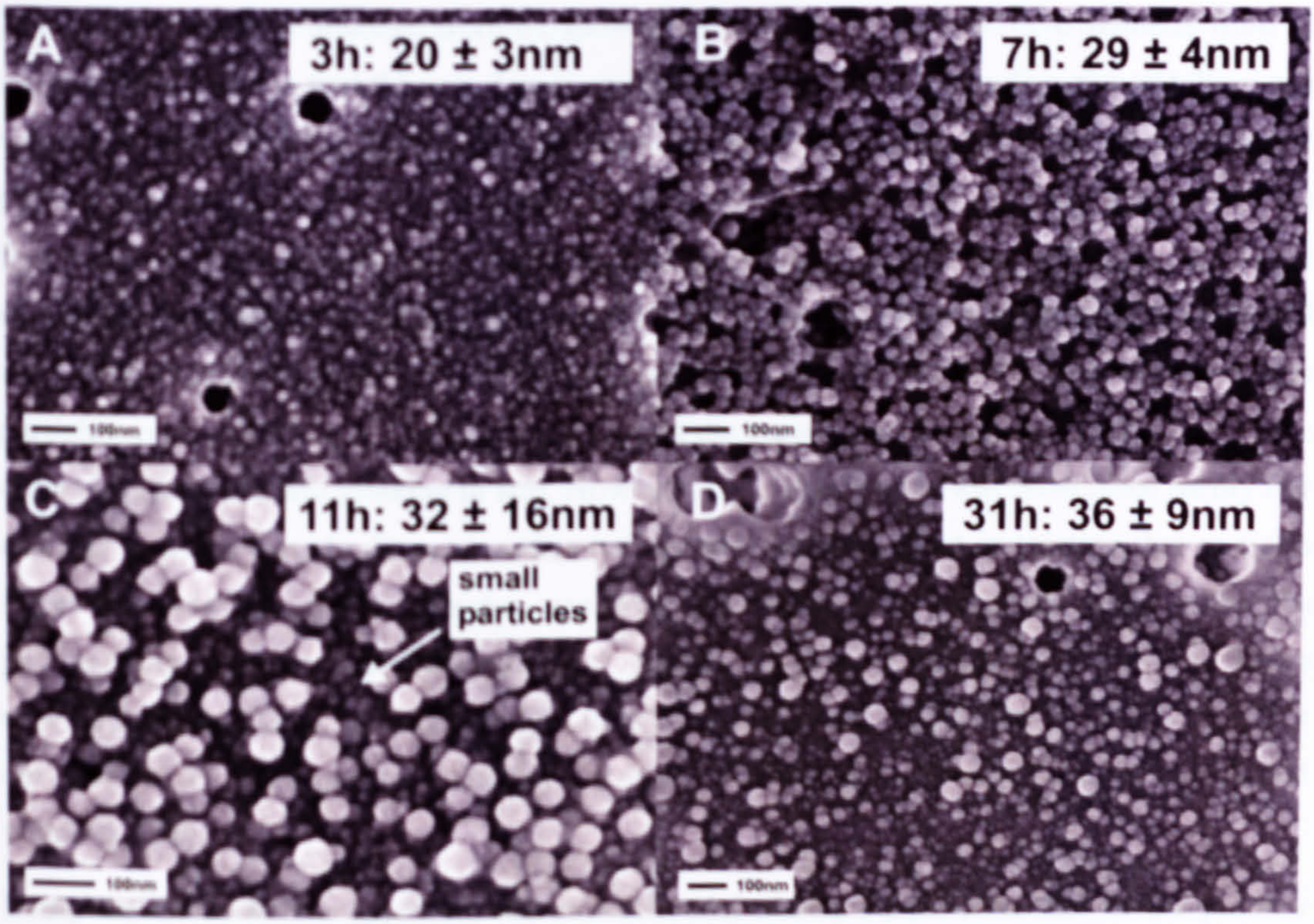

Figure 8.6: SEM photomicrograph of silica nanoparticles removed from the middle of the tray after 3, 7, 11 and 31 hours (E1 experiment) with the mean diameter and polydispersity for each time step.

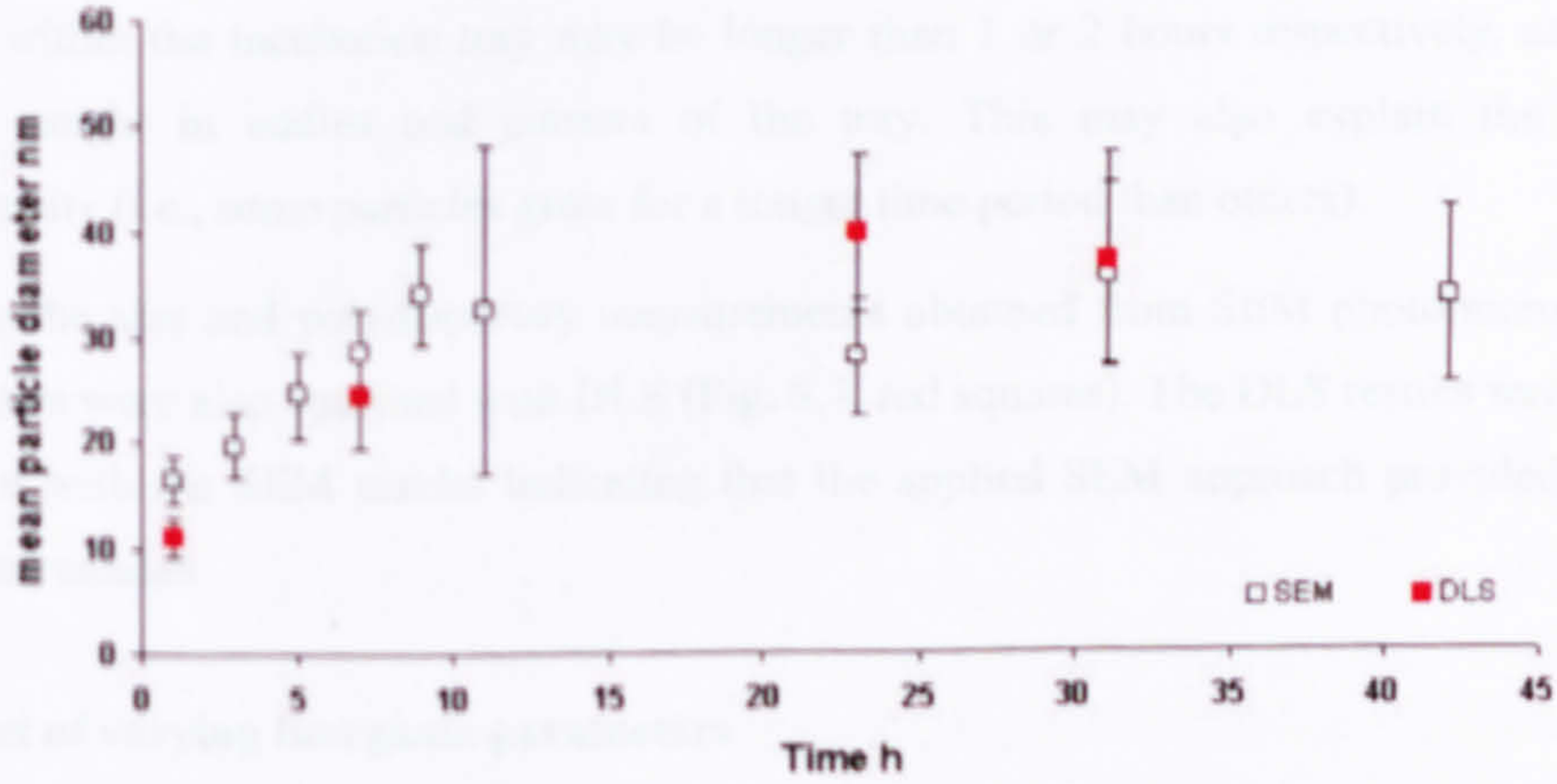

Figure 8.7: Variation in mean diameter and polydispersity (=error bars) of silica nanoparticles with incubation time for the E1 experiment (evaluated from SEM = open squares and DLS = full squares). For SEM ~100 particles were measured for each data point.

The size distributions obtained from E1 showed an increase in mean particle diameter from 16 nm to 34 nm over the first 9 hours. Upon continual reaction the particle diameter stabilised at a value between 30 and 35nm (Fig. 8.7, white squares). Similarly, the polydispersity of the particles (error bars in Fig. 8.7) continuously increased from ±2.3 to ±4.7 nm until t = 9h but then substantially increased to ±15.6 nm over the following 2 hours revealed by the occurrence of two size populations (see Fig. 8.6, 11h). At t >11 h, the polydispersity dropped to about ± 9 nm. These results suggested that due to the continuous re-supply of fresh silica solution, new particles were nucleating continuously throughout the entire experimental time period while the older particles were still growing in size. However, once steady state was established hardly any changes in mean particle diameter and polydispersity were observed suggesting that particles larger than ~60 nm (max. diameter measured after t = 11 h) were not stable within the polymerising solution and nucleation and growth of new particles was favoured. These observations correlated well with results from the time course of [SiO_2(aq)] (Fig. 8.3) which also showed an initial increase over the first 9 - 11 hours before a steady state was established within the tray.

Using the Gibbs-Kelvin approach, the critical nuclei radius, R_0 (i.e., the size of the primary particles) was determined to be 1.4nm (Table 8.1). This indicated that at the beginning of the experiments a nucleation event lead to the formation of many nuclei which then grew by addition of SiO_2 oligomers to the particle sizes described above. As a result, after only 1 hour (and under constant re-supply of fresh silica solution), these nuclei (diameter ~ 2.8nm) have grown to about 16nm in diameter (Fig. 8.7). Note that the residence time of these growing particles within the incubation tray may be longer than 1 or 2 hours respectively, as particles will get caught in eddies and corners of the tray. This may also explain the observed polydispersity (i.e., some particles grow for a longer time period than others).

To verify the size and polydispersity measurements obtained from SEM photomicrographs, a few samples were also analysed with DLS (Fig. 8.7, red squares). The DLS results were in good agreement with the SEM results indicating that the applied SEM approach provided accurate size measurements.

The effect of varying inorganic parameters

Influence of silica concentration. No particles were observed in the two experiments with the lowest SiO_2 concentrations (E2 and E3). This was not unexpected as the experiments were undersaturated with respect to SiO_2 (negative SI values, Table 8.1) and silica polymerisation did thus not occur ([SiO_2(aq)] = total SiO_2, Fig. 8.3).

The time course showing the size and polydispersity for the experiment with the highest SiO_2 concentration (E4) is shown in Figure 8.8 (black squares). The comparison to results from E1 (white squares) showed minor differences but all E4 size distributions were slightly shifted to lower values. This suggested that under these conditions (i.e., higher SiO_2) the size of the primary particles (i.e., critical nuclei) was smaller and / or the nucleation rate was enhanced both of which would result in slightly smaller mean particles sizes. This is not unexpected as the nucleation process has a far higher driving force in more concentrated solutions (Table 8.1) thus producing more nuclei but also enabling the stabilisation of smaller nuclei. At higher [SiO_2] the calculated critical nuclei radius (R_0 = 1.0) was almost 30% smaller than the R_0 obtained for E1 (R_0 = 1.4, Table 8.1) which correlates with the above observations.

Influence of ionic strength. No major differences were observed between the size distributions obtained from E5 (0.11 IS) and E1 (0.02 IS, Fig. 8.8, white triangles *vs.* squares) which indicated that the increase in ionic strength did not affect the growth pattern within the tray. This was not unexpected as the saturation state (SI =0.14) and the critical nuclei radius (R_0 = 1.4) were both identical to values obtained for E1 (Table 8.1). This demonstrated that the increase in IS from 0.02 to 0.11 was not sufficient to cause noticeable differences in particle size (see also chapter 6 and 7 where IS was shown to have a minor effect on silica particle size).

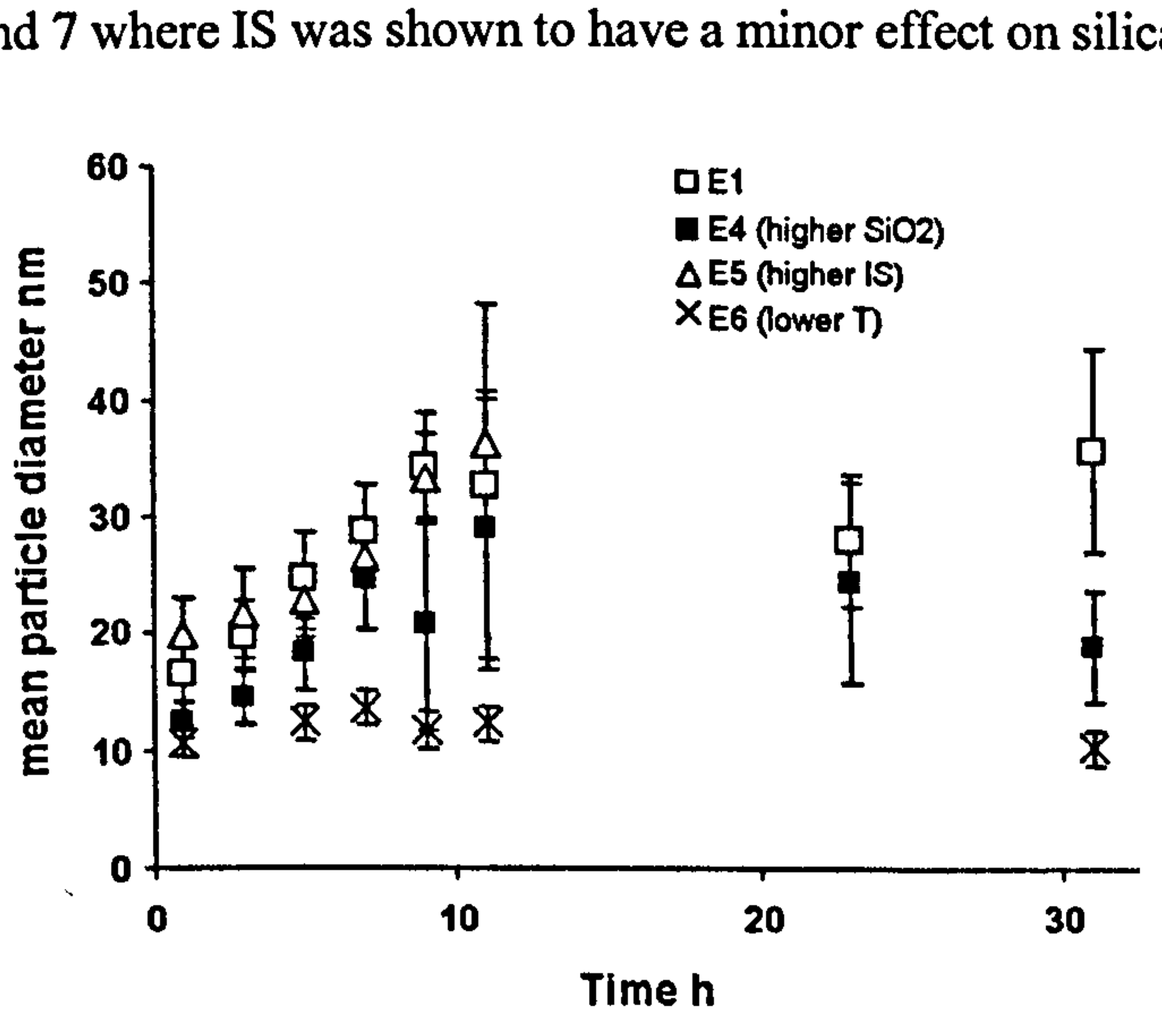

Figure 8.8: Variation in mean diameter and polydispersity (=error bars) of silica nanoparticles with incubation time as a function of varying parameters, i.e., [SiO_2], IS, T (evaluated from SEM; ~100 particles were measured for each data point).

Influence of temperature. The size distributions obtained at lower temperature (E6, Fig. 8.8, crosses), although constant over the studied 31 hours, differed substantially from all other inorganic experiments at T=58°C. Once nucleated, the particles did not grow larger than ~ 15nm

(max. particle diameter measured, Appendix C.4), and due to the continual re-supply of fresh solution the steady formation of new, smaller particles was favoured. Similar to E4 (higher SiO_2, Fig. 8.8, full squares), this is partly due to the formation of smaller primary particles (critical nuclei) as shown by the smaller R_0 value obtained for E6 compared to E1 (1.1nm *vs.* 1.4nm). This also correlates with the classical nucleation theory which predicts that with an increase in temperature, a decrease in the energy per unit volume of the nucleus versus matrix is needed. It follows, therefore, that the nuclei have to grow larger in size in order to reach stability. However, the constancy of both the mean particle diameter and the polydispersity in the experiment E6 (33°C) suggested that at this lower temperature particles with a sizes > 15nm were energetically not stable and the growth of new, smaller particles was favoured. Note that from the experiments described here, no particle number or volume could be evaluated but presumably if smaller particles dominated, a higher number of particles was expected (assuming similar degree of silica polymerisation).

The effect of organic additives

Influence of glucose. In the experiments with added glucose (E7) the size distribution followed the same trend as observed for the lower temperature experiment (E6, Fig. 8.9). However, the mean diameter and polydispersity of the particles in the glucose experiments were about 15% higher than in the purely inorganic experiment but at lower T (Fig. 8.9).

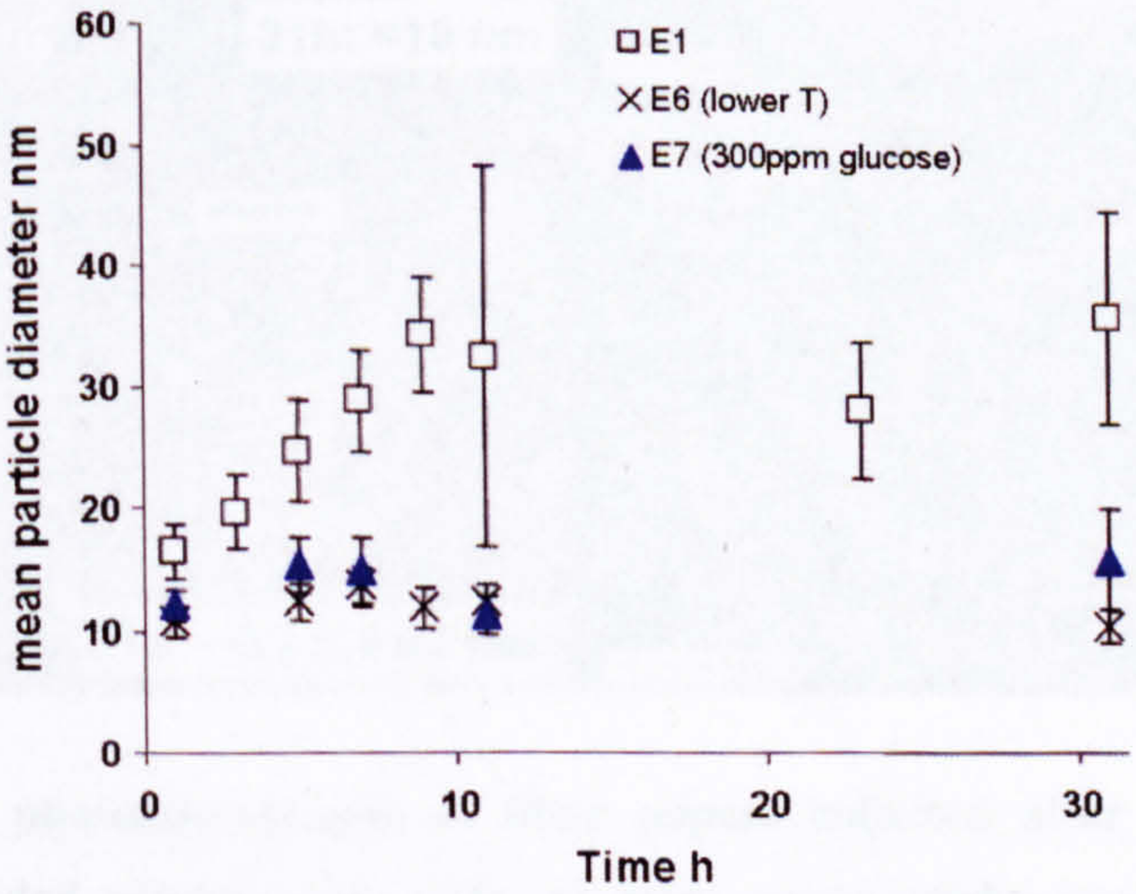

Figure 8.9: Variation in mean diameter and polydispersity (=error bars) of silica nanoparticles with incubation time as a function of T and added glucose (evaluated from SEM; ~100 particles were measured for each data point).

Although it has been shown in the literature (e.g., Richardson, 1957) and in Appendix B that glucose is unlikely to interfere with molybdic acid (i.e., the molybdate yellow method) and monomeric silica in solution, it is possible that the organic molecules acted as templates to stabilize / enhance the formation of small particles.

Influence of xanthan gum. In the presence of xanthan gum (E8) only few small particles (sizes <10nm) could be detected in suspension (i.e., in the middle of the tray, Fig. 8.10A). However, after 7 - 9 hours a thin film formed at the air-water interface where xanthan gum was added to the tray. SEM analysis showed that this film (Fig. 8.9B) consisted of large silica aggregates far bigger (~200nm, Fig. 8.10C) than the single particles observed in solution from the middle of the tray (~10nm, Fig. 8.10A). Furthermore, despite sterilisation of the system and the organic solutions, the tray and the thin film respectively were colonised by microorganisms (Fig. 8.10D). Most certainly, the complex structure of xanthan gum (i.e., high-molecular weight polysaccharide) enhanced the aggregation of silica (via hydrogen bonding / entrapment of colloids within the complex structure) but also provided substrate for microbial colonisation.

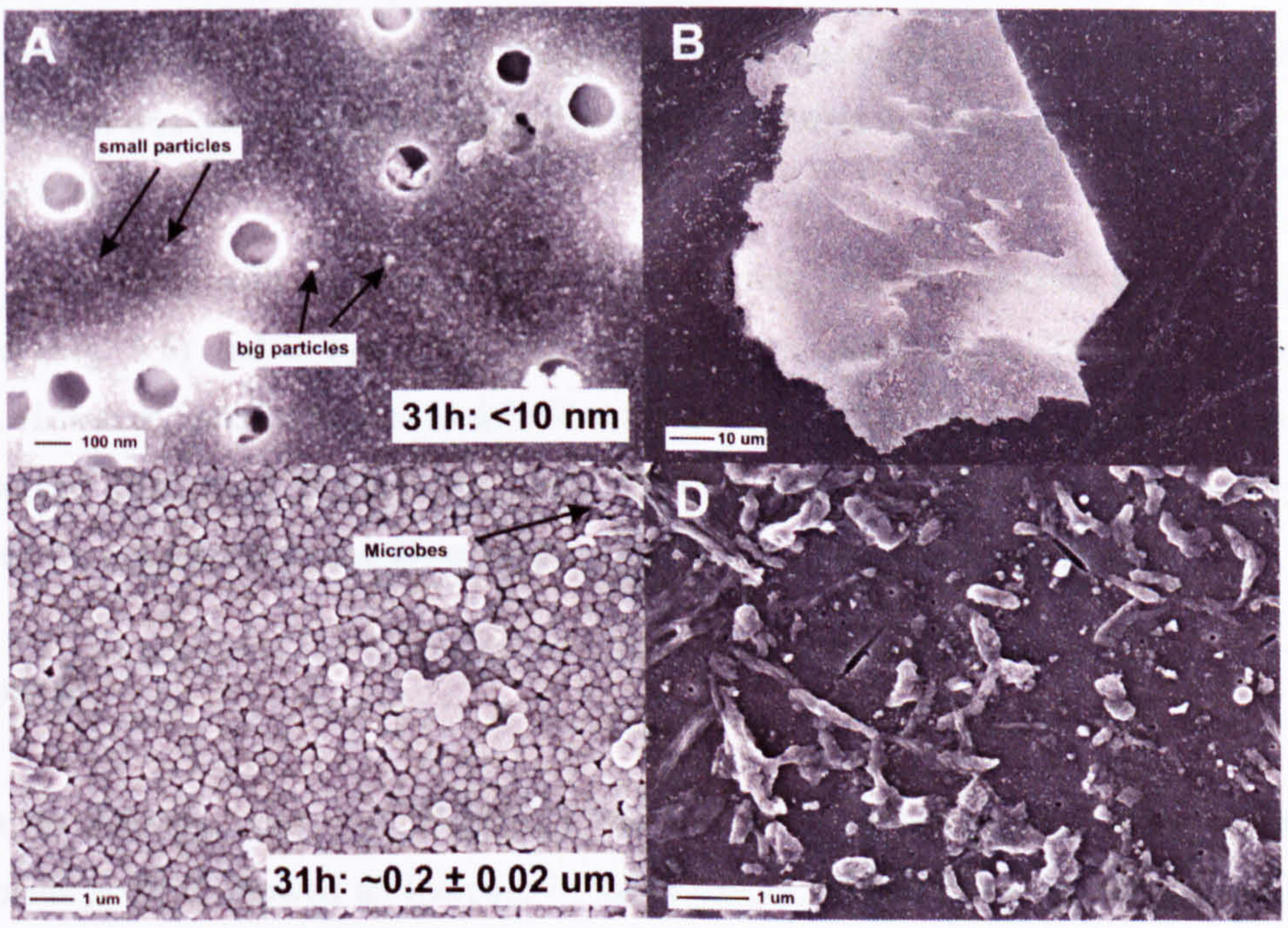

Figure 8.10: SEM photomicrographs of filter papers collected after 31 hours from the experiment with added xanthan gum (E8). A) Silica nanoparticles (sizes < 10nm) removed from the middle of the tray, B) thin film at the inlet of the tray, C) close-up of the thin film with the mean diameter and polydispersity of the aggregates and D) close-up of microorganisms within the tray.

8.4.3 Summary of observations

The monomeric and total silica concentration

In most inorganic experiments, the monomeric silica [SiO_2(aq)] measured in the tray showed that about 50% of [SiO_2(aq)] (~200-300ppm with respect to silica solubility) had polymerised. In the experiment with initial 960ppm SiO_2 (E4), ~80% of [SiO_2(aq)] (~600ppm) polymerised. In most inorganic experiments during the first 9-11 hours, a 10-15 % increase in [SiO_2(aq)] was observed which correlated with the time needed to establish a steady state within the tray (Fig. 8.3 and 8.4). At steady state, the [SiO_2(aq)] values were about twice as high as the silica solubility calculated for the tested conditions. This confirmed that the constant re-supply of new solution guaranteed a continual polymerisation reaction.

In terms of [SiO_2(aq)] few differences were observed as a consequence of changing temperature, [SiO_2], IS or organics, and the trends followed those dictated by the degree of silica saturation, i.e., silica polymerisation was enhanced in solutions with higher saturation indices (i.e., E4 and E6, Table 8.2). Despite constant re-supply of fresh silica solution, no polymerisation was observed in solutions that were undersaturated with respect to silica (E2 and E3, Table 8.2).

For the experiments with organics it is worth noting that large fluctuations in [SiO_2(aq)] were observed (Fig. 8.5) and it was thus difficult to ascertain their impact on the polymerisation process. However, interference of molybdic acid with the tested organics could be ruled out and the observed [SiO_2(aq)] fluctuations might thus be better explained by non-homogeneous mixing of the organics with the silica solution and the absence of a steady state.

Size analysis

Identical to the time course of [SiO_2(aq)], the size distributions obtained from all inorganic experiments at 58°C showed an increase in mean particle diameter and polydispersity over the first 9 hours followed by the stabilization at a constant value (Fig. 8.7 and 8.8). As the system stabilized (>11h), the polydispersity equilibrated and this suggests that new particles nucleated continuously while older particles were still growing. However, once steady state was established the mean particle diameter and polydispersity were constant and no additional growth was observed, i.e., continuous nucleation and growth of new, smaller particles was favoured.

The increase in IS from 0.02 to 0.11 did not affect the size and polydispersity observed at 58°C while the increase in [SiO_2] notably enhanced silica polymerisation and also induced slightly

smaller mean particle sizes. This was due to the higher silica saturation in the E4 experiment resulting in smaller critical nuclei and a higher nucleation rate (Table 8.2). Overall this led to a higher number of particles where the particles sizes were slightly smaller compared to E1.

The biggest effects on size distribution were observed with decreasing temperature and added glucose (Fig. 8.9). At 33°C (E6), smaller critical nucleii, R_0, and higher nucleation rates were noted (Table 8.2) but little growth was observed (i.e., particles did not grow larger than 12 ± 1.5 nm). This was due to higher degree of silica saturation, however, the lower average particle sizes further suggested that temperature had a major influence on the stability of the forming particles favouring the growth of smaller particles with decreasing temperature.

Glucose (E5) followed the same trend with particle growth being restricted to sizes around 15 ± 4 nm (Fig. 8.9) which suggested that the glucose molecules acted as templates to stabilize / enhance the formation of small particles. Conversely, in the presence of xanthan gum (E6) only few particles could be detected in suspension but a thin film developed at the AWI at the inlet of the tray (Fig. 8.10). This film enhanced the aggregation of silica to large clusters (<200nm). In contrast, the simple structure of glucose did not lead to the formation of a thin film which was not unexpected as glucose molecules are less likely to bind to each other (i.e., dispersed within the polymerising silica solutions) while the high molecular weight xanthan gum forms viscous solutions.

The findings from the inorganic experiments compared well with field observations from *in-situ* sinter growth studies carried out in Icelandic hot springs (Chapter 4) where the size range of silica nanoparticles within freshly deposited sinters (exhibiting low microbial activity) was found to be significantly larger in high-T geothermal waters (i.e., Reykjanes) than in low-T waters (i.e., Svartsengi) but were less affected by silica concentration or ionic strength. Similar observations were made by Iler (1979) who showed that particles grew only half as big at 50°C than at 90°C.

The observations from the xanthan gum experiments were in good agreement with the sinter growth study presented in chapter 4 which showed that in geothermal waters (e.g., Krafla, Geysir and Hveragerdi) where silica precipitation was less favoured (i.e., undersaturated conditions), substantial amounts of sinters nonetheless developed due to the presence of thick biofilms (i.e., microbial exopolymeric sheath, EPS) that enhanced aggregation of silica nanoparticles. This was also demonstrated by Benning et al. (2004a, b) and Lalonde et al. (2005). They showed that in the presence of increasing silica load, the sheath (i.e., EPS) of certain microorganisms (i.e., *Calothrix*, *S. azorense*) thickens. This occurs in parallel with the thermodynamically driven polymerisation of the monosilicic acid and the formation of silica nanoparticles. In a second step, the thick EPS acts as a template for the accumulation /

adsorption of amorphous silica nanoparticles on the sheaths surface (via hydrogen bonding or entrapment of particles within the complex structure of the EPS; e.g., Benning et al., 2004a, b and chapter 4). These results along with the findings presented above thus demonstrate that exopolysaccharides (e.g., xanthan gum, cyanobacterial sheath) are able to accelerate the process of silica nucleation and growth. This was also supported by other laboratory studies (e.g., Perry and Keeling-Tucker, 2000 and reference therein) that showed that other biopolymers such as proteinaceous extracts from diatoms, sponges and higher plants can enhance the process of silica formation.

A summary of all observations and interpretations of the experiments discussed in this chapter is given in Table 8.2.

Table 8.2: Summary of tested experimental conditions (within the tray), critical nuclei radius (R_0), saturation index (SI) and made observations and their interpretation (in comparison to E1) as discussed in the text.

Exp. #	SiO_2 (ppm)	IS	T (°C)	R_0^+ (nm) Gibbs - Kelvin	SI (pH8)	Silica poly-merisation	mean particle size	Cause/Effect
Inorganic experiments								
E1	640	0.02	58	1.4	0.14	-	-	-
E2	**320**	0.02	58	-	-0.17	no polym.	no particles	none
E3	**430**	0.02	58	-	-0.04	no polym.	no particles	none
E4	**960**	0.02	58	1.0	0.31	↑	↓	**↑nucl.rate,↓R_0**
E5	640	**0.11**	58	1.4	0.14	↑	=	none
E6	640	0.02	**33**	1.1	0.33	↑ ↑	↓ ↓	**↑nucl. rate, ↓R_0,↓ particle growth**
Organic experiments								
E7	same as E1 **+ 300ppm GL**		-	-		fluctuations	↓ ↓	**↑nucl. rate,↓particle growth**
E8	same as E1 **+ 50ppm XG**		-	-		fluctuations	thin film	**thin film, large silica aggregates**

8.5 Conclusions

A successful hydrothermal experimental approach that simulates processes observed in natural geothermal springs has been developed. In most tested solutions, silica was supersaturated and silica polymerisation and silica nanoparticle formation was initiated once the solution entered the tray (i.e., geothermal water is discharged at the surface). Over the duration of the experiments (31-42 hours), the major observations on the formation of silica nanoparticles were:

i) An increase in ionic strength or silica concentration affected the size and polydispersity of silica nanoparticles precipitated from a T – induced, supersaturated solution only in a minor way. In contrast, a temperature change (i.e., different spring water temperature) substantially influenced the size range of the forming particles (i.e., smaller particle sizes at lower temperatures).

ii) The addition of glucose restricted particle growth to sizes < 20nm whereas the addition of xanthan gum induced the development of a thin silica-rich film at the air-water interface. This showed that exopolysaccharides (abundant in natural biofilms) do enhance the aggregation of silica and thus aid in the silicification process observed in geothermal hot springs.

9 SUMMARY AND CONCLUDING REMARKS

This thesis contains (1) field studies in which the formation of silica sinters and the associated microbial diversity in Icelandic geothermal waters was quantified and (2) lab studies that focussed on the formation of silica nanoparticles under conditions mimicking the geothermal environments surveyed in the field. From the findings herein it is possible to get a more comprehensive understanding of the parameters that control silica precipitation (i.e., sinter formation) and the structure of microbial communities in modern hot spring environments. Furthermore, it allows the identification of the geochemical / hydrodynamic conditions needed for microbial silicification and fossilisation; essential knowledge in the search for extinct and extant life in the ancient Earth as well as on other planets. Lastly, a molecular level knowledge of the nucleation and growth of silica nanoparticles in inorganic experiments provide quantitative data on the rate and mechanisms of the initial steps of biosilicification.

9.1 Sinter growth and microbial diversity in Icelandic geothermal waters

The analysis of growth rates and the structural and textural developments of sinters from five diverse geothermal sites in Iceland showed that the inorganic silica precipitation rate was strongly influenced by temperature, pH, salinity, and silica concentration. Furthermore, the mesoscopic and microscopic textural development of the sinters was affected by the precipitation mechanism (subaqueously and/or subaerially) and the presence and absence of microbial communities. In turn, the microbial abundance and the diversity of microbial communities appeared to be directly affected by the physico-chemical conditions of the geothermal waters, i.e., T, pH, salinity and sinter growth rate.

In geothermal areas where the waters exhibited near neutral pH, high salinity, high T and high silica content (i.e., waters are highly supersaturated with silica; e.g., Reykjanes), silica precipitation rates were highest. These physico-chemical conditions led to the formation of porous and homogeneous sinters made of aggregates of silica nanoparticles (particle size range: 11 - 106 nm) that developed predominantly subaqueously. In turn, due to the high salt contents, high T and high growth rates, microbial activity could not be detected. In geothermal waters with a similar salinity and pH (e.g., Svartsengi) but lower temperatures and lower precipitation rates (due to lower total SiO_2), the forming sinters were also porous and dominated by aggregates of silica nanoparticles but with a significantly smaller size distribution (10-36 nm). Furthermore, microbial abundance and diversity was substantially higher and the most dominant phylotypes found in these waters belonged to marine genera of the *Proteobacteria* (e.g.

Marinobacter, Sphingpyxis, Oceanicaulis). The preservation and fossilization of microorganisms in the porous silica precipitates was argued to be low; partly due to the low affinity between the negatively charged silica nanoparticles and the neutral to negatively charged microbial surfaces at near-neutral pH (e.g., Fein et al. 1997; Cox et al. 1999, Yee et al. 2004) which hinder adhesion of silica nanoparticles onto microbial surfaces. In addition, as previously shown (e.g., Iler et al., 1979 and refernces therein; Smith et al., 2003), particle interaction is aided by the presence of salts such as Na cations (i.e., flocculation due to interparticle bonding through the cations). This suggests that in near-neutral geothermal waters with high salinity silica nanoparticles tend to aggregate with each other (forming porous precipitates) rather than adhering to microbial surfaces.

In geothermal areas that were characterised by alkaline pH, low salinity, high T and medium-high silica content (i.e., Geysir and Hveragerdi), silica was undersaturated and subaqueous silica precipitation was inhibited. As a result, sinter growth was mostly restricted to the air-water interface (AWI; where evaporation and condensation processes dominate) which led to the formation of dense and heterogeneous sinters with well defined spicules and silica terraces. Despite the temperatures being quite high (66 – 96°C) extensive biofilms developed in the submerged zones which were dominated by representatives of the class *Aquificae* (mostly related to *Thermocrinis*) and *Deinococci* (*Thermus* species). Note that *Aquificae* species can thrive in highly alkaline waters (up to pH 10) with temperatures up to 95°C (e.g., Geysir 1 and Krafla) while members of the *Deinococci* are restricted to water temperatures below 85°C and pH below 10 (e.g., Geysir 2 and Hveragerdi). Due to the low precipitation rates within these waters, microorganisms became fully silicified and were well preserved within the growing sinters. The fossilization process was further aided by the enhanced rate of particle growth / coalescence (to form smooth films) at high temperatures (see 9.3).

In geothermal waters characterised by highly alkaline pH, low salinity and high T (i.e., Krafla) even at high silica contents, silica was undersaturated. Nevertheless, the presence of thick microbial biofilms enhanced sinter growth within the geothermal waters by acting as a template for the adhesion of suspended silica nanoparticles on the microbial surface (via hydrogen bonding or entrapment of colloids within the biofilm). This process was aided by the complex structures of the EPS (e.g., Benning et al., 2004a, b; Benning et al., 2005; Lalonde et al. 2005) and eventually led to the complete silicification and fossilisation of the biofilm (which again was also aided by the higher water temperature). The microorganisms that thrived in these systems mostly belonged to freshwater and soil genera of the *Proteobacteria*, but representatives of the *Aquificae* as well as freshwater and soil species from other phylogenetic classes were also present (e.g., *Flavobacteria* and *Actinobacteria).*

These results demonstrate the importance of *in-situ* studies to identify the parameters controlling the diversity of microbial communities and their silicification and fossilisation in modern geothermal sinter deposits. Furthermore, it emerges that the observed differences between sites could not be explained by the variation of a single parameter. Instead, the combination of T, pH, salinity and precipitation rate together appeared to be most significant in determining the sinter growth rates and biodiversity patterns found at each site. In this study, the most extreme habitat was defined by temperatures ~ 75°C, high salinity (~ 4.7%) and high sinter growth rates (~ 300 kg y^{-1} m^{-2}) as a result of which no / low microbial activity was found. Conversely, geothermal waters that were characterised with T ~ 80°C, highly alkaline pH (~10), low salinity and medium-high precipitation rates (~ 20 kg y^{-1} m^{-2}) were "less extreme" environments and the development and fossilisation of microbial communities in these systems was frequently observed.

The results summarised above showed a close link between geochemical / hydrodynamic conditions and microbial fossilisation in modern hot spring sinters and inference and possibly reconstruction of the ecology and diversity of ancient microorganism (e.g., Precambrian Earth) from fossilized terrestrial hot spring sedimentary deposits may be possible. Similarly, the preponderance and close association of microbial communities with silica sinters on Earth, make this a good analogue for future missions to Mars, especially, since silica-rich hydrothermal deposits were recently described on the Martian surface (e.g., Squyres et al., 2007, 2008).

9.2 The initial steps of nucleation, growth and aggregation of silica nanoparticles

The initial steps of silica polymerisation and silica nanoparticle formation were quantified in both inorganic and organic solutions using synchrotron-based Small Angle X-ray Scattering (SAXS) and conventional Dynamic Light Scattering (DLS) combined with conventional or cryo-high-resolution scanning and transmission electron microscopy (SEM/cryo-HR-TEM). The experiments were carried out in near neutral pH solutions with initial SiO_2 between 640 – 1600 ppm and IS of 0.02 – 0.22 M (concentrations most often found in natural geothermal systems). Furthermore, the presence of specific organics (50 – 300 ppm of glucose, glutamic acid or xanthan gum; representing microbial cell envelope functional groups) on the nucleation and growth process was also examined. The polymerisation reactions were induced either by neutralising a high pH solution (from pH 12 to 7) or by rapid cooling of a supersaturated hot silica solution (from 230°C to T between 60 and 30°C).

Independent of the tested solutions and the protocols used to induce polymerisation (pH-drop *vs.* T-drop) the initial steps of nucleation and growth of silica nanoparticle could be divided into 3 main stages (Fig. 9.1):

(1) the nucleation stage characterised by homogeneous nucleation where monosilicic acid (H_4SiO_4) polymerises to form stable nuclei having a diameter of 1-2 nm.

(2) the 3-dimensional growth of silica nanoparticles following first order reactions kinetics coupled with a surface-controlled reaction mechanisms.

(3) the late growth stage where classical growth ends and processes including Ostwald ripening and particle aggregation set in.

Note that stage (1) and (2) were governed by a fast decrease of monosilicic acid concentration while during the last stages the solubility level was slowly established. At the end of this 3-stage process, regardless of the tested silica concentration, ionic strength or added organics, the final particle diameter was about 8nm, characterised by a mass fractal structure (i.e., open, polymeric structure).

In both pH-drop and T-drop experiments, SAXS and DLS results, along with the time-dependent depletion of monosilicic acid, showed that the rate of silica polymerisation and nanoparticle formation increased with increasing ionic strength and silica concentration (i.e., increasing silica supersaturation, Fig. 9.1).

The presence of added organics (i.e., glucose, glutamic acid or xanthan gum) did not modify the rate and mechanisms of silica nanoparticle formation (in the pH-drop experiments) compared to the equivalent inorganic experiment, as evidenced by comparable rates of silica polymerisation and particle growth (as obtained from the time-dependent depletion of monosilicic acid, SAXS and DLS data).

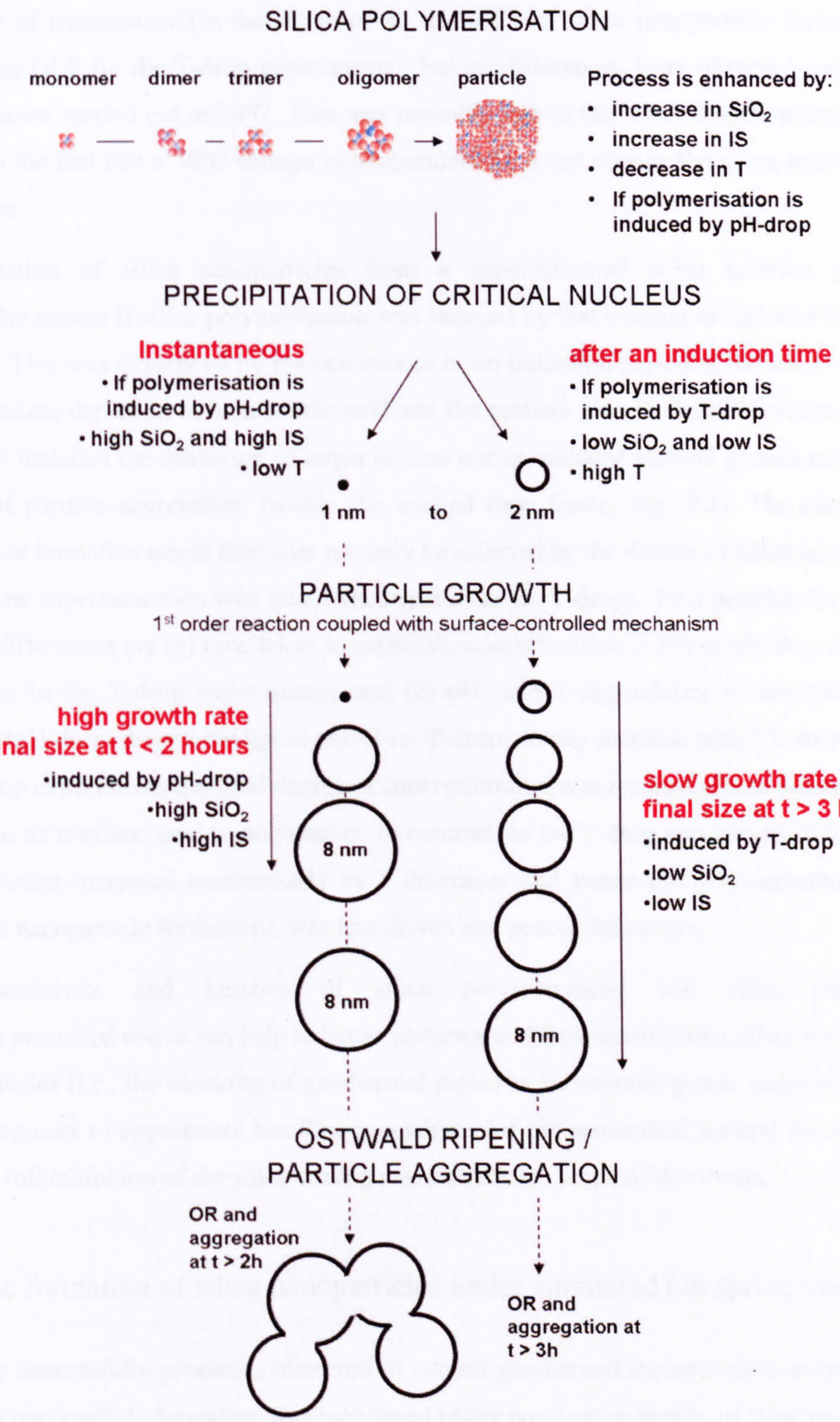

Note: the addition of glucose, glutamic acid and xanthan gum did not affect the processes illustrated above.

Figure 9.1: Schematic summary of the processes governing silica polymerisation and the formation of silica nanoparticles.

The effect of temperature (in the range of 40 to 60°C) on silica nanoparticle formation was tested using DLS (in the T-drop experiments), but no differences were observed compared to the experiment carried out at 30°C. This was probably due to the lower detection limit of DLS and due to the fact that a 30°C change in temperature does not change the silica solubility by a high degree.

The formation of silica nanoparticles from a supersaturated silica solution proceeded substantially slower if silica polymerisation was induced by fast cooling as opposed to pH-drop (Fig. 9.1). This was evidenced by the occurrence of an induction period at the start of both the time-dependent depletion in monosilicic acid and the particle growth. Further evidence for this retardation included the formation of larger critical nuclei, reduced particle growth rates and the absence of particle aggregation (within the studied time frame, Fig. 9.1). The rate of silica nanoparticle formation might therefore not only be affected by the degree of silica saturation but also by how supersaturation was established (pH-drop *vs.* T-drop). Two possible explanations for these differences are (1) time taken to establish supersaturation (~30s in pH-drop as opposed to 2-3 min in the T-drop experiments) and (2) pH- and T-dependency of amorphous silica solubility (pH-drop: drastic change at pH>9 *vs.* T-drop: steady increase with T). As a result, in the pH-drop experiments the final degree of supersaturation was reached almost instantaneously forcing the monosilicic acid to polymerise. In contrast, in the T-drop experiments the degree of supersaturation increased continuously as T decreases and hence the polymerisation process (i.e., silica nanoparticle formation), was less driven and proceeded slower.

The mechanisms and kinetics of silica polymerisation and silica nanoparticle formation presented above can help to better understand the parameters that affect the formation of silica scales (i.e., the blocking of geothermal pipes) in geothermal power stations. However, the development of appropriate handling procedures (of the geothermal waters) for a reduction or even a full inhibition of the silica scaling was outside the scope of this thesis.

9.3 The formation of silica nanoparticles under simulated hot spring conditions

To mimic successfully processes observed in natural geothermal springs, silica polymerisation and silica nanoparticle formation was monitored under constant re-supply of fresh polymerising solution using a high-temperature flow-through geothermal simulator system. The effect of silica concentration (320 – 960ppm SiO_2), ionic strength (0.02 M and 0.11 M), temperature (33°C and 58°C) and organic additives (glucose and xanthan gum) on the size and polydispersity of the forming silica nanoparticles was quantified and discussed.

In solutions with initial 640ppm SiO_2, IS=0.02 and T=58°C, the size distributions showed an increase in mean particle diameter from 16 nm to 34 nm over the first 9 hours followed by a plateau at a value between 30 and 35nm (up to t = 42h). Similarly, the polydispersity of the particles continuously increased from ±2.3 to ±15.6 nm until t = 11h before stabilising at ± 9 nm. These observations were supported by results from the time course for the monosilicic acid concentration which also showed an initial increase by ~50ppm SiO_2 over the first 9 - 11 hours before a steady state was established with a monosilicic acid concentration of about 420ppm SiO_2 (i.e., 50% polymerised with respect to silica solubility). Due to the continuous re-supply of fresh silica solution, new particles constantly nucleated throughout the entire duration of the experiment, while the older particles (first ones formed) were still growing in size, leading to a polydisperse particle size distribution (Fig. 9.2 B).

Interestingly, an increase in ionic strength (0.11 *vs.* 0.02 M) did not affect the size and polydispersity of silica nanoparticles precipitated from a T – induced, supersaturated solution. Conversely, the increase in silica concentration (960 *vs.* 640ppm) lowered the average particle diameter (22 ± 7 nm). This was associated with the higher polymerisation rate (evidenced by lower concentrations in monosilicic acid) resulting in smaller critical nuclei and a higher nucleation rate. Overall this led to a higher number of particles where the particles sizes were slightly smaller compared to those at lower SiO_2 concentrations (Fig. 9.2 A). These results were somewhat contradictory to the field findings where in geothermal waters with high IS and high SiO_2 (i.e., Reykjanes), the formed silica particles were generally larger and more polydisperse than at the site with lower IS and SiO_2 (i.e., Svartsengi). However, the temperatures at these sites were also very different (i.e. 75°C *vs.* 42°C respectively) which may have influenced the formation of silica nanoparticles much more than a change in SiO_2 and IS (see below).

The decrease in temperature (33 *vs.* 58°C) substantially enhanced the polymerisation rate and thus the nucleation process. While the size of the critical nucleus was almost identical to the experiment with higher silica concentrations, the average particle diameter (12 ± 1.5 nm) was substantially smaller than in all other inorganic experiments. This suggested that with decreasing temperature, the nucleation of small particles was favoured over particle growth resulting in the precipitation of small and fairly monodisperse silica nanoparticles (Fig. 9.2 A). These results better matched the particle sizes measured at Reykjanes (11 - 106 nm, 75°C) and Svartsengi (10-36 nm, 42°C) indicating that a change in temperature might have affected particle nucleation and growth substantially more than variations in IS and SiO_2.

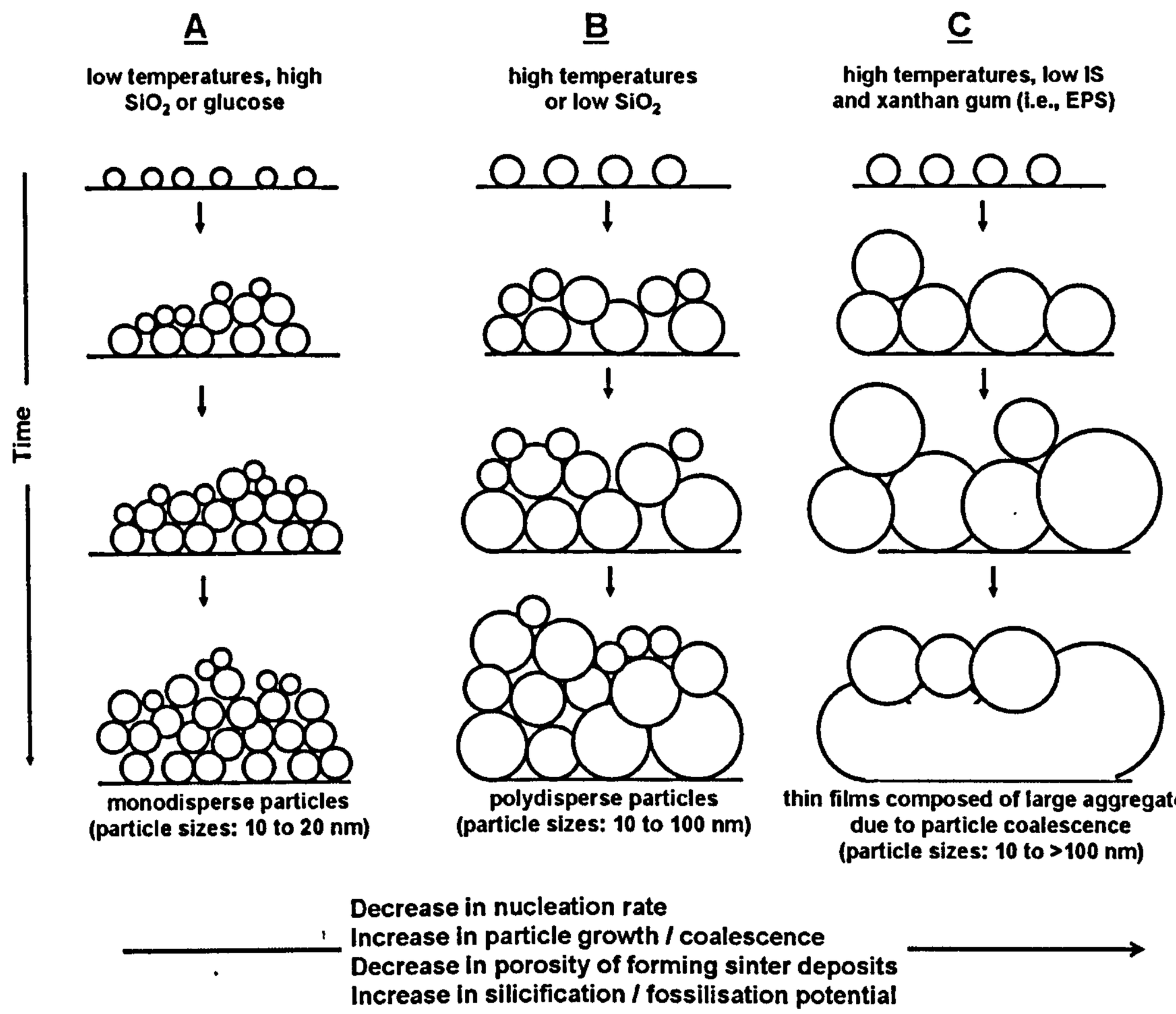

Figure 9.2: The effects temperature, IS, SiO_2 and added organics (A - C) on the growth and aggregation of silica nanoparticles under simulated hot spring conditions (i.e., constant re-supply of fresh silica solution).

The effect of added organics did not show any consistent trends; the addition of glucose restricted particle growth to sizes < 20nm (Fig. 9.2 A) whereas the addition of xanthan gum (i.e., complex EPS) induced the development of thin silica-rich films at the air-water interface. This showed that the presence of complex polysaccharides (i.e., EPS) does enhance the aggregation of silica (Fig. 9.2 C) and thus aid in the silicification process observed in geothermal hot springs while the addition of glucose did not induce the development of a thin film. This was not unexpected as glucose molecules are less likely to bind to each other (i.e., dispersed within the polymerising silica solutions) while the high molecular weight xanthan

gum forms viscous solutions. Nevertheless, the addition of glucose enhanced silica polymerisation and restricted particle growth to sizes below 20 nm which suggested that the nucleation rate was increased (Fig. 9.2 A). This might be because the dispersed glucose molecules acted as templates for the formation of small particles.

9.4 Links between field and lab observations

It has been shown that microbial silicification occurs by the immobilization of pre-formed silica nanoparticles (e.g., Schultze-Lam et al., 1995; Konhauser and Ferris, 1996; Phoenix et al., 2000; Benning et al., 2004b, 2005 and references therein). Therefore, an accurate knowledge of the mechanism and kinetics of nucleation, growth and aggregation of silica nanoparticles along with the parameters that control these processes is fundamental to understanding the pathways leading to silicification and fossilization of microorganisms in modern geothermal systems.

Using a flow-through geothermal reactor, a natural hot spring system was successfully simulated in the lab and the findings from these experiments accurately matched observations obtained from the field.

In both field and lab studies the enhancing effects of exoplysaccharides (EPS) on silica particle growth / coalescence (to from smooth silica films, Fig. 9.2 C) was demonstrated. In the field, at various field sites (e.g., Geysir sites, Hveragerdi and Krafla) despite the waters being undersaturated with respect to amorphous silica, the microbial communities (subaqueous) became fully silicified. Similarly, in the lab studies where silica nanoparticle formation was studied in the presence of xanthan gum (i.e. EPS), it was shown that xanthan gum acted as a template for silica aggregation which resulted in the development of a thin silica-rich film (which was absent in the inorganic experiments, Fig. 9.2 C).

Other similarities between field and lab studies included the strong influence of temperature on the size of silica nanoparticles, i.e., particle nucleation and growth. In the field, the particle size distribution at Svartsengi (10-36 nm, 42°C) was substantially smaller than at Reykjanes (11-106 nm, 75°C). Similarly in the lab, the sizes of the precipitating silica nanoparticles were observed to be significantly smaller at lower than at higher temperatures; at 33°C the particle size range was 8 – 14 nm whereas at 58°C the size range was 15 – 48 nm. This is also in agreement with previous results by Iler (1979) who showed that particles grown at 50°C were only half as big as those grown at 90°C. Thus with decreasing temperatures particle growth and coarsening is hindered and nucleation of new particles is favoured leading to the precipitation of small and fairly monodisperse particles (Fig. 9.2 A). As a result, sinter deposits forming at lower temperatures will be quite porous while at higher temperatures particle growth and coarsening

will lead to polydisperse size distributions and denser sinter textures and structures (Fig. 9.2 B, C). It should be noted that no major differences in particle size distribution were observed with increasing ionic strength (neither in the field nor in the lab experiments). However, the addition of salt cations (e.g., Na^+, Ca^{2+}, K^+) enhances particle-interactions resulting in the formation of gel-like structures (e.g., Iler et al., 1979). Similar structures were also observed at Svartsengi and Reykjanes where the geothermal waters exhibited high amounts of salts (≥ seawater concentrations).

In summary, the field and lab results presented above indicate that the complete microbial silicification involves the attachment of silica nanoparticles formed in solution (via hydrogen bonding or entrapment within the biofilm; e.g., Benning et al., 2004a, b and Lalonde et al., 2005) followed by the further growth and aggregation of these particles on the microbial surface until they coalesce (the individual precipitates are no longer distinguishable, i.e., smooth thin silica layers form). This silicification process is aided by the complex structure of the biofilms exopolysaccharides. Furthermore, as particle growth and coarsening are favoured with increasing temperatures and decreasing ionic strength (see above), silicification and preservation of microbial communities are more likely to occur in high-temperature geothermal waters characterized by low contents of dissolved solids (e.g., Krafla, Geysir; Fig. 9.2 C) than in low-temperature, saline waters (e.g., Svartsengi; Fig. 9.2 A). It should be noted that similar processes have been described by previous studies (e.g., Schultze-Lam et al., 1995; Konhauser and Ferris, 1996; Phoenix et al., 2000; Benning et al., 2005 and references therein).

9.5 Future work

The scope for possible future work in identifying the kinetics and mechanisms of biosilicification in modern geothermal systems is extensive. In the realm of field studies, due to the large variety of geochemical / hydrodynamic regimes of geothermal systems, the parameters controlling the abundance and diversity of microbial communities and hence the potential for microbial preservation within sinters are still not well understood. Future studies should thus focus more on the correlation of community diversity and geochemical variation in hot springs. More specifically, it would be of considerable interest to investigate the microbial diversity (both bacterial and archaeal) as a function of T, water chemistry (including potential energy sources, e.g., dissolved H_2, sulphide, dissolved oxygen, organic substrates) and sinter growth rate along an outflow channel of a single hot spring. In addition, such an approach would be strengthened by combining the genetic approach with culturing methods to obtain information on the metabolic pathways of the microbial communities. This in turn will help to better link the microbial community structure to specific geochemical environments. Lastly, a complementary

study of biomarkers (e.g., phospholipid fatty acids, ether lipids; Pancost et al., 2005, 2006) in both young and old sinter deposits that flank hot spring rims would help quantifying the preservation of specific organic molecules (or their degradation) in these ecosystems over time.

In the laboratory, to simulate geothermal waters more accurately it would be worthwhile to quantify the nucleation, growth and aggregation of silica nanoparticles in more complex solutions (e.g., different salts, presence of various mineral substrates, combinations of organics, free living or attached microorganisms) using the low temperature flow through system (i.e., pH-drop experiments) in combination with SAXS and DLS. In addition, experiments should be carried out at higher temperatures (e.g., 50 – 90°C) although this would require several modifications in the flow through system as well as data acquisition and data handling methods used in this work.

As shown in this thesis, a natural hot spring was successfully mimicked in the laboratory using a flow-through geothermal simulator (i.e., T-drop experiments). However, this system also has its limitations, specifically in terms flow rates as well as water chemistries that can be analysed: high salt contents lead to corrosion of the stainless steel tubing, high SiO_2 concentrations require higher temperatures to fully depolymerise but will also cause blockages within the tubing during cooling, etc. Nevertheless, as initially planned for this thesis, this system could be further used to determine the influence of specific organic functional groups derived from thermophilic and mesophilic microorganisms (by separating cell walls and sheath material, i.e., EPS) on growth and aggregation of silica nanoparticles under constant re-supply of silica supersaturated solution. In a second step silicification in the presence of bacteria could be simulated by using glass slides covered with cultures of different bacterial species (e.g., *Bacillus flavothermus* and *Calothrix*; both well studied isolates from geothermal waters in New Zealand and Iceland respectively). The degree of silicification could then be analysed over time and as a function of varying temperatures and silica concentrations using both SEM and TEM. Ultimately, the techniques could be developed so that these processes could be investigated in combination with SAXS and DLS in order to obtain more accurate measurements of the size and polydispersity of the particles that form in solution but also to derive information on the mechanisms and kinetics of biosilicification. Lastly, to better match temperatures regimes in hot spring environments, these processes should be also studied at higher temperatures ($50 < T < 100$°C).

REFERENCES

Alexander G. B. (1954) The polymerization of monosilicic acid. *Journal of the American Chemical Society,* **76,** 2094-2096.

Alexander G. B., Heston W. M. and Iler R. K. (1954) The solubility of amorphous silica in water. *Journal of Physical Chemistry,* **58,** 453-455.

Alfredsson G. A. and Kristjansson J. K. (1995) Ecology, distribution and isolation of *Thermus*. In *Thermus Species* (eds. R. J. Sharp and R. A. D. Williams), Biotechnology Handbooks Series, Plenum Press, London, pp 43-66.

Allia P., Barricco M., Tiberto P. and Vinai F. (1993) Kinetics of the amorphous-to-nanocrystalline transformation in $Fe_{73.5}Cu_1Nb_3Si_{13.5}B_9$. *Journal of Applied Physics,* **74,** 3137-3143.

Andreassen J.-P. (2005) Formation mechanism and morphology in precipitation of vaterite-nano-aggregation or crystal growth? *Journal of Crystal Growth,* **274,** 256-264.

Amann R. I., Ludwig W. and Schleifer K. H. (1995) Phylogenetic identification and in situ detection of individual microbial cells without cultivation. *Microbiological Reviews,* **59,**143–169

Arnórsson S. (1975) Application of silica geothermometer in low-temperature hydrothermal areas in Iceland. *American Journal of Science,* **275,** 763-784.

Arnórsson S. (1978a) Precipitation of calcite from flashed geothermal waters in Iceland. *Contributions Mineralogical Petrology*, **66,** 21-28.

Arnórsson S. (1978b) Major element chemistry of geothermal seawater at Reykjanes and Svartsengi, Iceland. *Mineralogical Magazine*, **42,** 209-220.

Arnórsson S., Gunnlaugsson E. and Svavarsson H (1983a) The chemistry of geothermal waters in Iceland. II Mineral equilibria and independent variables controlling water compositions. *Geochimica et Cosmochimica Acta*, **47,** 547-566.

Arnórsson S., Gunnlaugsson E. and Svavarsson H. (1983b) The chemistry of geothermal waters in Iceland. III. Chemical geothermometry in geothermal investigations. *Geochimica et Cosmochimica Acta*, **47,** 567-577.

Arnórsson S. (1985) The use of mixing models and chemical geothermometers for estimating underground temperatures in geothermal systems. *Journal of Volcanology and Geothermal Research*, **23**, 299-335.

Avrami M. (1939) Kinetics of phase change, I. *Journal of Chemical Physics*, **7**, 1103-1112.

Avrami M. (1940) Kinetics of phase change, II. *Journal of Chemical Physics*, **8**, 212-224.

Bailey J. K. and Mecartney M. L. (1992) Formation of colloidal silica particles from alkoxides. *Colloids Surfaces*, **63**, 151-161.

Bailly X., Olivieri I., Brunel B., Cleyet-Marel J.-C. and Béna G. (2007) Horizontal Gene Transfer and Homologous Recombination Drive the Evolution of the Nitrogen-Fixing Symbionts of *Medicago* Species. *Journal of Bacteriology*, **189**, 5223-5236.

Ball J. W. and Nordstrom D. K. (1992) *Geochemical model to calculate speciation of major, trace and redox elements in natural waters*, U.S. Geological Survey, International Groundwater Modeling Centre, 189pp.

Banfield J. F. and Zhang H. (2001) In *Nanoparticles in the Environment* (eds J. F. Banfield and A. Navrotsky). Reviews of Mineralogy and Geochemistry, Vol. 44, Mineralogical Society of America, Washington, DC, p 1-58.

Barghorn E. S. and Tyler S. A. (1965) Microorganisms from the gunflint chert. *Science*, **147**, 563-577.

Barns S. M., Fundyga R. E., Jeffries M. W. and Pace N. R. (1994) Remarkable archaeal diversity detected in a Yellowstone National Park hot spring environment. *PNAS*, **91**, 1609–1613.

Bartley J. K. (1996) Actualistic taphonomy of cyanobacteria: implications for Precambrian fossil record. *Palaios*, **11**, 571-586.

Baumann H. (1959) Polymerisation und Depolymerisation der Kieselsäure unter verschiedenen Bedingungen. *Kolloid-Zeitschrift*, **162**, 28-35.

Beelen T. P. M., Shi W., Morrison G. R., Van Garderen H. F., Browne M. T., Van Santen R. A. and Pantos E. (1997) Scanning Transmission X-Ray Microscopy; a new method for the investigation of aggregation in silica. *J. Colloid and Interface Science*, **185**, 217-227.

Bennett P. C. (1991). Quartz dissolution in organic-rich aqueous systems. *Geochimica Cosmochimica Acta*, **55**, 1781-1797.

Benning L. G., Phoenix V. R., Yee N. and Konhauser K. O. (2004a) The dynamics of cyanobacterial silicification: An infrared micro-spectroscopic investigation. *Geochimica et Cosmochimica Acta*, **68**, 729-741.

Benning L. G., Phoenix V. R., Yee N. and Tobin M. J. (2004b) Molecular characterization of cyanobacterial silicification using synchrotron infrared micro-spectroscopy. *Geochimica et Cosmochimica Acta*, **68**, 743-757

Benning L. G. and Mountain B. M. (2004) The silicification of microorganisms: a comparison between in situ experiments in the field and laboratory. In *Water-Rock Interaction* (eds. Wanty and Seal II). Taylor and Francis Group, London. pp. 3-10.

Benning, L.G., Phoenix V. and Mountain B.W. (2005) Biosilicification: the role of cyanobacteria in silica sinter deposition, In *Micro-organisms and earth systems: advances in geomicrobiology* (eds. G.M. Gadd, K.T. Semple and H.M. Lappin-Scott), Society for General Microbiology Symposium, Cambridge University Press, pp.131-150.

Benning L. G. and Waychunas G. (2007) Nucleation, growth and aggregation of mineral phases: Mechanisms and kinetic controls. In *Kinetics of Water-Rock Interaction* (eds. S. L. Brantley, J. D. Kubicki and A. F. White). Kluwer Academic/Plenum Publishers.

Berry A., Helsby W. I., Parker B. T., Hall C. J., Buksh P. A., Hill A., Clague N., Hillon M., Corbett G., Clifford P., Tidbury A., Lewis R. A., Cernik B. J., Barnes P. and Derbyshire G. E. (2003) The RAPIP2 x-ray detection system. *Nuclear Instruments & Methods in Physics Research Section A-Accelerators Spectrometers Detectors and Associated Equipment*, **513**, 260-263.

Bishop A. D. and Bear J. L. (1972) The thermodynamics and kinetics of the polymerisation of silicic acid in dilute aqueous solutions. *Thermochimica Acta*, **3**, 399-409.

Blank C. E., Cady S. L. and Pace N. R. (2002) Microbial composition of near-boiling silica depositing thermal springs throughout Yellowstone National Park. *Applied Environmental Mircobiology*, **68**, 5123-5135.

Borsboom M., Bras W., Crejak I., Detollenaere D., Glastra van Loon D., Goedtkindt P., Konijnenburg M., Lassing P., Levine Y.K., Munneke B., Oversluizen M., van Tol R. and Vlieg E. (1998) The Dutch-Belgian Beamline at the ESRF. *Journal of Synchrotron Radiation*, **5**, 518-520.

Bogush G. H., Tracy M. A. and Zukoski IV C. F. (1988) Preparation of monodisperse silica particles: controls of size and mass fraction. *Journal of Non-Crystalline Solids*, **104**, 95-106.

Boukari H., Lin J. S. and Harris M. T. (1997) Probing the dynamics of the silica nanostructure formation and growth by SAXS. *Chemistry of Materials*, **9**, 2376-2384.

Boukari H., Long G. G. and Harris M. T. (2000) Polydispersity during formation and growth of the Stöber silica particles from Small-Angle X-Ray Scattering measurements. *Journal of Colloid and Interface Science*, **229**, 129-139.

Bras W., Greaves G. N., Oversluizen M., Clark S. M. and Eeckhaut G. (2005) The development of monodispersed alumino-chromate spinel nanoparticles in doped cordierite glass, studied by in situ X-ray small and wide angle scattering and chromium X-ray spectroscopy. *Journal of Non-Crystalline Solids*, **351**, 2178-2193.

Braunstein D. and Lowe D. R. (2001) Relationship between spring and geyser activity and the deposition and morphology of high temperature (>73°C) siliceous sinter, Yellowstone National Park, Wyoming, USA. *Journal of Sedimentary Research*, **71**, 747-763.

Brock T. D. (1978) *Thermophilic Microorganisms and Life at High Temperatures*. Springer-Verlag, New York, pp. 465.

Brock T. D. and Freeze H. (1969) *Thermus aquaticus* gen. n. and sp. n., a nonsporulating extreme thermophile. *Journal of Bacteriology*, **98**, 289-297.

Brown T. A. (2006) *Gene cloning and DNA analysis: An introduction*. 5th edition, Blackwell Publishing Ltd, Oxford.

Bruno W. J., Socci N. D. and Halpern A. L. (2000) Weighted Neighbor Joining: A Likelihood-Based Approach to Distance-Based Phylogeny Reconstruction. *Molecular Biology and Evolution*, **17**, 189-197

Burnett P.-G. G., Daughney C. J. and Peak D. (2006) Cd adsorption onto Anoxybacillus flavithermus: Surface complexation modeling and spectroscopic investigations. *Geochimica et Cosmochimica Acta*, **70**, 5253-5269.

Cady S. L. and Farmer J. D. (1996) Fossilization processes in siliceous thermal springs trends in preservation along thermal gradient. In *Evolution of Hydrothermal Ecosystem on Earth (and Mars?)*. Ciba Foundation, Wiley, pp. 150-172.

Cao G. and Mallouk T. E. (1991) Topochemical Solid State Diacetylene Polymerization in Layered Metal Phosphonate Salts. *Journal of Solid State Chemistry*, **94**, 59-71.

Carroll S., Mroczek E., Alai M. and Ebert M. (1998) Amorphous silica precipitation (60 to 120 degrees C): Comparison of laboratory and field rates. *Geochimica et Cosmochimica Acta*, **62**, 1379–1396.

Carson G. A. (1991) Silicification of fossils. In *Taphonomy, Releasing the Data Locked in the Fossil Record* (eds. P. A. Allison and D.E.G. Briggs). Plenum Press, New York, pp. 455-499.

Cernik R. J., Barnes P., Bushnell-Wye G., Dent A. J., Diakun G. P., Flaherty J. V., Greaves G. N., Heeley E. L., Helsby W., Jaques S. D. M., Kay J., Rayment T., Ryan A., Tang C. C. and Terrill N. J. (2004) The new materials processing beamline at the SRS Daresbury, MPW6.2. *Journal of Synchrotron Radiation*, **11**, 163-170.

Chan S. H. (1989) A review on solubility and polymerisation of silica. *Geothermics*, **18**, 49-56.

Chandler D. P., Li S. M., Spadoni C. M., Drake G. R., Balkwill D. L., Fredrickson J. K. and Brockman F. J. (2000) A molecular comparison of culturable aerobi heterotrophic bacteria and 16S rDNA clones derived from a deep subsurface sediment. *FEMS Microbiological Ecology*, **23**, 131-144.

Chung A. P., Rainey F. A., Valente M., Nobre M. F. and da Costa M. S. (2000) *Thermus igniterrae* sp. nov and *Thermus antranikianii* sp. nov., two new species from Iceland. *International Journal of Systematic and Evolutionary Microbiology*, **50**, 209-217.

Cole J. R., Chai B., Farris R. J., Wang Q., Kulam-Syed-Mohideen A. S., McGarrell D. M., Bandela A. M., Cardenas E., Garrity G. M. and Tiedje J. M. (2007) The ribosomal database project (RDP-II): introducing *myRDP* space and quality controlled public data. *Nucleic Acids Research*, **35**, D169-D172.

Conrad C. F., Yasuhara H., Bandstra J. Z., Icopini G.A., Brantley S.L. and Heaney P.J. (2007) Modeling the kinetics of silica nanocolloid formation and growth in aqueous solutions as a function of pH and ionic strength. *Geochimica et Cosmochimica Acta*, **71**, 531-542.

Coradin T., Eglin D. and Livage J. (2004) The silicomolybdic acid spectrophotometric method and its application to silicate/biopolymer interaction studies. *Spectroscopy*, **18**, 567-576.

Cox J. S., Smith D. S., Warren L. A. and Ferris F. G. (1999) Characterizing heterogeneous bacterial surface functional groups using discrete affinity spectra for proton binding. *Environmental Science and Technology*, **33**, 4514-4521.

Crerar D., Axtmann E. V. and Axtmann R. C. (1981) Growth and ripening of silica polymers in aqueous solutions. *Geochimica et Cosmochimica Acta*, **45**, 1259-1266.

Davidson L. E., Shaw S. and Benning L. G. (2008) The kinetics and mechanisms of schwertmannite transformation to goethite and hematite under alkaline conditions. *American Mineralogist*, in press.

Dubois M., Gilles K. A., Hamilton J. K., Rebers P. A. and Smith F. (1956) Colorimetric method for determination of sugars and related substances. *Analytical Chemistry*, **28**, 350-356.

Eberl D. D., Drits V. A. and Sródón J. (1998) Deducing growth mechanisms for minerals from the shapes of crystal size distributions. *American Journal of Science*, **298**, 499-533.

Eder W. and Huber R. (2002) New isolates and physiological properties of the Aquificales and description of *Thermocrinis albus* sp. nov. *Extremophiles*, **6**, 309-318.

Egelhaaf S. U., Schurtenberger P. and Müller M. (2000) New controlled environment vitrification system for cryo-transmission electron microscopy: design and application to surfactant solutions. *Journal of Microscopy*, **200**, 128-139.

Evans J. S. O. and Radosavljević-Evans I. (2004) Beyond classical applications of powder diffraction. *Chemical Society Reviews*, **33**, 539-547.

Everett D. H. (1988) *Basic principles of colloid science.* Royal Society of Chemistry Paperbacks, London.

Fein J. B., Daughney C. J., Yee N. and Davis T. A. (1997) A chemical equilibrium model for metal adsorption onto bacterial surfaces. *Geochimica et Cosmochimica Acta*, **61**, 3319-3328.

Fein J. B., Scott S. and Rivera N. (2002) The effect of Fe on Si adsorption by *Bacillus subtilis* cell walls: insight into non-metabolic bacterial precipitation of silicate minerals. *Chemical Geology*, **182**, 265-273.

Ferris F. G., Beveridge T. J. and Fyfe W. S. (1986) Iron-silica crystallite nucleation by bacteria in a geothermal sediment. *Nature*, **320**, 609-611.

Ferris F. G., Beveridge T. J. and Fyfe W. S. (1988) Metallic ion binding by *Bacillus subtilis*: Implications for the fossilization of microorganisms. *Geology*, **16**, 149-152.

Flores G. E., Liu Y., Ferrera I., Beveridge T. J. and Reysenbach A.-L. (2008) *Sulfurihydrogenibium kristjanssoni* sp. nov., a hydrogen- and sulfur-oxidizing thermophile isolated from a terrestrial Icelandic hot spring. *International Journal of Systematic and Evolutionary Microbiology*, **58**, 1153-1158.

Fouke B. W., Bonheyo, G. T., Sanzenbacher, B. and Frias-Lopez J. (2003) Partitioning of bacterial communities between travertine depositional facies at Mammoth Hot Springs, Yellowstone National Park, USA. *Canadian Journal of Earth Sciences*, **40**, 1531-1548.

Fournier R. O. (1985) The behaviour of silica in hydrothermal solutions. In *Geology and Geochemistry of Epithermal Systems* (eds. Berger and Bethke). Society of Economic Geologists, Vol. 2, pp. 45-59.

Gedde U.W. (1995) *Polymer physics*. London, Kluwer Academic Publishers, Dordrecht, Netherlands.

Gibbs W. (1961) *The Scientific Papers, Vol. I.* Dover Publications, Inc. New York.

Glatter O. and Kratky O. (1982) *Small Angle X-ray Scattering*. Academic Press, New York.

Goto K. (1956) Effect of pH on polymerization of silicic acid. *Journal of Physical Chemistry*, **60**, 1007-1008.

Graber J. R., Kirshtein J., Speck M. and Reysenbach A. L. (2001) Community structure along a thermal gradient in a stream near Obsidian Pool, Yellowstone National Park. In *Thermophiles: Biodiversity, Ecology, and Evolution* (ed. A. L. Reysenbach, M. Voytek and R. Mancinelli). Kluwer Academic/Plenum Publisher, New York, pp. 81-89.

Graham, C. A. and Hill A. J. M. (2001) *DNA sequencing protocols*. Methods in Molecular Biology, Vol. 167, Human Press, Totowa, New Jersey.

Greenberg A. E., Trussell R. R. and Clesceri L. (1985) *Standard Methods for the Examination of Water and Wastewater*. American Public Health Association, New York, 209 pp.

Green D. L., Lin J. S., Lam Y.-F., Hu M. Z.-C., Schafer D. W. and Harris M. T. (2003a) Size, volume fraction, and nucleation of Stöber silica nanoparticles. *Journal of Colloid and Interface Science*, **266**, 346-358.

Green D. L., Jayasundara S., Lam Y.-F. and Harris M. T. (2003b) Chemical reaction kinetics leading to the first Stöber silica nanoparticles – NMR and SAXS investigation. *Journal of Non-Crystalline Solids*, **315**, 166-179.

Guidry S. A. and Chafetz H. S. (2002) Factors governing subaqueous siliceous sinter precipitation in hot springs: examples from Yellowstone National Park, USA. *Sedimentology*, **49**, 1253-1267.

Guinier A. (1939) La diffraction des rayons X aux tres petits angles: application al'étude de phénomenes Ultramicroscopiques. *Annals of Physics,* **12**, 161-237.

Gunnarsson I. and Arnórsson S. (2000) Amorphous silica solubility and the thermodynamic properties of H_4SiO_4 in the range of 0° to 350°C at P_{sat}. *Geochimica et Cosmochimica Acta*, **64**, 2295-2307.

Gunnarsson I. and Arnórsson S. (2003) Silica scaling: the main obstacles in efficient use of high-temperature geothermal fluids. *International Geothermal Conference Reykjavik*, 30-36.

Gunnlaugsson E. and Arnórsson S. (1982) The chemistry of iron in geothermal systems in Iceland. *Journal of Volcanology and Geothermal Research*, **14**, 281-299.

Handley K. M., Campbell K. A., Mountain B. W. and Browne P. R. L. (2005) Abiotic–biotic controls on the origin and development of spicular sinter: *in situ* growth experiments, Champagne Pool, Waiotapu, New Zealand. *Geobiology*, **3**, 93–114.

Hansen M. A. and Slavin S. E. (1993) Visualizing dispersion morphology via ultra-rapid freezing/transmission electron microscopy. *Progress in Organic Coatings*, **22**, 201-210.

Hardy S. C. and Voorhees P. W. (1988) Ostwald ripening in a system with a high volume fraction of coarsening phase. *Metallurgical Transactions A-Physical Metallurgy and Materials Science*, **19**, 2713-2721.

Harrison (now Perry) C. C. and Loton N. (1995) Novel routes to designer silicas: studies of the decomposition of $(M+)_2[Si(C_6H_4O_2)_3]\cdot xH_2O$. Importance of M+ identity of the kinetics of oligomerisation and the structural characteristics of the silicas produced. *Journal of Chemical Society, Faraday Transactions*, **91**, 4287-4297.

Heaney P.J. and Yates D.M. (1998) Solution chemistry of wood silicification. *Geological Society of America Annual Meeting, Abstract Program*, **30**, A-375.

Helsby W. I., Berry A., Buksh P. A, Hall C. J. and Lewis R. A. (2003) The RAPID2 interpolating system. *Nuclear Instruments & Methods in Physics Research Section A-Accelerators Spectrometers Detectors and Associated Equipment*, **510**, 138-144.

Herdianita N. R., Browne P. R. I., Rodgers K. A. and Campbell K. A. (2000) Mineralogical and textural changes accompanying ageing of silica sinter. *Mineralium Deposita*, **35**, 48-62.

Hetzer A., Daughney C. J. and Morgan H. W. (2006) Cadmium Ion Biosorption by the Thermophilic Bacteria Geobacillus stearothermophilus and G. thermocatenulatus. *Applied and Environmental Microbiology*, **72**, 4020–4027.

Hinman N. W. (1990) Chemical Factors influencing the rated and sequences of silica phase transitions: Effects of organic constituents. *Geochimica et Cosmochimica Acta*, **54**, 1563-1574.

Hinman N. W. and Lindstrom R. F. (1996) Seasonal changes in silica deposition in hot spring systems. *Chemical Geology*, **132**, 237-246.

Hjorleifsdottir S., Skirnisdottir S., Hreggvidsson G. O., Holst O. and Kristjansson J. K. (2001) Species composition of cultivated and noncultivated bacteria from short filaments in an Icelandic hot spring at 88°C. *Microbial Ecology*, **42**, 117-125.

Hollocher T. C. and Kristjansson J. K. (1992) Thermophilic denitrifying bacteria: a survey of hot springs in Southwestern Iceland. *FEMS Microbiology and Ecology*, **101**, 113–119.

Huang W.H. and Vogler D.L. (1972) Dissolution of opal in water and its water content. *Nature Physical Science*, **235**, 157-158.

Huber R., Eder W., Heldwein S., Wanner G., Huber H., Rachel R. and Stetter K. O. (1998) *Thermocrinis ruber* gen. nov., sp. nov., a pink-filament-forming hyperthermophilic bacterium isolated from Yellowstone national Park. *Applied and Environmental Microbiology*, **64**, 3576-3583.

Hudson J. A., Morgan H. W. and Daniel R. M. (1987) *Thermus filiformis* sp. nov., a filamentous caldoactive bacterium. *International Journal of Systematic Bacteriology*, **37**, 431-436.

Hugenholtz P., Pitulle C., Hershberger K. L. and Pace N. R. (1998) Novel division level bacteria diversity in a Yellowstone hot spring. *Journal of Bacteriology*, **180**, 366-376.

Hulbert S. F. (1969) Models for Solid-State Reactions in Powered Compacts: A Review. *Journal of the British Ceramics Society*, **6**, 11-20.

Hurst C. J., Crawford R. L., Knudsen G. R., McInernery M. J. and Stetzenbach (2002) *Manual of Environmental Microbiology*. ASM Press, Washington, D.C.

Icopini G. A., Brantley S. L. and Heaney P. J. (2005) Kinetics of silica oligomerization and nanocolloid formation as a function of pH and ionic strength at 25°C. *Geochimica et Cosmochimica Acta*, **69**, 293-303.

Iler R. K. (1973) Colloidal silica. In *Surface and Colloid Science* (ed. E. Matijevic), Wiley Interscience & Plenum Publisher, pp. 3–100.

Iler R. K. (1979) *The chemistry of silica*, John Wiley, New York.

Illeková E., Czomorová K., Kuhnast F. and Fiorani J. (1996) Transformation kinetics of $Fe_{73.5}Cu_1Nb_3Si_{13.5}B_9$ ribbons to the nanocrystalline state. *Material Science and Engineering A*, **205**, 166-179.

Inagaki F., Hayashi S., Doi K., Motomura Y., Izawa E. and Ogata S. (1997) Microbial participation in the formation of siliceous deposits from geothermal water and analysis of the extremely thermophilic bacterial community. *FEMS Microbiology and Ecology*, **24**, 41-48.

Inagaki F., Motomura Y. and Ogata S. (2003) Microbial silica deposition in geothermal hot waters. *Applied Microbiology and Biotechnology*, **60**, 605–611.

Johnson P. F. and Mehl R. F. (1939) Reaction kinetics in processes of nucleation and growth. *American Institute of Mining and Engineering, Technical Publication*, **1089**, 1-27.

Jones B. and Renaut R. W. (1996) Influence of thermophilic bacteria on calcite and silica precipitation in hot springs with water temperatures above 90C: Evidence from Kenya and New Zealand. *Canadian Journal of Earth Science*, **33**, 72-83.

Jones B., Renaut R. W. and Rosen M. R. (1997) Biogenicity of silica precipitation around geysers and hot spring vents, North Island, New Zealand. *Journal of Sedimentary Research*, **67**, 88-104.

Jones B., Renaut R. W. and Rosen M. R. (1998) Microbial biofacies in hot springs sinters: a model based on Ohaaki pool, North Island, New Zealand. *Journal of Sedimentary Research*, **68**, 413-434.

Jones B., Renaut R. W. and Rosen M. R. (1999) Actively growing siliceous oncoids in the Waiotapu geothermal area, North Island, New Zealand. *Journal of the Geological Society London*, **156**, 89-103.

Jones B., Renaut R. W. and Rosen M. R. (2000) Stromatolites forming in acidic hot springs waters, North Island, New Zealand. *Palaois*, **15**, 450-475.

Jones B., Renaut R. W. and Rosen M. R. (2001) Microbial construction of siliceous stalactites at geysers and hot springs: examples from Whakarewarewa geothermal area, North Island, New Zealand. *Palaois*, **16**, 73-94.

Jones B., Renaut R. W. and Rosen M. R. (2003) Silicified microbes in a geyser mound: the enigma of low-temperature cyanobacteria in a high-temperature setting. *Palaois*, **18**, 87-109.

Jones B., Kronhauser K. O., Renaut R. W. and Wheeler R. S. (2004) Microbial silicification in Iodine Pool, Waimangu geothermal area, North Island, New Zealand: implications for recognition and identification of ancient silicified microbes. *Journal of the Geological Society London,* **161**, 983-993.

Jones B. and Renaut R. W. (2004) Water content of opal-A: Implications for the origin of laminae in Geyserite and sinter. *Journal of Sedimentary Research*, **74**, 117-128.

Kandianis M. T., Fouke B. W., Johnson R. W., Veysey II J. and Inskeep W. P. (2008) Microbial biomass: A catalyst for CaCO3 precipitation in advection-dominated transport regimes. *Geological Society of America Bulletin*, **120**, 442-450.

Kitahara S. (1960) The polymerization of silicic acid obtained by the hydrothermal treatment of quartz and the solubility of amorphous silica. *The Review of Physical Chemistry of Japan*, **30**, 131-137.

Kolmogorov A.N. (1937) A statistical theory for the recrystallization of metals. *Bulletin of the Academy Sciences of the U.S.S.R. Physical series*, **1**, 355-359.

Knauth L. P. and Epstein S. (1982) The nature of water in hydrous silica. *American Mineralogist*, **67**, 520-520.

Knoll A. H. (1985) Exceptional preservation of photosynthetic organisms in silicified carbonates and silicified peats. *Philosophical Transactions of the Royal Society of London*, **311**, 11-122.

Konhauser K. O. and Ferris F. G. (1996) Diversity of iron and silica precipitation by microbial mats in hydrothermal waters, Iceland: Implications for Precambrian iron formations. *Geology*, **24**, 323-326.

Konhauser K. O., Phoenix V. R., Adams D. G., Bottrell S. H. and Head I. M. (1999) Microbial-silica interactions in modern hot spring sinter. In *Geochemistry of the Earth's surface* (ed. H. Armannsson). Balkema, pp. 263-266.

Konhauser K. O., Phoenix V. R., Bottrell S. H., Adams D. G. and Head I. M. (2001) Microbial-silica interactions in Icelandic hot springs sinter: possible analogues for some Precambrian siliceous stromatolites. *Sedimentology*, **48**, 415-433.

Konhauser K. O., Jones B., Reysenbach A.-L. and Renaut R. W. (2003) Hot spring sinters: keys to understanding Earth's earliest life forms. *Canadian Journal of Earth Science*, **40**, 1713–1724.

Konhauser K. O., Jones B., Phoenix V. R., Ferris F. G. and Renaut R. W. (2004) The microbial role in hot spring silicification. *Ambio*, **33**, 552-558.

Krauskopf K. B. (1956) Dissolution and precipitation of silica at low temperatures. *Geochimica Cosmochimica Acta*, **10**, 1-26.

Kröger N., Deutzmann R. and Sumper M. (2001) Silica precipitating peptides from Diatoms: The chemical structure of silaffin-1A from *Cylindrotheca fusiformis*. *Journal of Biological Chemistry*, **276**, 26066-26070.

Kristmannsdóttir H. (1989) Types of scaling occuring by geothermal utilization in Iceland. *Geothermics*, **18**, 183-190.

Kristjansson J. K., Hjorleifsdottir S., Merteinsson V. T. and Alfredsson G. A. (1994) *Thermus scotoductus*, sp. nov., a pigment-producing thermophilic bacterium from hot tap water in Iceland and including *Thermus* sp. X-1. *Systematic and Applied Microbiology*, **17**, 44-50.

Kristjansson J. K. and Alfredsson G. A. (1983) Distribution of *Thermus* spp. in Icelandic hot springs and a thermal gradient. *Applied and Environmental Microbiology*, **45**, 1785-1789.

Kvist T., Ahring B. K. and Westermann P. (2007) Archaeal diversity in Icelandic hot springs. *FEMS Microbiology Ecology*, **59**, 71-80.

Lalonde S. V., Konhauser K. O., Reysenbach A. L. and Ferris F. G. (2005) The experimental silicification of Aquificales and their role in hot spring formation. *Geobiology*, **3**, 41-52.

Langer K. and Flörke O. W. (1974) Near infrared adsorption spectra (4000-9000 cm^{-1}) of opals and the role of water in these $SiO_2 \cdot nH_2O$ minerals. *Fortschritte der Mineralogie*, **52**, 17-51.

Lasaga A. C. (1998) *Kinetic Theory in the Earth Sciences*. Princeton University Press, Princeton, New Jersey, 811 p.

Leo R. F. and Barghoorn E. S. (1976) Silicification of wood. *Havard University Botanical Museum Leaflets*, **25**, 1-46.

Lifshitz I. M. and Slyozov V. V. (1961) The kinetics of precipitation from supersaturated solid solutions. *Journal of Physics and Chemistry of Solids*, **19**, 35-50.

Lin M. Y., Lindsay H. M., Weitz D. A., Ball R. C., Klein R. and Meakin P. (1990) Universal reaction-limited colloid aggregation. *Physical Review A*, **41**, 2005-2020.

Lowe D. R., Anderson K. S. and Braunstein D. (2001) The zonation and structuring of siliceous sinter around hot springs, Yellowstone National Park, and the role of thermophilic bacteria in its deposition. In *Thermophiles: Biodiversity, Ecology, and Evolution* (ed. A. L. Reysenbach, M. Voytek and R. Mancinelli). Kluwer Academic/Plenum Publisher, New York, pp. 143-166.

Lu K. (1996) Nanocrystalline metals crystallized from amorphous solids: nanocrystallization, structure, and properties. *Materials Science and Engineering: R: Reports*, **16**, 161-221.

Lynne B. Y., Campell K. A. and Perry R. S. (2006) Alteration of sinter diagenesis in an active fumarole, Taupo volcanic zone, New Zealand. *Geology*, **34**, 749-752.

Madigan M. T., Martinko J. M. and Parker J. (1997) *Brock Biology of Microorganisms*, Prentice Hall International, 8th edition.

Madras G. and McCoy B. J. (2001) Distribution kinetics theory of Ostwald ripening. *Journal of Chemical Physics*, **115**, 6699-6706.

Madras G. and McCoy B. J. (2002) Transition from nucleation and growth to Ostwald ripening. *Chemical Engineering Science*, **57**, 3809-3818.

Malek J., Mitsuhashi T., Ramìrez-Castellanos J. and Matsui (1999) Calorimeteric and high-resolution transmission electron microscopy study of nanocrystallization in zirconia gel. *Journal of Materials Research*, **14**, 1834-1843.

Martin J. E., Wilcoxon J. P., Schaefer D. and Odinek J. (1990) Fast aggregation of colloidal silica. *Physical Review A*, **41**, 4379-4391.

Makrides A. C., Turner M. J., Harvey W. W., Slaughter J., Brummer S. B., Offenhartz P. O'D. and Pearson G. F. (1977) Study of silica scaling from geothermal brines. Master thesis, U.S. Department of Energy, pp. 72.

Makrides A. C., Turner M. and Slaughter J. (1980) Condensation of silica from supersaturated silicic acid solutions. *Journal of Colloid and Interface Science,* **73**, 345-367.

Marshall W. L. and Warakomski J. M. (1980) Amorphous silica solubilities – II. Effect of aqueous salt solutions at 25°C. *Geochimica et Cosmochimica Acta*, **44**, 915-924.

Marshall W. L. and Chen C.-T. A. (1982) Amorphous silica solubilities-V. Predictions of solubility behaviour in aqueous mixed electrolyte solutions to 300°C. *Geochimica et Cosmochimica Acta*, **46**, 289-291.

Matsoukas T. and Gulari E. (1988) Dynamics of Growth of Silica Particles from Ammonia-Catalyzed Hydrolysis of Tetra-ethyl-orthosilicate. *Journal of Colloid and Interface Science*, **124**, 252-261.

McElroy W. D. and Glass B. (1951) *Phosphorus Metabolism*, vol. I, Johns Hopkins University Press, Baltimore

Merz M. U. E. (1992) The biology of carbonate precipitation by Cyanobacteria. *Facies*, **26**, 81-102.

Meyer-Dombard D. R., Shock E. L. and Amend J. P. (2005) Archaeal and bacterial communities in geochemically diverse hot springs of Yellowstone National Park USA. *Geobiology*, **3**, 211-227.

McKenzie E. J., Brown K. L., Cady S. L. and Campell K. A. (2001) Trace metal chemistry of microorganisms in geothermal sinter, Taupo Volcanic Zone, New Zealand. *Geothermics*, **30**, 483-502.

Miyashiro A. (1975) *Metamorphism and Metamorphic Belts*, Unwin, 492pp.

Molisch H. (1886) Zwei neue Zuckerreactionen. *Monatshefte fur Chemie,* **7**, 198-209.

Monty C. L. V., Westall F. and Van der Gaast S. (1991) Diagensis of siliceous particles in sub-Antarctic sediments, ODP Leg 114, Hole 699A: possible microbial mediation. *Proceedings ODP Science Research*, **114**, 685-710.

Moreira J. E., Cesar M. L. and Aegerter M. A. (1990) Light Scattering of Silica Particles in Solution. *Journal of Non-Crystalline Solids*, **121**, 394-396.

Moulik S. P. and Mullick D. K. (1966) Catalysis in the polymerisation of silicic acid. *Journal of Polymer Science*, **4**, 811-820.

Mountain B. W., Benning L. G. and Graham D. J. (2001). Biomineralization in New Zealand Geothermal Areas. *Proceedings of NZ Geothermal Workshop*, **23**, 27-32.

Mountain B. W., Benning L. G. and Boerema J. (2003) Experimental studies on New Zealand hot spring sinters: rates of growth and textural development. *Canadian Journal of Earth Sciences*, **40**, 1643–1667.

Nakagawa T. and Fukui M. (2002) Phylogenetic characterization of microbial mats and streamers from a Japanese alkaline hot springs with a thermal gradient. *Journal of General and Applied Microbiology*, **48**, 211-222.

Ngwenya B. T., Sutherland I. W. and Kennedy L. (2003) Comparison of the acid-base behaviour and metal adsorption characteristics of a Gram-negative bacterium with other strains. *Applied Geochemistry,* **18**, 527–538.

Nielson A. E. (1964) *The kinetics of Precipitation*, McMillan, New York, pp 151.

Oehler J. H. (1976) Hydrothermal crystallization of silica gel. *Geological Society of America Bulletin*, **87**, 1143-1152.

Okamoto G., Okura T. and Goto K. (1957) Properties of Silica in Water. *Geochimica et Cosmochimica Acta*, **12**, 123-132.

Ostwald W. (1901) *Analytische Chemie*. 3rd edition, Englemann.

Pace N. R. (1997) A Molecular View of Microbial Diversity and the Biosphere. *Science*, **276**, 734 – 740.

Pancost R. D., Pressley S., Coleman J. M., Benning L. G. and Mountain B. M. (2005) Lipid biomolecules in silica sinters: indicators of microbial biodiversity. *Environmental Microbiology*, **7**, 66–77.

Pancost R. D., Pressley S., Coleman J. M., Talbot H. M., Kelly S. P., Farrimond P., Schouten S., Benning L. G. and Mountain B. W. (2006) Composition and implications of diverse lipids in New Zealand Geothermal sinters. *Geobiology*, **4**, 71-92.

Parkhurst D. L. and Appelo C. A. J. (1999) *User's guide to PHREEQC (version 2)-A computer program for speciation, batch-reaction, one-dimensional transport, and inverse*

geochemical calculations, US Geological Survey, Water-Resources Investigations Report 99-4259, pp. 312.

Peck L. B. and Axtmann R. C. (1979) A theoretical model of the polymerization of silica in aqueous media. International Symposium on Oilfield and Geothermal Chemistry, Society of Petroleum and Engineering, *American Institute of Mining and Metallurgical Engineers Transactions*, 239-247.

Perry C. C. and Keeling-Tucker T. (2000) Biosilicification: the role of the organic matrix structure control. *Journal of Biological Inorganic Chemistry*, **5**, 537-550.

Perry C. C. (2003) Biosilicification: structure, regulation of structure and model studies. In: *Silicon chemistry - from molecules to extended systems* (eds. P. Jutzi and U. Schubert), Weinheim, Wiley-VCH, pp. 475-487.

Pétursdóttir S. K. and Kristjánsson J. K. (1996) The relationship between physical and chemical conditions and low microbial diversity in the Blue Lagoon geothermal lake in Iceland. *FEMS Microbiology Ecology*, **19**, 39-45.

Phoenix V. R., Adams D. G. and Konhauser K. O. (1999) Photosynthetic controls on the silicification of cyanobacteria. In *Geochemistry of the Earth's surface*, (ed. H. Armannsson), Balkema, pp. 275-278.

Phoenix V. R., Adams D. G. and Konhauser K. O. (2000) Cyanobacterial viability during hydrothermal biomineralisation. *Chemical Geology*, **169**, 329-338.

Phoenix V. R. (2001) Microbial-biomineral interactions and their significance for the formation of chemical sediments. PhD thesis, University of Leeds.

Phoenix V. R., Adams D. G., Bottrell S. H. and Konhauser K. O. (2001) Role of biomineralization as an ultraviolet shield: Implications for Archean life. *Geology*, **29**, 823-826.

Phoenix V. R., Martinez R. E., Konhauser K. O. and Ferris F. G. (2002) Characterization and Implications of the Cell Surface Reactivity of Calothrix sp. Strain KC97. *Applied and Environmental Microbiology*, **68**, 4827–4834.

Phoenix V. R., Konhauser K. O. and Ferris F. G. (2003) Experimental study of iron and silica immobilization by bacteria in mixed Fe–Si systems: implications for microbial silicification in hot springs. *Canadian Journal of Earth Sciences*, **40**, 1669–1678.

Pfeifer P. and Obert M. (1989) *The Fractal approach to heterogeneous chemistry: Surfaces, colloids, polymers* (ed. D. Avnir), Wiley, New York.

Pontoni D., Narayanan T. and Rennie A. R. (2002) Time-resolved SAXS study of nucleation and growth of silica colloids. *Langmuir*, **18**, 56-59.

Purcell D., Sompong U., Yim L. C., Barraclough T. G., Peerapornpisal Y. and Pointing S. B. (2006) The effects of temperature, pH and sulphide on the community structure of hyperthemophilic streamers in hot springs of northern Thailand. *FEMS Microbiology and Ecology*, **60**, 456-466.

Renault R. W., Jones B. and Rosen M. R. (1996) Primary silica oncoids from Orakeikorako hot springs, North Island, New Zealand. *Palaios*, **11**, 446-458.

Reysenbach A. L., Wickham G. S. and Pace N. R. (1994) Phylogenetic analysis of the hyperthermophilic pink filament community in Octopus Spring, Yellowstone National Park. *Applied and Environmental Microbiology*, **60**, 2113-2119.

Reysenbach A. L., Ehringer M. and Herschberger K. (2000) Microbial diversity at 83 degrees C in Calcite Springs, yellowstone National Park: another environment where *Aquificales* and „*Korarchaeota*" coexist. *Extremophiles*, **4**, 61-67.

Richardson E. (1957) The effect of selected organic compounds on the determination of silica by the molybdenum blue method. *Research London*, **11**, 163-165.

Rimstidt J. D. and Barnes H. L. (1980) The kinetics of silica-water reactions. *Geochimica et Cosmochimica Acta*, **44**, 1683-1699.

Rothbaum H. P. and Rhode A. G. (1979) Kinetics of silica polymerisation and deposition from dilute solutions between 5 and 180°C. *Journal of Colloid and Interface Science*, **71**, 533-559.

Rothbaum, H. P., and Wilson, R. D. (1977) Effect of temperature and concentration on the rate of polymerization of silica in geothermal waters. In *Geochemistry 1977*. New Zealand Department of Science and Industrial Resources Bulletin, pp. 37-43.

Rothbaum H. P., Anderton B. H., Harrison R. F., Rohde A. G. and Slatter A. (1979) Effect of silica polymerisation and pH on geothermal scaling. *Geothermics*, **8**, 1-20.

Ruff S. W., Farmer J. D., Calvin W. M., Johnson J. R., Arvidson R. E., Squyres S. W., Christensen P. R. and Team T. S. (2007) Evidence for a possible siliceous sinter deposit at Home Plate in Gusev Crater. *Eos Transactions, AGU*, **88(52)**, P23A-1097 (abstr).

Sambrook J., Fritsch E. F. and Maniatis T. (1989) *Molecular cloning*. A laboratory manual, Cold Spring Harbor Press Laboratory Press.

Schinteie R., Campbell K. A. and Browne P. R. L. (2007) Microfacies of stromatolitic sinter from acid-sulphate-chloride springs at Parariki Stream. Rotokawa geothermal field, New Zealand. *Palaeontologia Electronica*, **10**, pp. 33.

Schultze-Lam S., Ferris F. G., Kronhauser K. O. and Wiese R. G. (1995) *In situ* silicification of an Icelandic hot spring microbial mat: Implications for microfossil formation. *Canadian Journal of Earth Sciences*, **32**, 2021-2026.

Schultze-Lam S., Fortin D., Davis B. S. and Beveridge T. J. (1996) Mineralization of bacterial surfaces, *Chemical Geolology*, **132**, 171-181.

Segnit E. R., Stevens T. J. and Jones J. B. (1965) The role of water in opal. *Journal of the Geological Society of Australia*, **12**, 211-226.

Shaw S., Pepper S. H., Bryan N. D. and Livens F. R. (2005) The kinetics and mechanisms of goethite and hematite crystallisation under alkaline conditions: An *in-situ* time-resolved Small Angle X-ray Scattering (SAXS) study. *Geochimica et Cosmochimica Acta*, **90**, 1852-1860.

Skírnisdóttir S., Hreggvidsson G. O., Hjörleifsdottir S., Marteinsson V. T., Pétursdóttir S. K., Holst O. and Kristjánsson J. K. (2000) Influence of sulfide and temperature on species composition and community structure of hot spring microbial mats. *Applied and Environmental Microbiology*, **66**, 2835-2841.

Smith B. Y., Turner S. J. and Rodgers K. A. (2003) Opal-A and associated microbes from Wairakei, New Zealand: the first 300 days. *Mineralogical Magazine*, **67**, 563-579.

Solomatov V. S. and Stevenson D. J. (1993) Kinetics of crystal growth in a terrestrial magma ocean. *Journal of Geophysical Research*, **98**, 5407-5418.

Sonne-Hansen J. and Ahring B. K. (1997) Anaerobic microbiology of an alkaline Icelandic hot spring. *FEMS Microbiology Ecology*, **23**, 31-38.

Spear J. R., Walker J. J., McCollom T. M. and Pace N. R. (2005) Hydrogen and bioenergetics in the Yellowstone geothermal ecosystem. *PNAS*, **102**, 2555-2560.

Squyres S. W. and Team A. S. (2007) Recent results from the Spirit Rover at Home Plate and "Silica Valley". *Eos Transactions, AGU*, **88(52)**, P21C-01 (abstr).

Squyres S. W., Arvidson R. E., Ruff S., Gellert R., Morris R. V., Ming D. W., Crumpler L., Farmer J. D., Des Marais D. J., Yen A., McLennan S. M., Calvin W., Bell III J. F., Clark B. C., Wang A., McCoy T. J., Schmidt M. E. and de Souza Jr. P. A. (2008) Detection of Silica-Rich Deposits on Mars. *Science*, **320**, 1063-1067.

Stefánsson A. and Arnórsson S. (2000) Feldspar saturation state in natural waters. *Geochimica et Cosmochimica Acta,* **64**, 2567–2584.

Stöber W., Fink A. and Bohn E. (1968) Controlled growth of monodisperse silica spheres in the micron size range. *Journal of Colloid and Interface Science*, **26**, 62-69.

Sutherland I. W. (1994) Structure-function relationships in microbial exopoly-saccharides. *Biotechnology Advances*, **12**, 393-448.

Svergun D. I. (1992) Determination of the regularization parameter in indirect-transform methods using perceptual criteria. *Journal of Applied Crystallography*, **25**, 495-503.

Svergun D. I. and Koch M. H. J. (2003) Small-angle scattering studies of biological macromolecules in solution. *Reports on Progress in Physics,* **66**, 1735–1782.

Takacs C. D., Ehringer M., Favre R., Cermola M., Eggertson G., Palsdottir A. and Reysenbach A. L. (2001) Phylogenetic characterisation of the blue filamentous bacterial community from and Icelandic geothermal spring. *FEMS Microbiology and Ecology*, **35**, 123-128.

Thompson R. W. (1992) Analysis of zeolite crystallizations using Avrami transformation methods. *Zeolites*, **12**, 680-684.

Thordarson H. and Tomasson T. H. (1989) Brine classification at Svartsengi, Iceland: Effect of pH and temperature on the precipitation of silica and its properties. *Geothermics*, **18**, 287-294.

Tréguer P., Nelson D. M., Van Bennekom A. J., Demaster D. J., Leynaert A. and Quéguiner B. (1995) The silica balance in the world ocean: a re-estimate. *Science*, **268**, 375–379.

Urrutia M. M., Kemper M., Doyle R. and Beveridge T. J. (1992) The membrane-induced proton motive force influences the metal binding ability of *Bacillus subtilis* cell walls. *Applied and Environmental Microbiology*, **58**, 3837-3844.

Urrutia M. M. and Beveridge T. J. (1994) Formation of fine-grained metal and silicate precipitates on a bacterial surface (*Bacillus subtilis*). *Chemical Geology*, **116**, 261-280.

van Blaaderen A., van Geest J. and Vrij A. (1992) Monodisperse Colloidal Silica Spheres from Tetraalkoxysilanes: Particle Formation and Growth Mechanism. *Journal of Colloid and Interface Science*, **154**, 481-501.

Verrecchia E. P., Freytet, P., Verrecchia, K. E. and Dumont J. L. (1995) Spherulites in Calcrete laminar crusts - biogenic $CaCO_3$ precipitation as a major contributor to crust formation. *Journal of Sedimentary Research Section A-Sedimentary Petrology and Processes*, **65**, 690-700.

Voorhees P. W. and Glicksman M. E. (1984) Solution to the multiparticle diffusion problem with applications to Ostwald ripening. I. Theory. *Acta Metallurgia*, **32**, 2001-2011.

Voorhees P. W. (1985) The Theory of Ostwald ripening. *Journal of Statistical Physics*, **38**, 231-252.

Wagner C. (1961) Theorie der Alterung von Niderschlagen durch Umlosen (Ostwald Reifung). *Zeitschrift fur Electrochemie*, **65**, 581-591.

Walter M. R., Bauld J. and Brock T. D. (1972) Siliceous algal and bacterial stromatolites in hot spring and geyser effluents of Yellowstone National Park, *Science*, **178**, 402-405.

Walter M. R. (1976). Hot-spring sediments in Yellowstone National Park. In: *Stromatolites* (ed. M. R. Walter), Elsevier, Amsterdam, pp. 489-498.

Ward D. M., Santegoeds C. M., Nold S. C., Ramsing N. B., Ferris M. J. and Bateson M. M. (1997) Biodiversity within hot springs microbial communities: molecular monitoring of enrichment cultures. *Antoine Van Leeuwenhoek*, **71**, 143-150.

Weast R. C. (1972) *CRC Handbook of Chemistry and Physics*, 53rd edition, Chemical Rubber Co.

Weres O., Yee A. and Tsao L. (1981) Kinetics of silica polymerization. *Journal of Colloid and Interface Science*, **84**, 379-402.

Westall, F. and Walsh, M. M. (2000) The diversity of fossil microorganisms in Archaen-age rocks. In *Journay to Diverse Microbial Worlds* (ed. J. Seckbach), Kluwer, Amsterdam, pp. 15-27.

Weitz D. A. and Huang J. S. (1984) In *Kinetics of Aggregation and Gelation* (eds. F. Family and D. P. Landau), Elsevier, Amsterdam, p. 19.

Weitz D. A., Huang J. S., Lin M. Y. and Sung, J. (1985) Limits of the Fractal Dimension for Irreversible Kinetic Aggregation of Gold Colloids. *Physical Review Letters*, **54**, 1416-1419.

White D. E., Brannock W. W. and Murata K. J. (1956) Silica in hot spring waters. *Geochimica et Cosmochimica Acta,* **10**, 27-59.

Williams R. A., Smith K. E., Welch S. G., Micallef J. and Sharp R. J. (1995) DNA relatedness of *Thermus* strains, description of *Thermus brockianus* sp. nov., and proposal to re-establish *Thermus thermophilus* (Oshima and Imahori), *International Journal of Systematic Bacteriology*, **45**, 495-499.

Williams L. A., Parks, G. A. and Crerar D. A. (1985) Silica diagenesis, I. Solubility controls. *Journal of Sedimentary Research*, **55**, 301-311.

Williams L. A. and Crerar D. A. (1985) Silica diagenesis, II. General mechanisms. *Journal of Sedimentary Research*, **55**, 312-321.

Wijnen P. W. J. G., Beelen T. P. M., Rummens K. P. J., Saeijs H. C. P. L. and van Santen R. A. (1991) Silica gel from water glass: a SAXS study of the formation and ageing of fractal aggregates. *Applied Crystallography*, **24**, 759-765.

Wong E. M., Bonevich J. E. and Searson P. C. (1998) Growth kinetics of nanocrystalline ZnO particles from colloidal suspensions. *Journal of Physical Chemistry B*, **101**, 7770-7775.

Yamamoto H., Hiraishi A., Kato K., Chiura H. X., Maki Y. and Shimizu A. (1998) Phylogenetic evidence for the existence of novel thermophilic bacteria in hot spring sulphur-turf microbial mats in Japan. *Applied and Environment Microbiology*, **64**, 1680-1687.

Yao J. H, Elder K. R. Guo G. and Gran M. (1993) Theory and simulation of Ostwald ripening. *Physical Reviews B*, **47**, 14110–14125.

Yee N., Fein J. B. and Daughney C. J. (2000) Experimental study of the pH-, ionic strength-, and reversibility behaviour of bacteria-mineral adsorption. *Geochimica et Cosmochimica Acta*, **64**, 609-617.

Yee N., Phoenix V. R., Konhauser K. O., Benning L. G. and Ferris F. G. (2003) The effect of cyanobacteria on Si precipitation kinetics at neutral pH: Implications for bacterial silicification in geothermal hot springs. *Chemical Geology*, **199**, 83-90.

Yee N., Benning L. G., Phoenix V. and Ferris F. G. (2004) Characterization of metal-cyanobacteria sorption reactions: A combined macroscopic and infrared spectroscopic investigation. *Environmental Science and Technology*, **38**, 775-782.

Yokoyama T., Taguchi S., Motomura Y., Watanabe K., Nakanishi T., Aramaki Y. and Izawa E. (2004) The effect of aluminium on the biodeposition of silica in hot springs water: chemical state of aluminium in siliceous deposits collected along the hot spring water stream of Steep Cone hot spring in Yellowstone National Park, USA, *Chemical Geology*, **212**, 329-337.

Zhai W., Yu J, Wu L., Ma W. and He J. (2006) Heterogeneous nucleation uniformizing cell size distribution in microcellular nanocomposites foams. *Polymer*, **47**, 7580-7589.

APPENDIX A

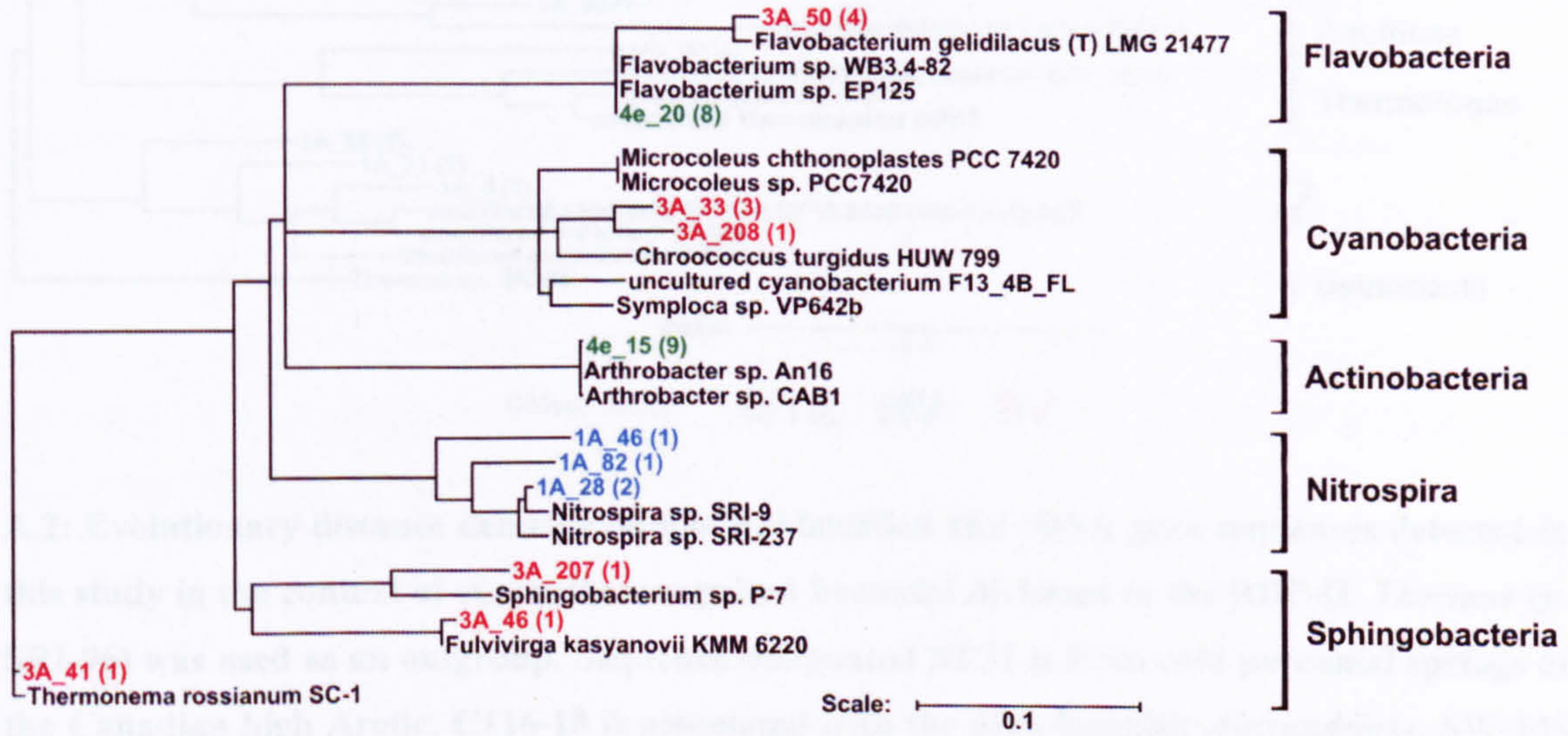

A.1: Evolutionary distance dendogramm of *Flavobacetria*, *Cyanobacteria*, *Actinobacteria*, *Nitrospira* and *Sphinobacteria* 16S rDNA gene sequences detected in this study in the context of currently recognized bacterial divisions in the RDP-II. *Thermonema rossianum* (detected in saline hot springs in Naples, Italy) was used as an outgroup. Sequence designated LGM 21477 was detected in microbial mats from Antarctic lakes, WB3.4-82 is from river water, EP125 from River Taff, Wales, HUW799 from a lake in the High Tatra Mountains, Slovakia, VP642P is a marine cyanobacteria, An16 is from deep sea in Antarctica, CAB1 from Canadian oil sand, SRI strains are from a high sulphide mat in Iceland, P-7 from paddy soil, and KMM 6220 from seawater. Origin of PPC7420 and F13_4B_FL is not known. The scale bar is in nucleotide substitution per sequence position.

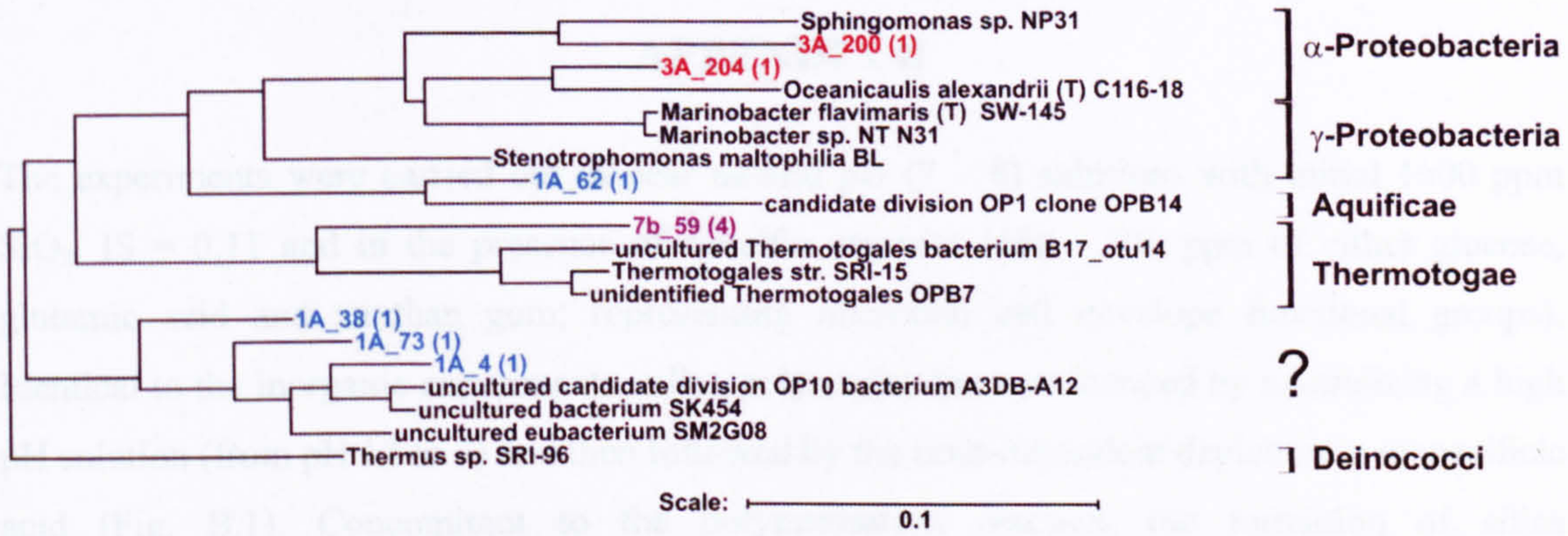

A.2: Evolutionary distance dendogramm of unidentified 16S rDNA gene sequences detected in this study in the context of currently recognized bacterial divisions in the RDP-II. *Thermus sp.* SRI-96) was used as an outgroup. Sequence designated NP31 is from cold perennial springs of the Canadian high Arctic, C116-18 is associated with the dinoflagellate *Alexandrium*, SW-145 is slightly halophilic organisms from seawater of Yellow Sea in Korea, NT N31 is a euryhaline halophilic strain isolated from deep sea sediments, BL from seawater, ODB14, OPB7 and A3DB-A12 are from Obsidian Pool in YNP, B17_otu14 from high-temperature horizons of the Dagang Oilfield in China, SRI strains are from a high sulphide mat in Iceland, SK454 from Rainbow and Joseph's Coat Hot Springs in YNP, and SM2G08 from Angel Terrace, Mammoth Hot Springs in YNP. The scale bar is in nucleotide substitution per sequence position.

APPENDIX B

The experiments were carried out in near neutral pH (7 – 8) solutions with initial 1600 ppm SiO_2, IS = 0.11 and in the presence of specific organics (150 - 300 ppm of either glucose, glutamic acid and xanthan gum; representing microbial cell envelope functional groups). Identical to the inorganic experiments, silica polymerisation was induced by neutralizing a high pH solution (from pH 12 to 7) and then followed by the time-dependent depletion in monosilicic acid (Fig. B.1). Concomitant to the polymerisation reaction, the formation of silica nanoparticles (i.e., change in particle size over time) was quantified *in-situ* using SAXS (Fig. B.2A) and DLS (Fig. B.2B)

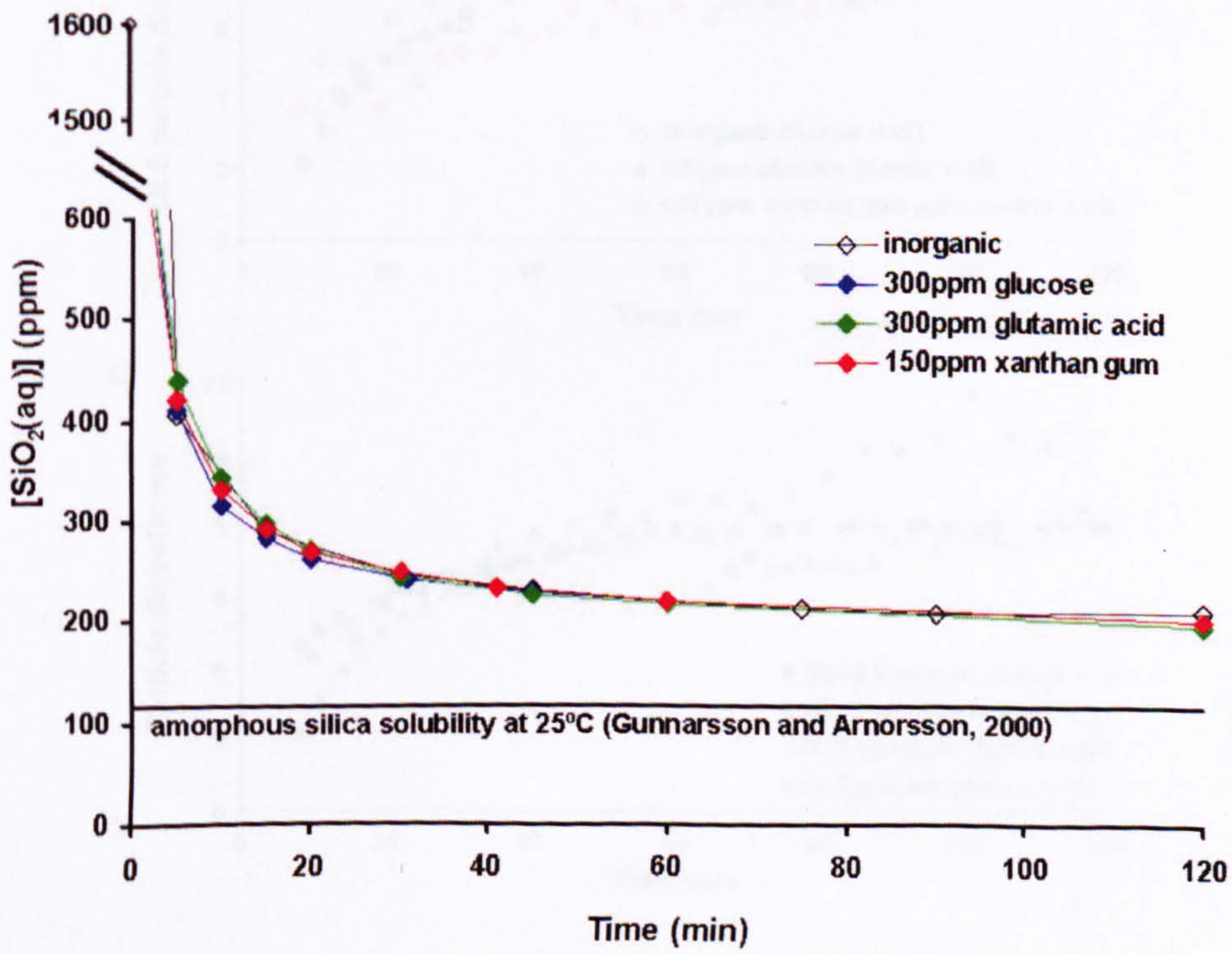

B. 1: Time dependent decrease in monosilicic acid, [SiO_2(aq)], in solutions with 1600ppm SiO_2, IS of 0.11 and added organics, i.e., glucose, glutamic acid or xanthan gum. Note that the errors (<6%) are about the size of the symbols.

The comparison to the inorganic experiment with identical SiO_2 and IS (1600 ppm SiO_2, 0.11 IS) showed that the presence of glucose, glutamic acid or xanthan gum did not affected the polymerisation reaction (Fig. B.1). In all organic and inorganic experiments with 1600 ppm SiO_2 and 0.11 IS, about 80% of $SiO_{2(aq)}$ (with respect to silica solubility at 30°C; solid line in Fig. B.1) polymerised within the first 5 minutes and after 2 hours a steady state was almost approached (~93% polymerised).

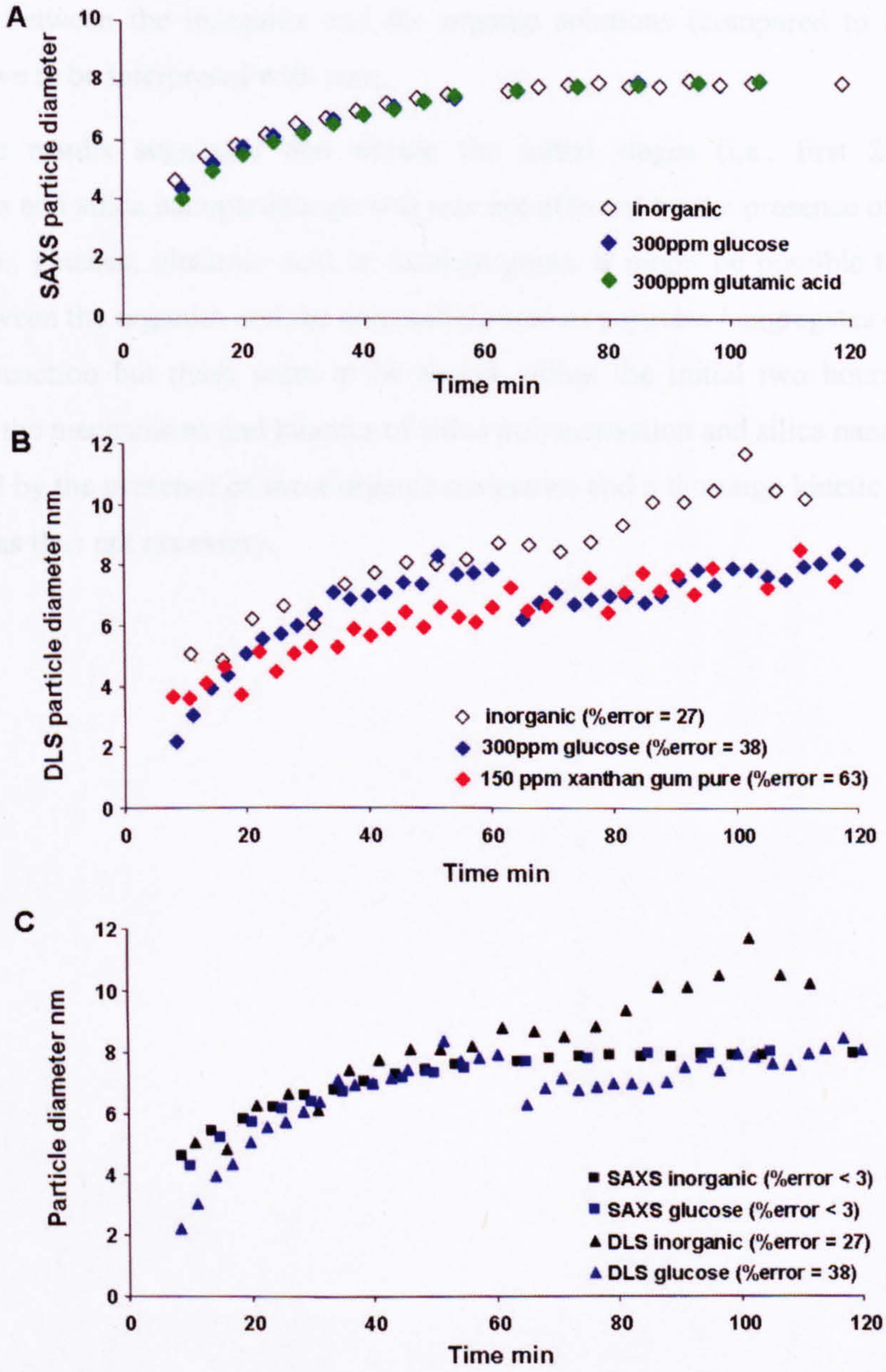

B. 2: Time evolution of the particle diameter obtained from A) SAXS (i.e., GNOM analysis) and B) DLS showing the growth of silica nanoparticles in solutions with 1600ppm SiO_2, IS = 0.11 without and with added organics (i.e., glucose, glutamic acid or xanthan gum). C) The comparison of results obtained from SAXS and DLS showed the agreement between these two methods (for solutions with 1600ppm SiO_2, IS = 0.11 and with / without added glucose).

Similarly, no major differences were observed in particle diameter (i.e., particle growth profile) between the inorganic and the organic experiments as illustrated by both SAXS (Fig. B.2A) and DLS (Fig. B.2B). It should be noted that the errors of the DLS experiments were quite high (specifically for the experiment with xanthan gum; Fig. B.2B) and the bigger differences in

particle sizes between the inorganic and the organic solutions (compared to SAXS results; B.2A) thus have to be interpreted with care.

Overall, these results suggested that during the initial stages (i.e., first 2 hours) silica polymerisation and silica nanoparticle growth was not affected by the presence of these organic molecules (i.e., glucose, glutamic acid or xanthan gum). It might be possible that interaction processes between the organics and the monosilicic acid or particles / aggregates occur at a later stage of the reaction but these seem to be absent within the initial two hours. This further indicated that the mechanisms and kinetics of silica polymerisation and silica nanoparticles were not influenced by the presence of these organic molecules and a thorough kinetic analysis of the SAXS data was thus not necessary.

APPENDIX C

	E1 Experiment 640ppm SiO_2, IS = 0.02, T = 58°C		E2 Experiment 320ppm SiO_2, IS = 0.02, T = 58°C		E3 Experiment 430ppm SiO_2, IS = 0.02, T = 58°C		E4 Experiment 960ppm SiO_2, IS = 0.03, T = 58°C		E5 Experiment 640ppm SiO_2, IS = 0.11, T = 58°C		E6 Experiment 640ppm SiO_2, IS = 0.02, T = 33°C	
Time h	monomeric SiO_2 (ppm)	total SiO_2 (ppm)	monomeric SiO_2 (ppm)	total SiO_2 (ppm)	monomeric SiO_2 (ppm)	total SiO_2 (ppm)	monomeric SiO_2 (ppm)	total SiO_2 (ppm)	monomeric SiO_2 (ppm)	total SiO_2 (ppm)	monomeric SiO_2 (ppm)	total SiO_2 (ppm)
1	627.4	643.4	329.9	323.1	418.6	412.8	921.0	934.9	601.8	609.5	665.9	631.6
3	601.0	638.7	324.5									
5	626.9	641.7			421.5	418.8	931.9	928.1				
7		640.2							621.3	609.8	662.8	653.7
9		659.4										
11		639.1	330.5	307.0	432.5	436.2	926.0	913.0	627.4	645.1	679.0	628.6
23	656.3	651.6	317.9	309.8	430.0	422.1	930.2	949.5			634.2	619.1
27	638.0	641.5			427.5	436.1			blockage in flow-through simulator			
31	608.4	644.4	317.6	302.2	432.8	430.4	941.1	922.4			630.8	
42	608.4	644.4	311.3	302.5								

	E7 Experiment same as E1 + 300ppm glucose		E8 Experiment same as E1 + 50ppm xanthan gum	
Time h	monomeric SiO_2 (ppm)	total SiO_2 (ppm)	monomeric SiO_2 (ppm)	total SiO_2 (ppm)
1	897.3	916.2	899.5	924.2
3				
5	852.6	945.5	931.4	929.8
7				
9				
11	931.9	939.3	745.0	919.9
23	902.8	980.7	922.2	931.5
27				
31	930.1	938.6	930.7	952.3

C.1: Summary of monomeric and total [SiO_2] measured at the BPR for all experiments. Note that in the organic experiments, the solutions passing through the high-T oven and BPR had a silica concentration of 960ppm SiO_2 in order to yield a silica concentration of 640ppm SiO_2 after mixing with the added organic solution at the inlet of the tray.

	E1 Experiment 640ppm SiO_2, IS = 0.02, T = 58°C		E2 Experiment 320ppm SiO_2, IS = 0.02, T = 58°C		E3 Experiment 430ppm SiO_2, IS = 0.02, T = 58°C		E4 Experiment 960ppm SiO_2, IS = 0.03, T = 58°C		E5 Experiment 640ppm SiO_2, IS = 0.11, T = 58°C		E6 Experiment 640ppm SiO_2, IS = 0.02, T = 33°C	
Time h	monomeric SiO_2 (ppm)	total SiO_2 (ppm)	monomeric SiO_2 (ppm)	total SiO_2 (ppm)	monomeric SiO_2 (ppm)	total SiO_2 (ppm)	monomeric SiO_2 (ppm)	total SiO_2 (ppm)	monomeric SiO_2 (ppm)	total SiO_2 (ppm)	monomeric SiO_2 (ppm)	total SiO_2 (ppm)
1	404.9	642.2	328.8	322.1	418.5	416.8	344.1	911.9	323.2	656.3	364.7	620.8
3	387.6	637.6	325.0	329.6	419.5	426.5	375.4	919.4	373.3	699.6	385.7	628.4
5	431.3	632.9	331.9	327.8	427.4	428.7	373.1	961.2	364.1		394.5	636.5
7	436.2	646.3	340.5	330.4	424.8	431.3	381.7	938.0	382.4		375.8	637.3
9	443.2	644.2	333.0	335.2	458.9	439.9	390.1	964.3	382.1	627.8	345.5	629.1
11	433.7	651.8	319.5	319.2	429.1	443.2	386.7	966.7	355.7	631.6	398.5	602.9
23	435.7	646.6	334.3	326.1	442.8	463.0	325.5	964.1	blockage in flow-through simulator		340.2	
27	424.6		340.7	344.6			349.5	928.8			346.7	630.5
31	420.7	633.5	334.7	341.6	426.4	445.0	386.2	948.2			325.7	
42	426.0	654.5	348.1	324.9	433.3	448.7						

	E7 Experiment same as E1 + 300ppm glucose			E8 Experiment same as E1 + 50ppm xanthan gum		
Time h	monomeric SiO_2 (ppm)	total SiO_2 (ppm)	glucose (ppm)	monomeric SiO_2 (ppm)	total SiO_2 (ppm)	xanthan gum (ppm)
1	360.9	633.0		384.4	628.6	
3	384.7	611.1	319.6	407.0	629.6	59.5
5	378.9	668.4		391.9	617.4	
7	321.0	639.0	311.7	402.0	649.1	50.1
9	335.3	680.0		381.5	643.5	
11	387.5	676.4	290.3	363.6	668.5	57.5
23	360.9		256.4	400.4	660.4	53.6
27	390.9	675.8	294.2	353.9	653.3	57.5
31	408.6	671.6	310.0	379.3	623.9	59.9

C.2: Summary of monomeric and total [SiO_2] and organics concentration measured in the middle of the tray for all experiments.

	E1 Experiment 640ppm SiO_2, IS = 0.02, T = 58°C		E2 Experiment 320ppm SiO_2, IS = 0.02, T = 58°C		E3 Experiment 430ppm SiO_2, IS = 0.02, T = 58°C		E4 Experiment 960ppm SiO_2, IS = 0.03, T = 58°C		E5 Experiment 640ppm SiO_2, IS = 0.11, T = 58°C		E6 Experiment 640ppm SiO_2, IS = 0.02, T = 33°C	
Time h	monomeric SiO_2 (ppm)	total SiO_2 (ppm)	monomeric SiO_2 (ppm)	total SiO_2 (ppm)	monomeric SiO_2 (ppm)	total SiO_2 (ppm)	monomeric SiO_2 (ppm)	total SiO_2 (ppm)	monomeric SiO_2 (ppm)	total SiO_2 (ppm)	monomeric SiO_2 (ppm)	total SiO_2 (ppm)
1	326.4	630.2	321.3	319.9	418.5	422.6	345.2	907.9	-	654.4	301.1	665.6
3	391.5	645.3	325.0	323.6	426.2	431.5	341.2	896.9	345.7	633.4	305.3	660.2
5	410.0	639.6	331.0	325.9	432.4	428.8	364.8	936.7	372.0	-	320.4	651.0
7	429.7	645.6	335.7	330.3	437.3	435.6	377.0	935.2	360.4	-	315.9	640.3
9	428.8	655.8	336.8	334.9	440.2	443.6	395.8	942.5	376.3	656.7	308.1	607.1
11	446.7	656.7	318.2	318.1	444.7	449.5	378.6	961.1	375.7	610.0	320.0	611.5
23	427.3	628.4	330.9	325.7	437.0	458.3	320.3	981.5	blockage in flow-through simulator		314.6	602.0
27	418.9	646.1	335.4	348.2	434.2	442.4	338.6	954.0			295.9	598.5
31	427.5	641.0	347.7	332.0	432.3	455.6	329.0	966.0			292.1	
42	410.2	671.3	319.4	325.5								

	E7 Experiment same as E1 + 300ppm glucose		E8 Experiment same as E1 + 50ppm xanthan gum	
Time h	monomeric SiO_2 (ppm)	total SiO_2 (ppm)	monomeric SiO_2 (ppm)	total SiO_2 (ppm)
1	375.2	657.2	407.3	651.2
3	365.8	615.1	410.8	619.9
5	368.9	673.4	386.9	629.5
7	322.4	628.9	362.3	644.9
9	341.7	645.0	361.3	650.3
11	352.7	672.1	398.4	677.4
23	340.3	735.6	369.8	663.2
27	390.2	665.9	341.5	660.6
31	401.2	536.9	364.1	608.6

C.3: Summary of monomeric and total [SiO_2] measured at the outlet of the tray for all experiments.

C.4: Summary of average particle diameter and polydispersity (i.e., standard deviation) measured in the middle of the tray for most experiments.

	E1 Experiment 640ppm SiO_2, IS = 0.02, T = 58°C		E4 Experiment 960ppm SiO_2, IS = 0.03, T = 58°C		E5 Experiment 640ppm SiO_2, IS = 0.11, T = 58°C		E6 Experiment 640ppm SiO_2, IS = 0.02, T = 33°C		E7 Experiment same as E1 + 300ppm glucose	
Time h	particle diameter	poly-dispersity	particle diameter	poly-dispersity	particle diameter	poly-dispersity	particle diameter	poly-dispersity	particle diameter	poly-dispersity
1	16.40	2.30	12.50	1.50	19.84	3.15	10.70	1.30	12.09	1.22
3	19.66	3.02	14.50	2.40	21.70	3.78	-	-	-	-
5	24.54	4.13	18.20	3.10	22.67	3.02	12.30	1.50	15.23	2.29
7	28.66	4.08	24.60	4.40	26.36	2.53	13.60	1.50	14.73	2.83
9	34.12	4.73	20.70	9.00	33.18	3.88	11.80	1.60	-	-
11	32.44	15.63	28.90	11.00	36.04	4.46	12.30	1.40	11.16	1.54
23	28.04	5.67	24.40	8.50			-	-	-	-
27	-	-	-	-	blockage in flow-through simulator		-	-	-	-
31	35.74	8.73	19.00	4.70			10.30	1.40	15.83	4.06
42	33.70	8.54								